

**DISSERTATION PRESENTED FOR THE DEGREE OF
DOCTOR OF NATURAL SCIENCE (DR. RER. NAT.)**

**CO-TUTELLE BETWEEN THE UNIVERSITY OF MONTPELLIER
AND THE UNIVERSITY OF REGENSBURG**

**Viscosity-control and prediction of
microemulsions**

**Presented by Maximilian PLEINES
06/11/2018**

**Under the supervision of Prof. Thomas ZEMB
and Prof. Werner KUNZ**

Composition of the jury :

Werner KUNZ, Prof., University of Regensburg
Epameinondas LEONTIDIS, Prof., University of Cyprus
Jean-Marie AUBRY, Prof., University of Lille
Thomas ZEMB, Prof., University of Montpellier
Dominik HORINEK, Prof., University of Regensburg
Jean-François DUFRÊCHE, Prof., University of Montpellier

Jean DUHAMET, Dr., CEA/DEN Marcoule

Referee/ Ph.D. Director
Referee
Referee
Examination Committee/ Ph.D. Director
Examination Committee
Jury President

Invited Member/ Supervisor



**UNIVERSITÉ
DE MONTPELLIER**



Acknowledgements

This work was carried out in the framework of a Co-Tutelle between the partner-universities of Montpellier (France) and Regensburg (Germany) from November 2015 to November 2018. In France, the main work was performed in the lab « Laboratoire du Tri ionique par les Systèmes Moléculaires autoassemblés » (LTSM), part of the Institut de Chimie Séparative de Marcoule (ICSM), and in the lab « HEC » of the building G1 situated at the French commissary for atomic energy (CEA) in Marcoule. In Germany, the work was carried out at the Institute of Physical and Theoretical Chemistry at the University of Regensburg. This thesis was supervised by my Ph.D. directors Prof. Thomas Zemb and Prof. Werner Kunz as well as my supervisor Jean Duhamet. Without the support and participation of the following people, this thesis would not have been possible.

The scheme on which this whole work was possible is an “amont-aval” thesis, the first of its kind to have been approved as a project, early 2014. This “thèse-phare” has been implemented by Yves Brechet, the 10th High-Commissar after Joliot-Curie, in order to give special support to PhD work that treat jointly a deep scientific open question and an important technological lock. In my case, the technological challenge was to find the best compromise between selectivity and viscosity in liquid-liquid extraction.

Gilles Bordier as former head of the department devoted to nuclear recycling identified the core problem which is the necessary replacement of phosphate-based extractants. I thank him for giving this very exciting and motivating final goal of this thesis.

Moreover, I want to thank Prof. Thomas Zemb for giving me the opportunity to work at the ICSM, to guide and support me with patience during the whole time of my Ph.D. in every possible way as well as to give me a certain degree of freedom to promote my abilities to work independently.

I also express my gratitude to Prof. Werner Kunz for making this Co-Tutelle possible, to encourage me in his calm manner and for his advice and expertise.

Moreover, I would like to thank Jean Duhamet for his co-supervision, especially for his moral support and help with administrative issues.

I also deeply thank Wolfgang Fieber who showed great interest and trust in my work and with whom I had incredibly productive and pleasant working sessions and discussions on my model, especially on the aqueous case.

Furthermore, I would like to express special thanks to H  l  ne Martin, Elisabeth Roussigne and

Vainina Russello for all their efforts and help in administrative and financial issues as well as for their permanent positive attitudes.

I also want to thank the whole team of the LTSM, with whom I have spent a great time and who supported and helped me whenever needed. Special thanks go to Sandrine who has supported me in organizing the SANS experiments. I also express my gratitude to the rest of my colleagues from the ICSM, from University of Regensburg as well as from GI who helped me in every technical, safety or administrative question. I also thank C. Sorel and M.C. Charbonnel for providing the monoamide extractants.

Many thanks go to all my friends that have made my stays in Marcoule/Avignon as well as in Regensburg to an unforgettable time and with whom I share many fantastic and funny memories. I thank by name Michael, Markus, Robert, Mario, Alla, Carlos, Ran, Damian, Tobias, Patrick, Max - but there are many others that I did not name here individually.

Außerdem möchte ich meinen Eltern, meiner Schwester und meinem Bruder danken. Ohne ihre Unterstützung jeglicher Art wäre mein Studium und meine Promotion nie möglich gewesen. Des Weiteren danke ich meinem Bruder für die geduldige Hilfe und Einführung in JavaScript für die interaktive Umsetzung des Programms.

Zu guter Letzt danke ich von ganzem Herzen meiner unglaublichen Frau, Sabrina. Ich danke ihr für ihre Geduld und ihr Verständnis, ihr durchweg positives Denken, ihr Vertrauen und ihre Liebe - auch in schweren Zeiten - und für all das, was Worte nicht ausdrücken können. DANKE.

Abstract in English

Viscosity is a fundamental property of complex fluids that is still difficult to predict quantitatively. This macroscopic property originates from molecular as well as mesoscopic properties. The understanding and prediction of the evolution of the viscosity with changing parameters is crucial for several applications, *e.g.* for liquid-liquid extraction processes or the formulation of aqueous surfactant systems.

In this work, a new “minimal” thermodynamic model taking into account the relevant free energies was developed that helps to understand, control and predict the evolution of the viscosity of microemulsions in presence of solutes. The term “minimal” means in that context that this model is based on a minimal set of parameters that are all measurable and have a physical meaning, thus minimizing the number of adjustable parameters. This model that considers the chemical terms at the molecular scale, the physical terms at the mesoscale as well as the flow characteristics at the macroscale was applied on water-poor extracting microemulsions as well as on aqueous anionic surfactant systems.

Liquid-liquid extraction is the central technology in metal recycling. The extraction is always driven by oil-soluble extracting surfactants. TBP (Tributyl phosphate) is one of those widely used extractants. This molecule allows selective extraction of actinides in the framework of the nuclear fuel cycle as well as lanthanides for the life-cycle of electronic devices. Emulsification and demulsification processes in extraction devices are only efficient when the difference in viscosity between organic and aqueous phase is small. Although the processes using TBP as selective extractant are known since World-War II, economic and technical reasons motivate the research for alternative extractants. One promising approach is the use of *N,N*-dialkylamides which also have good extraction properties and significant advantages over TBP. The main disadvantage of *N,N*-dialkylamides is the viscosity of the organic phase, which increases exponentially when processes are intensified by increasing heavy metal and extractant concentration.

By combining scattering and phase behavior analysis, we show that the viscosity increase with heavy metal concentration can be rationalized by the formation of a three-dimensional living network with different topologies. The mesoscopic structure consists of a one-dimensional ionic liquid of alternating metal-nitrate chains at well-defined distances embodied in a “bottlebrush” microstructure. The main component of the network are W/O cylinders in equilibrium with endcaps and junction units. The corresponding microphase distribution of endcaps, cylinders and junctions could be calculated and reasonably correlated with the

viscosity for given systems. Moreover, the model was used to propose general formulation approaches for extractant systems.

Giant wormlike micelles formed by anionic surfactants in aqueous solution exhibit interesting rheological properties with high impact on industrial applications, especially in home and personal care products. Their structural and consequently their viscoelastic properties change during salt addition. Usually, the addition of a few percent of salt leads to an increase of the zero-shear viscosity by several orders of magnitude up to a viscosity peak. Further salt addition leads to a decrease in viscosity which was explained by the presence of more and more branching points that serve as stress relaxation points allowing micellar chains to slide along the micellar contour. The position and intensity of the viscosity peak changes by addition of solutes or fragrances and varies also with the type of salt added. This work further shows that this general model developed can be adjusted for the aqueous case and allows to reproduce the viscosity curve of an anionic surfactant in the presence of salt with almost perfect agreement. Furthermore, the influence of the type of salt as well as of added fragrances was predicted successfully and understood.

Abstract in French

La viscosité est une propriété fondamentale des fluides complexes et qui reste encore difficile à prédire quantitativement. Cette propriété macroscopique provient de propriétés moléculaires et mésoscopiques. La compréhension et l'estimation de l'évolution de la viscosité avec des paramètres variables est importante pour plusieurs applications, entre autres pour l'extraction liquide-liquide et pour la formulation de systèmes tensioactifs aqueux.

Dans ce travail, un nouveau modèle "minimal" prenant en compte les énergies libres mises en jeu a été développé pour aider à comprendre, contrôler et prédire l'évolution de la viscosité des microémulsions en présence de solutés. Le terme « minimal » signifie dans ce contexte que ce modèle est basé sur un ensemble minimal de paramètres qui sont tous mesurables ou ont une signification physique, ce qui permet d'éviter le recours à des paramètres ajustables. Ce modèle développé dans cette thèse considère les termes chimiques à l'échelle moléculaire, les termes physiques à l'échelle mésoscopique ainsi que les caractéristiques d'écoulement à l'échelle macroscopique et a été appliqué sur des microémulsions pauvres en eau utilisées pour l'extraction des métaux notamment pour le cycle de combustible nucléaire ainsi que sur des systèmes tensioactifs anioniques aqueux.

L'extraction liquide-liquide est la technologie centrale dans le recyclage des métaux. L'extraction est toujours conduite par des molécules de tensioactifs solubles dans l'huile. Le TBP (phosphate de tributyle) est l'un de ces agents tensioactifs d'extraction largement utilisés (extractants). Cette molécule permet l'extraction sélective des actinides dans le cadre du cycle du combustible nucléaire ainsi que des lanthanides pour le cycle de vie des dispositifs électroniques. Les procédés d'émulsification et de déémulsification dans les dispositifs contacteurs ne sont efficaces que lorsque la différence de viscosité entre la phase organique et la phase aqueuse est typiquement inférieure à cinq. Même si les procédés utilisant le TBP comme extractant sélectif sont connus depuis la Seconde Guerre mondiale, des raisons économiques et techniques motivent la recherche de systèmes moléculaires d'extraction alternatifs. Une approche prometteuse est l'utilisation de *N,N*-dialkylamides qui ont également de bonnes propriétés d'extraction et des avantages significatifs par rapport au TBP. Le principal inconvénient des *N,N*-dialkylamides est la viscosité de la phase organique qui augmente de façon exponentielle lorsque les processus sont intensifiés en augmentant la concentration de métaux lourds et d'extractants.

En combinant des méthodes de la diffusion et l'analyse de l'évolution de comportements de phase, nous montrons que l'augmentation de la viscosité avec la concentration en métaux lourds

peut être compris par la formation d'un réseau des « polymères vivants » tridimensionnel. La structure mésoscopique est constituée d'un liquide ionique unidimensionnel de chaînes alternées métal-nitrate à une distance bien définie incorporée dans une microstructure "bottlebrush". Les composants principaux du réseau sont les cylindres E/H en équilibre avec des embouts et des points de connexion. La distribution des micro-phases correspondante des embouts, des cylindres et des jonctions pourrait être calculée et corrélée raisonnablement avec la viscosité pour des systèmes donnés. De plus, le modèle a été utilisé pour proposer des approches générales de formulation pour les systèmes chimiques extractants.

Les micelles géantes formés par des tensioactifs anioniques en solution aqueuse présentent des propriétés rhéologiques intéressantes avec un impact élevé sur les applications quotidiennes importantes en cosmétiques et détergence. Leur structure et par conséquent leurs propriétés viscoélastiques changent lors de l'ajout de sel. Habituellement, l'addition de quelques pourcents de sel conduit à une augmentation de la viscosité de cisaillement zéro de plusieurs ordres de grandeur jusqu'à un pic de viscosité. L'addition de sel supplémentaire conduit à une diminution de la viscosité que nous avons expliquée par la présence de plus en plus de points de ramification qui servent comme points de relaxation permettant aux chaînes micellaires de glisser le long du contour micellaire. La position et l'intensité du pic de viscosité changent par addition de solutés ou de parfums et varient également avec le type de sel ajouté. On montre que le modèle peut être ajusté pour le cas aqueux et permet de reproduire la courbe de viscosité d'un tensioactif anionique en présence de sel avec un accord presque parfait. En outre, l'influence du type de sel ainsi que des parfums ajoutés a été prédite avec succès et comprise.

Table of Contents

I	Introduction.....	9
I.1	Goal of this thesis and approach	10
I.2	State of the art	12
I.2.1	Liquid-liquid extraction in general.....	12
I.2.2	Extraction on industrial scale: Important factors	15
I.2.3	Viscosity – a simple explanation.....	20
I.2.4	Extractant solutions	27
I.2.5	Possible reasons for viscosity increase in the reverse space	40
I.2.6	The system dialkylamide – uranyl.....	55
II	Experimental Observations	66
II.1	Experimental methods and chemicals	67
II.1.1	Chemicals and materials.....	67
II.1.2	Preparation of the organic phase	67
II.1.3	Determination of uranyl content by potentiometric titration.....	67
II.1.4	Rheological investigations	68
II.1.5	Small- and Wide-Angle X-ray Scattering	69
II.1.6	Small-Angle Neutron Scattering	69
II.1.7	Methods to estimate the spontaneous packing parameter	71
II.2	Experimental observations leading to a mesoscopic model.....	79
II.2.1	Influence of extractant and uranyl concentration	79
II.2.2	Influence of temperature	83
II.2.3	Influence of shearing and rheological investigations	88
II.2.4	Influence of diluent	90
II.2.5	Small- and Wide-Angle X-Ray Scattering analysis	93
II.2.6	Small-Angle Neutron Scattering analysis	106

II.2.7	Conclusions and simplified image of the mesoscopic structuration in the organic phase	114
III	Development of a Minimal Model	117
III.1	Main idea and underlying theory	118
III.1.1	Main principle	118
III.1.2	Microphase distribution	119
III.1.3	Modification for the presence of a second extractant	122
III.1.4	Towards an intuition-driving image of the organic phase in 2D – Monte-Carlo-like simulation	122
III.1.5	Microphase equilibrium controlling the viscosity	127
III.2	Implementation in a user-friendly interface	131
III.3	General results of the model	136
III.3.1	Presentation of Accordion I: ‘General model – for understanding’	136
III.3.2	Variation of the packing parameter	139
III.3.3	Addition of a second extractant	143
III.3.4	Metal response	146
III.3.5	Bending constant	149
III.3.6	Concentration dependence and Onsager transition	151
III.4	Application of the model on the specific system	154
III.4.1	Presentation of Accordion II	154
III.4.2	Estimation of the packing parameter and fitting of the experimental values	156
III.4.3	Diluent dependence and solvent penetration	158
III.5	Conclusion and remarks	160
III.5.1	Summary of the model and critical remarks	160
III.5.2	Compatibility with a COSMO approach	162
III.5.3	Conclusion and propositions for the solution of the viscosity problem	164

IV Formulation Strategies to solve the Problem	167
IV.1 Changing the extractant geometry.....	168
IV.2 Changing the diluent by additives.....	172
IV.3 Mixing two extractants.....	177
IV.4 Conclusion.....	179
V Application of the Model to Aqueous Systems	180
V.1 Introduction	181
V.2 The “salt curve” in presence of model solutes and fragrances.....	183
V.3 Adapting the model for the aqueous case.....	188
V.3.1 General theory for the calculation of the microphase distribution and viscosity.....	188
V.3.2 Evolution of the spontaneous packing parameter	193
V.3.3 Co-solvent effect of fragrance molecules.....	195
V.3.4 Interface softening effect.....	196
V.4 Results of the model.....	198
V.4.1 10% SLES pure in water	198
V.4.2 Influence of added electrolytes on the viscosity curve	202
V.5 Conclusion.....	209
VI General Conclusion and Outlook	212
VI.1 Summary and general conclusion	213
VI.2 Strategies for refinement	217
VI.3 Further applications.....	221
VI.3.1 Prediction of the cloud point	221
VI.3.2 Parallelism to the HLD-NAC concept	225
VII Annex.....	230
VII.1 List of abbreviations.....	231

VII.2	Table of figures and tables	232
	Figures - short titles.....	232
	Tables	245
VII.3	Experimental methods – chemicals and underlying theory	247
VII.3.1	List of chemicals used in this work.....	247
VII.3.2	X-Ray and Neutron Scattering	248
VII.3.3	Rheology	250
VII.3.4	Potentiometric titration.....	251
VII.4	Short introduction to COSMO-RS	253
VII.5	Phase diagram of surfactant structures according to Cates	255
VII.6	Supplementary information to Chapter II.2	256
VII.6.1	Additional viscosity curves with variation of extractant concentration	256
VII.6.2	Assumptions and input values for the geometrical calculation of the spontaneous packing parameter	261
VII.6.3	Tables of viscosity data and distribution coefficients	262
VII.6.4	Additional SWAXS spectra and presentation in log-log and lin-lin	269
VII.6.5	Additional SANS spectra and fit results	272
VII.7	Supplementary information to Chapter III	275
VII.7.1	Hexagon definition and estimation of aggregation number per microphase ..	275
VII.7.2	JavaScript code.....	278
VII.7.3	Interfacial tension measurements of different extractants.....	278
VII.8	Supplementary information to Chapter V	280
VII.8.1	Table with necessary input parameters	280
VII.8.2	Details on the estimation of packing parameter, aggregation number and volume per microphase on a hexagonal grid.....	280
VII.9	References	284

I INTRODUCTION

I.1 Goal of this thesis and approach

Liquid-liquid extraction is the central technology in metal recycling. An important application is the recovery of major actinides – Uranium and Plutonium – in the framework of minimization of highly radioactive waste by using Mixed Oxide Fuel (MOX) and the required closing of the nuclear fuel cycle by use of fast neutrons in the future. Although the processes using Tributyl phosphate (TBP) as selective extractant are known since world-war II, economic and technical reasons motivate the research for alternative extractants. One promising approach that is under development since several years is the use of *N,N*-dialkylamides which also have a high affinity towards Uranium and Plutonium and significant advantages over TBP. The main disadvantage of *N,N*-dialkylamides is the viscosity of the organic phase which increases exponentially when processes are intensified by increasing uranyl and extractant concentration. Emulsification and demulsification in extraction devices are only efficient when the difference in viscosity between organic and aqueous phase is small.

Until now, the approaches to solve the problem and optimize formulations are based on experimental investigations along “*experimental design*”^[1] in order to find a compromise between selectivity and hydrodynamic properties such as viscosity and interfacial tension. To our knowledge, there is no published predictive model that explains the viscosity increase. The present work tries to understand the viscosity increase in three consecutive steps.

In the first step, the problem of the viscosity increase in presence of metal ions is analyzed by detailed investigation (*cf.* Chapter II). The influence of different parameters on the viscosity is investigated and scattering experiments are carried out in parallel. The experimental results lead to the identification of the type of microstructure in the organic phase which helps to understand the origin of the viscosity increase.

In a second step (*cf.* Chapter III), this picture is used to develop a “*minimal*” model at nanoscale. The term “minimal” means in this context that the model can be used with a minimum of necessary input parameters that are either measurable or have at least a precise definition and physical meaning. This model considers the chemical terms at molecular scale, the physical terms at mesoscale as well as the flow characteristics at macroscale. This concept allows to calculate the number distribution of the microphases, to obtain a qualitative picture of the microstructure by a Monte-Carlo-like simulation and to predict the viscosity evolution.

In the third step (*cf.* Chapter IV), the model is used to propose approaches to solve the problem of viscosity increase. Having identified the viscosity-determining parameters, knowledge-based

formulations are proposed and tested. The development of this simple mesoscopic model allows to make formulation in the field of extractant systems more predictable and helps to avoid strict trial-and-error formulation.

Moreover, this general theory is also applied and adjusted on an aqueous system (*cf.* Chapter V). The bell-shaped viscosity curve of an anionic surfactant in water in presence of salt can be reproduced by this theory. The influence of some hydrophobic model solutes as well as the type of salt on the position and intensity of the viscosity maximum can be predicted successfully.

In parallel, the underlying equations for both the aqueous and the organic case were implemented in a user-friendly interface. It is a useful tool to understand the new thermodynamic model and resulting tendencies. Therefore, it is recommended to every reader, to use the program and “play” with the sliders. The program can be assessed by the following link:

www.vyrix.de/sim

In the following, the background to this topic as well as the theoretical basics are described.

I.2 State of the art

I.2.1 Liquid-liquid extraction in general

I.2.1.1 Metal recovery and recycling

Metals are omnipresent and essential for everyday life.^[2] They are crucial for all kinds of electronic devices such as smartphones, but also for cars or the construction industry. Moreover, they are essential to produce electric energy by for example windmills or by nuclear power plants. According to their economic importance and their supply risk, the metals can be classified as “critical metals” or “strategic metals”. A metal is considered as “critical” by the European Union, when it follows the three following criteria^[3–6]:

- It has a significant economic importance for key sectors.
- The EU is faced with high supply risks.
- There is a current lack of substitutes for that metal.

In 2017, the EU has classified 27 raw materials as critical. For most of them, China is the main global producer. A list of potentially endangered elements can be found in **Figure 1**.^[7]

H

Hydrogen

He

Helium

3

Li

Lithium

4

Be

Beryllium

11

Na

Sodium

12

Mg

Magnesium

19

K

Potassium

20

Ca

Calcium

21

Sc

Scandium

22

Ti

Titanium

23

V

Vanadium

24

Cr

Chromium

25

Mn

Manganese

26

Fe

Iron

27

Co

Cobalt

28

Ni

Nickel

29

Cu

Copper

30

Zn

Zinc

31

Ga

Gallium

32

Ge

Germanium

33

As

Arsenic

34

Se

Selenium

35

Br

Bromine

36

Kr

Krypton

37

Rb

Rubidium

38

Sr

Strontium

39

Y

Yttrium

40

Zr

Zirconium

41

Nb

Niobium

42

Mo

Molybdenum

43

Tc

Technetium

44

Ru

Ruthenium

45

Rh

Rhodium

46

Pd

Palladium

47

Ag

Silver

48

Cd

Cadmium

49

In

Indium

50

Sn

Tin

51

Sb

Antimony

52

Te

Tellurium

53

I

Iodine

54

Xe

Xenon

55

Cs

Cesium

56

Ba

Barium

72

Hf

Hafnium

73

Ta

Tantalum

74

W

Tungsten

75

Re

Rhenium

76

Os

Osmium

77

Ir

Iridium

78

Pt

Platinum

79

Au

Gold

80

Hg

Mercury

81

Tl

Thallium

82

Pb

Lead

83

Bi

Bismuth

84

Po

Polonium

85

At

Astatine

86

Rn

Radon

87

Fr

Francium

88

Ra

Radium

Limited availability – supply risk

Rising threat from increased use

Serious threat in the next 100 years

57

La

Lanthanum

58

Ce

Cerium

59

Pr

Praseodymium

60

Nd

Neodymium

61

Pm

Promethium

62

Sm

Samarium

63

Eu

Europium

64

Gd

Gadolinium

65

Tb

Terbium

66

Dy

Dysprosium

67

Ho

Holmium

68

Er

Erbium

69

Tm

Thulium

70

Yb

Ytterbium

71

Lu

Lutetium

89

Ac

Actinium

90

Th

Thorium

91

Pa

Protactinium

92

U

Uranium

93

Np

Neptunium

94

Pu

Plutonium

95

Am

Americium

96

Cm

Curium

97

Bk

Berkelium

98

Cf

Californium

99

Es

Einsteinium

100

Fm

Fermium

101

Md

Mendelevium

102

No

Nobelium

103

Lr

Lawrencium

Figure 1: Endangered elements according to a research conducted by the Chemical Innovation Knowledge Transfer Network. Adjusted and replotted from [7].

The increased use of certain metals, the limited availability, the enormous prices of certain metals, particularly rare earth elements - due to their control by China - and environmental aspects are only some of the reasons why metal recycling should be intensified and promoted.

1.2.1.2 Liquid-liquid extraction

The central technology for metal recycling, but also for the recovery of metals by ore processing is *liquid-liquid extraction* (LLE). LLE, also known as solvent extraction, is a method to separate compounds based on their relative solubility in two different immiscible liquids.^[8] In the case of recovery of metals, the distribution of the solute takes place between a polar aqueous phase and an apolar organic phase. In order to quantify this distribution, the *distribution coefficient* D_M is defined:

$$D_M = \frac{[M]_{\text{org}}}{[M]_{\text{aq}}} \quad (1)$$

where $[M]_{\text{org}}$ and $[M]_{\text{aq}}$ represent the concentrations of the metal species M in the organic or respectively in the aqueous phase. When coexisting ions have different distribution coefficients, separation can be obtained. The understanding of the relying molecular driving forces^[9] in known regimes of the phase diagram of water-poor microemulsions^[10] is the basis for effective separation. For detailed information, the review about “*ienaics*”^[11] is recommended.

The final goal of a LLE process is to transfer ions that are aimed to extract selectively from phase A into phase B , while undesired ions stay in phase A . The term “*hydrometallurgy*” describes the recovery of metals from ores, concentrates and recycled or residual materials. Its main steps are dissolution, concentration and recovery. In the framework of hydrometallurgy, phase A represents in most cases an acidic aqueous phase loaded with desired and undesired ions. This phase is also called “*feed solution*” and results from treatment of either ores and minerals or - in the case of recycling – valuable waste, *e.g.* electronic and metallic scrap or spent nuclear fuel rods with acid. This wet-chemical process is called “*leaching*”. In a second step, the desired ions are extracted into the organic phase. In a last step, the metals are back-extracted from the organic phase – the “*extract*” - into a fresh aqueous phase.^[12] This process is also called “*stripping*”. The organic solvent is recuperated and can be reused for another extraction cycle. These steps are schematically represented in **Figure 2**.

¹ By similarity with electronics, “*ienaics*” (Greek: the object that is moving). *ienaics* is the science of controlled transfer of hydrated ions and other charged colloidal aggregates between coexisting complex fluids and denotes therefore the basis of separation processes of electrolytes^[11].

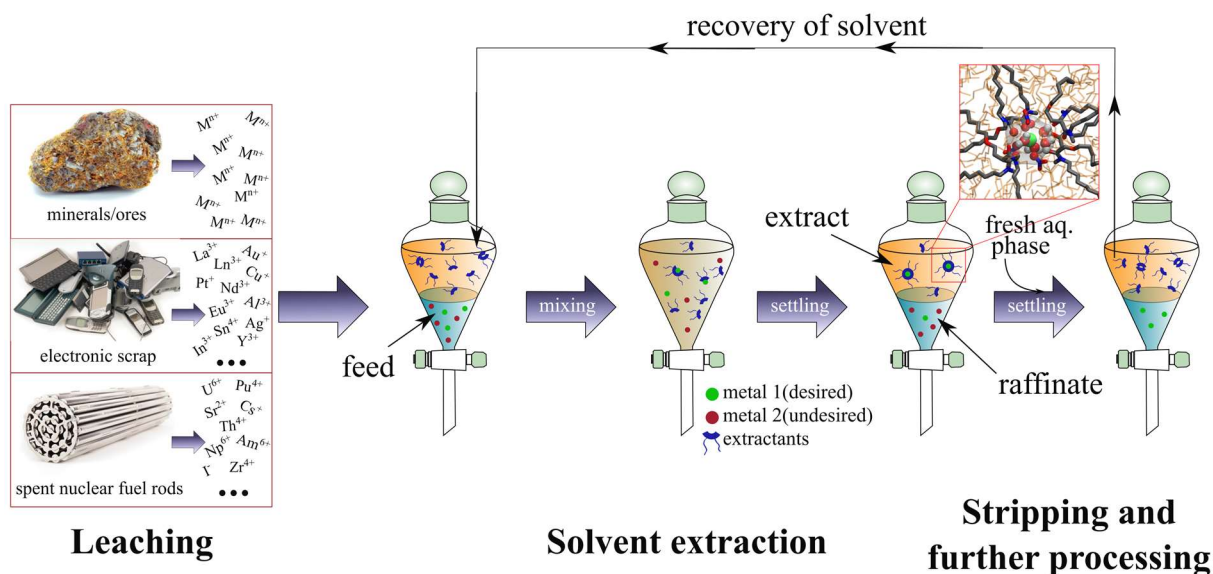


Figure 2. Schematic representation of a hydrometallurgical process starting from “leaching” over “solvent extraction” to “stripping”.

In order to make such a process efficient, the distribution coefficient D should be high, e.g. in the ideal case, the majority of the desired ions should “dissolve” in the apolar organic phase. According to the old alchemic wisdom “*Similia similibus solvuntur*” – “*Like dissolves like*” this seems to be counter-intuitive at first sight. Ions will prefer the polar aqueous phase which is true for most of the cases when the organic phase only consists of a simple diluent. This can be for example a linear or branched alkane. Therefore, liquid-liquid extraction of metals requires the use of so-called extractants. These molecules consist of a polar complexing group and hydrophobic chains. The most effective extractants have branched chains. This has only been understood recently in terms of entropy.^[13] Moreover, the often used di-ethylhexyl chains possess a high stability against radiolysis.^[14] Additionally, the chemical precursor for its production – 2-ethylhexanol – is cheap due to an annual production of 2 million tons per year from propylene.^[15] The amphiphilic character of extractants allows them to form complexes or aggregates with the desired ions. The resulting polar cavity surrounded by extractant chains permits the solubilization of the ions to be extracted. Knowledge-based choice of extractant type and conditions results in selectivity with respect to undesired ions. Since in pure form, the viscosity is quite high ($\sim 50 \text{ mPa}\cdot\text{s}$), the extractants are dissolved in a diluent that is immiscible with water. In most cases, an alkane or an aromatic compound is chosen for that purpose. The formation of complexes and aggregates will be discussed more in detail in Chapter I.2.4, after the extraction on industrial scale is introduced as well as the central topic of this thesis – the viscosity (*cf.* Chapter I.2.3).

I.2.2 Extraction on industrial scale: Important factors

Solvent extraction is not always carried out in separatory funnels as indicated in **Figure 2**. On industrial scale, special extraction devices are used to contact the immiscible phases. In the following, three important devices introduced and briefly discussed.

I.2.2.1 Mixer-Settler^[8,12,16,17]

The mixer-settler consists of two stages. In the first, smaller, chamber the two phases are mixed by an impeller to increase the contact surface between the phases and thereby to facilitate the mass transfer. In the second, larger chamber, the two phases are separated by gravity due to their density differences. The transportation of the liquids from one stage to the next occurs either by gravity or using pumps. The so-called “*settling*” of the phases is supported by coalescence plates. Each mixer-settler unit provides a single stage of extraction. The different stages can be coupled in a countercurrent process, so that multiple mixer-settlers are installed with mixing and settling chambers in alternating arrangement (so that the settled heavy phase outlet feeds the inlet of the adjacent stage mixing chamber). In that way, all extraction, washing and stripping steps necessary can be carried out by mixer-settlers (*cf.* **Figure 3**).

I.2.2.2 Centrifugal Extractors^[8,12,16–18]

Centrifugal contactors are like mixer-settlers discrete-stage units and provide one extraction stage. They can be also coupled for multi-stage extractions. Centrifugal extractors are equipped with a spinning rotor that a) mixes the two phases intensely and b) induces a separation of the two phases inside the rotor. The centrifugal forces can be up to 300 G, leading to a fast and efficient phase separation. Due to the low residence time (the liquid molecules usually remain not longer than about 2 min in a multistage industrial centrifugal extractor^[8, pp.398–399]), solvent degradation can be minimized. The separated phases exit the contactor via overflow and underflow weirs, similar to a mixer-settler (*cf.* **Figure 4**).

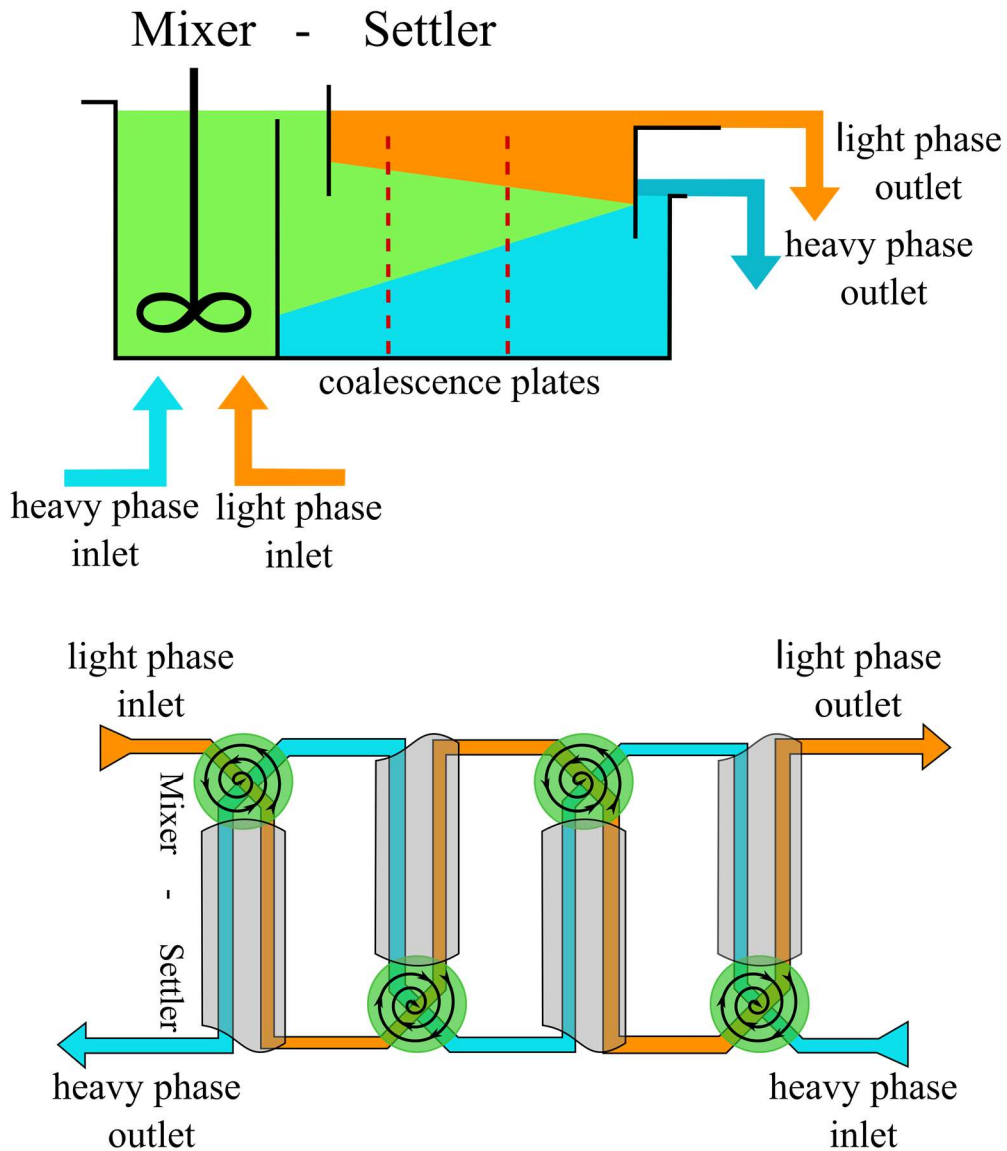


Figure 3. Top: Schematic representation of a mixer-settler. Bottom: Mixer-settler in a countercurrent arrangement

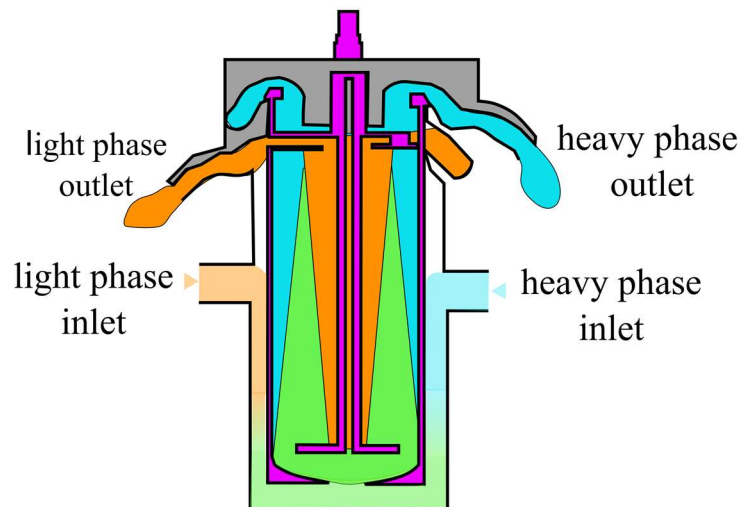


Figure 4. Schematic representation of a centrifugal extractor

I.2.2.3 Pulsed Column^[8,12,16,17]

Unlike mixer-settlers and centrifugal extractors, pulsed columns are contactors without individual extraction stages. The liquids are continuously fed to the column and flow in countercurrent, the lighter organic phase from bottom to top, the aqueous phase in the opposite direction. Mechanical energy is applied to pulse the liquids in the column up and down. The column is filled with perforated plates or other plates to promote droplet formation as the dispersed phase is pushed through the plates (*cf.* **Figure 5**). Due to the pulsing (often done by pressured air) droplet size of the dispersed phase is reduced, the interfacial area increased and mass transfer enhanced. The process can be carried out in aqueous continuous mode or organic continuous mode, *e.g.* either the organic or the aqueous phase can be dispersed. Pulsed columns are in use for the extraction of uranium and plutonium (PUREX process, *cf.* Chapter I.2.6.2) in la Hague, a nuclear fuel reprocessing plant in France.

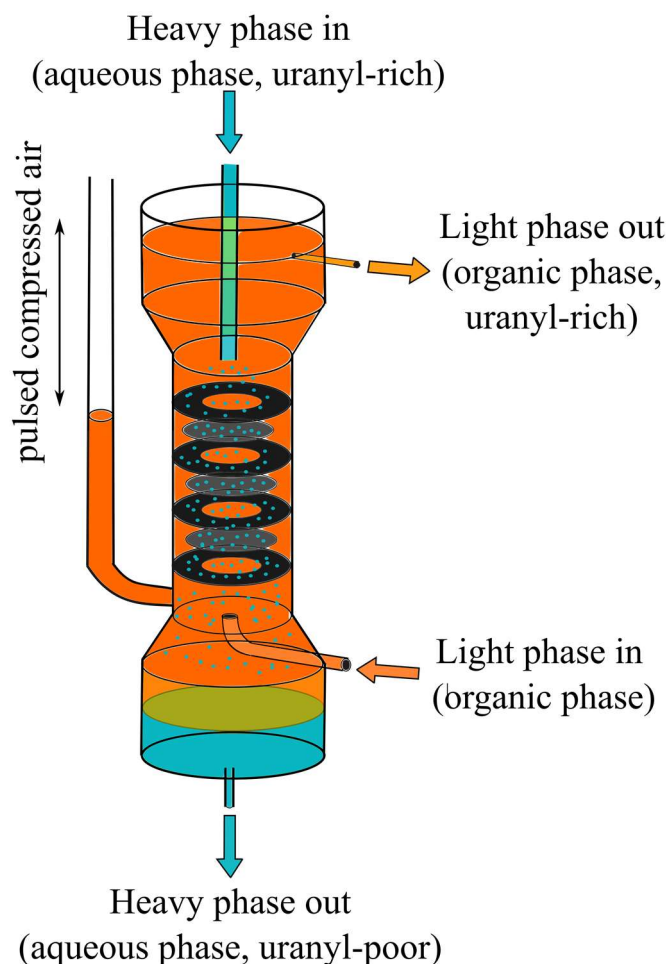


Figure 5. Schematic representation of a pulsed column. A typical extraction of uranyl by a pulsed column is shown. The organic phase is loaded with uranyl during the extraction.

1.2.2.4 Important factors

The choice of the right extracting system and the extraction device is crucial for the efficiency of the extraction process. The selection of the right solvent is the key for a successful separation. There is a set of important factors and parameters that have to be considered. A selection is mentioned in the following and roughly discussed:^[8,12]

- *Selectivity* towards certain ions: High distribution or respectively selectivity coefficients allow to minimize the number of steps needed for a certain purity or separation.
- *Capacity*: A high value of the solvent capacity for solutes permits to decrease the feed-to-solvent ratio. The capacity is often indicated by a high distribution ratio D_M .
- *Recoverability*: The solvent should be easy to recover, ideally by simple flash or a stripping column.
- *Economic aspects*: The solvents, e.g. the extractant and diluent should be readily available and the costs per year should be low. Furthermore, the chemical, thermal and radiolytic stability of the solvent as well as the corrosion properties can be also counted to economic aspects.
- *Security and environmental factors*: Toxicity and flammability as well as environmental impact has to be considered.
- *Density difference*: The difference in density between the heavy (aqueous) phase and the lighter (organic) phase should be high enough to enable fast settling.
- *Interfacial tension*: High interfacial tension enables a rapid settling due to easier coalescence. On the other hand, low interfacial tension facilitates phase dispersion increasing the interfacial areas and separation efficiency. If the interfacial tension is too low, stable emulsions can be produced. Therefore, a compromise has to be found. In most cases a higher interfacial tension is preferred.
- *Viscosity and viscosity ratio*: The viscosity η is an important factor. It is related to the molecular diffusion coefficient D via the Stokes-Einstein relation^[19]:

$$D = \frac{k_B T}{6\pi\eta R} \quad (2)$$

with k_B being the Boltzmann constant, T the temperature and R the radius of the moving particle. Therefore, high viscosities reduce the mass transfer efficiency and can lead to difficulties in pumping and dispersion.^[20,21] The deformation time τ_{def} is given by the ratio of solvent viscosity to the external stress σ_{ext} acting on the drop.

$$\tau_{\text{def}} = \frac{\eta}{\sigma_{\text{ext}}} \quad (3)$$

As a consequence, droplets with higher viscosities are more difficult to disperse. That means, a higher external stress such as a higher shear rate has to be applied to deform and break a drop.^[22] Accordingly, viscosity is related to emulsion stability and phase separation time.^[20]

More important than the viscosity itself is the viscosity ratio between the dispersed (η_D) and the continuous phase (η_C). In dilute systems, the viscosity ratio η_D/η_C is often close to 1. **Figure 6** shows, what happens if this viscosity ratio significantly deviates from 1. On the y-axis, the *capillary number* C_a is plotted as a function of the viscosity ratio of the dispersed phase η_D and the continuous phase η_C . This number (C_a) is an important, dimensionless quantity for fluid mechanics. It represents the “*ratio between viscous to capillary forces*”^[20, p.71, 23, pp.712–713] and is defined as follows:

$$C_a = \frac{\eta_C \dot{\gamma} r_0}{\sigma_I} \quad (4)$$

with σ_I being the interfacial tension and $\dot{\gamma}$ the applied shear rate. The value of the initial droplet radius r_0 can change with increasing shear rate. The droplet deformation depends on the viscosity ratio.^[22] The effect of droplet break-up is given by a certain *critical capillary number* C_a^* . If the capillary number for a certain viscosity ratio is below C_a^* , the applied energy does not break the droplets. Instead, the shear force is used to spin the droplet.^[23] That means, that the shear, or respectively, the droplet deformation is not fast enough to break the droplet compared to the drop ability to spin within the medium.^[24] Looking at **Figure 6**, one can learn, that it is easy to create an emulsion, if the viscosity ratio is close to 1. If the ratio strongly deviates from that value, it becomes more difficult. The same can be concluded for the phase separation. If the viscosity ratio strongly differs from 1, stable emulsions are formed. This is particularly true if the continuous phase is the more viscous one. In that case, coalescence is slowed down because the separating film of liquid between the drops cannot be drained quickly. As a rule of thumb for efficient mixing and demixing, the viscosity ratio between the two contacted phases should not exceed a ratio of 1:5.^[22,24, pp.110–120]

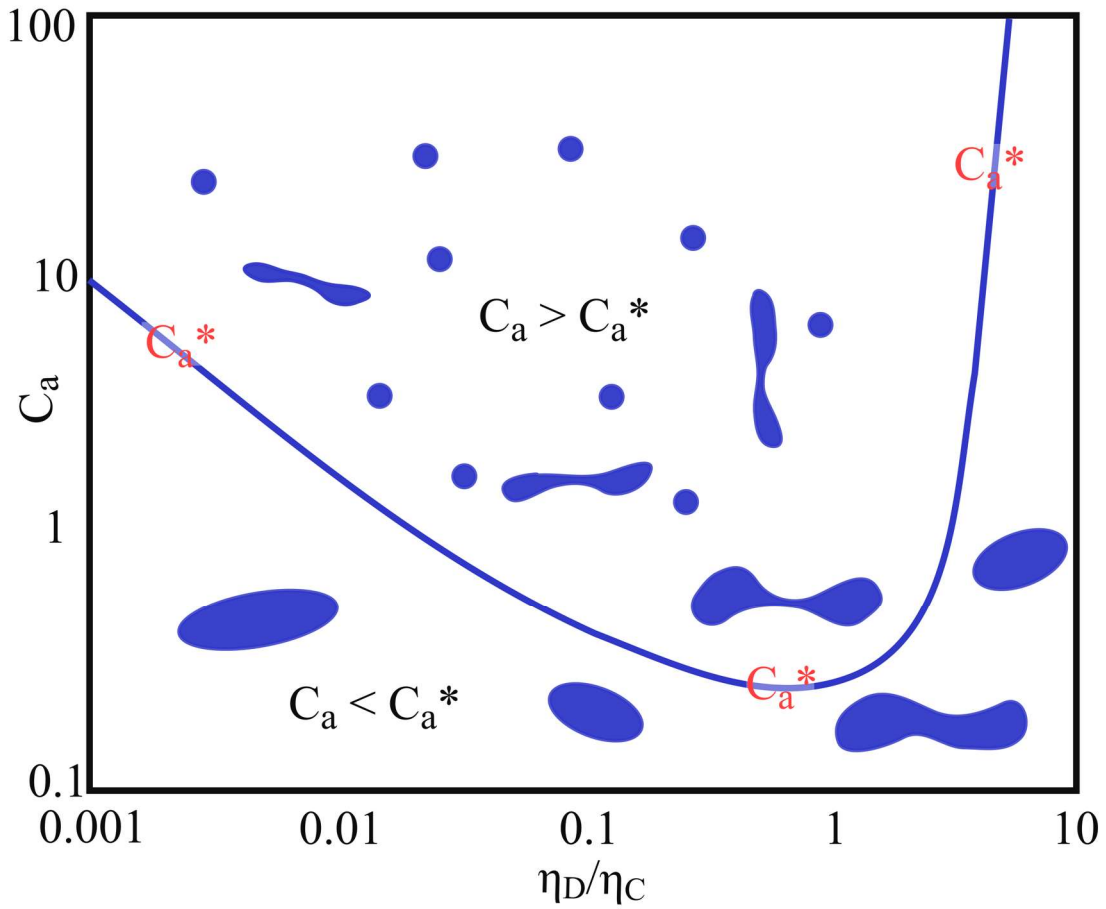


Figure 6. Schematic evolution of the critical capillary number as a function of the viscosity ratio. Figure replotted and adjusted from [24, pp.110–120].

The focus of this work is placed on the viscosity which is introduced in the next chapter and explained in a simple illustrative way.

I.2.3 Viscosity – a simple explanation

Viscosity is a fundamental and characteristic property of liquids – for pure ones as well as for mixtures and dispersions. Each liquid has a certain internal resistance against flow or shear. The viscosity is a measure of this resistance.^[25] It is a macroscopic property, but it originates from molecular and mesoscopic properties.^[26]

I.2.3.1 Two-Plate Model (Newton)

The dynamic viscosity is the tangential force per area that is required to slide a certain layer against another layer (*cf.* **Figure 7**).

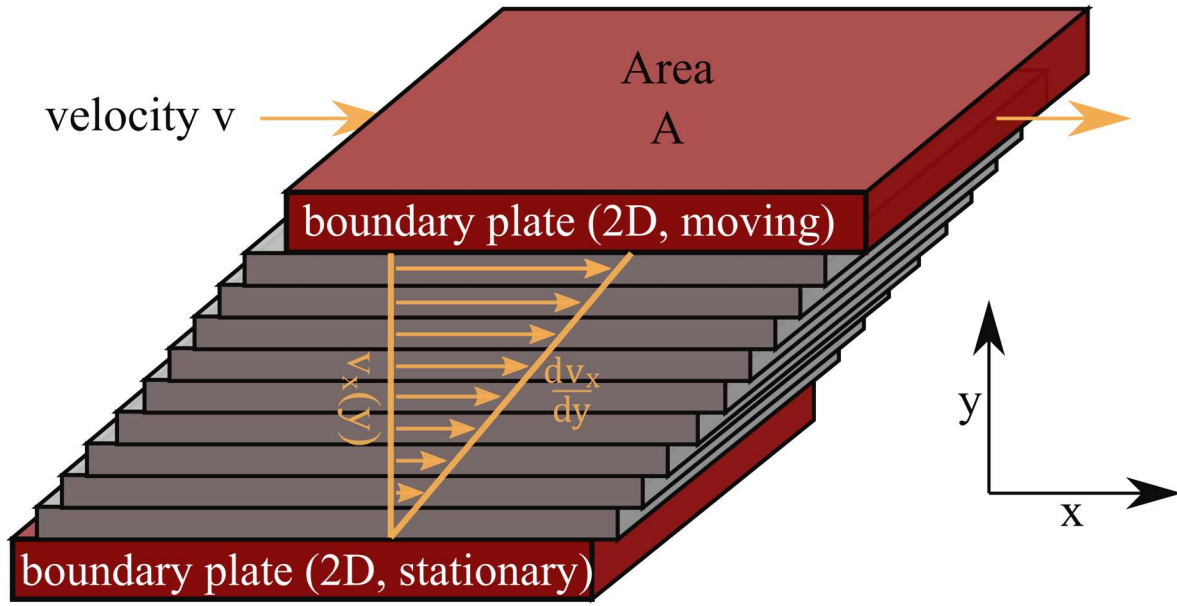


Figure 7: Schematic representation of simple shear of a liquid film

Imagine two parallel plates of fluid with equal area A . One plate is fixed, the other is forced to move with a constant velocity v . The force needed to move the plate is called *shear force* F and is dependent on the velocity v_x , the area of the plates A and inversely proportional to the distance dy between the plates.

$$F = \eta \cdot \frac{dv_x}{dy} \cdot A = \eta \cdot \dot{\gamma} \cdot A = \sigma \cdot A \quad (5)$$

The proportionality factor η is therefore a measure of how resistive the fluid is to flow and is called “*viscosity*”. This simple proportionality is only valid for so-called “*Newtonian fluids*” like for example water. For so-called “*viscoelastic fluids*”, the behavior can strongly deviate from this relation, dependent on the applied velocity gradient $\frac{dv_x}{dy}$. This velocity gradient is a measure of the speed at which the intermediate layers are moving with respect to each other. This gradient is also called “*shear rate*” $\dot{\gamma}$ and is given in the unit $[s^{-1}]$. The stress that has to be applied parallel to the surface of the liquid to cause that shear is called *shear stress* σ and is given in the unit of a pressure $[Pa = N/m^2]$.

1.2.3.2 A simple metaphore for viscosity

Another definition that can be found is that the viscosity is a measure for momentum transfer within a liquid.^[27] In gases, this momentum transfer is mainly dominated by translation of the molecules with only relatively few collisions and can be described by the kinetic theories of

gases. In the case of liquids, the momentum transfer is mainly dominated by collisions and interacting force fields.^[28,29] Consequently, it is a way to describe the effect of the movement of one constituent (depending on the type of the liquid – molecule, colloid or polymer) on the constituents that are adjacent. If the movement of one constituent *A* causes a strong movement of the neighboring constituents, the viscosity is high. The sliding of one layer is strongly coupled to the sliding of other layers and the momentum transfer is high. In contrast hereto, the viscosity is low if the neighboring constituents are hardly affected by the movement of the constituent *A*.

There are two general factors that cause viscosity. The first and obvious ones are intermolecular attractive forces between ‘constituents’ of the liquid. The stronger they are, the more difficult the layers can slip and the higher is the viscosity. However, there is a second, not negligible factor – intermolecular repulsive forces and excluded volume interactions. These effects become particularly important at higher concentrations. They are based on the idea that when one constituent of the liquid has to move from one position to another, other parts of the liquid have to get out of the way first and momenta are exchanged.^[30]

A very illustrative example drawn from life helps to understand the origin of viscosity that is crucial for this work. Imagine a person *P* being at a concert.^[30] This person has to go from Position *A* (e.g. next to the stage) to Position *B* (e.g. to the beer bar). In the following, different scenarios will be described to make the main origin of the viscosity clear. The scenarios are illustrated by **Figure 8**. In this figure, the spheres can represent either molecules, colloids, monomer units of polymers or – as in the example of a person at the concert – humans. The expression “spheres” used in the following will also indicate these different viscosity-determining constituents of a liquid.

- (1) The concert is not well attended. In order to get from Point *A* to *B*, the person *P* does not have to overcome strong resistance – *P* will have the beer after a short time. Transferring this case in the language of physical chemistry, the concentration of spheres is low and only a few spheres have to move and will undergo momentum transfer. The viscosity is expected to be low.
- (2) The concert is well-attended. The person *P* will have to make many people move in order to fetch the beer. Furthermore, *P* is popular and has to chat with a lot of people on his way to position *B*. As a consequence, he has arrived at the beer bar after quite a long time. In the analogy of physical chemistry, the concentration of spheres is high. A high

number of spheres will have to be moved to let the blue sphere pass. In addition, the blue sphere experiences intermolecular attractive forces. The viscosity is expected to be higher than in case (1).

- (3) The concert is well-attended, but boring. A lot of people are chatting with each other, building small groups of 2-3 persons. In addition, the person *P* decides to fetch his beer together with his girlfriend. Again, a lot of people have to be moved to arrive at point *B*. This is more complicated, since the small groups of chatting people do not want to split. *P* and his girlfriend will have to overcome a strong resistance or walk longer ways. Transferring this picture to chemistry, some spheres are linked to each other by intramolecular attractive forces or have a rod-like shape. A lot of spheres will have to move and turn around in order to let the blue spheres pass. The viscosity will be higher than in case (2).
- (4) The concert is well-attended and the band has distributed handcuffs to let the people handcuff themselves to big queues in order to start a 'conga line'. Person *P* is also trapped in such a queue, but wants to fetch the beer anyway. To make its way, a huge number of people has to move, even when they are far away from *P*. The queues have to wiggle around each other. Person *P* notices that sometimes two or three persons are an experienced team that can move fast out of the way. However, it takes a long time, until a whole queue is passed and even more time until person *P* has reached position *B*. In the analogy of physical chemistry, the spheres are connected to long chains. They cannot easily slip by each other, they have to disentangle and wiggle like snakes. There are small segments of a certain length that stay stiff during movement. This length is called the persistence length (*cf.* Chapter I.2.5.1). Due to the number of entanglements and the high number of momentum transfers that is needed to move through the solution, the viscosity is much higher than in case (3).
- (5) After the concert, people are chatting with each other, shake hands and change phone numbers. Some of them are still handcuffed together. The result is some kind of network of interconnected people, however the connections between them are not that strong as it was when they were handcuffed together. Person *P* wants to bring back his empty beer mug. In order to do so, person *P* has to interrupt the conversations between the queues of people that are still handcuffed together or at least to convince the people that are drunk - and really do not want to stop chatting - to talk with another person. Since

the bonding between the groups of people is not that strong, it is easier for person P to get to the beer bar. Transferring this analogy to physical chemistry, the spheres form a network of interconnected and branched chains. Some connections are strong, some others can be broken or at least shifted towards different positions. In total, the viscosity of such systems is smaller, since the segments and interactions that have to be overcome are overall smaller than in a non-connected system.

The viscosity of the systems can be changed by applying energy on the system. One way to do this is to apply a shear force.

Using the example of above, applying no shear force would be to wait patiently on the other people to move, so that you can pass by. Applying a medium shear force would correspond to asking the people kindly. Pushing other people out of the way and forcing them to move aside would consequently correlate with applying a high shear force. The result, if P faster arrives at the beer bar (if the viscosity decreases with shear force), depends on the crowd. There is the possibility that everybody stops talking immediately, and the queues form some kind of guard of honor for person P . In this case, P arrives much faster at position B . In words of physical chemistry, the chains align during shear flow leading to a shear-thinning behavior. The viscosity decreases with increasing shear force. A typical example of such a fluid is paint. The shear applied by brush or roller makes the paint thin and low-viscous, permitting to wet out the surface evenly. Once coated, the paint regains its higher viscosity and dries without dipping and running.

However, there is the possibility that some people are upset of the action of person P . They form some kind of barriers in order to block the way to the beer bar. That will slow down the way to position B for person P . In the analogy of physical chemistry, the spheres tend to agglomerate with increased shear flow. That leads to an increase in viscosity. This behavior is called shear-thickening. An example for this case is a solution of starch. At gentle shearing, a starch solution is fluid. As the shear rate is increased, the liquid becomes very viscous and thick. The exact mechanism of this phenomena is still under debate, but the majority attributes the increase in viscosity to a shear-induced formation of hydrodynamic clusters.^[31] It has to be mentioned that the use of starch for the thickening of sauces in kitchen undergoes a different mechanism. In that case, heating induces a transition from a dilute dispersion of individual ‘random coils’ to a network of entangled hydrocolloids.^[32,33]

And finally, there is also the possibility that pushing and shouting does not have any effect for

person P . The reason could be that it actually would not be necessary to push (case (1)), since the way to position B is easily accessible. Another possibility would be that the people are so immersed in a discussion, that pushing the people only leads to an interchange of discussing people, but does not change the accessibility of the way to position A . In the language of physical chemistry, this behavior is called Newtonian behavior. This can be explained by the fact that the spheres are too dilute, so that the way to position B is more or less free. Another possibility is that the spheres are strongly connected and shearing leads to a sliding of the connection points, but not to a reduction of connectivity. Therefore, such systems can also be shear-independent, since there are always segments perpendicular and some aligned to the shear flow.^[34]

Another way to apply energy to the system is to increase the temperature or in analogy to the illustrative example, to heat up the mood of the audience. As a result, the people will start dancing, move faster and the number and depth of conversations decreases. Consequently, it is easier for person P , to find gaps where he can slip in and he will arrive faster at the beer bar. In scientific language, increasing the temperature increases the kinetic energy of the spheres and accelerates the movement. Furthermore, intermolecular interactions are weakened. As a result, the coupling of the movement is decreased as well as the viscosity. Therefore, the viscosity of most of the systems decreases with increasing temperature.

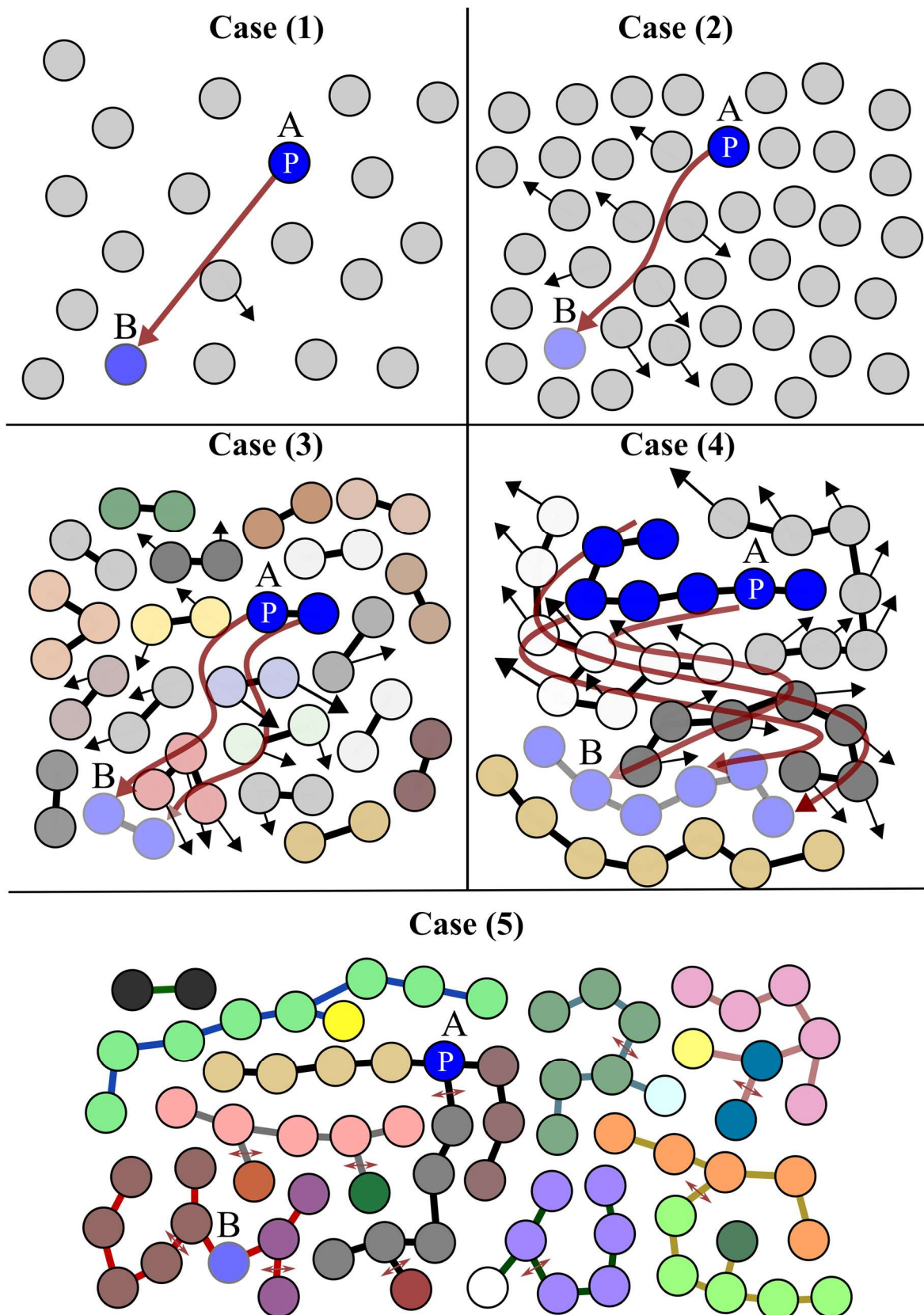


Figure 8. Simple picture of the origin of viscosity

I.2.4 Extractant solutions

I.2.4.1 Amphiphilic aggregation of extractants and surfactants

After the introduction of viscosity, we can come back to extraction. As indicated in Chapter I.2.1, for the extraction of metals, so-called extractants have to be added to the organic phase to induce selectivity and increase the solubility of ions in the apolar medium.

Since the pioneering work of Osseo-Asare^[35], it is well established that extractant solutions are complex fluids rather than molecular solutions. Extractants are amphiphilic. They consist of a polar chelating group and an apolar part of alkyl chains used to increase their solubility in an organic diluent. This property allows them to form reverse micelles and aggregates.

Since these reverse aggregates with a polar core represent a coexistence of “*two immiscible fluids separated by a well-defined interface*”^[36] built from an amphiphile two-dimensional fluid and since such solutions are clear, thermodynamically stable and macroscopically isotropic, they can be classified as water-in-oil microemulsions.^[36–38] Since in most cases, the polar core of these aggregates is relatively small (< 1 nm), the term “*water-poor microemulsion*” is a commonly used term for such systems.^[36]

Due to the amphiphilic molecular structure of extractants, interfacial activity can be observed at a macroscopic interface, indicated by a decrease in interfacial tension, as the extractant concentration in the organic phase increases.^[39] A typical curve is shown in a qualitative way in **Figure 9**. Important differences compared to surfactant systems have to be noted.

Surfactant molecules adsorb preferably at the interface where they find the energetically most favorable conditions due to their amphiphilic structure. At low surfactant concentration the surfactant molecules arrange at the interface and the interfacial tension of the solution starts to decrease rapidly since more and more surfactant molecules adsorb at the interface. Further surfactant addition leads to a saturation of the interface and micelles are formed to avoid the contact of water molecules and the hydrophobic chains. This concentration point is called *critical micelle concentration (cmc)*. After that concentration, the interfacial tension stays almost constant, since addition of new surfactant molecules leads only to the formation of new micelles, but does not change the interfacial properties. In terms of chemical potential, one could explain this phenomenon as follows. With c_s being the concentration of unimeric surfactants in water and c_{tot} the total concentration of surfactant, the chemical potential of a surfactant molecule is given by equation (6) or (9), respectively.

Below the *cmc*, one can assume that $c_{\text{tot}} \approx c_s$.

$$\mu_S = \mu_S^0 + RT \ln c_s \approx \mu_S^0 + RT \ln c_{\text{tot}} \quad (6)$$

Above the *cmc*, the total concentration of surfactants is approximately the concentration of micelles multiplied with the average number of molecules per micelle N_{agg} . This term can be also expressed in terms of the equilibrium constant of micellation K_{eq} and the monomer concentration c_s (*cf.* equation (7)). Rearranging this equation leads to an expression for the chemical potential μ_S .

$$\text{above cmc: } c_{\text{tot}} \approx N_{\text{agg}} \cdot c_{\text{micelle}} \approx N_{\text{agg}} \cdot K_{\text{eq}} \cdot (c_s)^{N_{\text{agg}}} \quad (7)$$

$$c_s = \left(\frac{c_{\text{tot}}}{N_{\text{agg}} \cdot K_{\text{eq}}} \right)^{1/N_{\text{agg}}} \quad (8)$$

$$\mu_S = \mu_S^0 + RT \ln c_s = \mu_S^0 + \frac{RT}{N_{\text{agg}}} \ln c_{\text{tot}} - \frac{RT}{N_{\text{agg}}} \ln(N_{\text{agg}} K_{\text{eq}}) \quad (9)$$

For surfactant systems, the aggregation numbers are large (usually 40-100). Therefore, the concentration dependent term $\frac{RT}{N_{\text{agg}}} \ln c_{\text{tot}}$ is negligible above the *cmc* and the interfacial tension stays almost constant.

In the case of extractant systems the situation is different. First, the break in the γ -log[extractant] curve at the oil/water interface is shifted to higher concentrations compared to surfactant systems. It shows that extractants exhibit higher solvophilicity than surfactants. The concentration of this break is called the *critical aggregation concentration (cac)* and can be related with the formation of aggregates in the solution.

Second, the break in the curve is much less pronounced in the case of extractants, *e.g.* the slope before and after the break differs less than in the case of surfactants. Furthermore, in most cases, surfactant molecules are more efficient in reducing the interfacial tension of the water-oil interface leading to a lower value at higher amphiphile concentration. Moreover, while the interfacial tension of surfactant molecules stays almost constant above the *cmc*, the slope stays negative and concentration dependent in the case of extractants. Equation (9) gives a first explanation of this phenomenon. In the case of extractants, the aggregation numbers are much smaller (typically 4-10) than in the case of surfactants. This makes the term $\frac{RT}{N_{\text{agg}}} \ln c_{\text{tot}}$ more significant. Furthermore, it has to be noted, that most extractants belong to the class of “*poor*”

surfactants^[40] that aggregate in a progressive stepwise process as was demonstrated by Eicke *et al.*^[41] Therefore, aggregation starts already below the *cac* and before the saturation of the interface, making a further decrease of the interfacial tension above the *cac* possible.

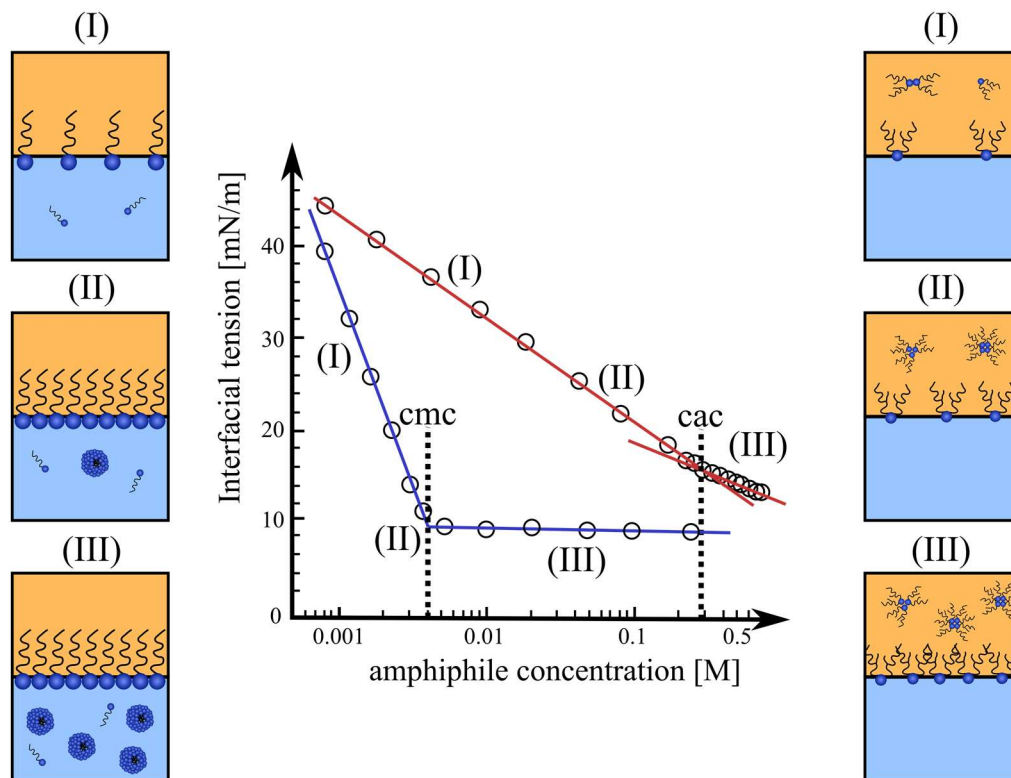


Figure 9. Qualitative evolution of the interfacial tension of a macroscopic water-oil interface in presence of an amphiphilic molecule and the corresponding mesostructural evolution. Red: Evolution in presence of an extractant diluted in an organic diluent. Blue: Evolution of a surfactant diluted in water. Remarks: The absolute values of the interfacial tension as well as the *cmc* and *cac* values are strongly dependent on the system and can vary significantly. Rough values are taken from [39,42] and [43]. The aggregation behavior is schematically drawn for **left**: surfactants and **right**: extractants.

It has to be noted, that the underlying driving force for the aggregate formation is completely different for surfactants and extractants.

For surfactants in water, the so-called “*hydrophobic effect*”^[44] leads to aggregate formation. Water molecules have a unique capacity for forming hydrogen bonds additionally to ordinary dipole-dipole interactions. Since each oxygen atom can contribute to two hydrogen bonds, every water molecule can form up to four hydrogen bonds with its neighbors.^[45] As a result, liquid water can be seen as a loose dynamic network of hydrogen bonds. Due to the high number of different configurations the hydrogen network can be arranged, the network is stabilized by entropy. A number of unique properties like the high surface tension or the elevated boiling point results from this stabilization. When hydrophobic compounds, that are not able to participate in that network, are added to water, the loose network structure is disrupted, since

water molecules next to the hydrophobic compound cannot freely participate in the network. This results in an entropy decrease. Therefore, for surfactants, the hydrophobic effect leads to a self-organization of the molecules with the goal to screen the oily chain as much as possible from water. In the case of a hydrophobic compound not having amphiphilic properties, the hydrophobic effect leads to phase separation, like in the case of water and a simple oil.

In contrast hereto, extractant molecules are dissolved in an organic diluent. A hydrophobic effect or a reverse equivalent effect does not take place. Furthermore, aggregation is entropically unfavored.^[46] Hence, an enthalpic effect must be the driving force. In non-aqueous solution, the aggregation depends on both the solvent and the structure of the amphiphile. Entropy and solvent-oily chain interactions prevent aggregation and minimize the size of the aggregate, while interactions between the polar groups of the amphiphile promote aggregation.^[47] Therefore, self-assembly in apolar solvents is the consequence of dipole–dipole and ion pair interactions of the polar groups of amphiphiles.^[47] These interactions can be enhanced by the presence of water or ions due to intermolecular hydrogen bonding or metal coordination bonds.^[48]

1.2.4.2 Extractant solutions and their structures: The packing parameter

There is a variety of extractants available that is heavily in research². They can be classified according to their mechanism of ion transfer in the organic phase.^[49,50] A visual overview of the following mechanisms is given in **Figure 10**:

- *Cation exchange*: Cation exchangers such as the organo-phosphorus extractant HDEHP have an acidic function and extract the desired ion by ion exchange and proton release.
- *Solvation*: Such extractants (for example DEHiBA, TBP, TOPO) exhibit a neutral (non-ionic) polar function and are assumed to extract metal ions by forming a solvation shell in the organic phase. The ions are extracted as neutral complexes or aggregates. Therefore, also water-soluble anions are part of the resulting coordination. This picture was refined by Dufrêche and co-workers, who have demonstrated that the ions not only interact by complexation or solvation with the first neighbors, but also via long-range

² Overview of number of publications of some common extractants (2000-2018):

- HDEHP: 3950
- TBP: 24100
- Dialkylamides: 2120
- Malonamide: 1850

forces beyond the first neighbors.^[51]

- *Formation of ion pairs:* Basic extractants such as the amine ligand tri-octylamine (TOA) extract the desired metal ion by forming ion pairs. Therefore they can be seen as ‘liquid anion exchangers’.^[50]

The mixing of two types of extractants can lead to advantageous effects, such as the “*synergistic effect*”^[52]. For certain combinations and ratios of extractants (for example HDEHP/TOPO) the extraction power is higher than expected from the values of the pure extractants.

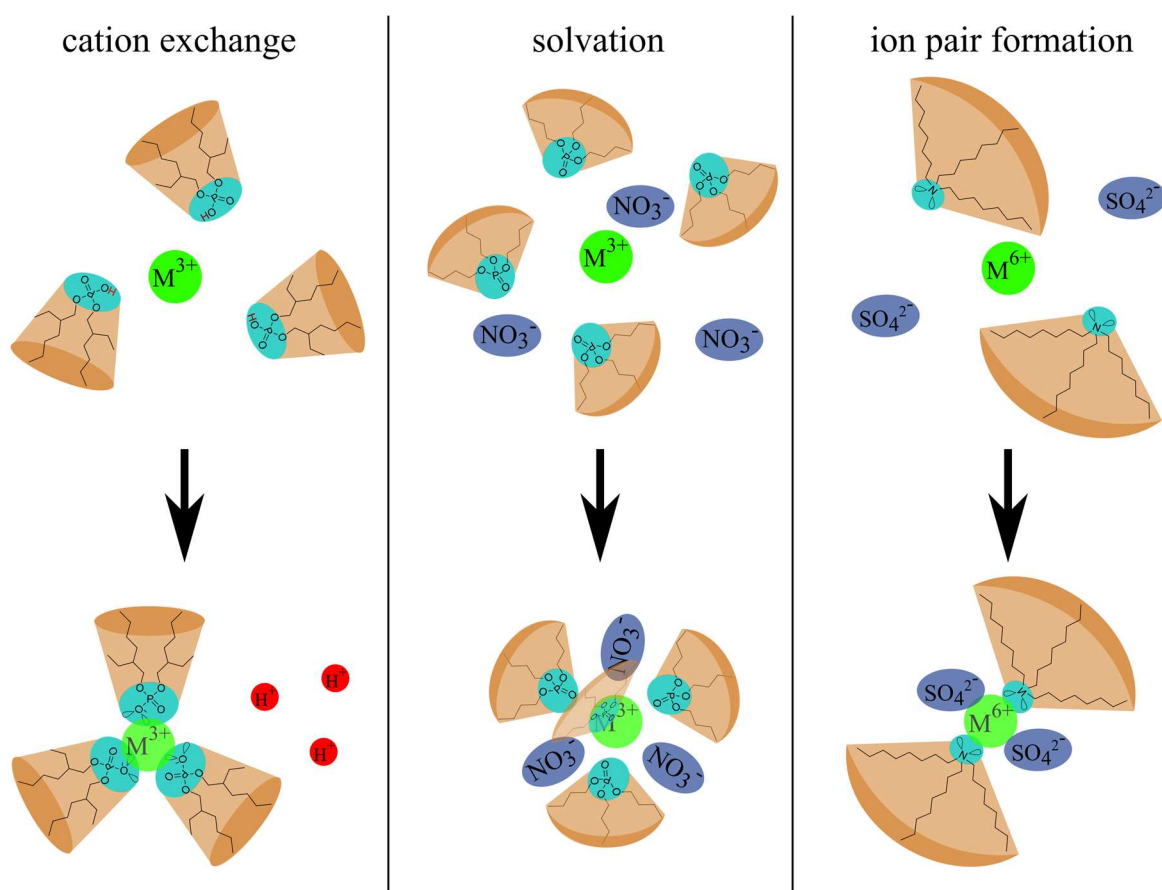


Figure 10. Schematic overview over the three main mechanisms of metal extraction

Besides their mechanism of extraction, the aggregates formed can have different sizes and shapes. Since the work of Osseo-Asare^[35], one knows that it is possible to transfer certain aspects of surfactant science to systems used for solvent extraction.

In the 1970's, several papers dealing with O/W micelles were expressing the difference in chemical potential in a reference state (μ^0) and the chemical potential for a given concentration (μ) not as a function of concentration and activity coefficients, but as radii of different cylinders, ellipsoids and folded bilayers^[46,53,54]. This allowed for the first time to predict the shape of micelles by including the concept of pseudo-phases^[44,55,56]. According to this concept

introduced by Shinoda^[55] and Tanford^[56], micelles can be thermodynamically treated as separate phases that are in chemical equilibrium with the surrounding continuous phase (*cf.* Chapter III). As a consequence, the chemical potential $\mu_{i,\text{mic}}$ of an amphiphile in a micelle must be same as that of an amphiphilic monomer dissolved in the surrounding continuous phase (water or respectively organic diluent) $\mu_{i,\text{continuous}}$:

$$\mu_{i,\text{mic}} = \mu_{i,\text{continuous}} \quad (10)$$

$$\mu_{i,\text{mic}}^0 + RT \ln a_{i,\text{mic}} = \mu_{i,\text{continuous}}^0 + RT \ln a_{i,\text{continuous}} \quad (11)$$

with:

- μ_i denoting the chemical potential - simply put “*the tendency of a system to give the particles of type i* ”^[57] - of compound i in the corresponding pseudo-phase,
- a_i denoting the activity of compound i in the corresponding pseudo-phase and
- μ_i^0 denoting the standard reference chemical potential of compound i in the corresponding pseudo-phase. The standard reference chemical potential is defined as the chemical potential at which the activity coefficient and the ideal activity is equal to 1 and depends on the choice of the ideal activity expression. For liquid and solid mixtures, this corresponds to the pure system. For solutions it is defined by convention for solutes as infinitely dilute solutes with a standard concentration (depending on the choice of the standard state) of either the molarity $c = c^0 = 1 \text{ mol/L}$, the molality of $m = m^0 = 1 \text{ mol/kg}$ or the mol fraction of $x = 1 \text{ mol/mol}$.^[57,58, pp.5–43]

The second crucial step was the development of the lateral equation of state which comprises the two “*opposing forces*”^[56] that govern the self-assembly: headgroup repulsion and an attractive interaction arising from hydrophobic forces at the hydrocarbon-water interface.^[59, pp.535–576] These two forces that mainly act at the interfacial region are shown in **Figure 11**.

The attractive interaction that originates mainly from interfacial tension forces μ_{IFT}^0 and that wants to decrease the interfacial area per molecule can be expressed as a positive interfacial free energy γ per unit area (typically between 20 and 50 mJ/m²):

$$\mu_{\text{IFT}}^0 = \gamma \cdot a \quad (12)$$

with a being the interfacial area per molecule.

The repulsive contributions μ_{rep}^0 are difficult to formulate^[60], but it is known that the first term

in any free energy expansion has to be inversely proportional to the surface area occupied by the headgroup a .

$$\mu_{\text{rep.}}^0 = \frac{K}{a} \quad (13)$$

with K being a constant.

The total interfacial free energy per molecule μ_N^0 can be therefore expressed as

$$\mu_N^0 = \gamma \cdot a + \frac{K}{a} \quad (14)$$

This function of a results in a minimum (*cf.* **Figure 11**) and is noted as the optimal area per headgroup a_0 at which the total interaction energy per molecule μ_N^0 is a minimum.^[59, pp.535–576]

The energy does not vary parabolically (*i.e.* elastically), since it is more difficult to reduce a than to increase.

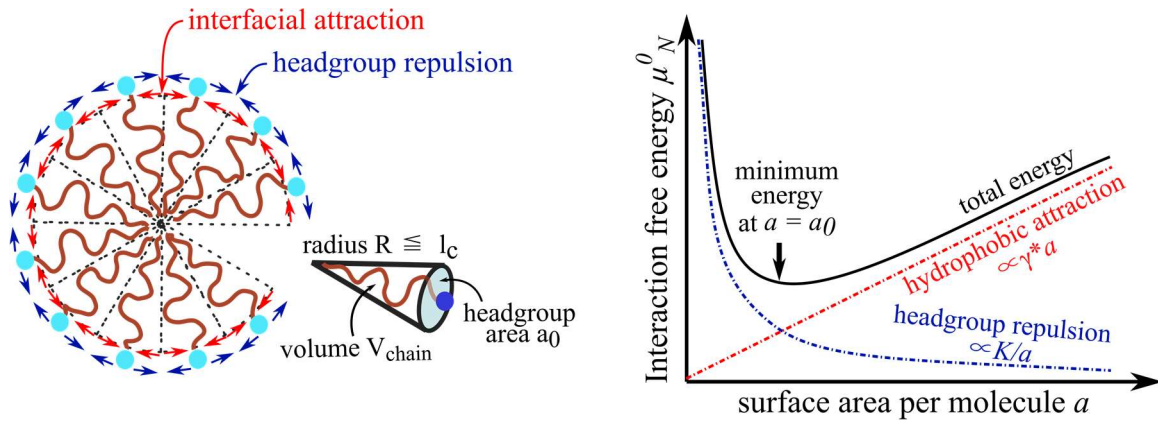


Figure 11. Left: Schematic view of a direct micelle with a hydrocarbon interior in fluid state. Headgroup repulsion and interfacial attraction determine the optimum headgroup area a_0 . **Right:** Lateral equation of state describing the opposing forces of headgroup repulsion and hydrophobic attraction. The total free energy exhibits a minimum at $a = a_0$. Adjusted and replotted from ^[59, pp.535–576].

The area and volume of any infinitely thin film has been calculated by Gauss and Helfrich who have introduced the final concept of spontaneous and nonspontaneous curvature and applied on thin solid films of lipid bilayers.^[61] This approach used the Gaussian and the spontaneous mean curvatures K_0 and H_0 influenced by the composition of the system as well as the corresponding values K and H in the absence of solution constraints to calculate the free energy of bending F per unit area.^[62–64]

$$F = 2k_c \cdot (\langle H \rangle - H_0)^2 + k' \cdot (\langle K \rangle - K_0) \quad (15)$$

with k_c being the curvature elastic modulus and k' the Gaussian elastic constant. The indication

$\langle \rangle$ is used to clarify that the mean and Gaussian curvatures are averaged over the whole sample. H and K are the local mean average and Gaussian curvatures. They are given by c_1 and c_2 - the local principal curvatures - as $H = 0.5(c_1 + c_2)$ and $K = (c_1 \cdot c_2)$ (cf. **Figure 12**). The contribution of the spontaneous Gaussian curvature K_0 was often regarded as negligible, although it leads to mathematical inconsistencies.^[65]

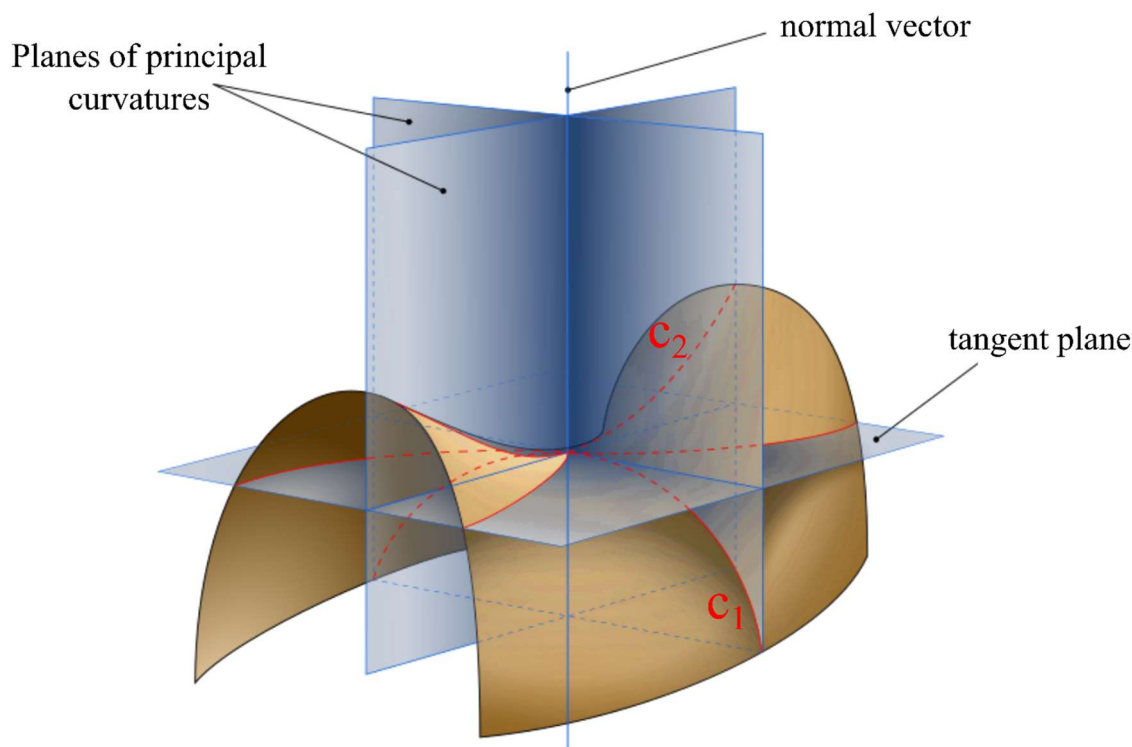


Figure 12. Schematic representation of the principal curvatures c_1 and c_2 of a saddle-like geometry. Replotted and adjusted from ^[66].

Due to this strong geometrical constraint of infinitely thin films introduced by Gauss, this concept cannot be correctly applied on amphiphile films without modification.

In surfactant science, the shape of the amphiphiles strongly influences the free energy of aggregation. In order to describe the amphiphile shape, Israelachvili and co-workers introduced the *spontaneous packing parameter* P_0 that postulates a preferred shape of the molecules in the surfactant film.^[46] The spontaneous packing parameter, a scalar number, must be precisely defined:

$$P_0(pH, T, c_{ions} \dots) = \frac{V_{\text{chain}}}{a_0 \cdot l_c} = \frac{a_s}{a_0} \quad (16)$$

with:

- V_{chain} being the molar volume of the hydrophobic chains. This requires precise definition

of the polar and the apolar parts. This is only possible when the neutral plane is well-defined.^[67,68]

- a_0 is the area per headgroup. Initially, in several papers, a_0 is wrongly referred to a , the crystallographic area. The only self-consistent definition of a_0 is the minimum of the lateral equation of state (*cf.* **Figure 11**).^[69] For a detailed discussion Ref. [70,71] are recommended.
- l_c is the chain length averaged over all configurations weighted with the probability of occurrence. It can be accessed via molecular dynamic simulations or NMR relaxation experiments. Since the rotation around the C-C axis is in the order of $1\ kT$, the vast majority of experimental findings conclude that l_c is about 80% of the fully stretched chain length. This length can be accessed via Tanford's formula^[72] that will be mentioned later.

Consequently, the spontaneous packing parameter can also be seen as the ratio between a “sterical” area a_s that is linked to fluid compressibility and the actual area a_0 of a amphiphile at the polar/apolar interface.^[64] Since these parameters are significantly sensitive to many factors such as ion content, solvent penetration, temperature, pH etc., this parameter is given for a certain condition and expresses the geometry that one surfactant would have preferentially. However, in order to fit into the interfacial film, the surfactant molecule must adopt its geometry. This actual geometry is expressed by the *effective packing parameter* P .

Fogden, Hyde and co-workers^[65,73] have shown that one can link the concept of a local spontaneous packing parameter P_0 and an effective packing parameter P with the concept of spontaneous and nonspontaneous curvature. For the case of thin films of thickness l and assuming that the surfactant film cannot disrupt and these scalars can be expressed as a serial expansion^[65]:

$$P = 1 - \langle H \rangle l + \frac{1}{3} \langle K \rangle l^2 \quad (17)$$

$$P_0 = 1 - \langle H_0 \rangle l + \frac{1}{3} \langle K_0 \rangle l^2 \quad (18)$$

For curved surfaces, the curvatures c_1 and c_2 can be approximated as $1/R_1$ and $1/R_2$ with R_1, R_2 being the radii of curvature in the two perpendicular principal planes of curvature (*cf.* **Figure 12**). As a consequence, one can calculate the effective packing parameter P dependent on the micellar shape (*cf.* **Table 1**).

Table 1. Local principal curvatures, mean and Gaussian Curvatures as well as effective packing parameters for different aggregate shapes according to Equation (17).

shape	l	R_1	R_2	c_1	c_2	H	K	P
spheres	R	R	R	1/R	1/R	1/R	1/R ²	1/3
cylinders	R	R	∞	1/R	0	1/R	0	1/2
symmetric saddle	R	R	-R	1/R	-1/R	0	-1/R ²	2/3
bilayers	R	∞	∞	0	0	0	0	1

The approximation to calculate the spontaneous packing parameter is mathematically only correct for liquid crystals and lamellar phases of bilayers, where the deviation of these packing parameters from 1 is small. To our best knowledge, there are only a few cases where Helfrich's description is valid for microemulsions because it requires that the average curvature is much higher than the film curvature.^[74–76]

In the cases studied in this work, the spontaneous packing parameters are far from 1 and the definitions of spontaneous and nonspontaneous curvature cannot be applied. Therefore, we express the cost in free energy associated with film deformation by the definition introduced by Hyde and co-workers. Using an harmonic approximation leads to an expression for the bending contribution to the free energy F per molecule in an aggregate.^[73]

$$F = \frac{\kappa^*}{2} \cdot (P - P_0)^2 \quad (19)$$

with κ^* being the generalized elastic constant.^[77,78] Physically, this definition of the elastic energy reduced to one constant, κ^* , means that defects in average curvature can be compensated by a variation in the Gaussian curvature.^[79] This so-called bending constant describes how much energy is needed to bend one amphiphile in an interfacial film and is also valid in case of strong curvatures where P and P_0 strongly differ from 1. In the case of extractants, this value has been reported to be in the order of 2-3 kT per molecule.^[80]

In other words, the free energy of bending is related to the deviation of the actual packing parameter from the preferred one (*cf.* **Figure 13**). This actual packing parameter is called effective packing parameter and is directly related to the possible shapes of the aggregates in solution (*cf.* **Table 1**).^[40,62,81] An overview of some possible aggregate shapes is shown in **Figure 14**. The approximate effective packing parameter as well as the corresponding curvatures are indicated as well. For O/W aggregates, these values are well defined.^[46,59,62] For extraction, this concept has to be transferred into O/W aggregates. This is possible since all three terms needed (V_{chain} , l_c and a_0) have a precise definition that is valid also for the organic

case after defining a certain neutral plane between the apolar and the polar part:

- V_{chain} takes into account the apolar chain volume as well as oils or additives that penetrate into the outer apolar chain layer.
- l_c denotes the chain length averaged over all configurations weighted by their probability of occurrence.
- a_0 represents the area per molecule at the neutral plane, *i.e.* at the apolar-polar interface.

Regarding the values of the effective packing parameters in the reverse case, the best consideration that can be taken is to assume that the values behave oppositely to the aqueous case, as indicated in [59, p.540]. However, these values can vary slightly in reality, but are taken to demonstrate the model presented in this work.

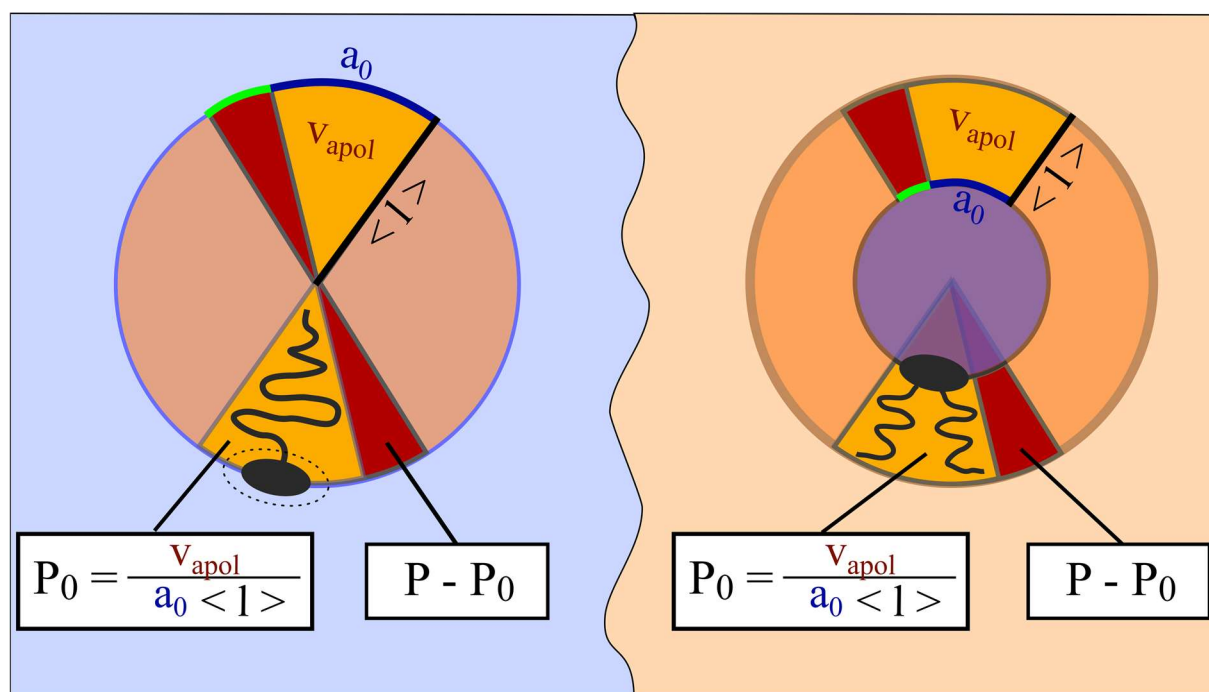


Figure 13. The spontaneous and the effective packing parameter in aqueous and organic media

By convention, one speaks of *positive curvature*, if the amphiphile prefers direct aggregates (curvature towards water) and of *negative curvature*, if reverse aggregates are formed (curvature towards oil). The size and shape of the self-assembly – or better said, the number distribution of these structures – results from the minimization of the free energy of the system (*cf.* Eq. (19)).

In the case of extractants, the packing parameter is higher than 1, so reverse aggregates are formed. These structures usually have low aggregation numbers ($N_{\text{agg}} < 10$) and mainly monomers, dimers or tetramers can be found. However, as introduced in Chapter I.2, on

industrial scale, the conditions are relative extreme. The metal content is high and also the extractant concentration is elevated. This can lead to different structures.

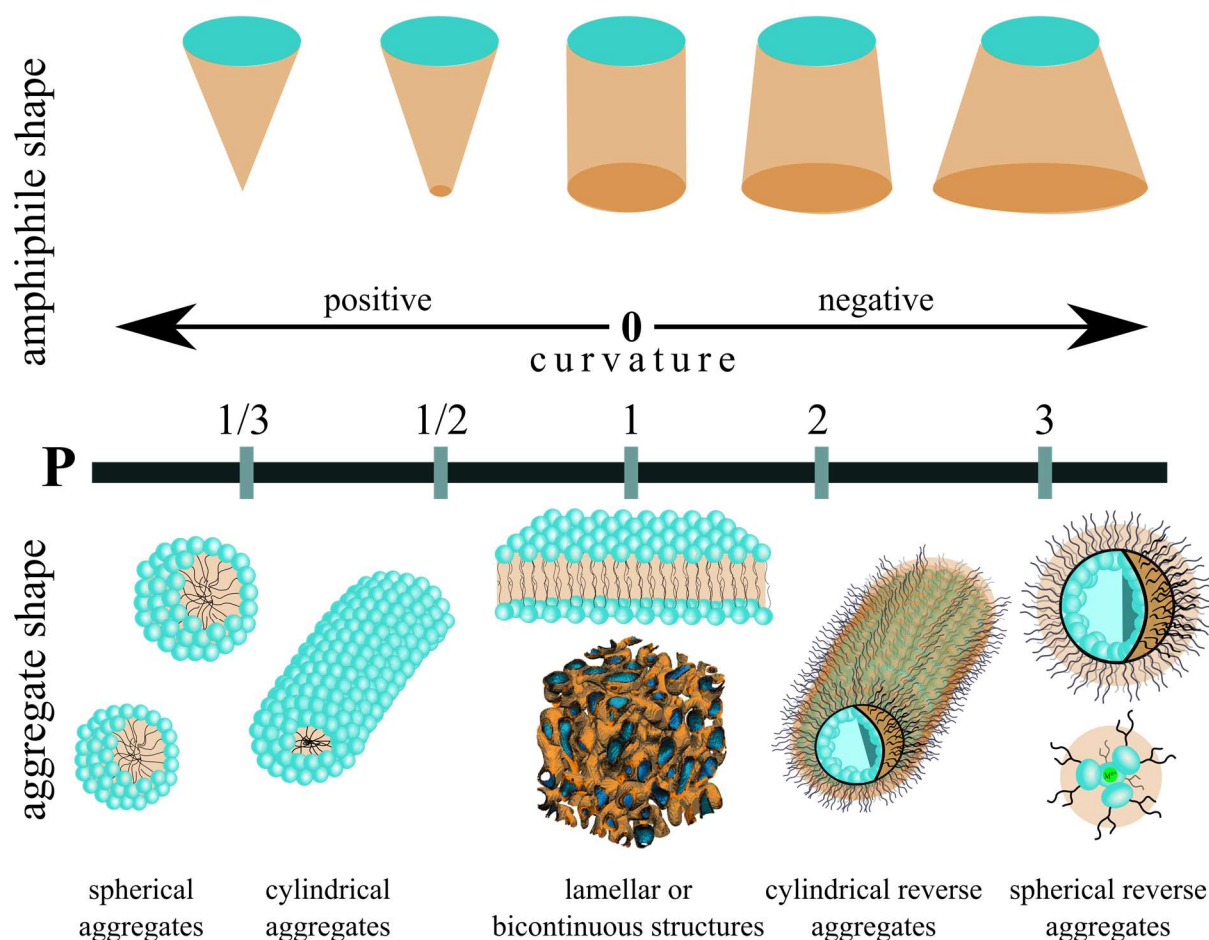


Figure 14. Overview of possible structures dependent on curvature and packing parameter.

Testard *et al.*^[82] have presented the “Four types of supramolecular of extractant molecules used in separation processes”. They describe four different microstructures at supramolecular scale in the extracting solvent.^[82] These are shortly summarized in the following:

- Swollen reverse W/O micelles.* The aggregates interact through a “sticky hard sphere potential”. The origin of this attractive van der Waals force is the polar core containing polarizable ions. The more polarizable the core, the stronger is the attractive force. This van der Waals potential is often used to explain the occurrence of the third phase.^[39,83–86] In some cases, heating of the solution leads to a transition to a regular solution of dispersed extractant molecules. The increase of the entropical contribution leads to a break-up of the self-assembled structure. A regular solution is also obtained by using extractant concentrations far below the *cac*.^[82]
- Quaternary microemulsion consisting of reverse aggregates formed by extractant

molecules with inclusion of other solutes acting as “*co-surfactants*”. In most cases, the stability of such aggregates as well as the dynamics of reactions are enhanced.^[87]

- c) *Random dynamical network* in an organized solvent acting like adsorption sites for solubilized complexing molecules. The microstructure can be seen as amphiphilic molecules coexisting with a living polymer.^[40,88]
- d) Microphase separation containing “*tactoids*”. Locally condensed structures such as a hexagonal phase coexist with domains of dilute phase.^[40,82,89–91]

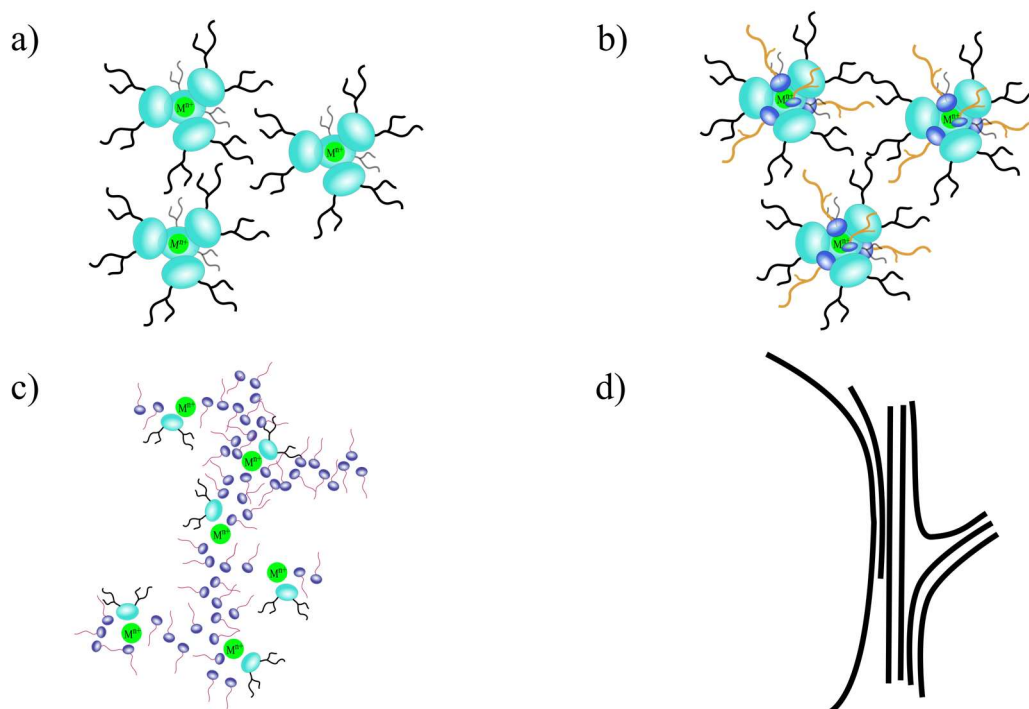


Figure 15. The four organized microstructures described by Testard *et al.*^[82]

However, if one approaches industrial conditions, even larger colloidal structures are possible. Bauduin *et al.* has investigated two different malonamide extractants at high extractant concentration.^[92] He compared a C5 with a C14 malonamide extractant that only differ in the length of the apolar chain. The spontaneous packing parameter of C5 is smaller than of C14 and gave indications on the experimental outcome. The C5 extractant has a higher tendency to form cylindrical aggregates, while C14 prefers spheres in the concentration range 1-1.5 M. Above this concentration, both extractants form lamellar structures. However, since the lamellar structure of the C14 extractant is better stabilized, its structure is more ordered. The C5 extractant forms a lamellar disordered structure (*cf.* **Figure 16**).^[40,92]

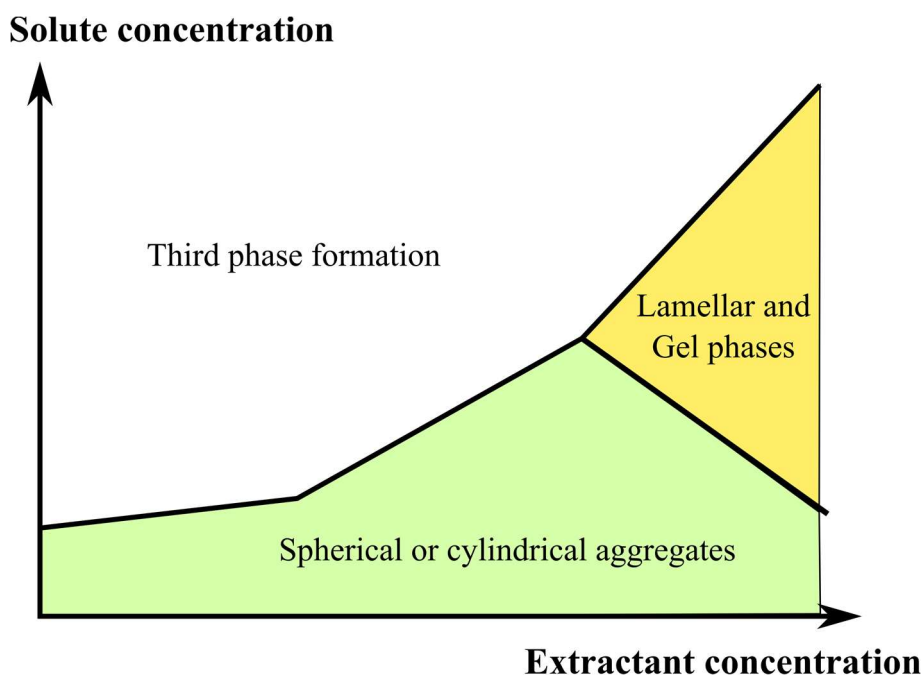


Figure 16. Schematic phase behavior of malonamides in presence of solutes/ions in the organic phase. Replotted and adjusted from [93].

Furthermore, VPO measurements^[94,95] have also evidenced the presence of large aggregates. The observed large aggregation numbers are incompatible with a spherical shape due to volume and surface constraints.^[40]

Another indication that the observed structures in extractant systems are strongly dependent on extractant and metal concentration was shown by Dozol *et al.*^[96] This work demonstrates the presence of three regimes observed via the self-diffusion coefficient D obtained by NMR-DOSY experiments. At low extractant concentration, mainly monomers are present and D remains constant. At medium concentration, D decreases slightly indicating the presence of reverse micelles. At high concentrations – the third regime – D decreases strongly demonstrating the presence of a supramolecular structure.

1.2.5 Possible reasons for viscosity increase in the reverse space

On one hand, aggregate formation can improve extraction properties such as selectivity, distribution coefficient or kinetics.^[50,97,98] On the other hand, this structuration of the organic phase can lead to unwanted effects such as a third phase formation, emulsion stability or viscosity increase.^[40,86,92,99,100]

As indicated in the section before, the structures formed in the organic phase are determined by the concepts of packing parameter or curvature. For extractants, in most cases, spherical

aggregates are considered, but also other structures were found and are possible.^[8,101]

A short overview of non-spherical structures found for extractants is given in **Table 2**.

Table 2. Short overview of non-spherical structures observed for extractants in literature

Shape	Extractant system	Counterions	References
cylindrical/rod-like	DMDBPMA, $c > 1 \text{ M}$	-	[92,96]
lamellar	DMDBPMA and DMDBTDMA, $c > 1.5 \text{ M}$	-	[92]
3-D hydrogen network	DMDOHEMA/octanol, $c = 0.7 \text{ M}$	-	[102]
cylindrical/polymer-like	HDEHP	$\text{Co}^{2+}, \text{Cu}^{2+}, \text{Fe}^{3+},$ $\text{Ln}^{3+}, \text{Nd}^{3+}, \text{Ni}^{2+},$ $\text{Th}^{4+}, \text{U}^{6+}, \text{V}^{4+}, \text{Y}^{3+},$ Zn^{2+}	[103–111]
cylindrical rod-like	DMDOHEMA, $c = 0.5 \text{ M}$	Eu^{3+}	[112]
cylindrical/rod-like	TBP/HDBP	Dy^{3+}	[113,114]
cylindrical/polymer-like	NaDEHP	-	[115]

Although the whole range of structures and concentrations is not investigated yet for oil-soluble extractant systems, one can assume that there is a parallelism between surfactants in water and extractants in the organic phase. Cates gives in his reviews an overview on possible structures in aqueous media dependent on the packing parameter, salt content and concentration of surfactants.^[116] A transfer in the world of extractants would result in the following qualitative diagram (*cf.* **Figure 17**). The phase diagram for the case of surfactants can be found in the Annex, **Suppl. Figure 4**.

According to this scheme, there is a dependence on both the extractant concentration as well as on the ion content in the organic phase. At concentrations below the *cac*, mainly monomers can be found. As soon as the extractant concentration is increased, separated reverse aggregates are formed in the dilute regime. The shape of these aggregates changes depending on the metal concentration according to the packing parameter. The addition of ion, complexed by the polar moiety of the amphiphiles promotes elongation and even branching of the aggregates. As soon as the concentration of amphiphiles is increased, the aggregates cannot be seen as separated anymore. The structures start to entangle and even to form networks. At high extractant and/or metal concentration, one can find either microphase separated systems, the so-called Onsager regime, or even phase separation – the third phase formation. This term describes the

phenomenon that the organic phase separates into an extractant-rich, condensed phase and a diluent-rich phase. The terms mentioned in this section will be described later in this section.

On industrial scale, about 1 - 1.5 M extractant are typically used, that means for the case of monoamides around 30-50 volume percent. In general, one can assume that the investigated systems will be located in the semi-dilute regime. Furthermore, in the organic phase, an elevated concentration of ions, for the example chosen in this thesis uranyl, nitrate and oxonium ions will be present. Therefore, one can estimate that the investigated systems in this work are located somewhere in the yellow region and a variety of structures is possible (*cf.* **Figure 17**).

Assuming that this map is also applicable in the reverse case, four general structures can be imagined as origin of viscosity increase in organic solutions. The descriptions are compacted by intention and written in a general way, so that they are applicable for the direct and reverse structures. Only the third phase formation in that specific way (*cf.* Chapter I.2.5.4) can only be found in extracting systems, since three phase systems in the direct case (Winsor III) phases have a different origin.

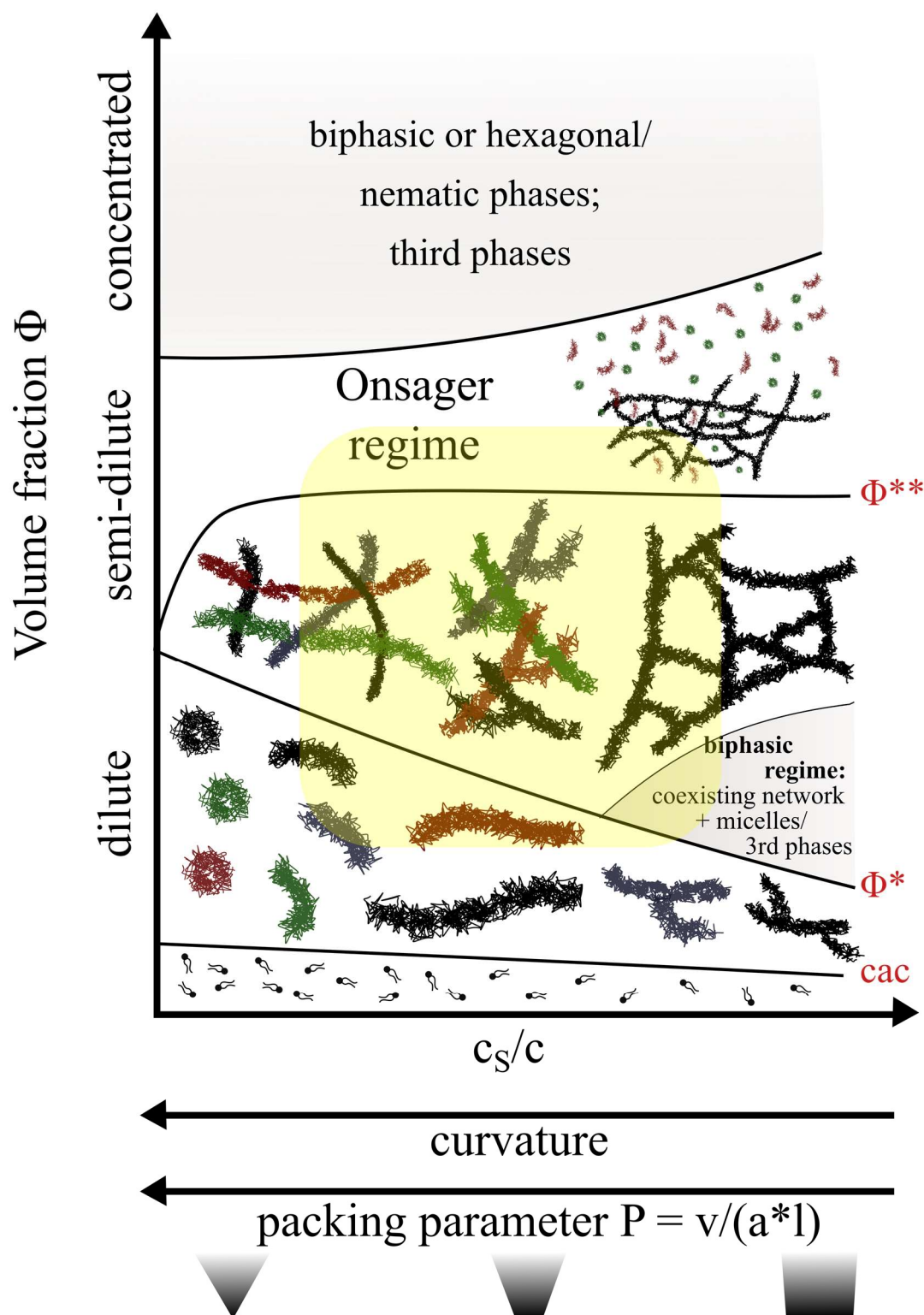


Figure 17. Possible phase diagram of structures in an extracting organic phase dependent on extractant concentration and normalized metal content c_s/c . Schema replotted and transferred in the reverse space from [116]. The “industrial” concentration range is indicated in yellow. This scheme is not proven yet, it only represents a possible transfer of the structure evolution in surfactant science to extractant science.

1.2.5.1 Linear wormlike micelles

In literature, this kind of shape has been given several names – *living polymers*^[117], *polymer-like*^[118], *spaghetti-like*^[119] or *threadlike*^[120], just to mention some of them. They cover a broad range of applications such as drag-reducing agents and thickeners for personal and home care, cosmetics or fracturing fluids in oil fields.^[121,122]

The behavior of wormlike micelles is strongly concentration dependent. Above a certain threshold concentration Φ^* - the so-called *overlap concentration* – the elongated structures start to entangle and form a transient network (*cf.* **Figure 17** and **Figure 18**). This network has many properties in common with polymer networks in semi-dilute solutions.^[116,123,124] In the case of long linear polymers, the main relaxation mechanism is *reptation* (latin: “creeping”).^[125] In principle, this de Gennes’ model assumes, that the long-range motion of the polymer is only allowed on its own contour. Simply put, the polymer has to slither through the other polymers – like a snake – in order to move forward. Therefore, the relaxation time τ_{rep} of reptation (order of magnitude $10 - 10^3 \text{ ms}$ ^[126]) and related to it, the viscosity, mainly depend on the length of the structures L and a mobility constant D_0 .^[117]

$$\tau_{\text{rep}} = \frac{L^3}{D_0} \quad (20)$$

$$\eta \cong G_0 \tau_{\text{rep}} \sim L^3 \quad (21)$$

with G_0 being the instantaneous shear modulus which is related to the number density of entanglements.^[117]

However, there is a crucial difference between polymer structures and elongated structures formed by amphiphiles. Micelles are formed under thermodynamic control. That means that their contour length distribution is not fixed by chemical synthesis like it is in the case of polymers. Their length characteristics strongly depend on solution parameters such as temperature or salt and amphiphile concentration.^[123] Furthermore, wormlike micelles are dynamic systems that constantly break and recombine. For this reason, such systems are often referred to as “*living polymers*”.^[117] Therefore besides reptation, a second mechanism of stress relaxation has to be considered.^[117,124] The *scission-recombination mechanism* implies that the chains of a network of wormlike micelles can break and recombine reversibly to release stress. For that, various mechanisms are possible:^[127]

- *Reversible scission*: a chain breaks randomly along its length and recombines the

resulting ends on the other side of the encountered micelles

- *End interchange*: the end of one chain attacks the central part of another. After that, another end leaves the intermediate structure
- *Bond interchange*: the central part of two chains combine to a four-armed transient intermediate and recombine on the other side of the encountered micelle. This process is also referred as “ghost-like crossing” in literature.^[34]

In that case, the fundamental relaxation time (and consequently the viscosity) depends on both the relaxation time of breakage and recombination τ_{break} as well as of reptation τ_{rep} . τ_{break} is dependent on the rate of breakage c_1 and inversely proportional to the mean length of the micelle L ^[117]:

$$\tau_{\text{break}} = \frac{1}{c_1 L} \quad (22)$$

The relaxation time of reptation stays as defined in equation (20). Two cases have to be distinguished. If the relaxation time of reptation is smaller or similar to τ_{break} , the scission-recombination mechanism can be neglected and the viscosity keeps its L^3 -dependence as defined in equation (21).

However, if the relaxation time of breakage and recombination becomes dominant ($\tau_{\text{break}} < \tau_{\text{rep}}$), the fundamental relaxation time and the viscosity is given by

$$\tau \cong \sqrt{\tau_{\text{rep}} \tau_{\text{break}}} = \frac{L}{\sqrt{c \cdot D_0}} \quad (23)$$

$$\eta = G_0 \tau \cong G_0 \frac{L}{\sqrt{c_1 \cdot D_0}} \quad (24)$$

with D_0 being the mobility constant and c being the probability of a break per unit length per unit time.^[117] The two mechanisms of stress release are drawn in **Figure 22**.

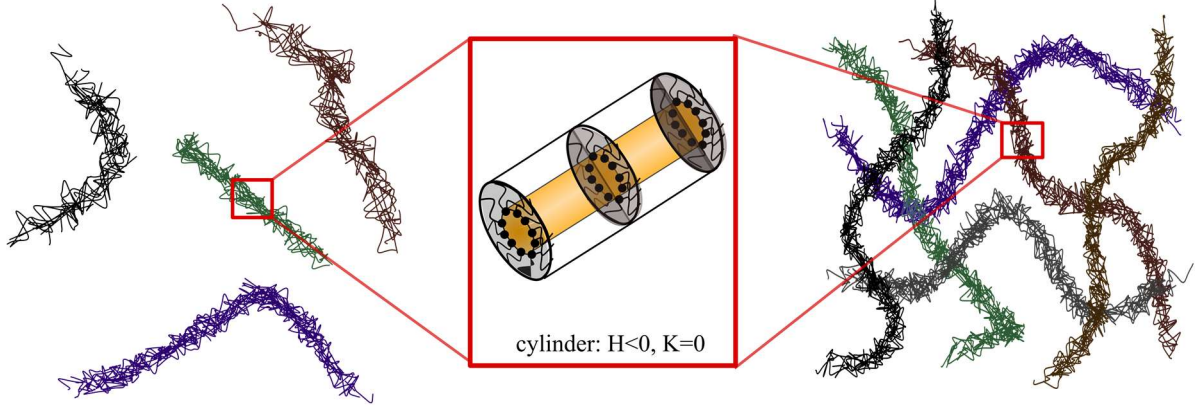


Figure 18. Reverse wormlike micelles in the dilute (*left*) and the semi-dilute (*right*) regime. A polar core is enclosed in a bottlebrush structure of extractant chains

The starting point of the formation of linear wormlike micelles is a so-called sphere-to-rod or *sphere-to-cylinder transition*.^[128,129] The driving force for micellar elongation is the change in endcap energy with solvent constraints associated with the two ends of a threadlike structure. The length distribution with an average contour-length \bar{L} scales with the volume fraction of amphiphilic monomer Φ and the endcap energy ε_{EC} :^[59,123,130,131]

$$\bar{L} \sim \sqrt{\Phi} \cdot e^{\frac{\varepsilon_{EC}}{k_B T}} \quad (25)$$

Linear wormlike micelles can have viscoelastic characteristics. In the dilute regime, these structures behave as Newtonian fluids, with a shear-independent viscosity. At higher concentrations, the solutions become shear-thinning, that means that above a certain critical shear rate, the wormlike chains align in the shear-flow. This leads to a significant decrease in viscosity.^[130,132,133] This behavior is shown schematically in **Figure 19**.

At very high concentrations, the wormlike micelles entangle and form a network. In this case, after application of a deformation, an elastic response can be observed. This response is related to the number of entanglements or the mesh size of the network, respectively.^[130]

Another important parameter to describe elongated wormlike micelles is the persistence length l_p . Its value signifies the length over which the worm stays rigid. It is therefore a measure of the flexibility of the micelle. A demonstrative image of the characteristic length-scales of wormlike micelles is given in **Figure 20**.

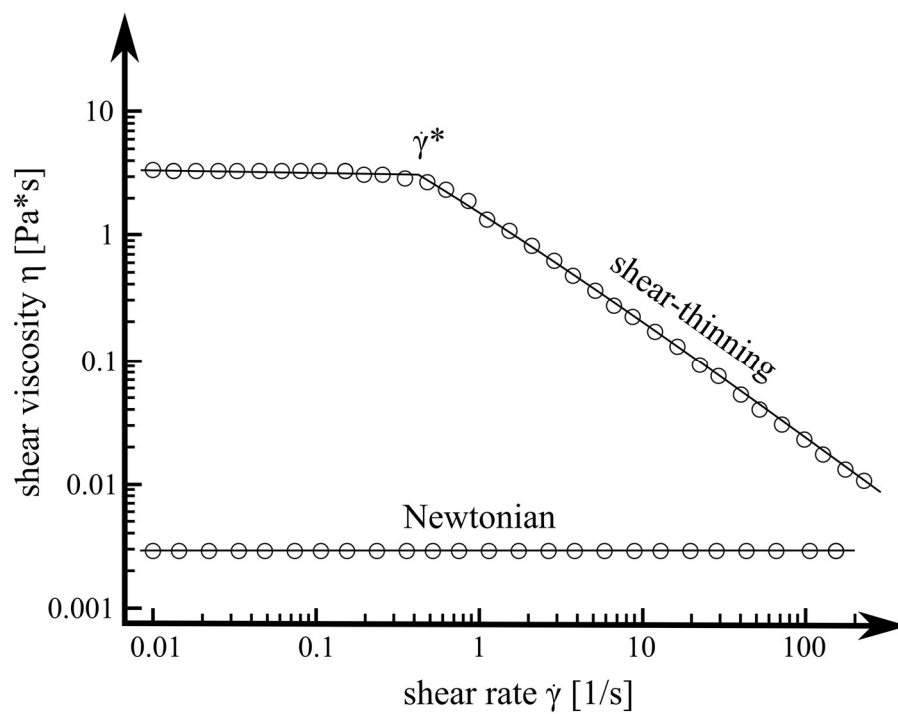


Figure 19. Schematic representation of shear thinning and Newtonian viscosity behavior.

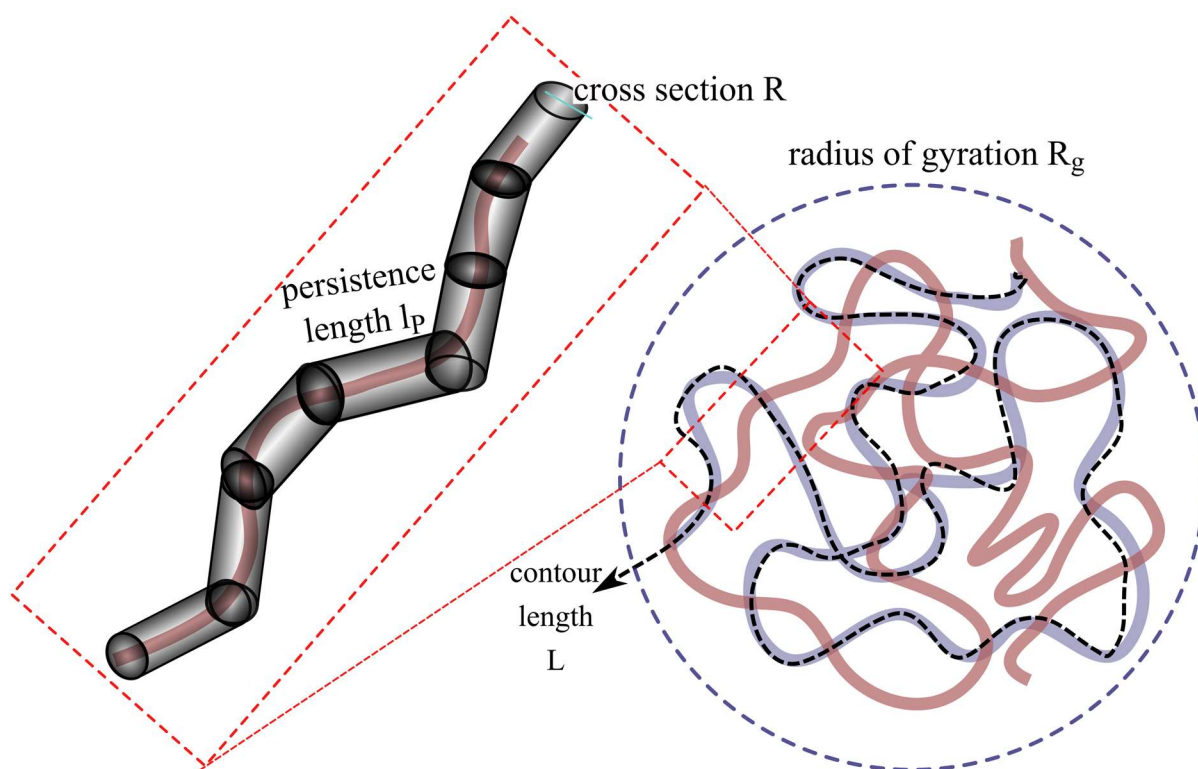


Figure 20. The characteristic length-scales of wormlike micelles: the radius of gyration, the contour length, the persistence length and the cross section

1.2.5.2 Living network

Wormlike micelles cannot only elongate and entangle. There is also the possibility of micellar branching. The formation of intermicellar junctions leads to a multiconnected network.

The driving force of forming junctions having a mean curvature opposite to that of endcaps is to compensate the elevated endcap energy.^[130] This increase and consequently the elongation and branching of such structures is strongly affected by the presence of ions and low molecular weight additives.^[123] For this reason, industry uses salt (NaCl) to adjust the length and branching density of their primarily aqueous systems and the resulting viscosity.^[126] A typical salt curve is shown schematically in **Figure 21**. The addition of salt causes a transition from an entangled to a branched network of wormlike micelles.^[122] Such branching points can freely slide along the micellar body and offer a further possibility of stress release.^[34,130,134] This alternative relaxation mechanism was first proposed by Porte and Lequeux.^[34,135]

The presence of three-fold junctions can lead to a relaxation mechanism that results in a relaxation time that is much faster than of that described above (eq. (20) and (22)). This mechanism is often denoted as the mechanism of sliding connection points^[34] and describes the relaxation by sliding the crosslinks along the micelles through the viscous flow of the amphiphilic network. The activation energy to slide a branch point along the contour is assumed to be very low allowing a very fast relaxation time and leading to a shear-independent viscosity in some cases.^[34] The viscosity of such connected systems is also reduced. According to the theory of Lequeux^[135], the viscosity can be correlated with the following relation:

$$\eta_c = \eta_{nc} \sqrt{\frac{2L_3}{L_1 + 2L_3}} \quad (26)$$

with η_c being the viscosity of the connected network, η_{nc} being the viscosity of a system with the same density of worms and of free ends, but with no connections and L_1 and L_3 being the mean distances along a given path to the first free end or respectively to the first branching point encountered. The three mechanisms of stress relaxation are summarized in **Figure 22**.

This last mechanism is often used to explain the viscosity peak often observed for systems of wormlike micelles with increasing salt concentration (*cf.* **Figure 21**). However, two hypotheses were found in literature to explain the re-descending of the viscosity at elevated salt content. The first hypothesis assumes that the worms grow linearly up to the peak and the branching starts first at the maximum. As described above, theoretical studies have predicted that the

branching influences the relaxation time and viscosity of such systems.^[136,137] Consequently, the evolution of the viscosity could be explained with this theory.

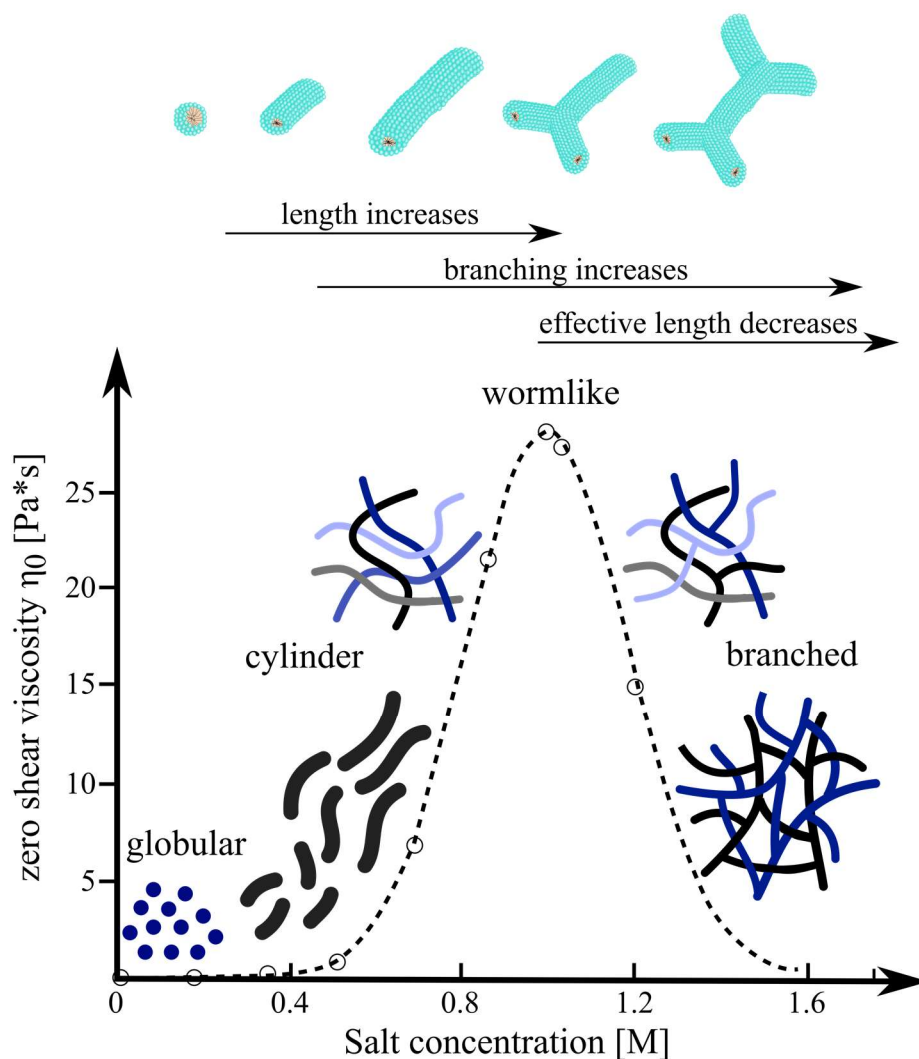


Figure 21. Schematic evolution of viscosity and structure dependent on salt concentration. As example, the experimental data are shown for a solution of 10 wt% SLES in water. Data taken from [126].

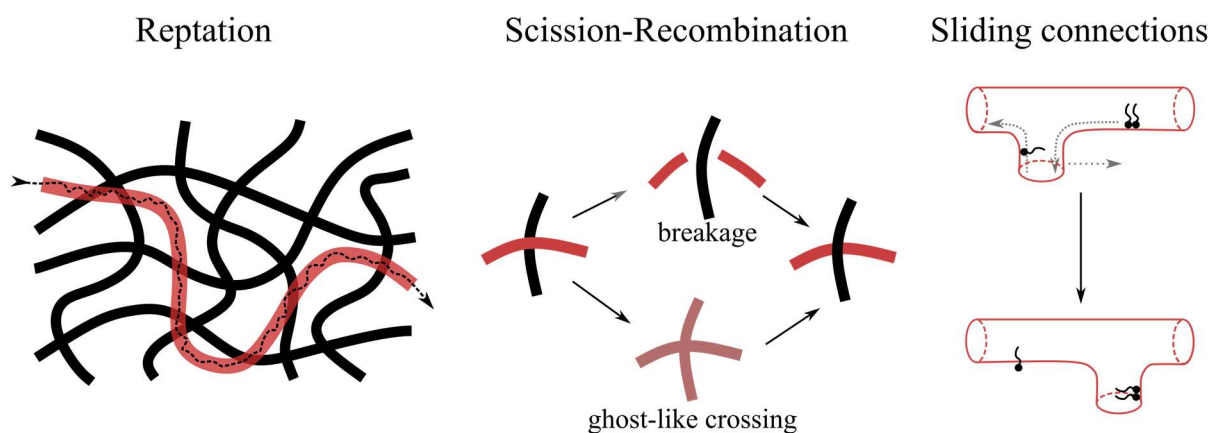


Figure 22. The three mechanisms of stress relaxation for wormlike micelles

The second hypothesis claims that the viscosity related to micellar size is responsible for the decrease in viscosity and that the worm length reaches its maximum at the viscosity peak. It also implies that branching is possible before the viscosity maximum and that above a certain branching density the presence of junctions leads to a decrease of micellar size.^[138–140] The question which of the two hypothesis is true was for long time under discussion. The reason why this question is very hard to answer is that it is difficult to distinguish entanglements from branching points by conventional methods like scattering or rheology.

Croce *et al.*^[141] studied a cationic surfactant in water by cryo-TEM. They observed that mainly linear worms are found on the left of the peak and mostly branched worms are found after the drop in viscosity. Ziserman *et al.*^[71] investigated a mixed catanionic system, also by cryo-TEM. They could show unambiguously that branching start before reaching the maximum in viscosity and junctions, endcaps and cylindrical microphases can coexist. Therefore, they suggest that the decrease in viscosity is rather related to a decrease of the contour length (endcap to endcap distance in purely linear micelles without junctions) of the micelles induced by the presence of junctions. Khatory *et al.* investigated the structure of entangled and branched wormlike micelles^[142]. Especially the presence of junctions necessitated a new definition of the contour length L as an *effective length* L_c , which was defined as the “*the harmonic mean between the average distance from one point along the micelle to the first cross-link and the average distance from that point to the first endcap, or equivalently, the ratio of the total length over the concentration of endcaps plus twice that of connections.*”^[142] This characteristic length replaces the contour length as the appropriate micellar length scale.^[122]

Results from Parker *et al.*^[126] confirm that the branching starts well below the viscosity maximum in the case of SLES in water in presence of NaCl. Their results are in agreement with conclusions drawn by Khatory *et al.*^[142] that say that the viscosity maximum is reached when the concentration of branching points and endcaps are equal.

Thlusty and Safran *et al.* have used several theoretical approaches to describe the transition from entangled networks to branched networks driven by the energies of formation of endcaps, cylindrical micelles and branch points.^[143–147] They did not only focus on wormlike micelles, but on all kinds of entropic networks in colloidal, polymeric and amphiphilic systems, amongst others gels, dipolar colloids or microemulsions.

The concentration dependent structure can be imagined as in **Figure 23**.

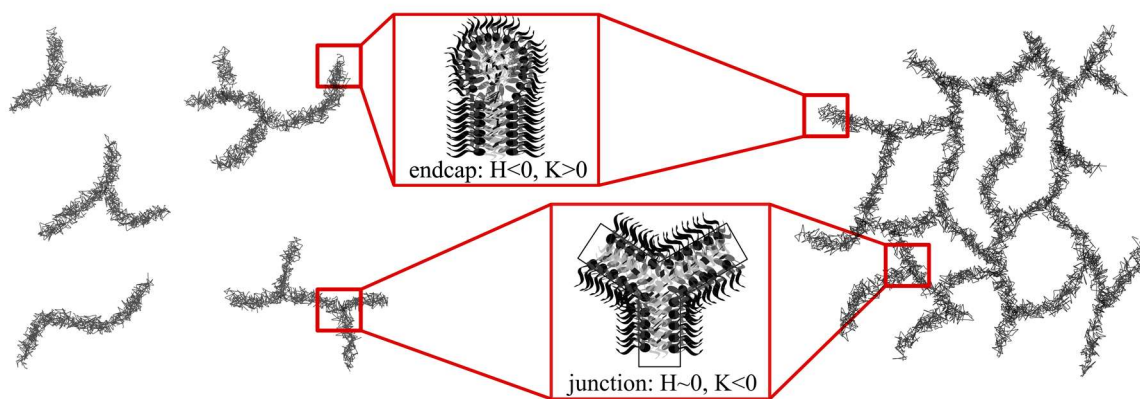


Figure 23. Schematic representation of a connected network of reverse wormlike micelles. Spherical endcaps and saddle-like z-fold junctions coexist. The cylindrical units between these two microphases can be flexible (**left**) and rigid (**right**).

1.2.5.3 Tactoids and microphase separation

The presence of entangled and branched networks as described above can have an additional effect – *microphase separation* – in this context on another length scale (*cf.* **Figure 17**). The theory of Safran and co-workers proposed that entropic effects cause an attractive force between branch points.^[145] This picture was recently completed by Bharti *et al.*^[148] with the proof of effective nanocapillarity. These attractive forces can lead to phase separation when a network reaches its saturation with junctions. Drye and Cates^[149] also report a theory of cross-links in viscoelastic surfactant solutions that predicts phase separation due to network saturation.

According to Zilman *et al.* such phase separations can occur in the following ways:

- Coexistence of a connected network with a phase of dilute chains
- Two coexisting networks
- A coexistence of a dilute and a dense network

Cristobal *et al.* have also developed a model according to which phase separation can occur between a saturated network and structures of free ends such as spherical micelles.^[150] They further conclude that if the network is unsaturated, the viscosity depends on the proportion of free ends and cross-links in solution based on the theory of Lequeux.^[135] When the network reaches saturation, reptation can be neglected and the flow mechanism is assumed to be similar to that used to explain the Newtonian behavior of sponge phases, *e.g.* cross-links sliding along the strands.^[150]

The changes in micellar morphologies can have consequences for the thermodynamic stability and the morphology of the neighboring phases. Therefore, linear entangled wormlike micellar solutions are found close to hexagonal phases while branched networks are located more closely

to lamellar phases.^[122]

In some cases, before macroscopic phase separation, a microphase separation occurs. A more crystalline phase coexists with a domain of diluted phase.^[40] In classical colloidal literature, such cases are described under the term ‘*dispersion tactoids*’ in the form of small ‘nano’ liquid crystals.^[89–91,151] Such solutions form macroscopically a gel, but can be detected by electron microscopy or small angle scattering experiments. In scattering, such nanocrystals are indicated by an increase at very low q values, indicating a large mesoscopic structure.^[152]

The attraction between particles via van-der-Waals forces is strongly influenced by the shape and orientation of the particles.^[153, pp.1–37] The attraction between two parallel cylinders is significantly stronger than between two spheres. For a short demonstration, we consider the interaction energy W_C between parallel cylinders with radii R_1 and R_2 and length L and W_S between spheres, also of radii R_1 and R_2 in vacuum. The bodies are located at a certain distance D . The interaction potential between them can be then calculated as follows:^[59, pp.254–255]

$$W_C = \frac{-A \cdot L}{12\sqrt{2}D^{3/2}} \left(\frac{R_1 R_2}{R_1 + R_2} \right)^{0.5} \quad (27)$$

$$W_S = \frac{-A}{6D} \left(\frac{R_1 R_2}{R_1 + R_2} \right) \quad (28)$$

with $A = \pi^2 \cdot C \cdot \rho_1 \cdot \rho_2$ being the Hamaker constant with ρ_1, ρ_2 denoting the number densities of the interacting particles and C describing the particle-particle interaction potential. The Hamaker constants of most condensed phases are found to lie in the order of $0.4 - 4 \cdot 10^{-19}$ J.^[59, pp.254–255] Assuming $R_1 = R_2 = 0.5$ nm, $A = 1 \cdot 10^{-19}$ J, $L = 5$ nm and $D = 0.5$ nm gives an interaction potential $W_C = -4 \cdot 10^{-20}$ J ≈ -10 kT and $W_S = -8 \cdot 10^{-21}$ J ≈ -2 kT. This simple exemplary calculation already shows the strong influence of the geometry on the van-der-Waals interaction between particles. Even if the cylinder is only 5 times longer than the diameter of the sphere, the attraction is significantly stronger. Therefore, a sphere-to-rod transition can also lead to a stronger attraction between particles. This is also often referred as one origin of the so-called third phase formation (*cf.* next subchapter).^[40]

The physical basis of the interaction of dispersions of anisotropic colloids has been described in the work of Onsager.^[154,155] Such colloids interact via an electrical double layer repulsion at sufficiently low concentration.^[156] As the concentration increases, a gradual transition from an isotropic to a nematic phase occurs.^[154,156] According to his work, anisotropic particles interact via an attractive steric interaction which is due to the impenetrability of the particles. This can

be understood as follows. In a gas of anisotropic particles, there are two kinds of entropy. The first one is due to the translational degrees of freedom, the others due to the different possibilities of orientation. These two types of entropy are linked via the effect of excluded volume. If two rods are parallel, the excluded volume is minimal. This arrangement is favored by translational entropy. However, such an arrangement significantly decreases the orientational entropy, since the number of possible configurations is limited. At low density, orientational entropy always wins since the gain in excluded volume is small. If the density of particles increases, excluded volume becomes more and more important, since more and more particles start to collide. Therefore, at some density the particles start to form a nematic liquid crystal phase.^[157]

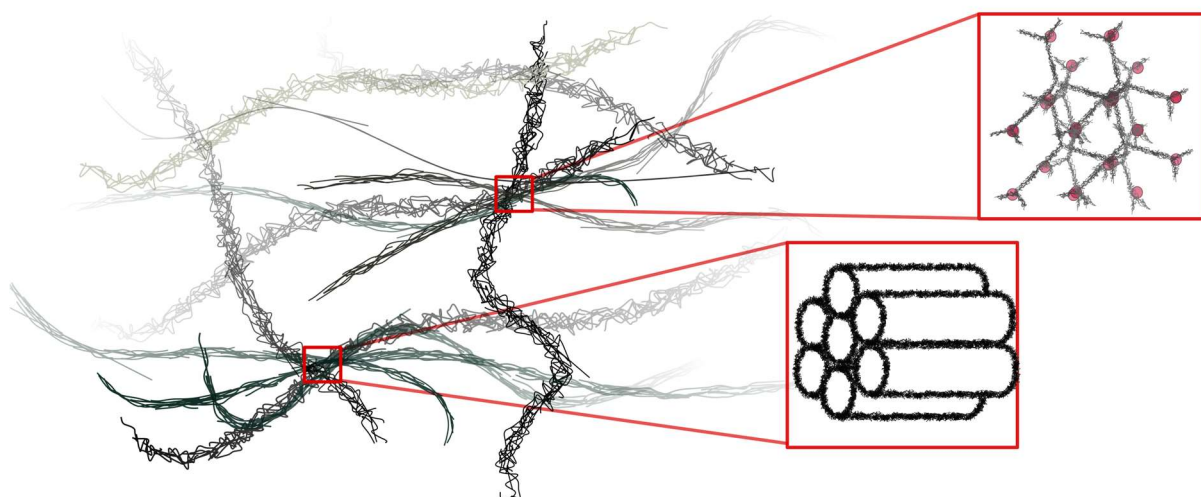


Figure 24. Locally condensed nanocrystals coexisting with a dilute solution

I.2.5.4 Sticky ellipsoids leading to the third phase formation

Another way of phase separation is the *third phase formation* in the framework of liquid-liquid extraction of metals. This term describes the splitting of the organic phase into a light diluent-rich phase and a heavy and viscous extractant-rich phase.^[92] This phenomenon occurs especially in industry, where extractant and ion concentrations are elevated. This splitting represents a significant drawback for industrial liquid-liquid extraction processes. Typical contactor devices (*cf.* Chapter I.2.2) are not designed for such resulting viscous phases and their stability. Moreover, in the case of nuclear reprocessing, this splitting can cause danger. In the third phase, extractants and ions are concentrated.^[40] This locally high concentration of fissile material can lead to criticality with significant consequences as demonstrated by the disastrous accident in Tokaimura in 1999 during a cleaning process.^[158]

The origin of the third phase formation has been investigated for more than 20 years.^[35,40,83,84] It is now well-established that the origin of this phase instability is a direct consequence of the mesoscale organization of the extractant. Approaching the third phase limit, the attractive potential between the aggregates and/or their sizes induces phase separation.^[39,84,86,92,159] There are two competing energies that have to be considered. The thermal energy keeps the aggregates dispersed in the organic phase. This entropic contribution stands in competition with the intermicellar attraction due to a van der Waals attraction between the polar cores of micelles. The organic phase becomes unstable when the energy of attraction exceed a value of around $2 kT$.^[40,160] The attractive force becomes stronger, when the polar core size increases, the shape changes towards cylinders (*cf.* subchapter before) or when polarizable ions such as nitrates or uranyl are added.^[83,161,162]

It is well known that third phase formation can be prevented by the using diluents that are more polar, smaller and/or branched and thus have a tendency to penetrate into the shell of protruding hydrophobic chains.^[87] Therefore, to our knowledge, the third phase formation was never observed with aromatic diluents.^[40] Nevertheless, alkane diluents are preferred to use in liquid-liquid extraction processes due to their excellent hydraulics, high stability and resistance against degradation, lower toxicity, low water solubility and low density. Also the addition of so-called phase modifiers, or '*lipotropes*' can be advantageous to prevent the phase splitting.^[102,163]

To our knowledge, there is no indication in the literature of the relation between approaching the third phase limit and viscosity increase. However, it is conceivable that the evolving mesoscale structures of attracting aggregates also lead to a structure that hinders shearing and thus the flow mechanism of the liquid (*cf.* **Figure 25**).

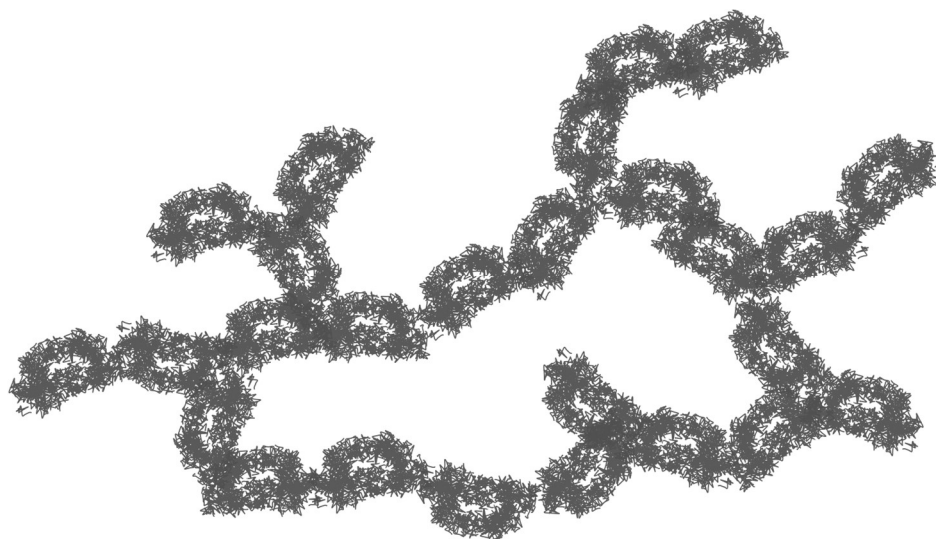


Figure 25. Sticky ellipsoids forming a chain bracelet. The ellipsoidal reverse aggregates stick together due to a strong attractive interaction between the polar cores.

The viscosity η of a dilute dispersion of “simple” spheres is given by Einstein’s formula^[164]:

$$\eta = \eta_0(1 + 2.5\Phi) \quad (29)$$

with η_0 is the viscosity of the pure solvent and Φ being the volume fraction of spheres. For concentrated suspensions, Mooney introduced a so-called self-crowding factor k to expand Einstein’s formula:^[165]

$$\eta = \eta_0 \exp\left(\frac{2.5\Phi}{1 - k\Phi}\right) \quad (30)$$

The formula of Vand has a similar form:^[26,166]

$$\ln \frac{\eta}{\eta_0} = \frac{v\Phi}{1 - Q\Phi} \quad (31)$$

where v is the particle shape factor and Q is the interparticle interaction parameter.

From the equations above, one can see that the viscosity of a dispersion of spheres can strongly vary with varying volume fraction of spheres. This dependence can even be exponential when the concentration is high and the spheres are interacting.

I.2.6 The system Dialkylamide – Uranyl

I.2.6.1 Introduction

In the framework of this thesis, the viscosity of a particular group of extraction systems is investigated. *N,N*-dialkylamides are an important class of extractants and its use is a promising

approach to replace TBP as extractant in the reprocessing of nuclear fuels. Furthermore, the monoamide extractant DEH/BA was proved to be a promising extractant for the first cycle of the GANEX process.^[167] In this subchapter, first the context is introduced – nuclear fuel processing. After that, *N,N*-dialkylamides in particular as well as previous studies related to this problem will be presented.

1.2.6.2 Nuclear fuel reprocessing

Electricity plays a huge role in everyday life. Its demand ranges from industry to single citizens as well as from the simple demand of turning on the lights to keep humans alive in intensive care units. In France (as of 31 December 2015)^[168], 419 TW·h were delivered by nuclear power which corresponds to 76.6 percent of its total need of electricity. Worldwide, 441 operational power reactors are in use and further 68 are under construction (as of 31 December 2015).^[168] Although nuclear power positively contributes to limit global warming and greenhouse gas emissions, it comes with disadvantages which must not be ignored. Besides safety issues, especially the management of nuclear waste is still difficult. During the process, fissile atomic nuclei such as uranium-235 and plutonium-239 interact with thermal (slow) neutrons. A fission reaction may occur and the heavy atoms are split in lighter, short-lived elements – the fission products.^[169] It is also possible that a neutron is captured and elements that are heavier than uranium such as neptunium, americium or curium are created by successive beta-decay.^[170] The resulting transuranic elements are long-lived and have a strong impact on the long-term radiotoxicity of the used fuel.

The resulting fuel can be handled in two different ways. The approximate composition of used fuels from light water reactors is the following:^[169]

- 95.6% uranium (less than 1% U-235)
- 2.9% stable fission products
- 0.9% plutonium
- 0.3% cesium and strontium (fission products)
- 0.1% iodine and technetium (fission products)
- 0.1% other long-lived fission products
- 0.1% minor actinides (americium, curium, neptunium)

One strategy of handling the nuclear waste is the direct disposal and has been chosen for example by USA and Sweden.^[171] After a certain period of interim storage, the fuel is transported to storage facilities and stored either “*wet*” in pools or “*dry*” vitrified in vaults or

casks.^[171] France and other countries such as Russia, Japan, India and China have chosen to reprocess their spent fuel. The spent fuel rods are dissolved in nitric acid and reprocessed in order to recover valuable elements, especially unused uranium and other fissionable isotopes, notable plutonium. The obtained isotopes can be transformed to mixed oxide fuels (MOX fuels) which behave similar to common nuclear fuels and can be used in common thermal nuclear reactors. The process of choice to recycle spent fuel is the hydrometallurgical PUREX (Plutonium Uranium Redox Extraction) process (*cf.* **Figure 23**). This process was developed in the 1940's in the framework of the Manhattan project. This project was originally set up for the recovery of plutonium for military purposes. However, this process is still used today and was optimized during the last 70 years to a well-matured one. In the framework of this process, the used fuel rods are chopped up and dissolved in concentrated nitric acid. In a first step, uranium and plutonium are separated from the fission products by extraction into an organic phase composed of tributyl phosphate (TBP) diluted in an organic solvent. The fission products as well as other elements remain in the aqueous raffinate. In a second step, uranium and plutonium are separated by contacting the loaded organic phase with a nitric acid aqueous solution containing a reducing agent. Typically used agents are iron(II) or uranium(IV) ions or hydroxylamine.^[172] As a consequence, plutonium(IV) is reduced to plutonium(III) and passes into the aqueous solution. Uranium (IV) and (VI) ions which remain in the organic phase can be stripped in a following step with dilute nitric acid.

Figure 27 represents the relative radioactivity of spent nuclear fuel with time. As can be seen, after the first 100 years, the radioactivity is dominated by the presence of actinides and their daughters.^[170] Removing the transuranic elements from the waste could diminish radiotoxicity and storage time. The obtained actinides could be used in new fuels for fast neutron reactors, where they are transmuted to elements with a shorter half-life or even stable ones. In other words, these Generation IV reactors can be configured for the fission of all actinides and consequently – after a given time – may drastically reduce the total amount of actinides in spent nuclear fuel produced by thermal neutron reactors. The nuclear fuel cycle can thus be seen as closed. In order to follow up this approach, alternative separation processes were developed. While the TALSPEAK (Trivalent Actinide - Lanthanide Separation by Phosphorous reagent Extraction from Aqueous Komplexes), DIAMEX (DIAMide EXtraction)/SANEX (Selective ActiNide EXtraction) follow the conventional PUREX process, the GANEX (Group ActiNide EXtraction) process was developed to replace the PUREX process. The aim of this process was to avoid a pure plutonium stream.

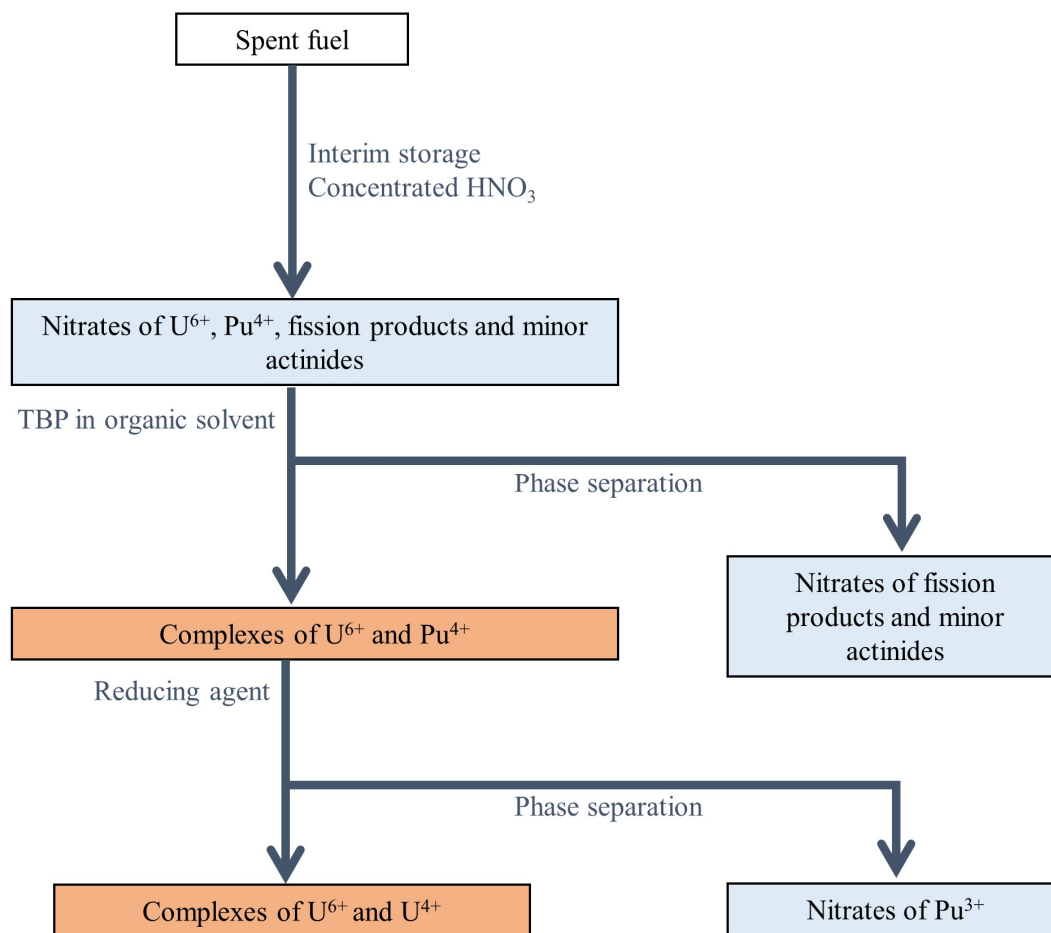


Figure 26. Simplified scheme of the PUREX process. Organic Phase are represented in orange, aqueous phases in blue

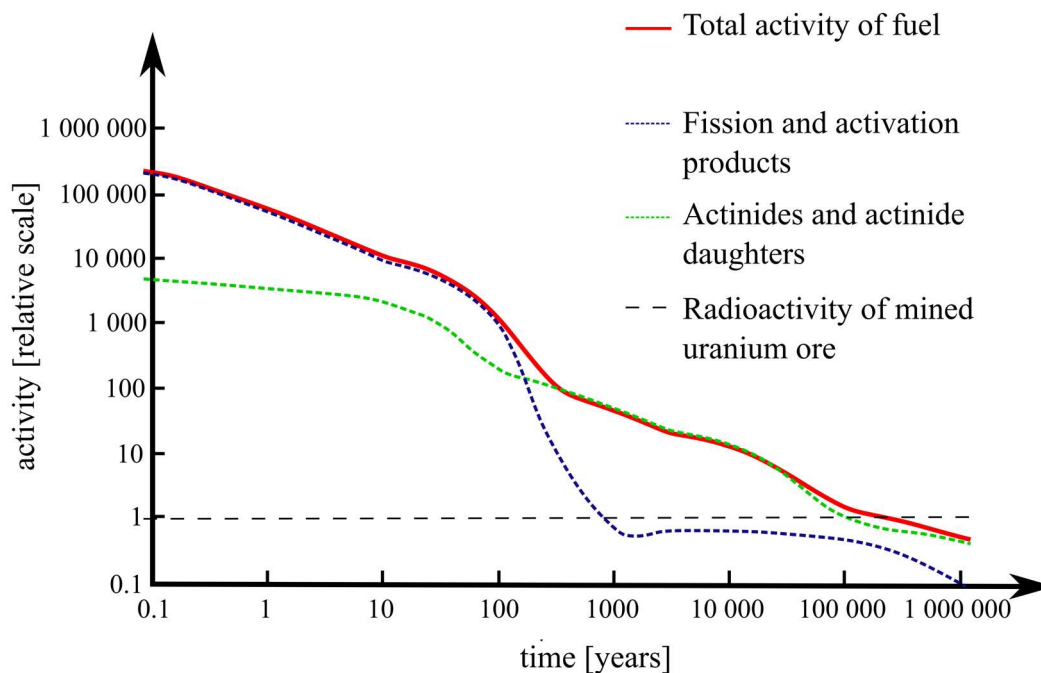


Figure 27. Relative radioactivity of spent nuclear fuel with a burn-up of 38 MWd/kg U. Figure replotted from [170]. During the first 100 years, the activity is dominated by fission products, thereafter by actinides.

An overview on the main separation processes is given in **Table 3**.

Table 3. Summary of the most common recovery processes for spent fuel

	Extractant	Description
PUREX ^[172,173]	TBP	Separation of U and Pu from fission products and minor actinides followed by separation of U and Pu by reducing agent
TALSPEAK ^[174–177]	HDEHP (org. phase) DTPA (aq. phase)	Extraction of lanthanides from trivalent actinides (An) followed by partition of extracted elements by selective stripping of An(III) from the loaded solvent
DIAMEX/SANEX ^[178,179]	DMDOHEMA (DIAMEX) HDEHP (SANEX)	<u>DIAMEX</u> : Coextraction of trivalent actinides and lanthanides directly from PUREX raffinate in order to decrease radiotoxicity of nuclear waste <u>SANEX</u> : Selective stripping of An(III) by suitable aqueous reagents followed by stripping of the lanthanides
GANEX ^[167,180,181]	DEHiBA (1 st cycle) DMDOHEMA-HDEHP (2 nd cycle)	1. Removal of bulk uranium from spent fuel 2. – Coextraction of actinide and lanthanide cations – Selective stripping of actinides by mixture of aqueous complexing agents – Stripping of lanthanides and other fission products

I.2.6.3 Monoamides as possible alternative to TBP

The PUREX process described above is widely used on industrial scale. However, this process suffers from certain disadvantages which are mainly caused by the use of TBP as extractant.^[172] First of all, TBP does not follow the CHON principle. That means that this molecule contains further elements besides carbon, hydrogen, oxygen and nitrogen. As a consequence, used solvents cannot be easily processed by incineration and large amounts of secondary waste are produced. Furthermore, the degradation products due to hydrolysis and irradiation of TBP form insoluble salts with most ions present in the solution to reprocess. Moreover, the need and use of additional reducing agents in the second reprocessing step are connected to certain problems.

The commonly used agents like iron(II), uranium(IV) or hydroxylamine are not sufficiently stable under the prevailing conditions. The degradation products of hydrazine which is added to improve the stability, cause supplemental problems.^[172] With increased Pu(IV) and Th(IV) loading, as intended for future processes, the tendency towards third phase formation is increased.^[100]

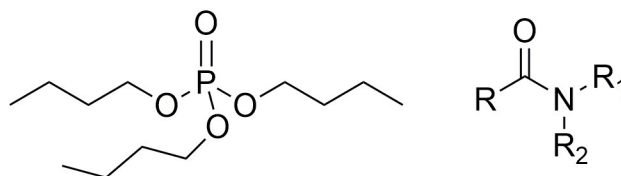


Figure 28. Structure of tributyl phosphate (*left*) and general monoamide structure (*right*)

During the research for possible alternatives to TBP, the studies of Siddall *et al.*^[182,183] attracted the interest of many research groups. *N,N*-dialkylamides (or equivalently, monoamide extractants) were demonstrated to be a promising group of extractants for the extraction of actinides. They exhibit good affinities towards hexavalent and tetravalent ions of actinides and low affinities towards the main fission products. This group of extractants is only barely soluble in aqueous solution and stable against chemical degradation and radiolysis. The synthesis and purification is also not laborious and physicochemical properties and selectivities can be easily adjusted by variation of the three hydrocarbon chains. Monoamides are compatible with alkanes which can be branched or straight. This fact offers various advantages. Alkanes exhibit a high chemical stability in nitric medium and a high flash point. Furthermore, they are less toxic than aromatic compounds. Moreover, the organic phase has a low density facilitating settling and decanting of phases. The main advantage of *N,N*-dialkylamides is the possibility of simultaneous uranium and plutonium extraction without the need of a redox step and additional reducing agents as it the case for TBP. Separation of uranium and plutonium can be obtained by *pH* adjustment of the aqueous solution. It was demonstrated that branching suppresses the complex formation with actinide(IV) more than with actinide(VI) due to sterical hindrance^[184]. Verma *et al.*^[185] and Pathak *et al.*^[186] show that the selectivity towards uranyl can be adjusted by the branching in the alkyl substituents of C_α atom. As a result, branched-alkyl monoamides are suitable for the selective separation of uranium and plutonium, while *n*-alkane substituents exhibit higher extractant efficiency for uranyl.^[185] A possible solvent for the replacement of TBP in the PUREX process is for example a diluted mixture of DEHBA and DEHBA.^[187] By use of this solvent, it is possible to extract uranium and plutonium at low nitric acidity in a first step simultaneously. In a second step, plutonium and uranium can be separated by increasing the acidity. This process can be performed in any conventional extraction apparatus (mixer

settlers, pulsed columns or centrifugal extractions). Recovery is possible by simple contact with dilute nitric acid at ambient temperatures while for TBP elevated temperatures are needed for this step. Furthermore, the degradation products do not disturb and incineration leads only to gaseous waste. As a consequence, secondary waste can be reduced by burning.^[172]

I.2.6.4 Extraction with monoamides

Actinides such as uranium and plutonium exhibit an elevated affinity to higher oxidation states. Therefore, according to the HSAB concept, actinides prefer to interact with hard Lewis bases, *i.e.* strong electron donors.^[188,189] Typical O-donors are able to extract actinides.

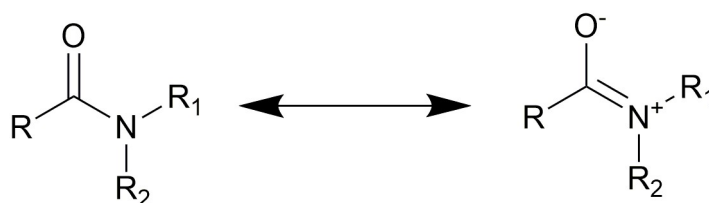


Figure 29. Mesomeric structures of monoamides indicating a partial negative charge on the oxygen atom

As indicated in **Figure 29**, monoamides exhibit a partial negative charge on the oxygen atom. The presence of this charge was confirmed by Rabbe *et al.* and calculated to a value of about -0.37.^[190] This value and consequently the complexation power slightly depend on the substituents due to an inductive donor effect favoring the delocalization of the electrons. As a result, the extractants will always interact with uranyl by the carbonyl function. This was demonstrated by Ferru using IR spectroscopy^[191] and also by other groups^[182,187,192,193].

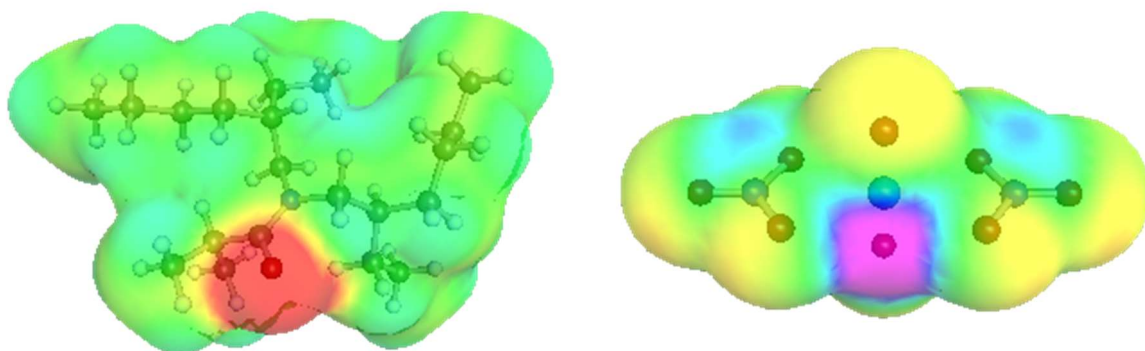


Figure 30. Polarization charge density (σ) surface of **left:** DEHiBA and **right:** uranyl nitrate calculated by COSMO-RS. The best screening of the complex is obtained if the red surface (carbonyl group) interacts with the purple surface of the uranyl ion.

Calculating the σ (polarization charge density) surface of the typical monoamide extractant DEHiBA and uranyl nitrate confirms this evidence (*cf.* **Figure 30**). The best screening can be obtained if the red area (the carbonyl group) interacts with the purple area (the positive polarized uranyl ion). A short introduction to the principle behind COSMO-RS can be found in

Annex VII.4.

I.2.6.5 Viscosity increase

Since the distribution and selectivity coefficients are not the only parameters which are important to evaluate, Pathak *et al.* compared the hydrometallurgical parameters of TBP and *N,N*-dialkylamides.^[100] He investigated interfacial tension, phase separation time, density and viscosity of 1.1 M extractant diluted in dodecane. A significant lower phase-disengagement rate was observed for DHOA compared to TBP. Interfacial tension, phase separation time and viscosity increase significantly with increasing uranyl loading of the organic phase.^[100]

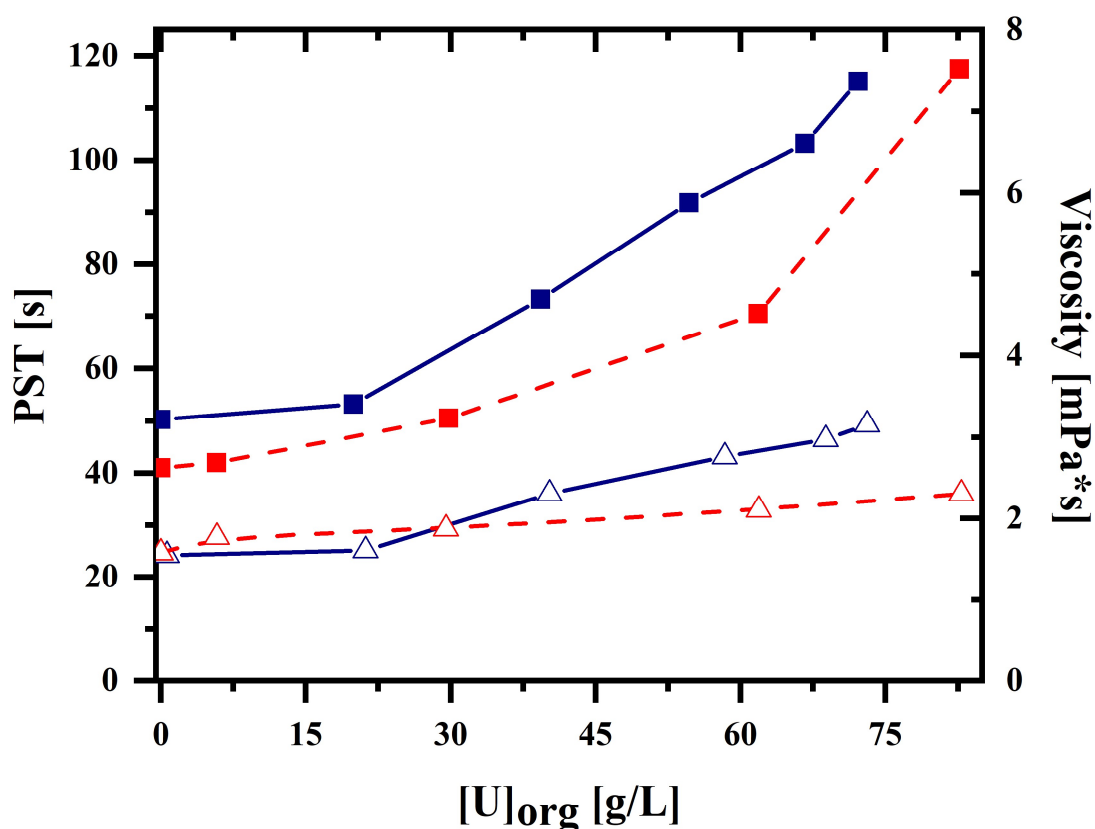


Figure 31. Viscosity of organic phase (red dashed) and phase separation time (blue solid) with increasing uranium loading at ambient temperature. Organic phase composed of Δ 1.1 M TBP or \blacksquare DHOA in dodecane. Acidity of aqueous phase: 3.5 M HNO_3 . Figure replotted from [100].

As a result, the hydrodynamic properties have to be adjusted for efficient use of monoamide extractants on industrial scale and in sufficient high concentration. The focus of this thesis lies on the viscosity of the organic phase. The three following different monoamide extractants will be investigated in order to evaluate the influence of the alkyl chain linked to the carbonyl group (*cf.* Figure 32).

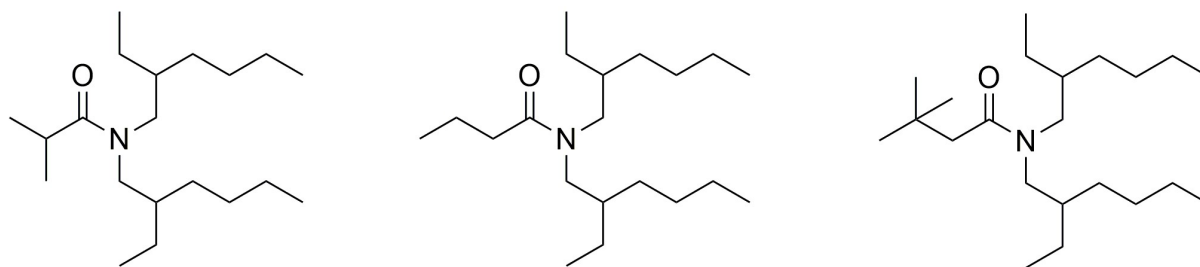


Figure 32. Structures of the monoamides DEHiBA (left), DEHBA (middle) and DEHDMBA (right)

1.2.6.6 Molecular Dynamics – First hint of supramolecular organization

Ferru *et al.* investigated the organization of DEHiBA and DEHDMBA diluted in heptane on molecular and supramolecular scale in the presence of water, nitric acid and uranyl nitrate^[191,194–196]. In the presence of water and below 0.5 M, mainly monomers are present in solution. At higher concentration, the formation of dimers, trimers and tetramers start to form. For elevated concentrations (0.9 M for DEHDMBA and 1.25 M for DEHiBA), more aggregates are present than monomers. Due to the formation of aggregates, up to 8 times more water is extracted compared to the presence of only monomers. However, 5-10 times less water is extracted compared to TBP. In the presence of nitric acid, structuration is favored demonstrated by a reduction of monomer concentration. A model using the species $\overline{L_2}$, $\overline{L_3}$, $\overline{L_2(HNO_3)_2}$, $\overline{L_2(HNO_3)(H_2O)}$ and $\overline{L_2(HNO_3)_3(H_2O)}$ allows a satisfying description of the water and acid extraction of the system and the structuring of the solution. The situation becomes more interesting, when uranyl nitrate is involved. Water extraction decreases with increasing concentration of uranyl. As a result, increased water solubilization can be excluded as reason for viscosity increase. The coordination sphere around uranyl does not change with the concentration of monoamide or uranyl, but the supramolecular organization does.^[191,196] In contrast to temperature and nitric acid coextraction, extractant concentration and uranyl concentration seem to be the decisive parameter for aggregation. The coordination around nitrates changes with uranyl and extractant concentration and nitrates bridging between uranyl ions can be found. Using a combination of SWAXS and molecular dynamics, the structuration of the organic phase could be identified. For an extractant concentration below 0.5 M, uranyl extraction leads to the formation of small aggregates with an average size of 4 extractant molecules. For solutions containing between 0.5 M and 1.0 M of monoamide, uranyl extraction leads to the formation of larger aggregates. Nitrate anions bridge UO_2^{2+} molecules resulting in long $UO_2(NO_3)_2$ -threads (*cf.* **Figure 33**, left). This polar phase is surrounded by DEHiBA molecules. At very high concentrations (>1.5 M), also a significant structuration of the organic

phase is observed, but it is not possible to speak of aggregates of defined size and shape. Rather the formation of a network with a correlation between uranium atoms was proposed. However, it was concluded that uranyl ions are still bridged by nitrate anions, but the aggregate sizes produced seem to be smaller (*cf.* **Figure 33**, right). The authors have explained this structural difference by the extractant polar head concentration that is higher for 1.5 M extractant. That promotes a stronger competition between $\text{UO}_2^{2+}/\text{NO}_3^-$ and $\text{UO}_2^{2+}/\text{DEHiBA}$ interactions leading to smaller aggregates.^[191,194–196] In spite of these images, the origin of the viscosity increase is still unclear and under discussion. Furthermore, these calculations underestimate the experimentally observed stoichiometric ratio of around 2 extractant molecules per uranyl.^[187,196]

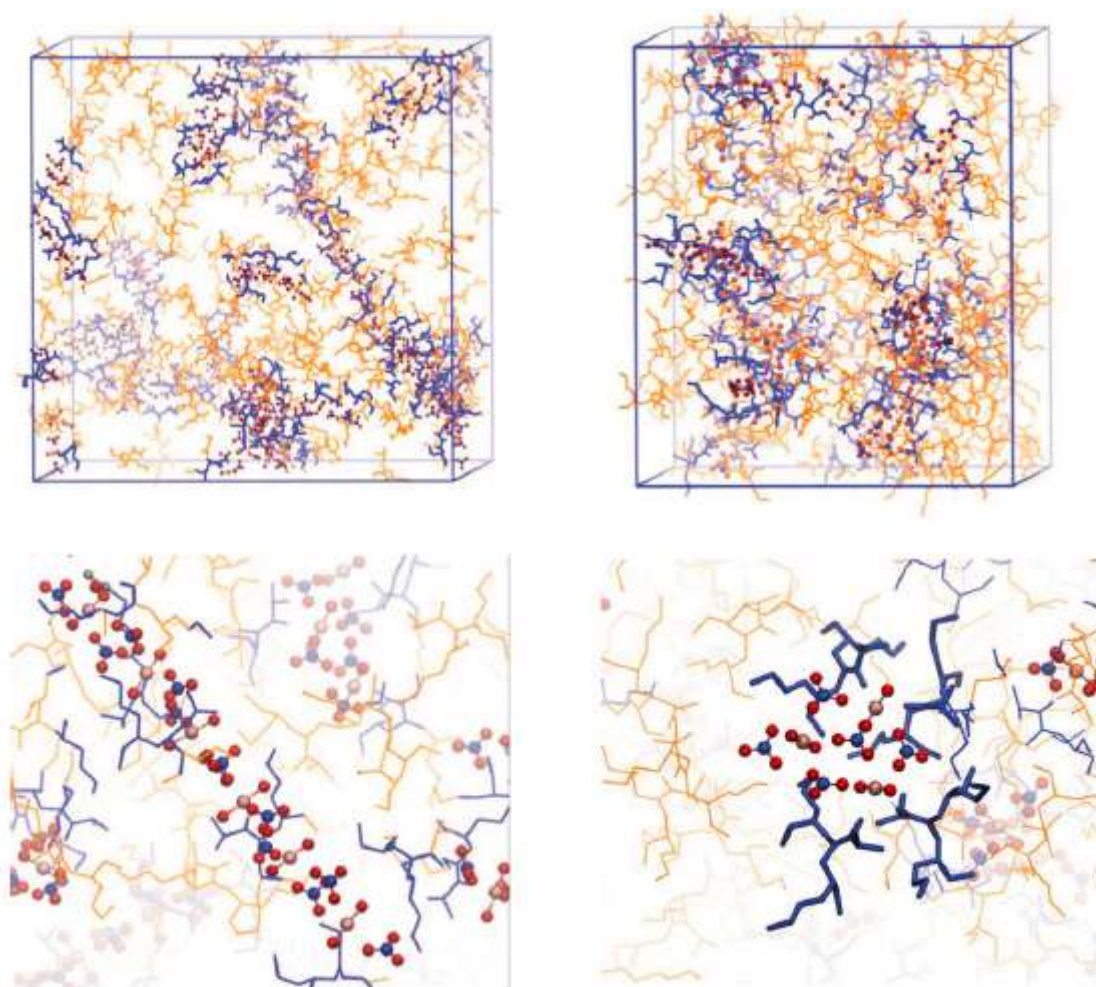


Figure 33. MD simulation snapshots taken from [196]. **Left:** 0.5 M DEHiBA diluted in heptane in presence of 0.22 M uranyl nitrate. **Right:** 1.5 M DEHiBA diluted in heptane in presence of 0.42 M uranyl nitrate. The **top** images show the corresponding simulation boxes while at the **bottom** the characteristic structures are represented. The diluent is removed from this representation. The molecules in cyan and red represent UO_2^{2+} , in blue and red NO_3^- and in grey and red H_2O . Blue DEHiBA molecules are directly connected with a uranyl ion, orange ones are “free”.

Since there are still ambiguities such as the explanation of the viscosity increase or the role of

the diluent in the extraction process, this case is further investigated experimentally in Chapter II. In order to get a feeling for tendencies and to explain the evidences, a minimal thermodynamic model is developed. In Chapter IV, this model is applied to propose formulation strategies to solve the problem of viscosity increase.

II EXPERIMENTAL OBSERVATIONS

In this chapter, the first step to achieve the objective of this thesis (*cf.* Chapter I.1) is presented. First, experimental methods and the used chemicals are introduced. Then, the observations are presented and later interpreted. From these experimental indications and the theoretical background (Chapter I), a simple picture of the mesoscopic organization that leads to the increase in viscosity is developed. This picture is then used in Chapter III to develop a model at nanoscale, in order to explain and understand the origin of this viscosity increase as well as to propose different formulation approaches to limit this problem of industrial importance.

Parts of this Chapter are used for the following Publication:

*M. PLEINES, J. DUHAMET, T. ZEMB, A minimal model at nanoscale leading towards a new formulation principle for extracting microemulsions, submitted to Hydrometallurgy **2018**.*

II.1 Experimental Methods and Chemicals

II.1.1 Chemicals and materials

All chemicals were used without further purification. A list of used chemicals and their suppliers can be found in the Annex, **Suppl. Table 1**.

In the following, the main working protocols are described in order to understand the experimental results. The theory behind these techniques is summarized in the Annex, Chapter VII.3.

II.1.2 Preparation of the organic phase

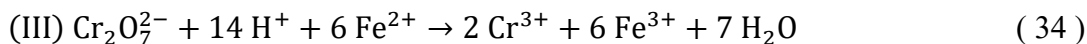
Organic phases were prepared by diluting a certain extractant (DEHBA, DEH/BA, DEHDMBA or TBP) in a diluent to reach a definite molarity. After that, the solutions were contacted with aqueous phase in equal volumes using a Stuart rotator SB3 for 3 hours. The aqueous phase was chosen according to the investigation and composed of either distilled water, 3 M nitric acid or aqueous solutions of uranyl nitrate at different concentrations. These were prepared by dilution of a stock solution (374 g/L uranyl in 2 M nitric acid) with distilled water and nitric acid to obtain an acidity of 3 M. The two phases were separated after centrifugation. In order to prepare an organic phase of a definite uranyl content, the concentration of uranyl in the aqueous phase was chosen so that the intended concentration of the organic phase is reached after contact of the two phases according to the known distribution coefficients.

II.1.3 Determination of uranyl content by potentiometric titration

Due to the high concentration of uranyl, the concentration of uranyl in aqueous and organic phase was determined volumetrically. First, a certain amount of solution containing uranyl (40 – 200 μ L) was added to 60 mL of an acid mixture (H_2SO_4 1 N, HNO_3 1 N and sulfamic acid 0.1 M). In the case of organic solution, 1 mL of ethanol was added and stirred for 5 min, in order to facilitate the transfer from the organic into the aqueous phase. After that, a hydrochloric solution of titanium(III) chloride (Merck, 15%) was added to the solution in order to reduce Uranium(VI) to Uranium(IV) quantitatively and stirred for 300s (reaction I).

After that, 3 drops of FeCl_3 (27%, VWR) were added to the solution (in excess). These Fe^{3+} ions serve as oxidizing agent for U^{4+} ions to obtain hexavalent uranyl (reaction II). The amount of Fe^{2+} which is related to the amount of U^{6+} is determined by potentiometric titration with

0.1 N Titrimetric potassium dichromate solution (Volusol) (reaction III).^[197,198]



In the case of viscous organic solutions, the amount of uranyl in the organic solution was determined by mass balance due to better reproducibility.

II.1.4 Rheological investigations

Rheological investigations were carried out with an Anton Paar DSR 301 Rheometer under thermostatic control. For most of the samples, a couette CC17 T200 SS geometry was used (diameter 16.666 mm; length 24.995 mm). The sample volume was 4 mL. The geometry of concentric cylinders was chosen because of security reasons and to minimize evaporation effects. Only for viscosities larger than 100 mPa*s a plate-plate geometry was used (diameter 24.981 mm). Since all measured solutions exhibited Newtonian behavior above shear rates of 2 1/s, a certain shear rate (50 1/s) was chosen as representative value to measure the viscosity. It was deliberately avoided to extrapolate the curves to obtain the zero-shear viscosity, since the data at low shear rates were noisy and the presence of a yield stress could not be excluded for each case. Moreover, for industrial application the viscosity value under shear is probably more relevant, since in extraction devices like pulsed columns, strong shear forces are also applied to the liquids.

Shear viscosities were measured under thermostatic control from shear rates of 0.1 to 1000 1/s with 10 points per decade and a measurement duration of 6 seconds/point. Each measurement was carried out three times and the mean value was taken for plotting. The standard deviation for these measurements was approximately 0.1-0.2 mPa*s. Since this standard deviation is small for elevated viscosities, the error bars were not plotted by reason of better clarity. Amplitude sweeps were carried out in a strain range from 0.01 to 5000% at a constant frequency of 1/s, with 10 points/decade and a measurement duration of 30 s per point. Frequency sweeps were carried out in the linear viscoelastic range, in most cases at a strain of 0.2%. The frequency range was chosen from 0.01 to 100 1/s with 10 points per decade. Before each measurement the samples were heated up at 50°C for 15 min under slight shearing, cooled down under slight shearing for further 15 min at 25°C and kept another 15 min without shearing. Between extraction and rheological measurements, there was at least 24 h to ensure that the equilibrium

in the organic phase has been reached.

In order to quantify the measured viscosity increase, the viscosities have to be normalized. With regard to the goal to take both the viscosity of the diluent as well as the volume fraction of the extractant and its viscosity into account, the apparent viscosities were divided by the viscosity of the extractant/diluent mixture before contact with the aqueous phase. For higher accuracy for smaller viscosities, the falling ball method was chosen to obtain the dynamic viscosity of the solvent. For this purpose, an Anton Paar AMVn automated microviscosimeter was used and combined with an Anton Paar DSA5000 densimeter. After temperature calibration, each sample was measured four times and the resulting viscosity values were averaged.

II.1.5 Small- and Wide-Angle X-ray Scattering

Small- and Wide-Angle X-Ray Scattering experiments were carried out on a bench built by Xenocs using X-Ray radiation from a molybdenum source ($\lambda = 0.71 \text{ \AA}$) delivering a 1 mm large circular beam of energy 17.4 keV. The scattered beam was recorded by a large on-line scanner detector (MAR Research 345) which was located 750 mm from the sample stage. Off-center detection was used to cover a large q range simultaneously ($0.2 \text{ nm}^{-1} < q < 30 \text{ nm}^{-1}$, $q = \left[4\pi/\lambda\right] \sin(\theta/2)$).

Collimation was applied using a 12: ∞ multilayer Xenocs mirror (for Mo radiation) coupled to two sets of Forvis scatterless slits which provides a $0.8 \text{ mm} \times 0.8 \text{ mm}$ X-ray beam at the sample position. A high-density polyethylene sample (from Goodfellow) as a calibration standard was used to obtain absolute intensities. Silver behenate in a sealed capillary was used as scattering vector calibration standard. Integration of the 2-dimensional spectra was performed using the software FIT2D. Data were normalized taking into account the electronic background of the detector, transmission measurements and empty cell subtraction. Due to the uranyl L-edge X-Ray absorption, fluorescence phenomena increase the intensity background (Mo radiation: 17.45 keV). After solvent extraction and after checking with a calibration curve of uranyl nitrate in 3 M nitric acid if the fluorescence represents a constant value over the q range, the fluorescent background was subtracted using the assumption that the solvent peak is not influenced by the presence of uranyl. From each sample, a constant value was subtracted in order to adjust the solvent peak to the same level.

II.1.6 Small-Angle Neutron Scattering

Small-angle neutron scattering measurements were performed at the French neutron facility Laboratoire Léon Brillouin/Orphée (LLB/Orphée) on the PAXY spectrometer. Within the

framework of two beamtimes, different configurations were used to cover a wide q -range. The configurations are listed in **Table 4**.

Table 4: Configurations used for SANS measurements at the LLB

Beamtime 1		
<i>Wavelength</i>	<i>Sample-to-detector-distance</i>	<i>q-range [\AA]</i>
4 \AA	1 m	[5.5E-2; 6.7E-1]
4 \AA	6.7 m	[8.3E-2; 1.5E-1]
12 \AA	6.7 m	[2.8E-3; 5.1E-2]
Beamtime 2		
<i>Wavelength</i>	<i>Sample-to-detector-distance</i>	<i>q-range [\AA]</i>
4 \AA	1 m	[5.4E-2; 6.4E-1]
6 \AA	3 m	[9.3E-3; 1.5E-1]
8.5 \AA	5 m	[4.6E-3; 6.7E-2]
15 \AA	6.7 m	[1.9E-3; 2.8E-2]

Using these configurations, a total q -range from 0.0028 to 0.67 \AA^{-1} or, respectively, 0.0019 to 0.64 \AA^{-1} could be covered. All measurements were done under atmospheric pressure and room temperature. Measurements were performed in quartz Hellma cells with an optical path of 1 mm. Standard corrections for sample volume, neutron beam transmission, empty cell signal subtraction and detector efficiency were applied to obtain the scattered intensities. The absolute scale (cm^{-1}) was calculated by normalization with the incident neutron beam. The data reduction has been done using ‘PASINET’ software. Due to the high concentration of non-deuterated extractant, the incoherent background is elevated. In order to estimate the order of magnitude of the incoherent background, a calibration curve using different ratios of $\text{D}_2\text{O}/\text{H}_2\text{O}$ was recorded. The recorded intensities were plotted against the sample transmission or respectively against the concentration of protons. With help of this curve, the approximate incoherent background could be calculated for a certain sample transmission or respectively for a certain number of protons.

However, for data fitting using the software ‘SASfit’, the incoherent background was added as a flat contribution to the fit, implementing the estimated value from the calibration curve as starting value und setting the parameter range close to this value.

The curves were fitted with both an Ornstein-Zernike fit and a fit for very anisotropic particles

with local cylindrical geometry coupled with a random rod structure factor. Both were already implemented in the software^[199].

The Ornstein-Zernike fit characterizes the exponential decay of the composition fluctuations correlation function, with correlation length ζ . The Fourier transform of this Lorentzian profile corresponds to correlations dying out as $\gamma = \frac{1}{r} \exp(\frac{r}{\zeta})$. The Ornstein-Zernike general scattering is therefore well-adapted when there is an exponential decay of the instantaneous aggregation numbers with correlation length ζ .^[152,200–203]

$$I(q) = \frac{I_0}{1 + q^2 \zeta^2} \quad (35)$$

For very anisotropic random orientated particles the form factor can be factorized in a cross section term $P_{cs}(q)$ for the shorter dimension and a shape factor $P'(q)$ for the longer dimension.

$$I(q) = P'(q) \cdot P_{cs}(q) \quad (36)$$

Knowing the scattering contrast ΔSLD , the form factor of local cylindrical particles P_{cs} is given by

$$P_{cs}(q, \sigma_R, R) = \int_0^\infty \text{LogNorm}(x, \sigma_R, R) \left[(\Delta SLD) \pi x^2 \frac{2J_1(qx)}{qx} \right]^2 dx \quad (37)$$

assuming a centro-symmetric scattering length density distribution. R represents the cylinder radius and J_1 the first order Bessel function.^[199] The problem with randomly oriented cylinders is that the interaction depends on the angle between two neighboring cylinders. Instead of the standard separation of form and structure factor, we should better talk about a tensor integration. At compositions close to a phase transition, the volume exclusion compensates the attractions, $P'(q)$ can be considered as close to 1 and therefore be neglected.^[152]

$P_{cs}(q)$ and $P'(q)$ are both already integrated as a plug-in in the ‘SASfit’ software and were used without modifications. Further more detailed information can be found in the manual.^[199]

II.1.7 Methods to estimate the spontaneous packing parameter

As was indicated in Chapter I.2.4.2, the spontaneous packing parameter of an extractant molecule plays a significant role for the microstructure of the organic phase. In order to evaluate

the results obtained in this chapter and especially in Chapter III, a safe and simple method is needed to estimate the spontaneous packing parameter of an extractant molecule.

The estimation of the spontaneous packing parameter is especially difficult at elevated extractant concentration ($c > 1$ M) where the scattering results from both structure and interactions.^[92] The most precise way to determine the packing parameter is to combine SAXS and SANS experiments.^[204] Since X-Rays are sensitive to the electronic contrast between the polar heads and the apolar part composed of extractant chains and diluent, the radius of the polar core can be determined. In contrast hereto, neutron scattering is sensitive to the contrast between hydrogen and deuterium. By use of a hydrogenated extractant and a deuterated diluent one can induce a contrast between the diluent and the aggregate formed by the extractant.^[204] Although the explanatory power of the scattering experiments is weakened due to the high volume fraction of extractant used (in part, volume fractions $> 50\%$ of extractant), the scattering curves nevertheless have an informative value according to Babinet's principle of optics. This theorem indicates that two complementary structures (as shown in **Figure 34**) produce exactly the same scattering.^[152, p.53]

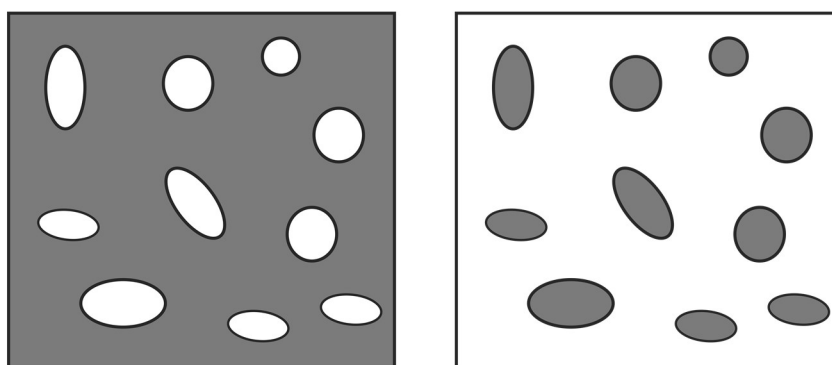


Figure 34. Schematic representation of Babinet's principle. Both structures - "white" holes in a "grey" matrix - and - "grey" holes in a "white" matrix result in the same scattering pattern.

As a result, the radii R_1 (core) and R_2 (aggregate) can be obtained (cf. **Figure 35**). The spontaneous packing parameter P_0 can then be calculated from these two radii^[205]:

$$P_0 = \frac{v}{a_0 \cdot l} = \frac{\frac{4}{3}\pi(R_2^3 - R_1^3)}{4\pi R_1^2 \cdot (R_2 - R_1)} \quad (38)$$

$$P_0 = \frac{1}{3R_1^2} \cdot \frac{(R_2 - R_1)(R_2^2 + R_1R_2 + R_1^2)}{(R_2 - R_1)} \quad (39)$$

$$P_0 = \frac{1}{3} \left(\frac{R_2^2}{R_1^2} + \frac{R_2}{R_1} + 1 \right) \quad (40)$$

However, the modelling of scattering data of strongly interacting anisotropic objects is not an

easy task. The structure factor is not easy to determine, whereby the shape factor cannot be determined with a non-negligible uncertainty. Therefore, the spontaneous packing parameter in this work was not determined by scattering in this work.

A simple and safe value is needed to classify the structure of extractant molecules and compare different extractants in a qualitative way. In the following, this value is called the ‘*spontaneous packing parameter*’ although it can differ from the real packing parameter. This value is estimated in order to have a tool to compare extractants and to be able to predict the microstructural properties in a qualitative way.

In the following, different approaches are presented to obtain a qualitative order of a series of extractant molecules.

II.1.7.1 The minimal spontaneous packing parameter

A simple and parameter-free method to estimate the minimal packing parameter of extractants from their molar volumes was described in the thesis of C. Bauer.^[205] The chain length l_c as well as the volume $V_{\text{apolar, linear}}$ of the apolar part in case of linear chains can be calculated by Tanford’s formulas:^[56,58]

$$l_c \leq 0.15 + 0.127n_c \text{ [nm]} \quad (41)$$

$$V_{\text{apolar, linear}} = 0.0274 + 0.0269n_c \text{ [nm}^3\text{]} \quad (42)$$

where n_c represents the number of carbon atoms. For more than one chain, the volumes of all alkyl chains have to be summed up to obtain the total apolar volume. The equation for l_c calculates the length of the fully extended chain. In aqueous systems, the effective chain length of surfactant molecules in the micellar core is about 80% of the extended chain. For extractant molecules, where the chains point towards the organic solution, the chains are also expected to be smaller than the calculated chain length. But since to our knowledge, there is no general rule for the chain length in extractant systems, no factor is applied to implement the effective chain length and the maximal possible value is taken. Since this shortening is expected to be approximately by the same factor for the systems investigated, this assumption does not change the qualitative trends.

For branched chains, the table of Fedors can be used to calculate the apolar volume:^[206]

$$V_{\text{apolar, branched}} = n_{\text{CH}_3}V_{\text{CH}_3} + n_{\text{CH}_2}V_{\text{CH}_2} + n_{\text{CH}}V_{\text{CH}} + n_{\text{C}}V_{\text{C}} \quad (43)$$

with n_x being the number of alkyl group x and V_x the corresponding molecular volume taken from the table of Fedors. Solvent penetration^[87] is excluded in this calculation. The volume of the polar head of the molecule can be calculated by the difference of the total volume of the molecule and the volume of the apolar part:^[205]

$$V_{\text{polar head}} = V_{\text{molecule}} - V_{\text{apolar}} = \frac{M_{\text{mol}}}{\rho \cdot N_A} - V_{\text{apolar}} \quad (44)$$

where M_{mol} represents the molar mass of the amphiphile molecule, ρ its density and N_A the Avogadro number. As was further shown by Bauer and above, the spontaneous packing parameter P_0 of extractants forming a sphere having a radius R_1 for the polar core and a radius R_2 as the total sphere radius (*cf.* **Figure 35**) can be calculated by following expression:^[205]

$$P_0 = \frac{1}{3} \left(1 + \frac{R_2}{R_1} + \frac{R_2^2}{R_1^2} \right) \quad (45)$$

Assuming a closest packing of four spherical head groups in a tetrahedral arrangement forming the minimum hydrophilic core allows to estimate the approximate radius of the polar core R_1' and of the spherical aggregate R_2' (*cf.* **Figure 35**).^[205]

$$R_1' = \sqrt{\frac{3}{2}} \cdot R_{\text{polar head}} = \sqrt{\frac{3}{2}} \cdot \left(\frac{3V_{\text{polar head}}}{4\pi} \right)^{1/3} \quad (46)$$

$$R_2' = \left(\frac{3V_{\text{apolar}}}{4\pi} + (R_1')^3 \right)^{1/3} \quad (47)$$

Knowing these two radii allows to estimate a value for the packing parameter just from the molecular geometry and to compare different amphiphiles by this value. It has to be noted that this value can strongly vary from the experimentally obtained values since solvent penetration or the influence of ions and water is not taken into account. However, the trends obtained by this method should be similar to those obtained experimentally.

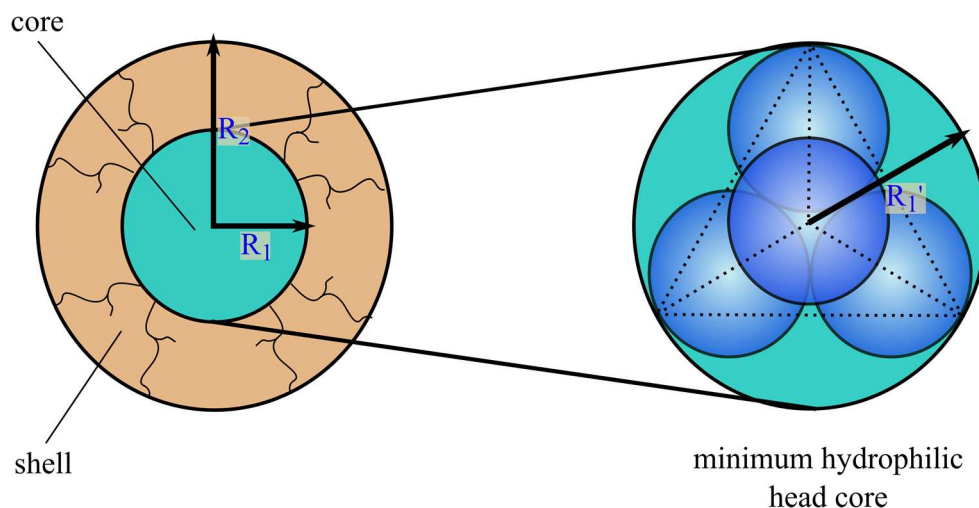


Figure 35. *Left:* Core (R_2) and shell (R_1) radius of the model aggregate. *Right:* Minimum hydrophilic head core radius R_2' . Figure based on [205].

II.1.7.2 The spontaneous packing parameter P_0'

In the following, the assumption that a spherical micelle is formed by 4 extractant molecules is further elaborated and extended to a micellar core containing metal and acid. That assumption is a general experience and is a valid approximation for common extractants such as TBP^[207], DEHiBA^[191] or DMDOHEMA^[92] – at least for lower concentrations.

It is further assumed that the geometry stays spherical, but the polar core can swell due to addition of water, acid and metal ions. The length of the extractant chains as well as its volume is not significantly influenced by this swelling. Only the area per headgroup at the polar/apolar interface increases with metal addition (*cf.* **Figure 36**).

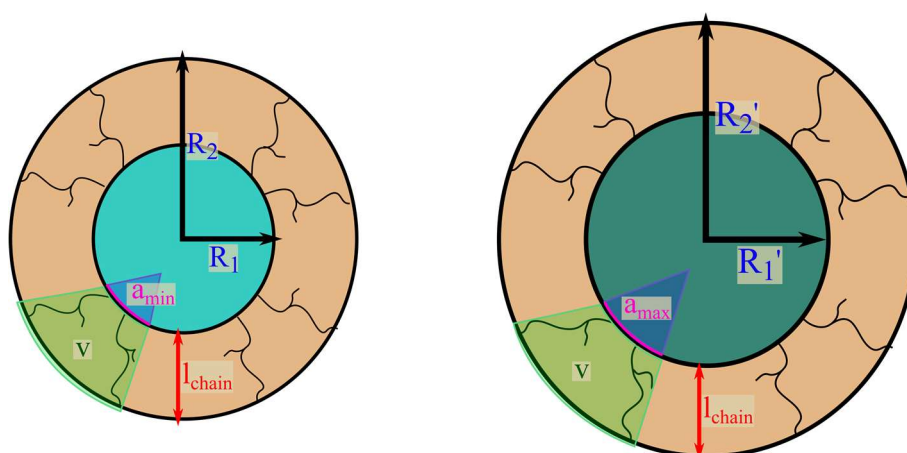


Figure 36. Schematic evolution of the area per headgroup per extractant due to volume increase of the polar core.

Therefore, the spontaneous packing parameter will decrease with metal addition.

The volume and the length of extractant chains can be calculated as described above.

For the estimation of the area per headgroup, one can assume the polar core as formed by different geometries, either as a tetrahedron or an octahedron embedded in the polar core. One triangular face, or in the case of octahedron two faces, represent the estimated interfacial area that is needed for the calculation of the spontaneous packing parameter P_0' (cf. **Figure 37**)

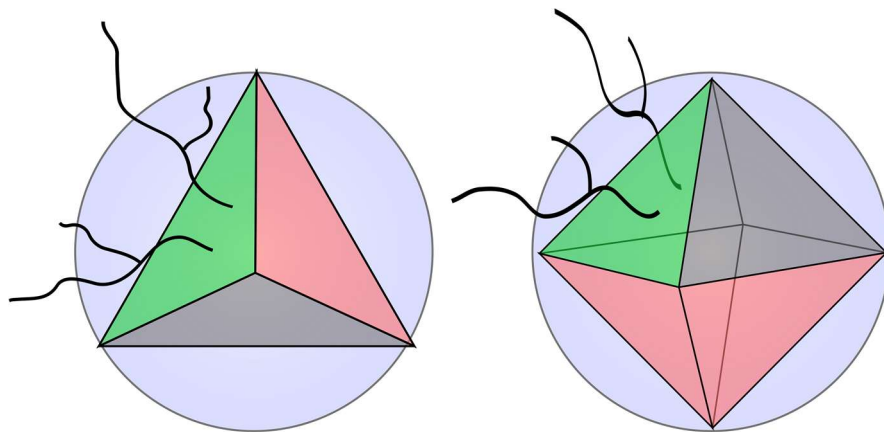


Figure 37. Estimation of the interfacial area per extractant to calculate the pseudo spontaneous packing parameter. **Left:** Approximation of the polar core as a tetrahedron. **Right:** Approximation of the polar core as an octahedron. Two triangular faces represent the polar area per extractant.

The radius of the polar core at ‘zero loading’ and at ‘maximum loading’ with uranyl can be calculated as follows. At zero loading, the size of the polar core is determined by the sum of the volume of four polar head groups and the water and acid uptake. In the case of maximum loading, the volume of the complexed uranyl must be also considered. In total, the volume of a polar core V_{core} can be approximated by the mean stoichiometry of a spherical aggregate.

$$V_{core} = 4 \cdot \left(V_{polar\ head} + \frac{n_{H_2O}}{n_{Ex}} \cdot V_{H_2O} + \frac{n_{NO_3^-}}{n_{Ex}} \cdot V_{NO_3^-} + \frac{n_{UO_2}}{n_{Ex}} \cdot V_{UO_2} \right) \quad (48)$$

with $V_{polar\ head}$ being the polar head volume derived from equation (44), $\frac{n_x}{n_{Ex}}$ being the stoichiometric mol ratio between compound x and the extractant and V_x being the molecular volume of compound x .

The core radius yields then to

$$R_{core} = \left(\frac{3V_{core}}{4\pi} \right)^{\frac{1}{3}} \quad (49)$$

For a tetrahedron with edge length b that is embedded in the polar core, the area a_0 of one triangular face or respectively of the extractant polar part can be calculated as follows:

$$b_{\text{tetrahedron}} = \frac{4 \cdot R_{\text{core}}}{\sqrt{6}} \quad (50)$$

$$a_0(\text{tetrahedron}) = a_0(\text{extractant}) = \frac{b_{\text{tetrahedron}}^2 \cdot \sqrt{3}}{4} \quad (51)$$

In case of assuming octahedral geometry, the polar surface area of an extractant is twice that of one triangular face of the octahedron.

$$b_{\text{octahedron}} = \frac{2 \cdot R_{\text{core}}}{\sqrt{2}} \quad (52)$$

$$a_0(\text{octahedron}) = 0.5 \cdot a_0(\text{extractant}) = \frac{b_{\text{octahedron}}^2 \cdot \sqrt{3}}{4} \quad (53)$$

The equations for the calculations of the volume, the surface area and the radius of the circumcircle of tetrahedrons and octahedrons were taken and rearranged from [208].

For the molecules TBP, DEHBA, DEH*i*BA and DEHDMBA that are mainly investigated in this work, the following pseudo spontaneous packing parameters can be calculated (*cf.* **Table 5** and **Table 6**). The estimated stoichiometries of the aggregates as well as other input parameters for the calculation are listed in the Annex (*cf.* Chapter VII.6.2)

Table 5. Characteristic properties of the main extractants investigated

	TBP	DEHBA	DEH <i>i</i> BA	DEHDMBA
Formula	C ₁₂ H ₂₄ O ₄ P	C ₂₀ H ₄₁ NO	C ₂₀ H ₄₁ NO	C ₂₂ H ₄₅ NO
Molar mass [g/mol]	266.32	311.55	311.55	339.61
Molar volume [Å ³ /molecule]	451.2	595.4	604.4	652.8
<i>l</i> _{chain} [Å]	6.5	9.1	9.1	9.1
<i>V</i> _{apolar} [Å ³]	407.4	486.5	486.5	486.5
<i>V</i> _{polar} [Å ³]	43.8	108.9	117.9	166.3
<i>V</i> _{pol.core} [Å ³] at <i>x</i> = 0	335	564	576	770
<i>V</i> _{pol.core} [Å ³] at <i>x</i> = 0.43	422	673	709	903

Table 6. The minimal packing parameter as well as the pseudo packing parameter assuming a tetrahedral and octahedral arrangement calculated for the main extractants investigated

	TBP	DEHBA	DEHiBA	DEHDMBA
minimum packing parameter				
$R_{\text{core}} [\text{\AA}]$	2.677	3.629	3.726	4.178
$R_{\text{tot}} [\text{\AA}]$	4.883	5.473	5.516	5.740
$P_{0,\text{min}}$	2.05	1.594	1.558	1.420
Spontaneous packing parameter at $x = [\text{U}]/[\text{Ex}] = 0$ and 0.43 assuming a tetrahedral arrangement of the extractant headgroups around the core				
$b_{\text{tetrahedron at } x = 0} [\text{\AA}]$	7.038	8.368	8.429	9.284
$b_{\text{tetrahedron at } x = 0.43} [\text{\AA}]$	7.597	8.880	9.035	9.792
$a_{0,\text{tet at } x = 0} [\text{\AA}^2]$	21.4	30.3	30.8	37.3
$a_{0,\text{tet at } x = 0.43} [\text{\AA}^2]$	25.0	34.1	35.3	41.5
P_0' at $x = 0$	2.90	1.77	1.75	1.44
P_0' at $x = 0.43$	2.49	1.57	1.52	1.29
Spontaneous packing parameter at $x = [\text{U}]/[\text{Ex}] = 0$ and 0.43 assuming an octahedral arrangement of the extractant headgroups around the core				
$b_{\text{octahedron at } x = 0} [\text{\AA}]$	6.10	7.25	7.30	8.04
$b_{\text{octahedron at } x = 0.43} [\text{\AA}]$	6.58	7.69	7.83	8.48
$a_{0,\text{oct at } x = 0} [\text{\AA}^2]$	16.09	22.74	23.07	27.99
$a_{0,\text{oct at } x = 0.43} [\text{\AA}^2]$	18.74	25.61	26.51	31.14
P_0' at $x=0$	3.87	2.36	2.33	1.92
P_0' at $x=0.43$	3.32	2.10	2.03	1.72

These estimated values are used in the following chapter to correlate the experimental results with the molecular extractant geometry as well as to combine them with the thermodynamic model developed in Chapter III based on an estimation of frustration of microphases which is given by the difference of spontaneous and effective packing.

II.2 Experimental Observations leading to a mesoscopic model

In the following, a large set of experiments in different conditions was carried out in order to find hints on the origin of the viscosity increase as well as to identify the crucial parameters.

II.2.1 Influence of extractant and uranyl concentration

The shear viscosities of organic phases after uranyl nitrate extraction were measured depending on the type of extractant and concentration of uranyl. The result for an extractant concentration of 1.5 M diluted in Isane IP 175, a mixture of alkanes with isoparaffinic structure (C11 – C12), is shown in **Figure 38**.

A significant difference can be seen in the behavior of the four investigated extractants. The viscosities are plotted on absolute scale against the mass concentration of uranyl as well as in reduced scale. For that, the viscosity was normalized by the viscosity of the extractant/diluent mixture before contact with the aqueous phase. As can be noticed, the viscosity normalized to the non-contacted solvent is not 1, but approximately 2 at $x = 0$. That shows that the viscosity already increases by a factor of around 2 after contact with 3 M nitric acid. While the viscosity of the organic phase with TBP extractant only slowly and almost linearly increases with uranyl concentration, the viscosity of the organic phases containing monoamide extractant increases exponentially and much faster than in the case of TBP. As a result, the viscosity difference between organic and aqueous phase at a concentration of around 100 g/L – a common concentration for industrial extraction processes like PUREX – is much too high for efficient extraction and fast separation times (*cf.* Chapter I.2.2.4).

Since the viscosity evolution is exponential and well pronounced, larger structures can be assumed, either by coalescence or attraction of aggregates.^[35] A sole increase of the volume fraction of aggregates, *e.g.* increase in the number of aggregates would have a linear effect on viscosity (*cf.* Chapter I.2.5.4).^[164]

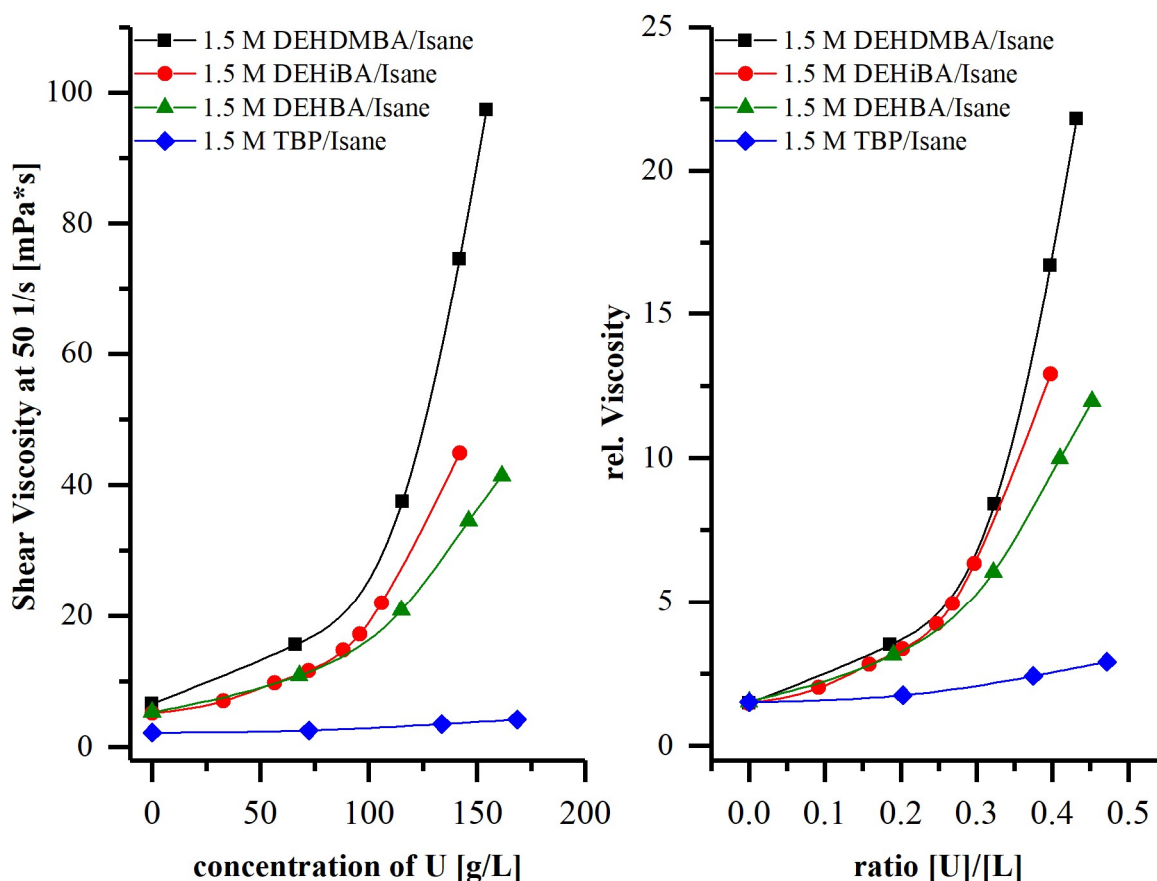


Figure 38. Viscosity increase due to increasing uranyl concentration in the organic phase for different extractants at 25 °C. Left: Apparent viscosity at a shear rate of 50 1/s. Right: Relative viscosity normalized by the viscosity of the non-contacted extractant/diluent mixtures ■ 1.5 M DEHDMBA ● 1.5 M DEHiBA ▲ 1.5 M DEHBA ◆ 1.5 M TBP diluted in Isane IP 175 versus the molar ratio uranyl/extractant.

For an extractant concentration of 1.5 M, the normalized viscosity increases only by a factor of around 3 for TBP approaching full loading of the organic phase ($[U]/[L] \approx 0.5$) while for DEHDMBA the viscosity increases 22-fold compared to the non-contacted solvent.

Furthermore, also a difference between the *N,N*-dialkylamides themselves is visible, although the shorter chain bound to the carbonyl group do not differ that much. The extent of viscosity increase follows the order DEHDMBA > DEHiBA > DEHBA. The difference between DEHBA and DEHiBA becomes obvious at higher uranyl concentration.

A rough comparison of the spontaneous packing parameters estimated from the extractant geometry as described in Chapter II.1.7 is shown in **Figure 39**.

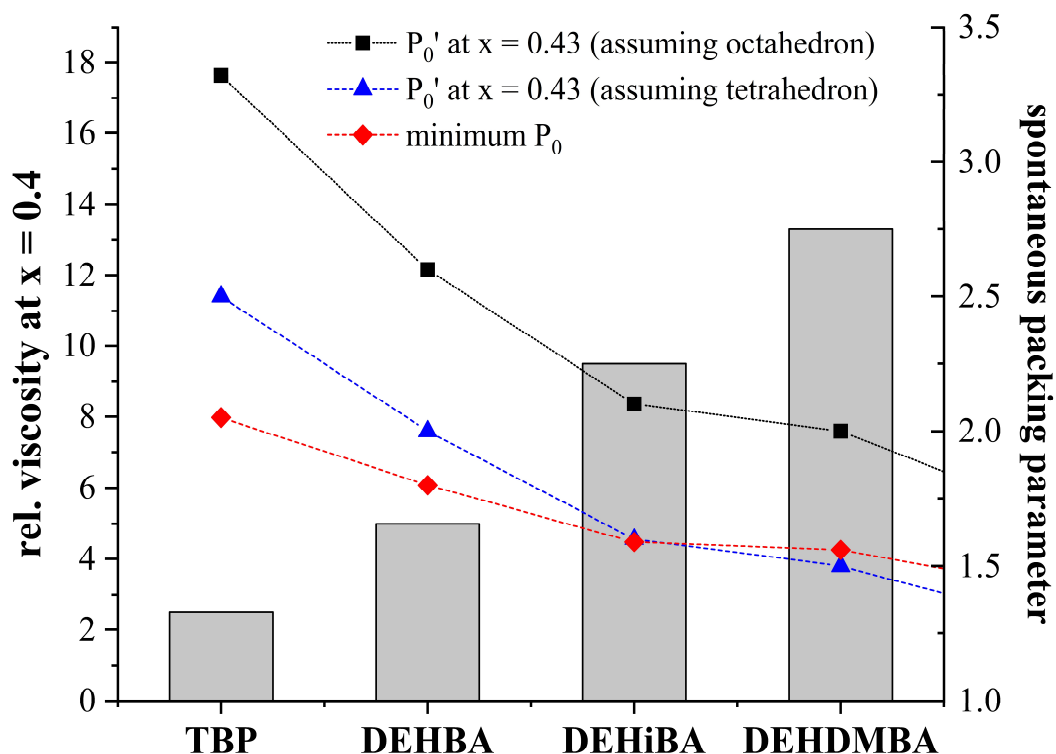


Figure 39. Correlation between the estimated spontaneous packing parameters by three methods (Table 5) and the observed viscosity curve (in grey). For illustration the viscosity of TBP, DEHBA, DEHiBA and DEHDMBA is shown at a uranyl content of $x = [\text{uranyl}]/[\text{Ex}] = 0.4$.

As pointed out in **Figure 39**, there seems to be a strong link between the estimated spontaneous packing parameters and the observed viscosity. A higher spontaneous packing parameter seems to favor lower viscosities, while a low packing parameter, *e.g.* aggregates formed by a less curved extractant, leads to higher viscosity. This is an important result and information for the development of the minimal model at nanoscale in Chapter III.

Figure 40 shows the dependence of the shear viscosity on the extractant concentration as a function of the uranyl concentration. In this example, the evolution for the extractant DEHiBA is shown, but the same evolution is observed for all extractants investigated. The other viscosity curves based on variation of the extractant concentration of DEHBA or respectively DEHDMBA are available in Annex, Chapter VII.6.1. The higher the extractant concentration, the more elevated is the viscosity and its increase. This evolution was expected and logical, since viscosity increases with volume fraction of the colloids, as described in Chapter I. However, it was important to see the magnitude of the viscosity increase at higher extractant concentration.

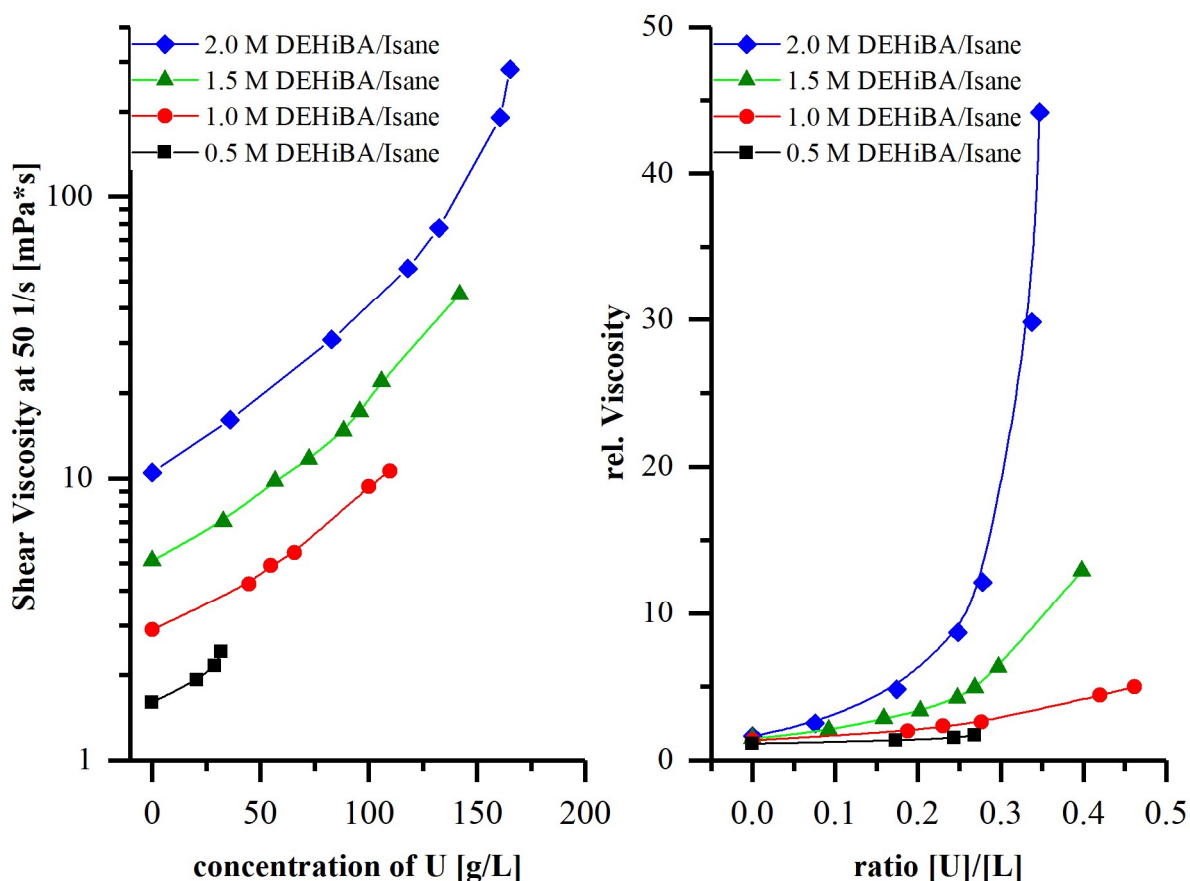


Figure 40. Viscosity increase due to increasing uranyl concentration in the organic phase for different extractant concentrations at 25 °C. Left: Apparent viscosity at a shear rate of 501/s in logarithmic scale. Right: Relative viscosity normalized by the viscosity of the non-contacted extractant/diluent mixtures ■ 0.5 M ● 1.0 M ▲ 1.5 M ◆ 2.0 M DEHiBA diluted in Isane IP 175 versus the molar ratio uranyl/extractant.

Due to the strong differences in viscosity for different extractant concentrations, the absolute viscosity values are plotted in logarithmic scale (*cf.* **Figure 40**). The order of magnitude of the viscosity increase is even much more elevated in the case of DEHDMBA as can be seen in the Annex (*cf.* **Suppl. Figure 5** and **Suppl. Figure 6**), while for DEHBA the viscosity increase is less elevated compared to DEHiBA.

Figure 41 shows the dependence of viscosity increase for TBP. Since the rise is much less elevated, a logarithmic scale was unnecessary to plot the curves. For the highest concentration, 2.0 M, the increase in viscosity is less than 4 times approaching the loading capacity. In strong contrast hereto, the viscosity rises up to 45 times higher for the same molarity of DEHDMBA (*cf.* **Suppl. Figure 6**). This also indicates that the smaller molar volume of TBP compared to monoamides (*cp.* **Table 5**) is not the decisive reason for the significant difference between these neutral extractants. Even at similar volume fraction of extractant ($\phi_{\text{Ex}} \approx 0.5$ for 1.5 M dialkylamide as well as for 2.0 M TBP), the viscosity increase for TBP is much less pronounced

than in the case of dialkylamides. Moreover, TBP shows also a smaller dependence on the extractant concentration. Therefore, a “jamming” transition that is known for aqueous solutions, where the viscosity of complex fluids increases as a function of solute concentration above a critical concentration of particles, can be excluded as the decisive difference between the viscosity of the extractants.^[209] As we will see later (*cf.* Chapter II.2.6.4 and III.3.6), a similar effect can play a role and has to be considered as origin of the viscosity. However, the difference in viscosity increase between extractants must be understood at molecular scale.

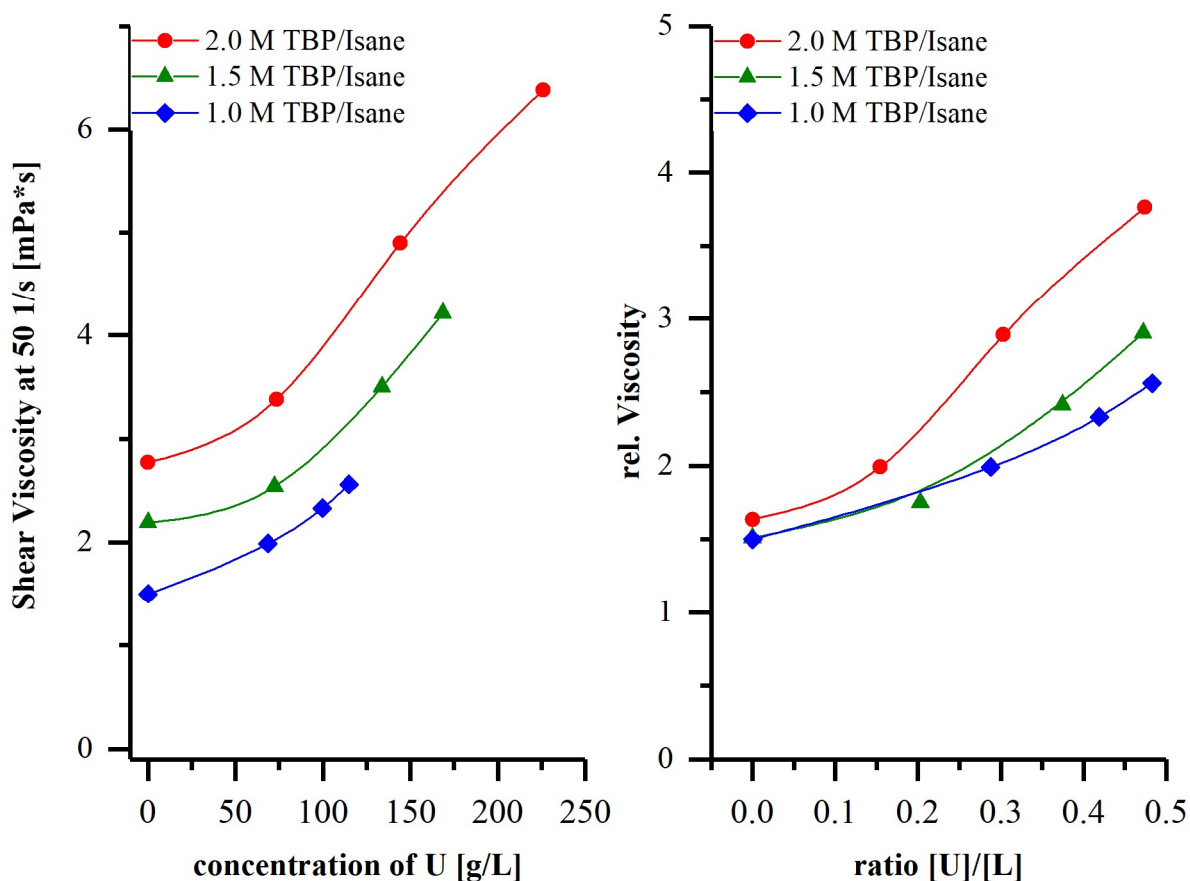


Figure 41. Viscosity increase due to increasing uranyl concentration in the organic phase for different extractant concentrations at 25 °C. Left: Apparent viscosity at a shear rate of 501/s in linear scale. Right: Relative viscosity normalized by the viscosity of the non-contacted extractant/diluent mixtures ■ 0.5 M ● 1.0 M ▲ 1.5 M ◆ 2.0 M TBP diluted in Isane IP 175 versus the molar ratio uranyl/extractant.

II.2.2 Influence of temperature

Figure 42 shows the viscosity decrease with increasing temperature. The figures **a** to **c** show the shear viscosities depending on uranyl concentration. It can be observed that the curves at higher uranyl concentration approach at higher temperature and the difference in viscosity due to uranyl concentration diminishes. For a better representation, the viscosity decrease from 20 °C to 50 °C was plotted for 1.0 M, 1.5 M and 2.0 M versus uranyl concentration (Figures **d** and

e). For all three concentrations, the temperature dependence is more elevated for systems with higher uranyl concentration, *e.g.* for systems where the viscosity rose more compared to the systems without uranyl. This could be an indication for a mesoscopic structure that evolves more and more with uranyl charging of the organic phase and a change of structure with increasing uranyl concentration. The strong decrease in viscosity could be then - besides the faster movement of molecules and colloids (*cf.* Chapter I.2.3) - related either to an increased flexibility of the evolving structure or to a structural change arising from an increased entropical term.

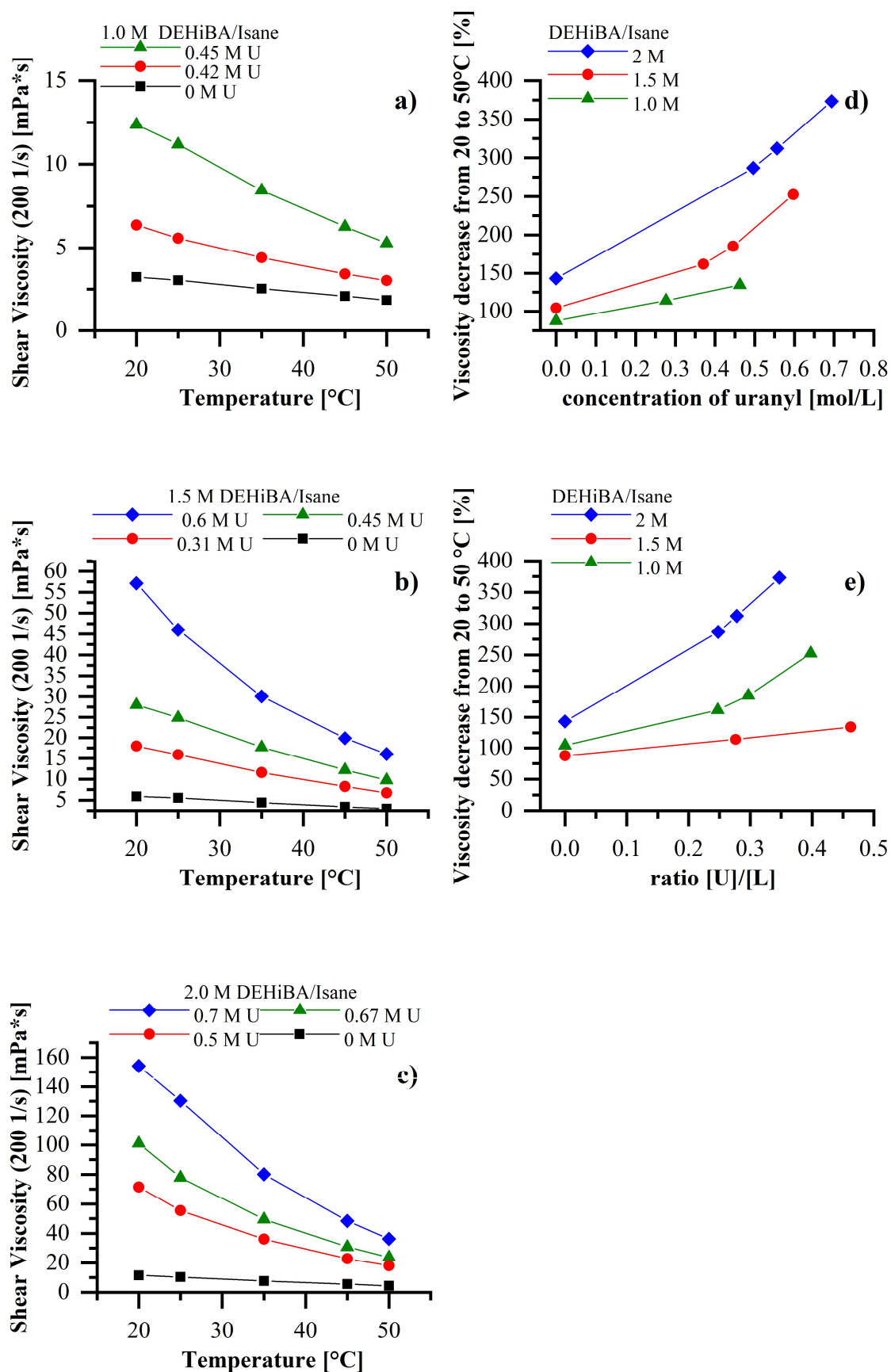


Figure 42. Temperature dependence of shear viscosities (200 1/s) of organic phases depending on uranyl and extractant concentration. a) – c) Temperature dependent shear viscosities of a) 1 M b) 1.5 M c) 2 M DEHiBA diluted in Isane and charged with different concentrations of uranyl. d) and e) viscosity decrease versus concentration of extractant and uranyl or respectively extractant/uranyl ratio.

For a better comparison, the temperature dependence was fitted with the simple Arrhenius equation, the application of which to liquid viscosity was first attributed to de Guzman, but popularized by Andrade.^[210] Now the equation is used to fit viscosity data of small molecules but also polymers. It has to be noted that this equation is very similar to the original Arrhenius equation that describes the temperature dependence of the rate constant k of a chemical reaction.^[211] The only difference is the positive sign in the exponential, since the viscosity decreases with increasing temperature, while the rate constant increases.

$$\eta = A \cdot \exp\left(\frac{E_A}{RT}\right) \quad (54)$$

$$\ln\eta = \ln A + E_A \cdot \frac{1}{RT} \quad (55)$$

In the Arrhenius equation for liquid viscosity (eq. (54)), the preexponential factor A is correlated to contributions due to disorder, entropy and motion.^[212] Another interpretation is also to see the parameter A as the viscosity at infinite temperature^[212], η_∞ . The parameter E_A is related to a certain activation energy that is needed for viscous flow.^[212,213]

As can be seen in **Figure 43** for the example 1.5 M DEHiBA in Isane IP 175, the activation energy for viscous flow increases with increasing uranyl concentration. In contrast hereto, the preexponential factor A decreases with increasing uranyl concentration. As a result, at higher uranyl content, more energy is needed for viscous flow at a certain temperature, while the parameter A , therefore the entropical contribution decreases. Interpreting A as the viscosity value at infinite temperature, A is a measure for the pure structural contribution of the components to viscosity since interactions leading to viscosity at room temperature vanish at very high temperature. One can also speak of its viscosity in the vapor phase.

Similar results as in **Figure 43** are obtained for 2.0 and 1.0 M of the extractant DEHiBA in Isane IP 175. The results are summarized in **Table 7**.

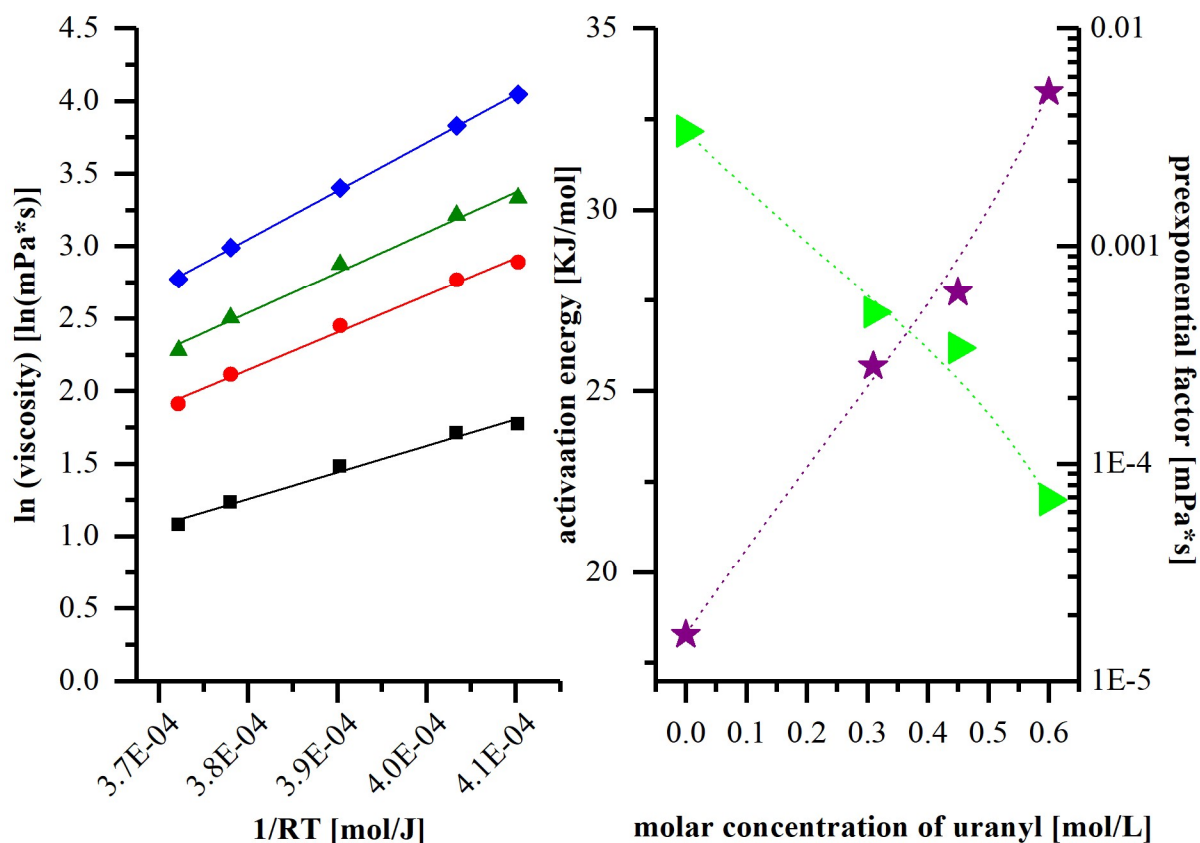


Figure 43. Left: Linear fits using equation (55) for 1.5 M DEHiBA diluted in Isane IP 175 charged with \blacksquare 0 M \bullet 0.31 M \blacktriangle 0.45 M \blacklozenge 0.6 M Uranyl. Right: Resulting fit parameter from Arrhenius fits; \blacktriangle preexponential factor, \star activation energy.

Table 7: Results from fitting the temperature dependence of viscosity using the Arrhenius equation.

Uranyl concentration [mol/L]	Activation energy [kJ/mol]	$\ln A$ [$\ln(\text{mPa}\cdot\text{s})$]	A [mPa*s]
<i>1.0 M DEHiBA in Isane IP 175</i>			
0	14.9 (≈ 6 kT)	-4.92	0.00125
0.42	19.4 (≈ 8 kT)	-6.12	0.00219
0.45	22.5 (≈ 9 kT)	-6.68	0.00733
<i>1.5 M DEHiBA in Isane IP 175</i>			
0	18.3 (≈ 7 kT)	-5.69	0.00338
0.31	25.7 (≈ 10 kT)	-7.61	0.00049
0.45	27.7 (≈ 11 kT)	-7.99	0.00034
0.6	33.3 (≈ 13 kT)	-9.59	6.68E-5
<i>2.0 M DEHiBA in Isane IP 175</i>			
0	24.5 (≈ 10 kT)	-7.56	0.00052
0.5	35.7 (≈ 14 kT)	-10.37	3.14E-5
0.67	37.4 (≈ 15 kT)	-10.72	2.22E-5
0.7	38.2 (≈ 15 kT)	-10.59	2.52E-5

As it is summarized above, the activation energy that is needed for shearing increases with uranyl and extractant concentration. In contrast hereto, the preexponential factor A is significantly higher in absence of uranyl and only if the organic phase is contacted with 3 M nitric acid than it is in presence of uranyl. We have interpreted the fact that the activation energy increases with uranyl and extractant concentration as an indication for mesoscopic organization, while the change in A shows a change of the composition and the formation of probably less but larger aggregates.

Comparison of the values with the literature shows that the activation energy is significantly higher than for water (16 kJ/mol) and in the range of ionic liquids (17-30 kJ/mol).^[212,214]

II.2.3 Influence of shearing and rheological investigations

Figure 44 illustrates the shear-dependence of organic phases containing 1.5 M and 2.0 M of monoamide extractant diluted in Isane IP 175 with increasing loading of uranyl. These two systems were only picked as examples, the shear-dependence was checked for all systems investigated. For all of them, the viscosity is shear-independent, even at high concentration of extractant (up to 70 vol%). As a result, a microstructure of entangled non-intersecting wormlike micelles can be excluded as reason for the viscosity increase, since such systems are expected to be shear-thinning for that elevated volume fraction (*cf.* Chapter I.2.5.1). Elongated species align during shear-flow leading to less friction and entanglements between each other resulting in lower viscosity. However, it should be noted, that a network of branched wormlike micelles shows shear-independent behavior due to a very short viscoelastic relaxation time (smaller than 1 ms).^[34] The obtained viscosity range observed for the extractant system (10-1000 mPa*s) fits to a so-called living network as described by Appel *et al.*^[34]

Suppl. Figure 9 shows amplitude sweeps of organic phases with increasing uranyl content comparing DEHiBA and TBP. The loss modulus which is related to the viscosity increases with increasing uranyl content in both cases. In the case of DEHiBA the loss modulus is higher than for TBP, confirming the strong difference in viscosity behavior. In the case of DEHiBA, an elastic response is observed up to a strain of 2%, which is higher than the loss modulus (gel-like behavior). At higher strains the elastic response disappears, indicating a break-up of the present structure. Using the hypothesis that a 3-dimensional living network of wormlike micelles (see later) is present and starts to glide along the connection points, could interpret this strain of 2% as the strain that is needed to make the network gliding. However, the elastic response is visible in the same magnitude for TBP, where no formation of a network is expected,

only the presence of “sticky hard spheres”. Due to this fact and the similarities between the plots, no real conclusions can be drawn from rheology concerning the structuration of the organic phase.

The results of frequency sweeps at 0.2% strain – so in the linear viscoelastic range - for the same systems are similar (*cf.* **Suppl. Figure 10**). At a certain frequency ($f = 2 \text{ 1/s}$) the elastic response of the system breaks and the storage modulus becomes very low. As in the case of amplitude sweeps, no significant difference can be seen between TBP and DEHiBA and no conclusions regarding behavior and structure can be drawn.

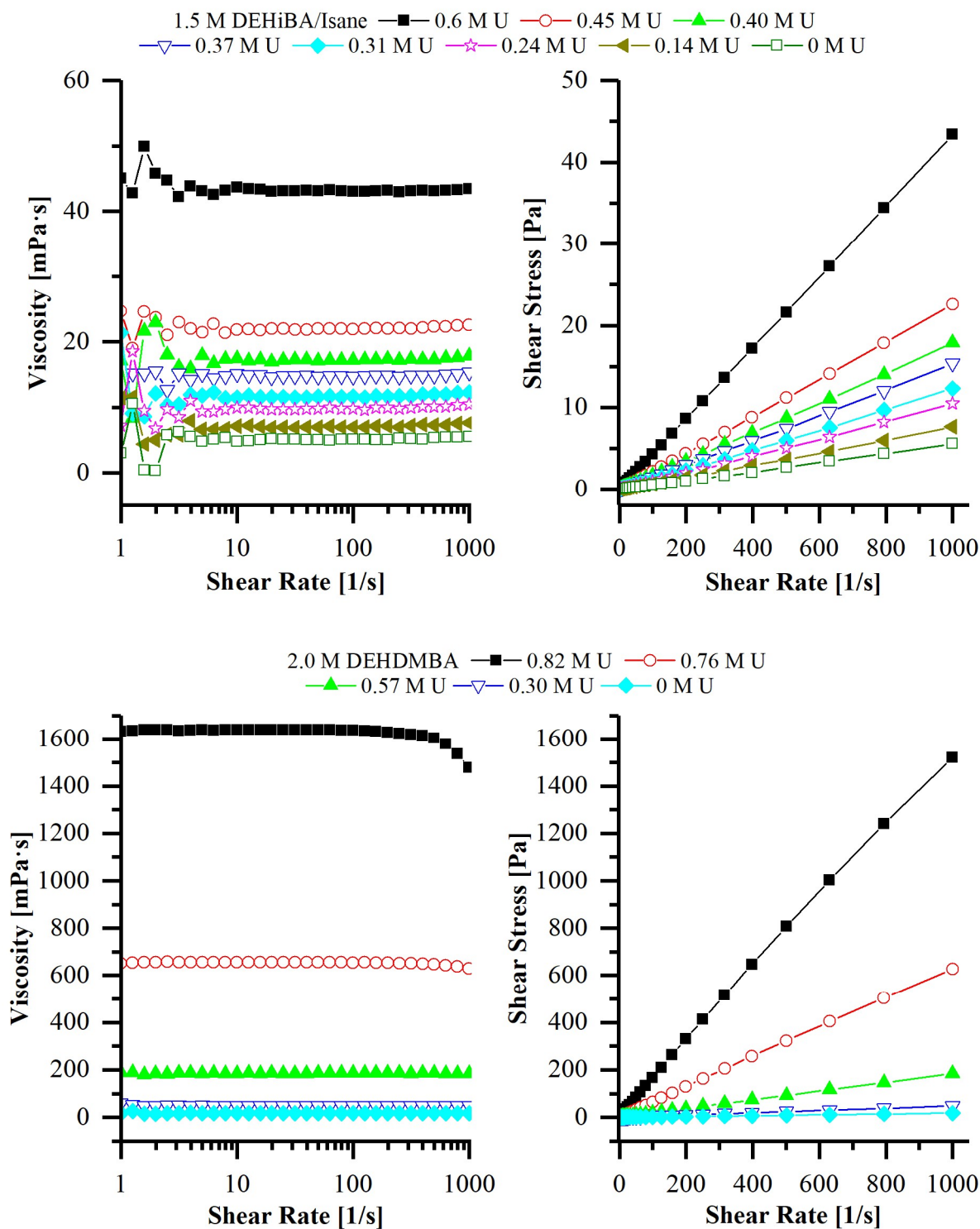


Figure 44. Apparent viscosities (left) and shear stresses (right) depending on the shear rate. Above: 1.5 M DEHiBA and below 2.0 M DEHDMBA diluted in Isane IP 175 and charged with different concentrations of uranyl.

II.2.4 Influence of diluent

Figure 45 shows the viscosity dependence on uranyl concentration and diluent used to dissolve the extractant DEHiBA. As can be seen, in both cases the viscosity increases with uranyl concentration for all diluents investigated, but with a different magnitude. The viscosity

increase is much smaller for xylene as diluent, while for octanol as diluent the viscosity is much higher compared to the reference system with Isane. However, comparing the viscosity rise from an acid-contacted organic phase to an organic phase that is around 2/3 loaded with uranyl shows that the viscosity rise of octanol is relatively small. The order of viscosity increase follows the series Dodecane > Isane IP 175 > Isooctane > Xylene > Octanol. Within this series the penetration power increases from a long-chain alkane (dodecane) over branched short-chain alkanes (isooctane) over small aromatic compounds (xylene) to an amphiphile oil (octanol).^[87] The denomination of octanol as a penetrating diluent has to be taken with care, since it is expected to participate actively in the aggregation process with influence on the apolar and the polar part. Therefore, it acts rather as a co-solvent than as a pure diluent.

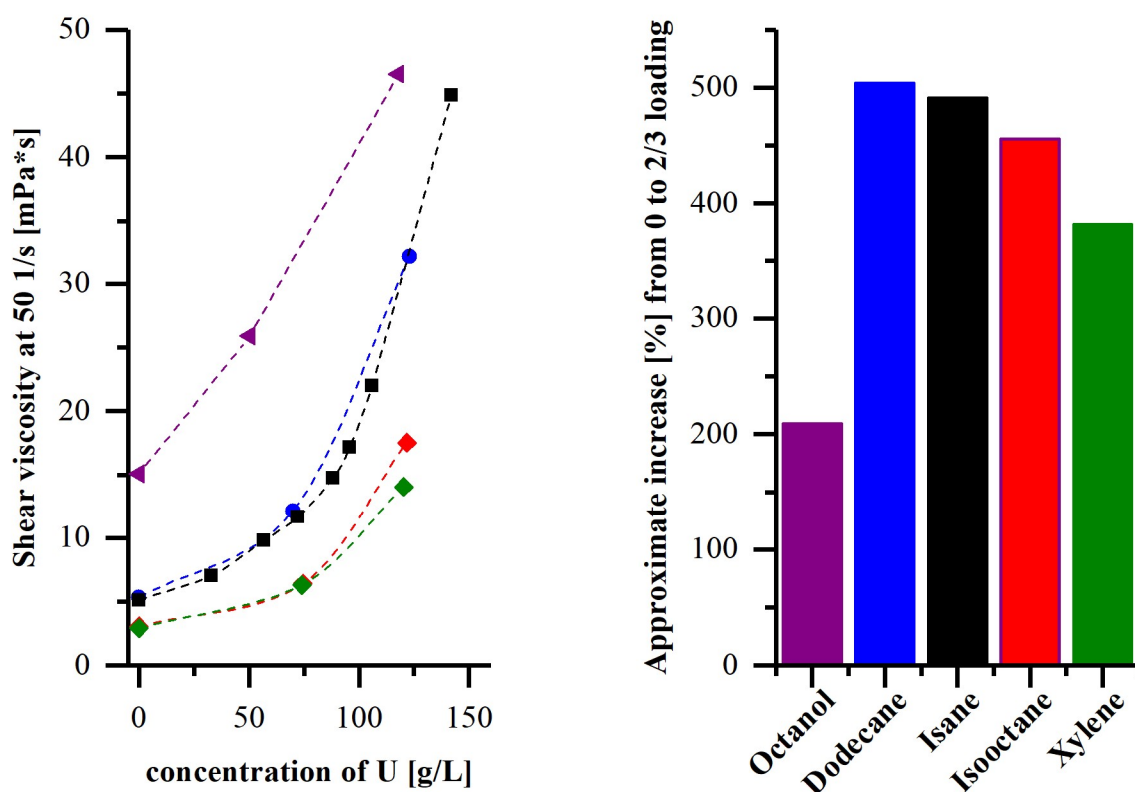


Figure 45. Left: Shear viscosities at 25 °C dependent on diluent and uranyl concentration. Investigated system: 1.5 M DEHiBA in different diluents contacted with different aqueous phases (uranyl nitrate dissolved in 3 M nitric acid). Right: Approximate viscosity increase from contact with nitric acid (0 M) to 2/3 loading of the organic phase (0.5 M uranyl)

The same tendencies are observed for the system 1.5 M DEHDMBA in different diluents. The figure is presented in the annex, **Suppl. Figure 8**.

The penetration power of a diluent into extractant chains can be quickly verified by a COSMO-RS approach performing an imaginary partitioning of the extractant molecules between two

possible diluents.

The resulting $\log P'$ value is defined as follows. It is called $\log P'$, in order to separate this term from the $\log P$ value, which is mainly reserved for the partitioning between water and 1-octanol as a measure for lipophilicity or hydrophobicity.^[215, p.38]

$$\log P' = \log \frac{[\text{extractant } i]^{\text{phase II}}}{[\text{extractant } i]^{\text{phase I}}} = \log \left[\exp \left(\frac{\mu_i^{(1)} - \mu_i^{(2)}}{RT} \right) \cdot \frac{V_1}{V_2} \right] \quad (56)$$

$\log P'$ therefore represents the partition coefficient of extractant I between phase II and phase I. In COSMO-RS, it is based on calculation of the corresponding chemical potentials μ_i in infinite dilution in the pure diluents (phase II or phase I respectively).^[216] V_1/V_2 represents the Volume quotient (by default 1). Consequently, if $\log P'$ is positive, the extractant prefers to be in phase II. If this value is negative, the extractant prefers to be in phase I. This preference to be in one or another phase can be seen as a measure of the affinity of an extractant for one phase. In other words, the interactions with that phase are more advantageous. Consequently, the extractants being in an aggregate will be “wetted” better by the phase with higher affinity and this phase will be more penetrating.

Table 8. shows an overview over partitioning simulations carried out by COSMO-RS. In **Table 9**, the values were transferred into free energy of transfer from phase II to I by $\Delta G_{\text{tr}} = RT \ln P'$. If the resulting value for the free energy is positive, phase II is preferred.

Table 8. $\log P'$ values accomplished by COSMO-RS calculation for different phase II/phase I combinations demonstrating the affinity of the extractant in the corresponding phases. If the values are bold, the extractant has a higher affinity for phase 2.

$\log P'$	Phase I: dodecane				Phase I: xylene			
	Phase II:				Phase II:			
	xylene	isooctane	pentamethyl-heptane	1-octanol	dodecane	isooctane	pentamethyl-heptane	1-octanol
DEHiBA	0.798	0.110	0.071	0.699	-0.798	-0.688	-0.727	-0.100
DEHBA	0.792	0.106	0.072	0.795	-0.792	-0.686	-0.720	0.003
DEHDMBA	0.657	0.102	0.060	0.277	-0.657	-0.555	-0.596	-0.380
TBP	0.832	0.096	0.096	0.709	-0.832	-0.735	-0.736	-0.122

Table 9. $\log P'$ values accomplished by COSMO-RS calculation for different phase II/phase I combinations demonstrating the affinity of the extractant in the corresponding phases transferred into free energy of transfer $\Delta G_{tr} = RT \ln P$. If the values are positive (bold), the extractant has a higher affinity for phase 2.

$\Delta G_{tr} = RT \ln P'$ [kJ/mol]	Phase I: dodecane				Phase I: xylene			
	Phase II:				Phase II:			
	xylene	isooctane	pentamethyl-heptane	1-octanol	dodecane	isooctane	pentamethyl-heptane	1-octanol
DEHiBA	4.55	0.63	0.41	3.99	-4.55	-3.92	-4.15	-0.57
DEHBA	4.52	0.60	0.41	4.54	-4.52	-3.91	-4.11	0.02
DEHDMBA	3.75	0.58	0.34	1.58	-3.75	-3.17	-3.40	-2.17
TBP	4.75	0.55	0.55	4.04	-4.75	-4.19	-4.20	-0.7

These tables show that the series found above can be reproduced by this simple COSMO-RS simulation. Each diluent investigated (xylene, isooctane, pentamethyl heptane and octanol) is a better diluent for the extractants than dodecane. Only the values for 1-octanol do not represent exactly the penetration tendency expected. Actually, octanol should be more penetrating than xylene due to the polar hydroxy group promoting the penetration. Probably this effect is not taken into account sufficiently resulting in that deviation. Since these calculations can be also applied on solvent mixtures, this imaginary partitioning is a promising method to get an approximate idea on the solvent penetration power of diluents and could help to choose the most effective diluent for certain extraction processes. However, it should be noted that as soon as there is an interface, the orientation of the extractant is not random. Therefore, this calculation can only provide an approximate idea.

The fact that for penetrating oils the viscosity increase is much less elevated could lead to a solution of the problem. It is remarkable that also no third phase formation is usually observed, when aromatic diluents are used in extraction processes.^[40] A more detailed discussion will be given in Chapter III and Chapter IV when the model and the proposed solution of the problem is presented.

II.2.5 Small- and Wide-Angle X-Ray Scattering Analysis

In this subchapter, investigations using Small- and Wide-Angle X-Ray Scattering (SWAXS) are presented. Different parameters and trends are discussed. Since this work is focused on systems close to industrial application, mainly systems with high extractant concentration are investigated. Modelling of SWAXS spectra becomes difficult, when the objects become anisotropic and strongly interactive as it is expected for highly concentrated solutions.

Therefore, the patterns will only be discussed qualitatively. Data reduction and treatment is discussed in Chapter II.1.5. For better understanding and representation of the peaks at higher q , most of the spectra are plotted in both logarithmic and linear scale. Further spectra in linear scaling can be found in the Annex.

II.2.5.1 Observations in absence of uranyl

Figure 46 shows organic phases with the monoamide extractant DEHiBA in different concentrations after contact with water and 3 M nitric acid.

First, the scattering curve of organic phases contacted with water are discussed (*cf.* **Figure 46**, left). The curves can be separated into three characteristic regions.

- A peak at around $q^* = 1.4 \text{ \AA}^{-1}$ increases with increasing extractant concentration and can be attributed to the potential between the relative location of neighboring alkyl chains of diluent and/or extractant. In all cases, this peak is broad indicating the absence of crystalline chains. Since the diluent is subtracted, the peak amplitude increases at higher volume fraction of extractant. Furthermore, the peak shifts slightly and gradually from 1.31 \AA^{-1} (0.7 M DEHiBA) to 1.44 \AA^{-1} (1.5 M DEHiBA) indicating that at elevated extractant concentration, extractants must also partly serve as diluent for themselves and extractant chains are penetrating into the apolar parts of neighboring extractants. This is often referred as “*interparticle wetting*” and can drastically affect structuration and phase stability.^[59, pp.415–468,217,218] This confirms that aggregate coalescence comes into play when concentration increases.^[160]
- A second broad peak evolves at around $q^* = 0.77 \text{ \AA}^{-1}$ with increasing extractant concentration above a concentration of 0.7 M DEHiBA. This peak can be related to the correlation between two electron rich regions in an average distance of $2\pi/q^* = 8.2 \text{ \AA}$. In the case of *N,N*-dialkylamides, this can be associated with the dipole-dipole interaction between two amide groups which come close together, when aggregates are formed. The peak shifts from 0.75 \AA^{-1} (2 M DEHiBA) to 0.79 \AA^{-1} (1.2 M DEHiBA). In the case of 1.0 M DEHiBA, the maximum was not clearly resolved. The shift indicates that the correlation distance decreases with increasing extraction concentration. This could be a hint for the formation of bigger aggregates, *e.g.* trimers and tetramers that are able to solubilize more water, increasing the distance between two headgroups. This observation is consistent with the molecular dynamics results of Ferru *et al.*^[191] demonstrating the formation of trimers and tetramers of DEHiBA in heptane at higher

extractant concentration. Furthermore, this intermediate peak is well-known for alcohols and other organized apolar fluids.^[102,219]

- At low q ($q < 0.2 \text{ \AA}^{-1}$), all curves are quite flat (slope $< q^{-0.05}$). The forward scattering, *i.e.* the intensity at very low q increases with increasing extractant concentration. As indicated in Annex, Chapter VII.3.2, this intensity can be related to the volume of the aggregates. **Table 10** shows the change in size assuming a structure factor of 1. Since this is not valid at higher concentration, this table only demonstrates the qualitative trend and the absolute volume was not calculated using the scattering contrast (which is the same for all 5 samples).

Table 10. Qualitative trend of aggregate volume obtained from forward scattering

Extractant concentration [mol/L]	Volume fraction	Forward scattering [cm^{-1}]	Particle volume $\cdot \Delta SLD$ [cm^{-1}]
2	0.73	0.045	0.062
1.5	0.55	0.026	0.048
1.2	0.44	0.019	0.043
1	0.36	0.016	0.044
0.7	0.25	0.009	0.034

A similar behavior regarding behavior of the solvent and the correlation peak can be observed after contact with 3 M nitric acid (*cf.* **Figure 46**, right).

- The solvent peak at 1.4 \AA^{-1} increases as in the case of water extraction, but the shift is less elevated. This could be explained by the fact that extractant molecules that stay monomeric can be neglected after acid extraction and at higher extractant concentration.^[191] As a consequence, the extractant molecules are almost all involved in aggregates, where the distance between alkyl chains varies less.
- After acid extraction, a correlation hump evolves at 0.75 \AA^{-1} , even at the lowest concentration investigated (0.7 M DEHiBA). This indicates that after acid extraction, most of the extractants participate at aggregation resulting in a headgroup-headgroup correlation. The peak shifts from 0.79 \AA^{-1} at lowest to 0.75 \AA^{-1} at highest extractant concentration indicating an increasing correlation distance between two electron-rich centers, *i.e.* polar headgroups. Consequently, the size of the aggregates also increases with increasing extractant concentration. Its sizes are very similar to the sizes observed after water extraction.

- The behavior at lower q is different compared to the water extraction. Up to a concentration of 1.0 M DEHiBA, a progressive increase at low q is observed. Above this concentration, the signal starts to decrease again. This can be explained by the influence of the structure factor $S(q)$ on the signal intensity (*cf.* Annex, Chapter VII.3.2). The interaction between polar cores is dominated by dispersion forces as was shown by Erlinger *et al.*^[160]. Addition of polarizable nitric acid to the water core leads to an increase in attractive interaction and consequently to an increase in intensity.^[102] At higher extractant concentration (> 1.2 M), the intensity at low q goes down, probably caused by a strong repulsive structure factor ($S < 1$) between extractant chains, when the extractant concentration goes up.

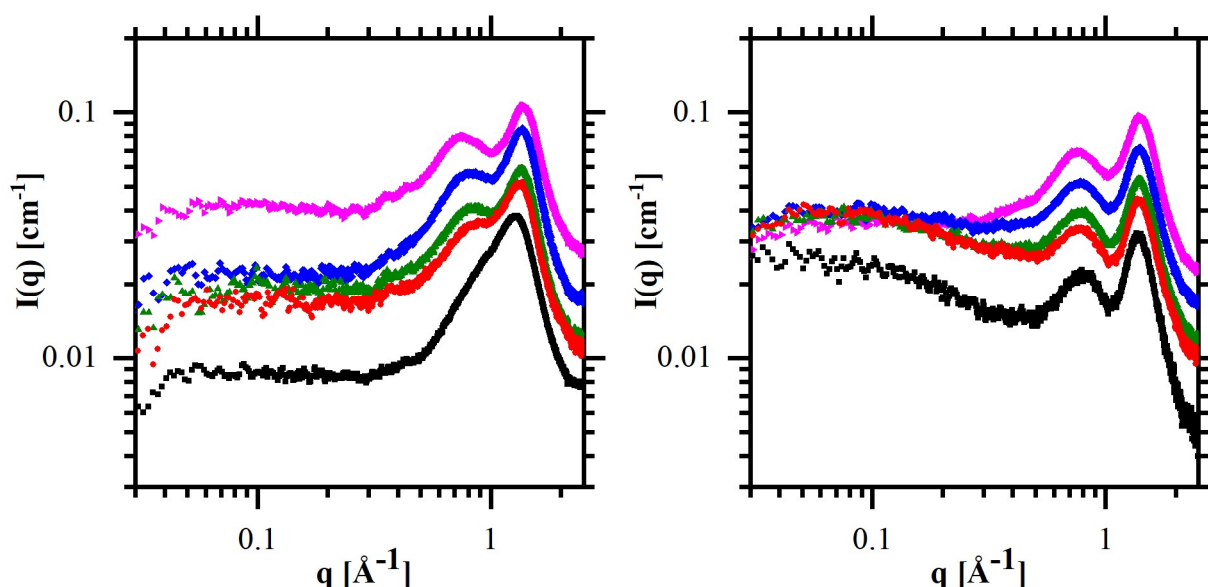


Figure 46. SAXS spectra of organic phases containing \blacksquare 0.7 M \bullet 1.0 M \blacktriangle 1.2 M \blacklozenge 1.5 M \blacktriangleright 2.0 M DEHiBA dissolved in Isane IP 175 and contacted with aqueous phase. **Left:** water contacted; **Right:** contact with 3 M HNO_3 .

As conclusion, the presence of water and nitric acid promotes aggregation. The addition of polarizable nitric acid influences the interaction between the aggregates. At lower extractant concentration, the attractive forces between the cores seem to dominate, while above a concentration of 1.2 M monoamide extractant, the structure factor becomes smaller than 1.

II.2.5.2 Observations with increasing Uranyl content

In order to investigate the evolution of the structuring with increasing concentration of uranyl in the organic phase, a mixture of 1.5 M DEHiBA/Isane IP 175 was contacted with different aqueous phases composed of 3 M nitric acid and a certain concentration of uranyl. The results from X-Ray scattering are presented in **Figure 47** in logarithmic (log-log-plot) as well as in

linear scale. It has to be noted that due to the delicate step of fluorescence subtraction (*cf.* Chapter II.1.5), the absolute intensities have to be handled with care.

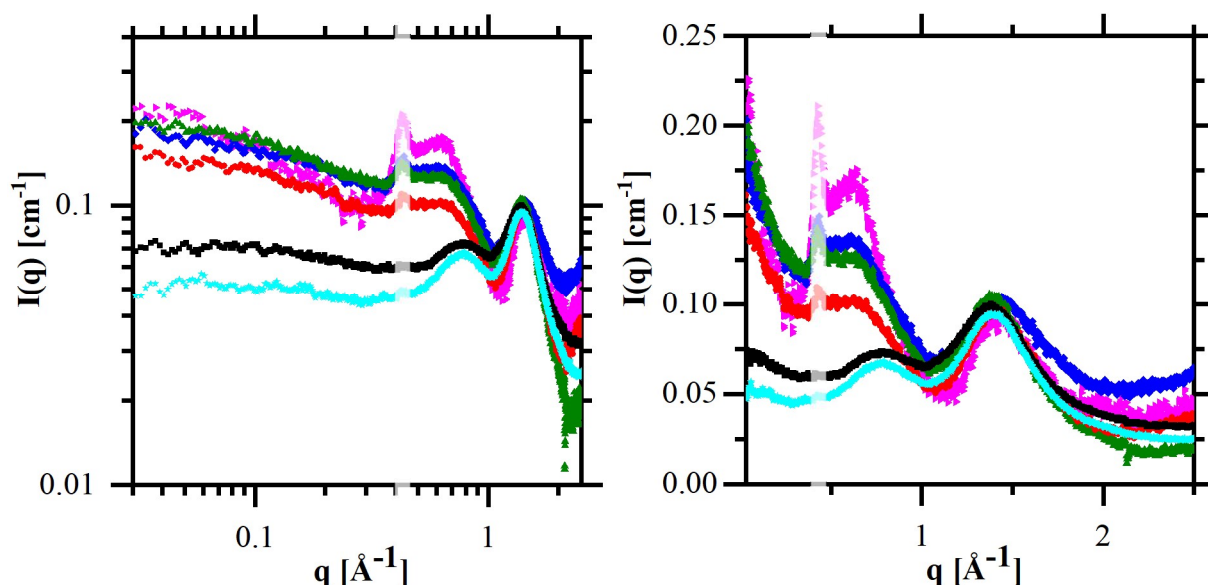


Figure 47. SAXS spectra of organic phases containing 1.5 M DEHiBA dissolved in Isane IP 175 and charged with $\star 0\text{ M}$ $\blacksquare 0.04\text{ M}$ $\bullet 0.24\text{ M}$ $\blacktriangle 0.30\text{ M}$ $\blacklozenge 0.37\text{ M}$ $\blacktriangleright 0.61\text{ M}$ uranyl by contact with aqueous phases. **Left:** logarithmic scale; **Right:** linear scale.

The spectra can be again separated into different characteristic regions:

- At high q (1.4 Å^{-1}), as in the spectra above, the solvent peak can be observed. For these samples containing uranyl, co-extracted nitric acid and water, the system is more complex. Therefore, these peaks are not discussed according to eventual shift. The height of the solvent peak is at a constant level because the concentration of diluent and extractant is almost constant for each of the samples.
- In the middle q range, a broad hump evolves for all of the spectra. In the absence of uranyl and at low uranyl concentration (0.04 M) the peak evolves at a q -value of 0.77 Å^{-1} corresponding to a correlation between electron-rich centers in at a distance of around 8.2 Å . This corresponds to the same distance that was observed for aggregates in the presence of water and nitric acid. That indicates that in the presence of traces of uranyl the dominating structure are still the aggregates that are found after nitric acid extraction.

The situation changes, when more uranyl is present in the organic solutions. The correlation hump is shifted towards lower q indicating that the correlation distance between two electron-rich regions increases. The hump maximum is found at $q^* = 0.64\text{ Å}^{-1}$ ($2\pi/q^* = 9.8\text{ Å}$). Due to the Kapton window at 0.43 Å^{-1} (*cf.* next passage), the determination of the peak (*cf.* Chapter II.1.5) was delicate and the estimated deviation

can be set to $\pm 0.2 \text{ \AA}^{-1}$. Within this deviation, the position of the broad correlation peak does not change with uranyl concentration. At higher uranyl concentration, uranyl ions are the scatterers with the highest electron density:

- SLD (diluent) $\sim 0.007 \text{ nm}^{-1}$
- SLD (monoamide) $\sim 0.008 \text{ nm}^{-1}$
- SLD (uranyl nitrate) $\sim 0.02 \text{ nm}^{-1}$
- SLD (water/nitrate) $\sim 0.01 \text{ nm}^{-1}$

Moreover, this correlation hump increases with uranyl concentration. Therefore, it is reasonable to attribute the hump to the correlation between uranyl ions. This indicates that the uranyl ions do not distribute homogeneously in the organic solution. The actinides rather arrange in a certain direction and keep a definite mean distance of $9.8 \pm 0.2 \text{ \AA}$. A possible explanation for this phenomenon is the presence of uranyl-nitrate-uranyl chains. These were also already observed by molecular dynamic simulations by Rodrigues *et al.* in heptane.^[196] The fact, that this hump is quite broad could indicate the presence of vacancies within these chains or respectively this network or a mixture of different structures. As pointed out in the paragraph before, at higher extractant concentration, wetting energies are involved, facilitating the endcap-endcap bridges (*cf.* **Figure 48**). Therefore, it is possible, that the uranyl-uranyl distance is smaller than 10 \AA as was indicated by molecular dynamics. However, the hump is shifted towards a larger distance resulting from a larger mean distance or diffuse scattering respectively (*cf.* **Figure 48**).

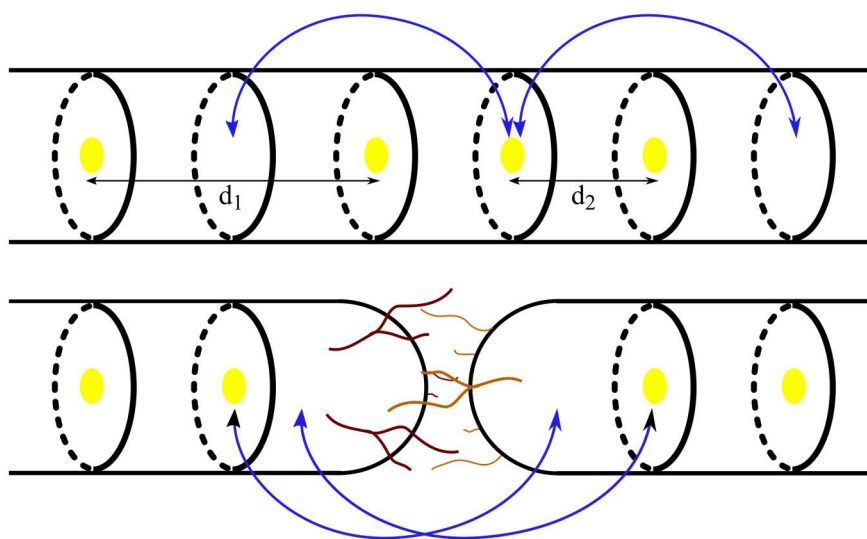


Figure 48. *Top:* Schematic representation of possible vacancies within a uranyl-nitrate-uranyl chain. Only the position of uranyl ions is presented. In between, nitrate ions and protons can be imagined. *Bottom:* Two bridging endcaps resulting in wetting energy.

- As already mentioned above, the peak at 0.43 \AA^{-1} corresponds to the Kapton window which is not sufficient subtracted due to the low transmission values of the sample (down to 4 % for the most concentrated samples). This peak also appears in the case of SWAXS measurements of uranyl nitrate in water, which was carried out for the calibration curve of fluorescence (*cf.* Chapter II.1.5). The peak of the Kapton window will be ignored in the following discussions of the spectra and is plotted with decreased color intensity.
- The region at low q is difficult to interpret since a strong structure factor is expected that overlaps the form factor. The curves are almost flat (slopes of -0.2 to -0.5), but the intensity is quite high ($\sim 0.2 \text{ cm}^{-1}$). That means the scattering of the microstructure is homogeneous for length scales above 4 nm. There are two possibilities that result in this scattering pattern. First, the aggregation of extractants results in a mesh of a certain mesh size.^[79] Second, the structure is quite polydisperse composed of small and larger aggregates resulting in a structure that is homogeneous in average.

As it is well-known, SAXS spectra alone do not give the structure unambiguously. However, we can rule out certain hypotheses from the observation that the weak hump does not shift as a function of the UO_2^{2+} /extractant mole ratio while a flat but pronounced scattering exists at low q .

Small repulsive spherical aggregates, almost all filled with uranyl would result in a strong and sharp peak at the corresponding mean correlation distance between the spheres. This peak should furthermore shift to higher q with uranyl concentration, since the number of spheres is expected to increase while the number of monomers decreases. Furthermore, the intensity at low q should decrease due to the presence of a strong structure factor.

Sticky hard spheres interacting in a attractive potential as described by the Baxter model^[161] should result in a steep increase at low q .

II.2.5.3 Influence of extractant concentration

In order to investigate the influence of extractant concentration in the presence of uranyl, two cases have to be considered. **Figure 49, left** shows the results of SWAXS experiments of samples with increasing extractant concentration, where the uranyl concentration was kept constant at 0.35 M. **Figure 49, right** shows the spectra of samples, where the uranyl-to-extractant mol ratio was kept constant to a value of 0.25. At this value the organic phase is almost half saturated. Maximum loading is reached at a value around 0.4-0.5, slightly depending on the extractant concentration.

In order to interpret these spectra, one has to consider that the q -range can be separated into three important regimes (*cf.* **Figure 50**):

- The solvent peak.
- The “intratube” regime, where scattering mainly results from the potential between uranyl ions inside the cylindrical aggregates.
- The “intertube” regime, where scattering originates from the form factor and the structure factor of cylindrical segments. At high concentrations, the structure factor is expected to be dominant and results from the sum of every single contribution due to interaction between cylindrical segments.

First, the influence of extractant concentration at constant uranyl content is discussed.

- The solvent peak increases with increasing extractant concentration due to higher density of alkyl chains.
- “*Intratube*” regime: A correlation hump evolves with increasing extractant concentration. It slightly shifts from 0.63 \AA^{-1} to 0.65 \AA^{-1} , but due to the uncertainty, the peak position can be seen as constant and set to the same value observed in the subchapter before (*cf.* Chapter II.2.5.3). After subtraction of the “intertube” contribution, the “intratube” contribution is hardly dependent on the extractant concentration. This is consistent with the hypothesis of the previous subchapter. As indicated schematically in **Figure 50**, the number of uranyl-nitrate-uranyl segments (“intertube” contribution (*cf.* **Figure 50**, left, blue arrows)) is constant and independent on the extractant concentration, since it is given by the uranyl concentration. Therefore, the “intratube” is independent on the extractan concentration.
- “*Intertube*” regime: At lower q , the maximum slope decreases gradually from $q^{-0.98}$ (0.7 M DEHiBA) over $q^{-0.78}$ (1.0 M), $q^{-0.60}$ (1.2 M), $q^{-0.31}$ (1.5 M) to $q^{-0.01}$ (2.0 M) indicating a significant impact of the structure factor ($S < 1$). The presence of a q^{-1} at 0.7 M DEHiBA indicates the presence of elongated species or cylindrical subunits of a network or at least the presence of strongly polydisperse cylindrical aggregates. As indicated in **Figure 50**, the strong structure factor and the resulting flattening of the curve originates not from a significant change in structure, but of a higher number of interacting tubes (*cf.* **Figure 50**, left, red arrows)).

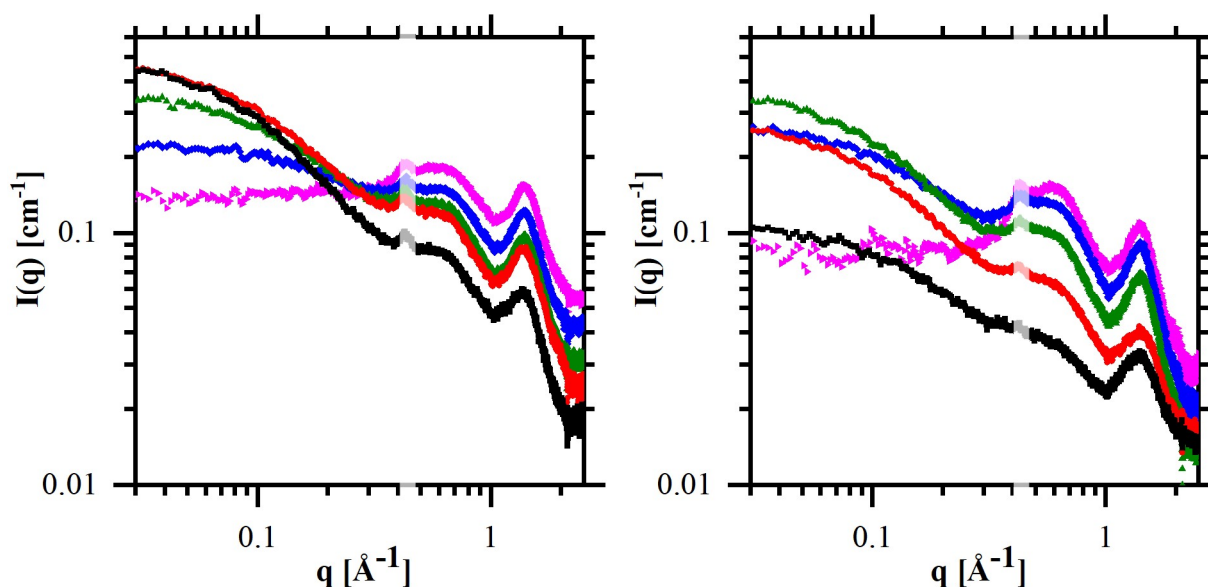


Figure 49. SAXS spectra of organic phases containing DEHiBA in different concentrations dissolved in Isane IP 175 and charged with different concentrations of uranyl. **Left:** ■ 0.7 M ● 1.0 M ▲ 1.2 M ◆ 1.5 M ► 2.0 M DEHiBA dissolved in Isane IP 175 and charged with a constant concentration of uranyl of 0.35 ± 0.05 M. **Right:** ■ 0.4 M ● 0.8 M ▲ 1.2 M ◆ 1.5 M ► 2.0 M DEHiBA dissolved in Isane IP 175 and charged with a constant uranyl/extractant ratio of 0.25, i.e. uranyl concentration of ■ 0.1 M ● 0.2 M ▲ 0.3 M ◆ 0.35 M ► 0.5 M. The region between 0.40 \AA^{-1} and 0.5 \AA^{-1} is plotted with decreased color intensity, in order to indicate that this q -range is affected by the signal of the Kapton window and that no conclusions can be drawn from this range.

In the following, the impact of extractant concentration at half loading of the organic phase with uranyl is discussed.

- As in the paragraph before, the solvent peak intensity increases with extractant concentration.
- “*Intratube*” regime: A correlation hump evolves with increasing extractant concentration. The position does not shift in the range of uncertainty. As it is indicated schematically in **Figure 50, right**, a constant uranyl/extractant ratio leads to a higher number of “intratube” segments, therefore a stronger “intratube” hump at elevated extractant concentration after subtraction of the “intertube” contribution (*cf.* **Figure 50, right**, increase in number of blue arrows).
- “*Intertube*” regime: The behavior at low q differs from **Figure 49, left**. The shape and slopes of the curves at low to medium extractant concentration (0.4 - 1.2 M DEHiBA) are similar and the curves rise with a slope of approximately $q^{-0.8}$. At higher concentration, the slope decreases to $q^{-0.52}$ (1.5 M), until it is almost flat for 2.0 M DEHiBA. As drawn schematically in **Figure 50, right**, a similar microstructure is expected for all concentrations and defined by the constant uranyl/extractant ratio. However, the total concentration and therefore the number of interacting segments changes with extractant concentration. Above a certain concentration ($c > 1.2$ M), the

cylinders start to see each other, the structure factor and consequently the behavior at low q -values depends on the extractant concentration.

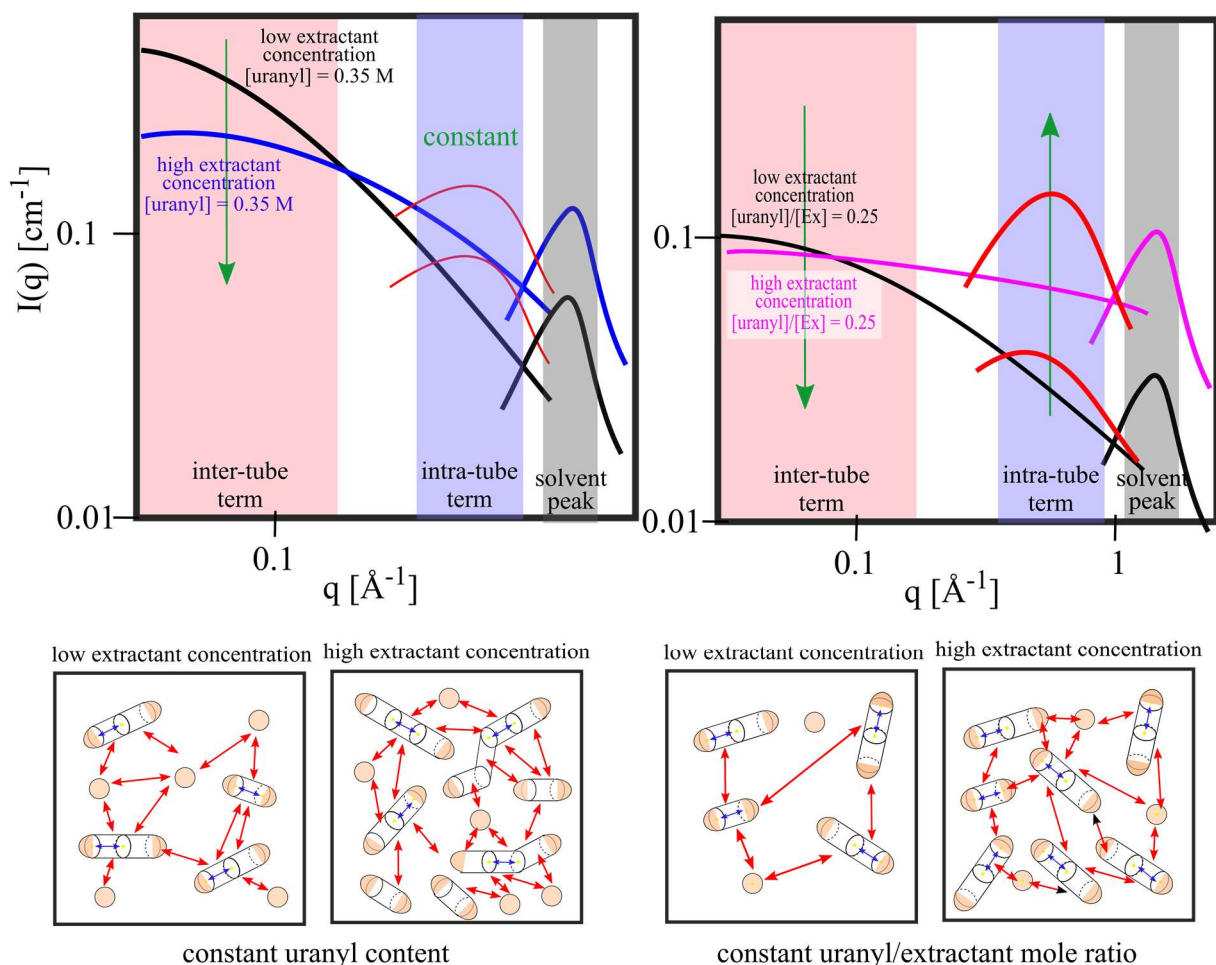


Figure 50. Schematic interpretation of the SAXS experiment with increasing extractant concentration at **left**: constant uranyl content and **right** constant uranyl extractant ratio (cf. **Figure 49**). Red arrows indicate “intertube” interactions, blue arrows “intratube” ones. The corresponding qualitative trend with increasing extractant concentration is indicated in green.

II.2.5.4 Influence of the diluent

In order to compare the influence of the diluent, two cases were investigated. **Figure 51** shows the comparison of DEHiBA, DEHBA and DEHDMBA in a non-penetrating solvent, dodecane, and a penetrating solvent, toluene. The extractant concentration as well as the concentration of uranyl was kept almost constant. Dodecane and toluene were chosen since they are very different in penetration and both available in deuterated form. This opens the possibility to perform SANS experiments and compare them with the results from SAXS.

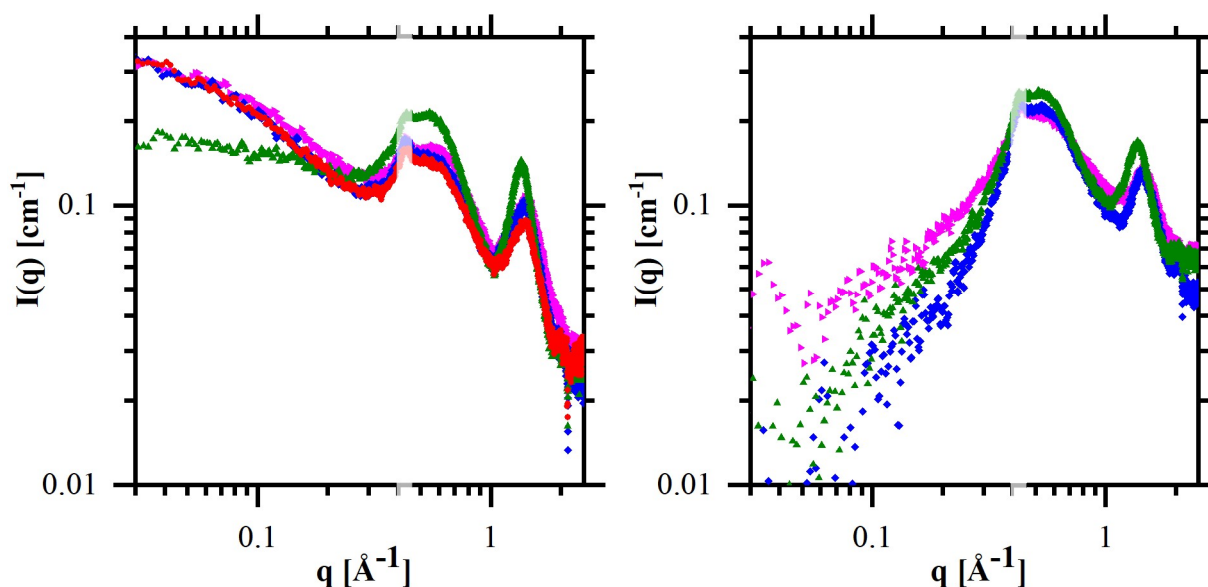


Figure 51. SAXS spectra of organic phases containing 1.5 M monoamide extractant dissolved in **left:** dodecane and **right:** toluene and both charged with 0.5 ± 0.05 M uranyl. Additionally, to \blacktriangle DEHDMBA \blacklozenge DEHBA \blacktriangleright DEHiBA, left: \bullet mixture of 0.9 M DEHiBA and 0.6 M DEHBA is plotted. The region between 0.40 \AA^{-1} and 0.5 \AA^{-1} is plotted with decreased color intensity, in order to indicate that this q -range is affected by the signal of the Kapton window and that no conclusions can be drawn from this range.

A comparison of both spectra shows differences between the three investigated monoamides as well as between the diluents that were used to dissolve the extractants.

Concerning the extractants themselves, for both diluents, the correlation peak for DEHDMBA at 0.64 \AA^{-1} is more pronounced than for the two other extractants. That correlates with the observations of Chapter II.2.1, where the viscosity increase was also the most elevated for DEHDMBA. For the two other extractants, it is difficult to determine the difference since slight differences in uranyl concentration or errors in fluorescence subtractions could make a significant difference. At low q , in the case of dodecane, the curve of DEHDMBA is almost flat, while for DEHiBA, DEHBA and a mixture of the two, an increase in intensity is observed. In the case of toluene, the differences in the low q region are too small to make meaningful conclusions. The fact that the signal is high at low q for a non-penetrating solvent indicates that the osmotic compressibility is high – a sign for high polydispersity or a mesh.

Regarding the influence of the diluent, only slight differences can be observed by means of this one experiment. For a better understanding, an additional experiment was carried out, comparing dodecane and xylene. Toluene was replaced by xylene due to the lower water solubility of xylene and consequently better comparability to dodecane. The uranyl content was increased for 1.5 M DEHiBA dissolved in diluent. The results are shown in **Figure 52**.

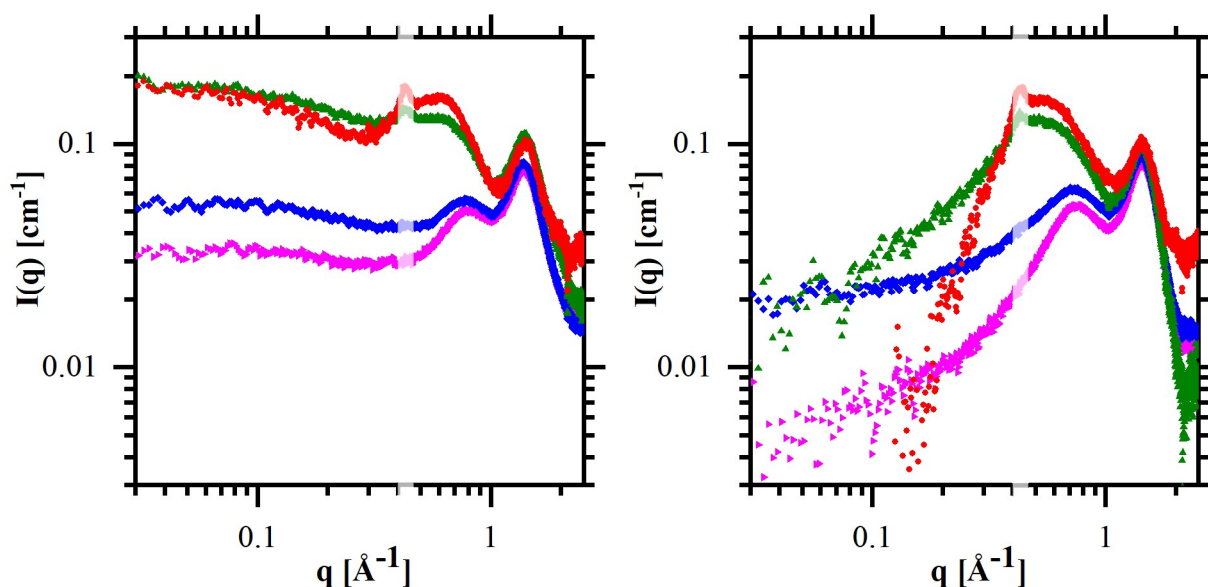


Figure 52. SAXS spectra of organic phases containing 1.5 M DEHiBA dissolved in **left:** dodecane and **right:** xylene and both charged with increasing uranyl concentration. **Left:** ● 0.54 M ▲ 0.33 M ◆ 0.04 M ► 0 M uranyl; **Right:** ● 0.58 M ▲ 0.34 M ◆ 0.04 M ► 0 M uranyl. . The region between 0.40 Å⁻¹ and 0.5 Å⁻¹ is plotted with decreased color intensity, in order to indicate that this q -range is affected by the signal of the Kapton window and that no conclusions can be drawn from this range.

Combining the results from **Figure 51** and **Figure 52** gives two results. First, the correlation hump is less defined in the case of the penetrating solvent xylene/toluene. That means that either the interaction between the correlation centers is screened by the presence of the π -system or that the hump is broadened due to the presence of more predominating structures. Statements about a broadening of the hump cannot be made due to the overlap with the peak of the Kapton window at 0.43 Å⁻¹. The second observation is a strong difference in the behavior at low q . While the curves are flat or slightly rising in the case of a non-penetrating solvent like Isane IP 175 of dodecane, the intensity goes rapidly down for the penetrating solvents toluene and xylene. That indicates either a difference in form factor or a much stronger repulsive structure factor ($S < 1$) for penetrating solvents. The latter was already demonstrated by Berthon *et al.*^[87] She and her co-workers demonstrated for different malonamides in different alkanes that short penetrating oils swell the apolar layer of reverse aggregates and decrease the attractive potential between their polar cores. This fact was discussed more in detail in Chapter I.2.5.4 in the context of the third phase. It is not possible to say if a change of the form factor also appears due to the dominating influence of the structure factor.

II.2.5.5 Temperature dependence

In order to determine if the decrease of viscosity with temperature is related to a change of the mesoscopic structure, three samples were measured at 25 °C, 40 °C and 70 °C. Since the fluorescence is temperature dependent^[220], for the samples at 70 °C, the fluorescence that was

subtracted had to be reduced, so that the solvent peak level stays constant. After this correction, no temperature dependence was observed for the three different samples containing 1.5 M DEHiBA diluted with Isane IP 175 and charged with different concentrations of uranyl (*cf.* **Figure 53**). This observation gives two indications. First, the structure stays preserved over a wide range of temperature and the decrease in viscosity with temperature is not related to a structural change. This indicates that the bending constant of such systems is well above $1 kT$. Second, the absence of a temperature dependence of the structure supports the hypothesis that sticky hard spheres can be ruled out. Attractive potentials are in general temperature-dependent and therefore one should see a difference in scattering at different temperatures.

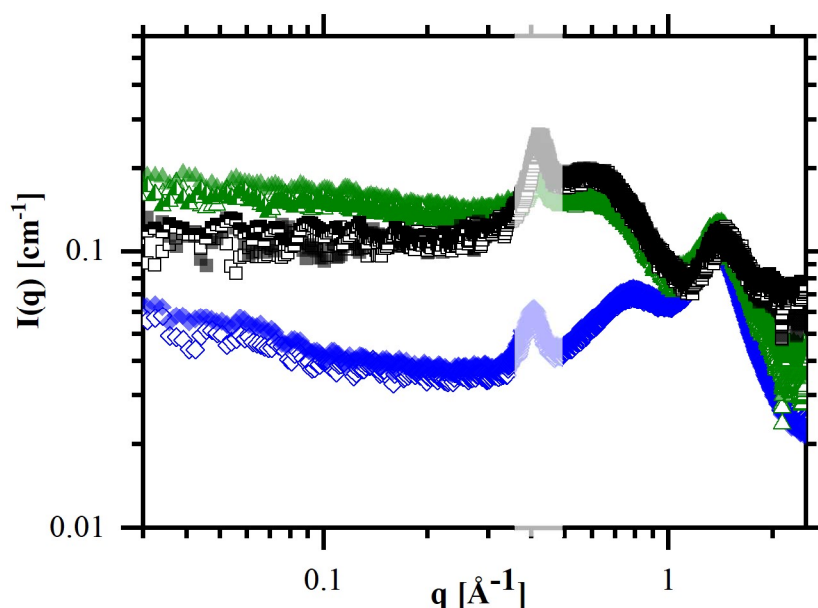


Figure 53. Temperature dependent SWAXS spectra of organic phases containing 1.5 M DEHiBA dissolved in Isane IP 175 and charged with different concentrations of uranyl. Organic phases charged with blue: 0 M uranyl, green: 0.33 M uranyl and black: 0.54 M. \diamond , \square and \triangle measured at 25 °C; \blacklozenge , \blacksquare and \blacktriangle measured at 40 °C; \blacksquare and \blacktriangle measured at 70 °C. The region between 0.40 \AA^{-1} and 0.5 \AA^{-1} is plotted with decreased color intensity, in order to indicate that this q -range is affected by the signal of the Kapton window and that no conclusions can be drawn from this range.

II.2.5.6 Investigation of the third phase

Figure 54 shows the SWAXS spectra of two third phases and a pure extractant charged with uranyl. Third phases were prepared by contacting 1.5 M DEHiBA or DEHDMBA diluted in Isane IP 175 several times with 10 M nitric acid and a highly concentrated aqueous solution of uranyl nitrate (343 g/L, 3 M). After centrifugation, a small amount of diluent was squeezed out and separated as upper phase from the highly viscous and predominating third phase. The two third phases are alike, only the correlation hump is slightly more intense for DEHDMBA. A comparison of the two spectra with the spectra before (*e.g.* 1.5 M DEHiBA in Isane charged with uranyl, *cf.* **Figure 47**) points out a strong similarity, which indicates that the structure

leading to a viscosity increase can be seen as a pre-state of the third phase. The absence of crystalline peaks indicates that the third phase is not crystalline, but density reticulated. The fact that structures at lower concentrations can serve as precursor for more condensed phases was already observed by Mitchell *et al.* who have investigated different polyoxoethylene surfactants and concluded that an increased volume fraction mainly leads to compression, so that spheres tend to form cubic phases first, while rod-like micelles directly form hexagonal phases when volume fraction is increased.^[221]

Charging the pure extractant DEHiBA with uranyl also shows the same buildup of the region at high q and a strong decrease of the signal at low q . Also, in this case, we have referred the strong decrease in intensity to a strong repulsive structure factor. At high q , the correlation hump is much better defined as in the presence of diluent.

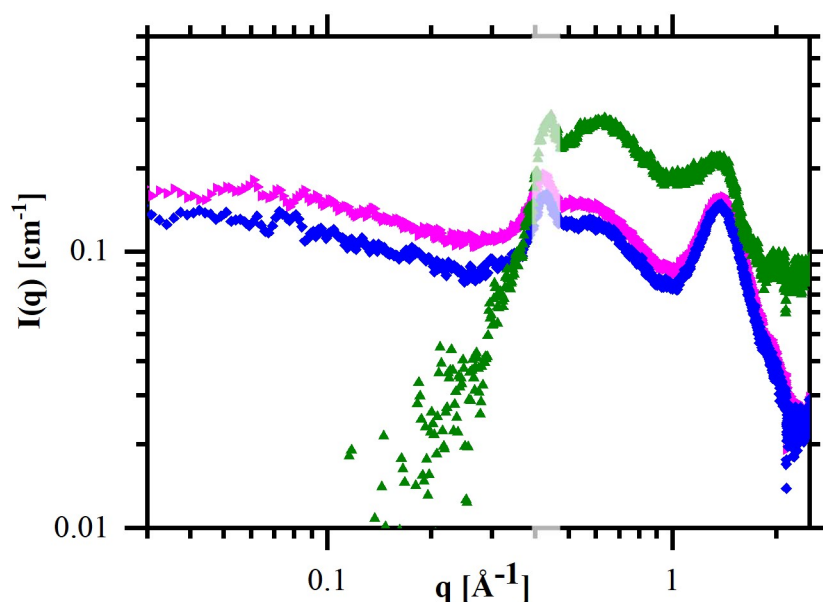


Figure 54. SAXS spectra of concentrated organic phases charged with uranyl. \blacktriangle pure DEHiBA charged with estimated 0.8 M uranyl, \blacklozenge third phase of the system DEHiBA/Isane \blacktriangleright third phase of the system DEHDMBA/Isane.

II.2.6 Small-Angle Neutron Scattering Analysis

Since the scattering contrast between the alkyl chains of the extractant and the organic diluent is not sufficient in SWAXS, small-angle neutron scattering was used to get more insight in the colloidal structure that leads to the viscosity increase. The experiments were carried out in deuterated diluent and hydrogenated extractant to have a sufficient high contrast between the extractant chains and the diluent. After normalization and solvent subtraction, the data were treated with the software SASfit. The incoherent background was estimated first by a calibration with different D₂O/H₂O ratios and fitted as a flat background (*cf.* Chapter II.1.6).

II.2.6.1 Investigations with increasing uranyl concentration and diluent dependence

Figure 55 shows the results from organic phases composed of 1.5 M DEHiBA diluted in deuterated dodecane and charged with increasing concentrations of uranyl. The incoherent background is similar for all four samples since the dominating contribution – the concentration of extractant – is constant. Each of the curves increases until a flat plateau is reached. The intensity at low q increases with increasing uranyl concentration. At the highest concentration, a slope close to q^{-1} is reached in the range between 0.05 \AA^{-1} and 0.14 \AA^{-1} , typical for a cylindrical unit. This slope is also present for a moderate concentration of uranyl in the range from 0.11 \AA^{-1} to 0.20 \AA^{-1} but at lower concentration and while in the absence of uranyl this slope is not observed. The same trend can be identified in “weaker” form in isooctane, but not in toluene (*cf.* **Suppl. Figure 17** and **Suppl. Figure 18**).

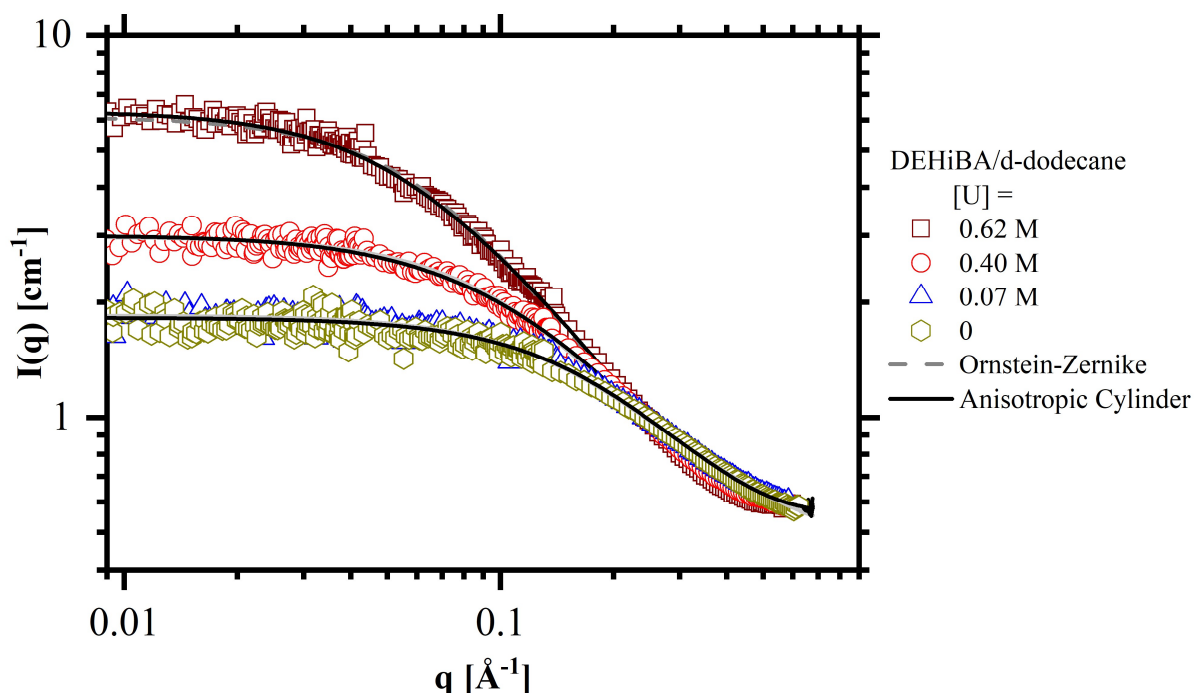


Figure 55. SANS spectra of organic phases containing 1.5 M DEHiBA in deuterated dodecane charged with \square 0.62 M \circ 0.40 M \triangle 0.07 M \hexagon 0 M uranyl. Grey dashed lines represent fits obtained with a simple Ornstein-Zernike fit. Black lines represent fits using a local cylindrical form factor and random rod structure factor for anisotropic objects.

Due to the observed slope close to q^{-1} as well as due to the conclusions drawn in the sections before, the presence of cylindrical objects can be assumed. However, a strong structure factor is also present due to the high concentration of extractants and the possibility of the formation of a network of cylindrical units is given. Other mesoscopic arrangements are also possible.

For a first semi-quantitative analysis of the spectra, two fitting models were chosen to obtain

qualitative trends. Due to the elevated volume fraction of scatterers, the results only give a rough overview and show tendencies, since the structure factor is crucial, but difficult to estimate properly.

The first model chosen is a simple Ornstein-Zernike fit that indicates the correlation between two correlation centers. The interpretation of the obtained correlation length has to be done from case to case. It can represent the mean size of fluctuating particles or also the mean entanglement length in the case of semi-dilute polymers. The second model chosen to obtain further information, is a fit for strongly anisotropic particles with local cylindrical shape. The form factor and the structure factor were already implemented in the software SASfit and are further described in its manual^[199] and in Chapter II.1.6.

The results of both fits are summarized in **Table 11**.

Table 11. Fit parameter obtained from fits of organic phases charged with uranyl (cf. Figure 55)

System: 1.5 M DEHiBA/d-26-dodecane	0 M Uranyl	0.07 M Uranyl	0.40 M Uranyl	0.62 M Uranyl
Ornstein-Zernike				
Number density of scatterers N	0.42	0.44	0.60	0.90
Forward scattering I_0 [cm ⁻¹]	3.1	3.2	4.2	6.3
Correlation length ζ [nm]	0.46	0.51	0.80	1.3
Background [cm ⁻¹]	0.44	0.44	0.45	0.45
Anisotropic structure with local cylindrical form factor and random rod structure factor				
Number density of scatterers N [cm ⁻³]	3.8E+20	1.8E+20	7.4E+19	2.8E+19
Most probable radius R [nm]	0.42	0.40	0.46	0.46
Radius width σ_R (logNorm)	0.22	0.22	0.29	0.35
Most probably length L of rod/segment [nm]	0.8	1.8	2.1	5.3
Width of length (logNorm)	0.7	0.4	0.6	0.4
$\eta(\text{object})$ [10 ¹⁰ cm ⁻²]	-0.08	-0.08	-0.08	-0.08
$\eta(\text{diluent})$ [10 ¹⁰ cm ⁻²]	6.7	6.7	6.7	6.7
Background [cm ⁻¹]	0.55	0.56	0.58	0.57

The fit results demonstrate a structuring of the organic phase that is more and more pronounced with increasing uranyl content. The Ornstein-Zernike fit indicates an increase in correlation length as well as in number density of scatterers. The correlation length is in the order of

magnitude of around 1 nm. Using a fit for anisotropic particles with local cylindrical geometry indicate local cylinders with a radius of around 0.45 nm and a length of up to 5 nm. The number density of scatterers decreases indicating that larger particles are forming with increasing uranyl concentration. Furthermore, the obtained lengths are quite polydisperse, which was already concluded from the high osmotic compressibility seen in X-Ray scattering experiments (*cf.* Chapter II.2.4).

Similar results were obtained for DEHiBA in isooctane and toluene. The results are shown in Chapter VII.6.5, **Suppl. Figure 17**, **Suppl. Figure 18**, and **Suppl. Table 18**. The radius as well as the contour length increases with increasing uranyl concentration while the number density decreases. However, the more penetrating the diluent (dodecane < isooctane < toluene) the smaller the most probable length. For better comparison, each spectrum was fitted with the same model, even if for some samples, especially at lower uranyl concentration, probably other models would have been more suitable. However, for each of the spectra satisfactory fit accuracy could be observed. Moreover, especially in the case of toluene, a larger radius is observed than for dodecane, demonstrating the penetration power of toluene.

II.2.6.2 Investigations with increasing extractant concentration

Figure 56 demonstrates the scattering curves recorded in order to investigate the influence of the extractant concentration at constant uranyl/extractant molar ratio. The fit results are listed in **Table 12**.

The number density as well as the correlation length seem to have a maximum between 0.8 M and 1.2 M DEHiBA for a half-saturated organic phase. Moreover, according to the fit for anisotropic objects, the most probable length decreases with increasing extractant concentration. However, for these lengths, there is a maximum in polydispersity between 0.8 M and 1.2 M DEHiBA.

The reasons for these facts are difficult to identify. With increasing extractant concentration many parameters may change. Due to the higher concentration and less free space, the activity of the extractant will go down.^[222] Furthermore, with increasing extractant concentration the solvent polarity increases, the number of monomers can change and the interaction between aggregates and solutes could be influenced.

The theory of a maximum for a definite extractant/uranyl ratio is also encouraged by comparing the absolute intensities of **Figure 49** and **Figure 56**. Although the structure factor is unknown, the crossing of the forward scattering intensities can be seen as an indication for a maximum in

size or respectively contour length.

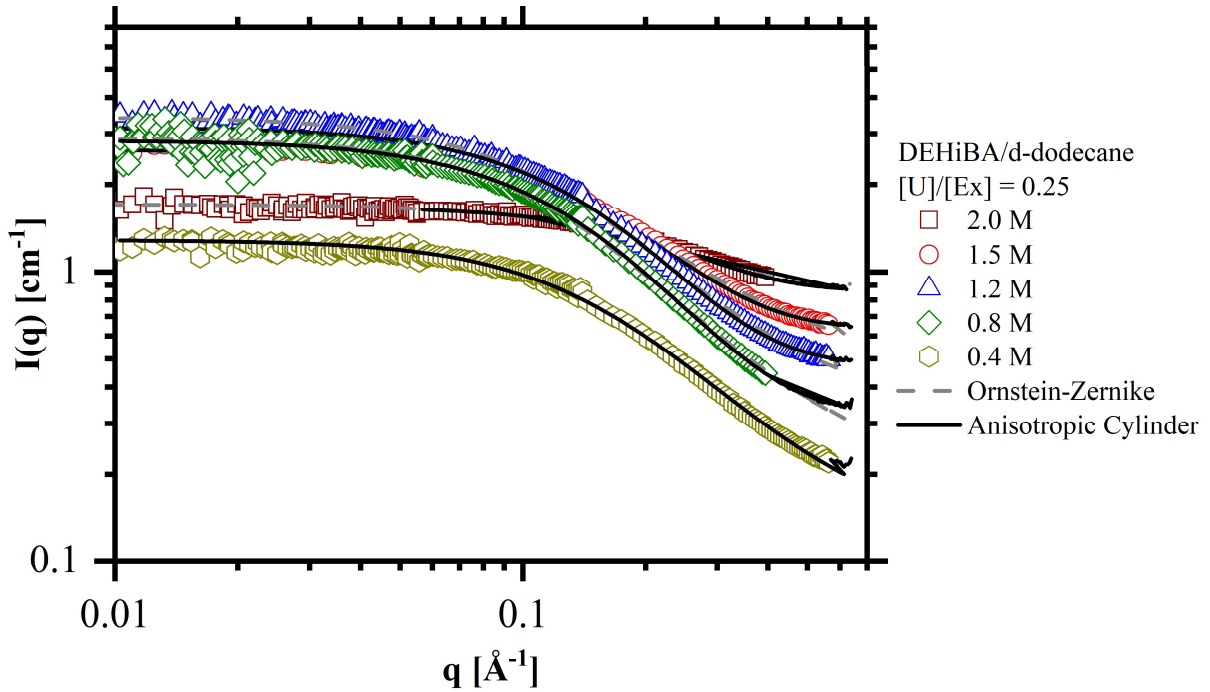


Figure 56. SANS spectra of organic phases containing different concentrations of DEHiBA in deuterated dodecane charged with a defined mol ratio $[uranyl]/[extractant]$ of 0.25 ± 0.05 (half saturation). Extractant concentrations are represented as following: \square 2 M \circ 1.5 M \triangle 1.2 M \diamond 0.8 M \pentagon 0.4 M uranyl. Grey dashed lines represent fits obtained with a simple Ornstein-Zernike fit. Black lines represent fits using a local cylindrical form factor and random rod structure factor for anisotropic objects.

Table 12. Fit parameter obtained from fits of organic phases charged with uranyl (cf. Figure 56)

System: DEHiBA/dodecane	0.4 M DEHiBA 0.1 M Uranyl	0.8 M DEHiBA 0.2 M Uranyl	1.2 M DEHiBA 0.3 M Uranyl	1.5 M DEHiBA 0.35 M Uranyl	2.0 M DEHiBA 0.5 M Uranyl
Ornstein-Zernike					
Number density of scatterers N	0.71	0.654	0.702145	0.603	0.402
Forward scattering I_0 [cm ⁻¹]	1.63	4.13	4.40114	3.77	2.4
Correlation length ζ [nm]	0.601	0.791	0.798	0.65	0.45
Background [cm ⁻¹]	0.121	0.203	0.332	0.477	0.74
Anisotropic structure with local cylindrical form factor and random rod structure factor					
Number density of scatterers N [cm ⁻³]	6.3E+19	1.6E+20	5.7E+19	3.5E+20	1.5E+20
Most probable radius R [nm]	0.42	0.33	0.34	0.38	0.40
Radius width σ_R (logNorm)	0.23	0.43	0.47	0.48	0.30
Most probably length L of rod/segment [nm]	2.6	2.1	1.2	1.0	1.4

Width of length (logNorm)	0.2	0.5	0.6	0.1	0.2
$\eta(\text{object}) [10^{10} \text{ cm}^{-2}]$	-0.08	-0.08	-0.08	-0.08	-0.08
$\eta(\text{diluent}) [10^{10} \text{ cm}^{-2}]$	6.7	6.7	6.7	6.7	6.7
Background [cm^{-1}]	0.19	0.32	0.43	0.64	0.89

II.2.6.3 Investigations with monoamide variation and diluent dependence

The SANS spectra of three different monoamides in both deuterated dodecane and toluene and charged with 0.5 ± 0.05 M uranyl are presented in **Figure 57**. The fit results are documented in **Table 13**.

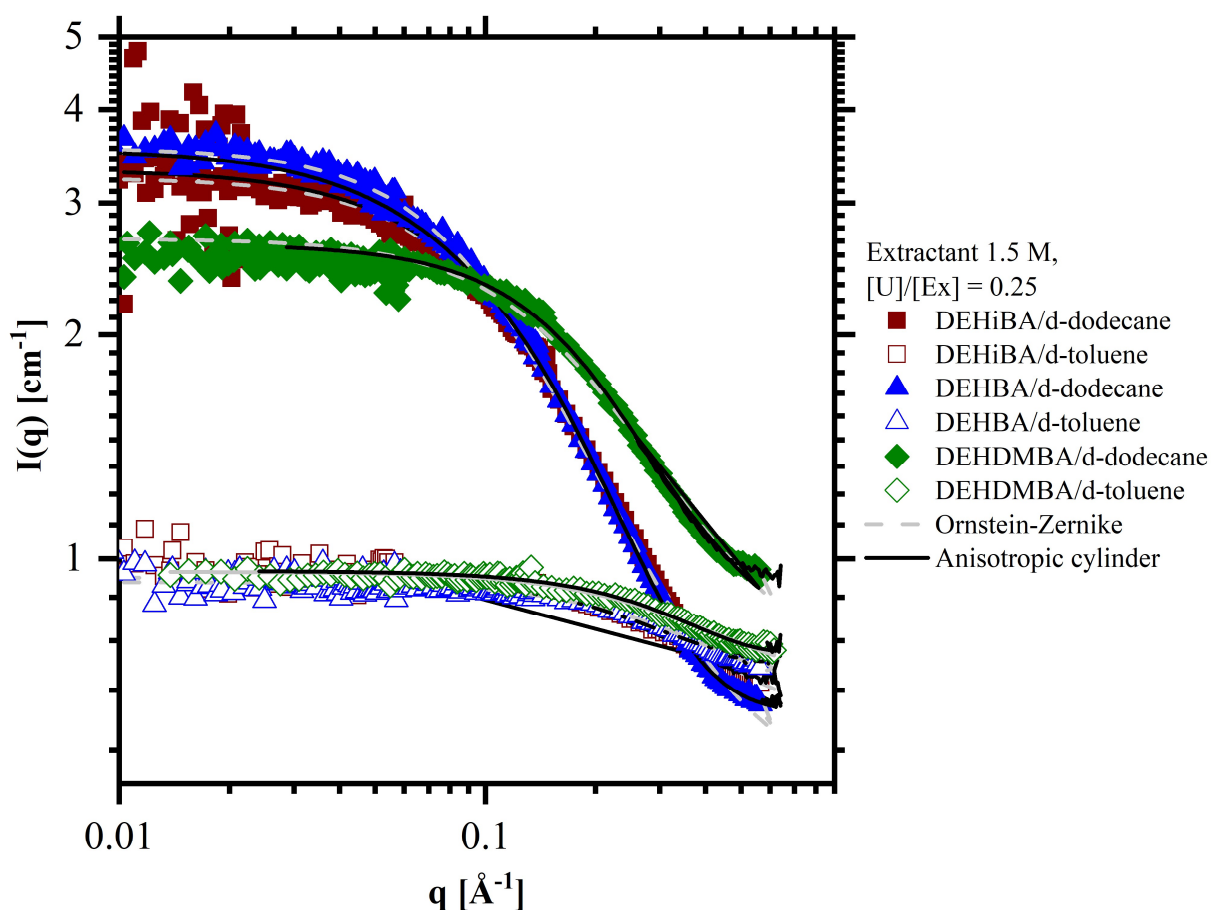


Figure 57. SANS spectra of organic phases containing 1.5 M of extractant in two different deuterated diluents. Solid symbols: extractant diluted in deuterated dodecane. Unfilled symbols: charged with a defined uranyl concentration of $0.5 \text{ M} \pm 0.05$. Following extractants were investigated: \square DEHiBA \triangle DEHBA \diamond DEHDMBA. Grey dashed lines represent fits obtained with a simple Ornstein-Zernike fit. Black lines represent fits using a local cylindrical form factor and random rod structure factor for anisotropic objects.

Just from comparing the samples prepared in deuterated dodecane and toluene, one can see the same trend observed in Chapter II.2.5.4. The scattering intensity is much less elevated compared to dodecane and probably not only due to the lower scattering contrast. The OZ-fit

results indicate that the number density as well as the correlation length is more elevated for samples diluted in less-penetrating dodecane. A local cylinder fit indicates that the radius of the cylinder-shaped structures increase in a penetrating diluent by swelling of the outer layer.^[87] Moreover, the length of the cylinders are longer and more polydisperse in dodecane than in toluene.

Table 13. Fit parameter obtained from fits of organic phases charged with uranyl (cf. **Figure 56**)

System: monoamide in diluent charged with $0.5 \pm$ 0.05 uranyl	1.5 M DEH/BA		1.5 M DEHBA		1.5 M DEHDMBA	
	d-26- dodecane	d-8- toluene	d-26- dodecane	d-8- toluene	d-26- dodecane	d-8- toluene
Ornstein-Zernike						
Number density of scatterers N	0.637	0.222	0.731	0.22	0.71	0.711
Forward scattering I_0 [cm^{-1}]	4.35	1.71	4.23	1.46	2.82	0.43
Correlation length ζ [nm]	0.75	0.263	0.82	0.26	0.49	0.254
Background [cm^{-1}]	0.474	0.564	0.471	0.614	0.68	0.65
Anisotropic structure with local cylindrical form factor and random rod structure factor						
Number density of scatterers N [cm^{-3}]	2.4E+20	1.3E+20	1.8E+20	7.4E+19	2.2E+20	3.0E+20
Most probable radius R [nm]	0.40	0.54	0.45	0.60	0.42	0.52
Radius width σ_R (logNorm)	0.41	0.05	0.37	0.05	0.14	0.07
Most probably length L of rod/segment [nm]	1.0	0.7	0.9	0.7	2.2	0.5
Width of length (logNorm)	0.7	0.5	0.8	0.5	0.05	0.1
$\eta(\text{object})$ [10^{10} cm^{-2}]	-0.08	-0.08	-0.08	-0.08	-0.08	-0.08
$\eta(\text{diluent})$ [10^{10} cm^{-2}]	6.7	5.6	6.7	5.6	6.7	5.6
Background [cm^{-1}]	0.62	0.70	0.62	0.74	0.85	0.75

Looking at the difference between the three monoamide extractants, longer cylinder units are formed with DEHDMBA than with the other two monoamides. This is consistent with the viscosity that increases in the order DEHBA < DEHiBA < DEHDMBA. However, this fact is in discrepancy with the correlation length observed by OZ-fits, where for DEHDMBA, the smallest value was observed.

II.2.6.4 The behavior at low q

In the framework of the SANS measurements, it was quickly checked for most of the samples, if there is an increase at low q . However, since the flux at larger wavelengths is weak, the error bars are quite large and the certainty is not high. It seemed that there is an increase at very low q ($< 0.004 \text{ \AA}^{-1}$, so larger than 160 nm) for some samples, especially at lower and medium uranyl concentration or with penetrating diluents. For the other samples, the possibility of an increase at even lower q (< 0.002) could not be excluded. To proof the existence of this increase, one sample of 1.5 DEHBA in deuterated dodecane and an elevated uranyl concentration of 0.5 M was counted 4 hours in order to have sufficient high statistics. The result is shown in **Figure 58**. For this specific sample, an assured increase is observed at very low q . After the plateau, the curve rises with a slope close to $q^{-3.8}$. This increase can have different origins. One possibility is the formation of a large mesoscopic structure with a macroscopic interface, that is larger than 160 nm, but not continuous. One could call them also nanocrystals. Another possibility is the formation of a large-scale structure that is formed by the cylinder units that are detected by the small region with q^{-1} behavior. In the case of branched wormlike micelles, Vogtt has developed a model, that relates the second increase with the branching density d_f .^[223] However, in his model, no plateau between the q^{-1} region and the q^{-df} is observed.

It was not possible in the framework of the beamtime at the LLB to measure every sample with a sufficient long counting time at very low q . Consequently, tendencies and trends are difficult to determine.

The observations are consistent with the indications of a sphere-to-rod transision. As was explained in Chapter I.2.5.3, cylinders, especially in elevated concentration, attract each other much stronger than spherical objects. As a result, the formation of nanocrystals or similar structures are favored at higher uranyl concentration. This signal is further and more detailed discussed in Chapter III.3.6 in the context of Onsager transition, interparticle wetting and the model developed in this work.

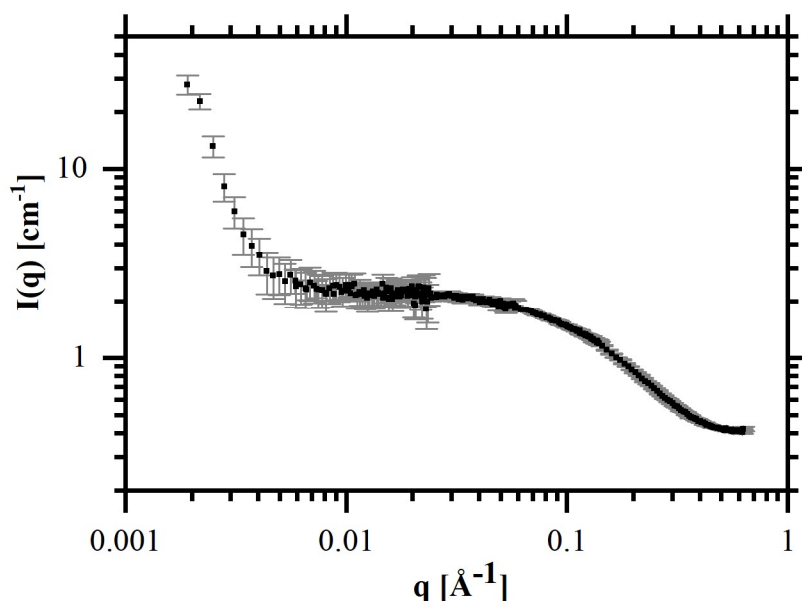


Figure 58. Example of a rise in low q as seen for some of the samples. This present example was measured with 1.5 M DEHBA diluted in deuterated dodecane charged with 0.5 M uranyl. In grey the error bars are presented.

II.2.7 Conclusions and simplified image of the mesoscopic structuration in the organic phase

In the subchapters before, the observations were presented objectively and separately. In this chapter, the results will be summarized as well as combined to an overall image of the structure. This will help to develop and understand the model that is presented in Chapter III. It has to be noted that none of the experimental observations proves the identity of the structure. Only the sum of the indications by experimental facts leads to it.

First, the viscosity increase was quantified and investigated in detail. The viscosity of the organic phase rises for all extractants investigated:

- With extractant concentration
- With uranyl concentration
- With decreasing temperature
- In the order TBP < DEHBA < DEHiBA < DEHDMBA, therefore with decreasing spontaneous packing parameter
- With decreasing penetration power of the diluent, *e.g.* in the order octanol < toluene \approx xylene < isooctane < Isane IP 175 < dodecane.

The temperature dependence is consistent with the Arrhenius model and it was shown that the activation energy for shearing increases with uranyl concentration.

Regarding the rheology of the systems, all systems are shear independent over a wide range of

shear rates, even at highest uranyl and extractant concentration. Amplitude sweeps and frequency sweeps were difficult to carry out and to interpret. The mesoscopic organization seems to be too weak for quantitative results and no definite trends could be observed. However, a break-up of the structure is observed at a certain frequency which is indicated by a break-down of the storage modulus.

Small- and wide-angle X-ray scattering experiments show a characteristic correlation hump at a q -value of $q^* = 0.64 \text{ \AA}^{-1}$ corresponding to a correlation distance of approximately 10 \AA . That shows that the uranyl ions are not distributed homogeneously in the space. There is rather a defined distance between some of them. The broadness of the hump indicates either a mixture of different structures or a certain variation of the distances, *e.g.* various definite distances due to fluctuating vacancies in the mesoscopic structure. The behavior at low q is strongly dependent on the extractant concentration and the diluent. The curves become more and more flat with increasing extractant concentration and even get a positive slope for penetrating diluents. We have interpreted the flattening of the curve either as a strong repulsive structure factor or the formation of a network with a given mesh size. The very low forward scattering in case of penetrating diluent can be attributed to the absence of larger aggregates and an increase in repulsion between them. Therefore, penetrating diluents seem to avoid larger aggregates. The microstructure seems not to change with temperature. Moreover, the spectra of the third phase resemble the spectra of the organic phases charged with uranyl. Also, during preparation, it appears that there is no structural change during third phase formation. One can rather speak of a squeezing out of diluent out of the colloidal structure that is formed.

In the framework of SANS experiments, slopes close to q^{-1} were detected indicating cylinder-like objects or subunits. An Ornstein-Zernike-Fit as well as a fit for anisotropic particles reveal qualitative trends. Due to the high volume fraction of extractants, the structure factor is expected to be important and difficult to determine. Therefore, only trends can be extracted from the values. The fits indicate partially cylindrical units with a radius of around $0.4\text{-}0.6 \text{ nm}$. The length of these units increases with uranyl concentration and is longer for extractants diluted in solvents that are considered as non-penetrating. Furthermore, for some samples, an increase at very low q was observed while others were flat down to a q -value of 0.004 \AA^{-1} . This indicates either the formation of large, but finite structures of a size larger than $150\text{-}200 \text{ nm}$ (nanocrystals) or that the scattering is contributed to the global scattering of branching points.^[223] The formation of nanocrystals is favored due to a higher attractive potential between cylinders than between spheres (*cf.* Chapter I.2.5.3).

As a conclusion, considering all these experimental observations, the following structural model of the organic phase is proposed. The viscosity-determining structure is mainly built-up of small cylinder-shaped units. Inside these tubes, uranyl-nitrate-uranyl chains of a definite uranyl-uranyl correlation distance are enclosed. Due to the shear-independence of the viscosity and due to the large size of the global structure indicated by SANS, the formation of a loose living network of fast relaxation time (*cf.* Chapter I.2.5.2) is more likely to be formed than separated, intercepting worms.

The functional groups of the three dialkylamides are the same. A big difference to TBP is the spontaneous packing parameter, that is expected to be significantly smaller for monoamides due to the third chain in the case of TBP. Tributyl phosphate is more curved and so cylindrical objects will be disfavored. Also, within the monoamides, the spontaneous packing parameter will vary due to the difference in the short amide bound alkyl chain. The spontaneous packing parameter will also strongly vary with the diluents. Penetrating diluents like toluene will penetrate the outer chains and increase the packing parameter. As a result, the spontaneous packing parameter plays an important role for the mesoscopic structure and the resulting viscosity of the organic phase.

In the next chapter, this model structure will be described more in detail and translated into a model that helps to understand and explain the interesting viscosity increase of dialkylamides in the presence of uranyl. This model should also be able to propose solutions for the problem of viscosity increase that will be applied in Chapter IV.

III DEVELOPMENT OF A MINIMAL MODEL

In the framework of this chapter, the second step to achieve the goals of this thesis are presented. First, the main idea and the picture developed in Chapter II.2.7 are recapitulated in detail. Then, the implementation of the model into a program is presented. After that, the resulting trends will be discussed. The results will be compared with the experimental observations and critically reviewed. Finally, the formulation approaches resulting from this minimal model at the nanoscale will be presented and applied in Chapter IV. As it will be demonstrated in Chapter V, this minimal model can also be also adjusted for the case of surfactant self-assembly in aqueous solution.

Parts of this Chapter are used for the following Publication:

*M. PLEINES, J. DUHAMET, T. ZEMB, A minimal model at nanoscale leading towards a new formulation principle for extracting microemulsions, submitted to Hydrometallurgy **2018**.*

III.1 Main idea and underlying theory

III.1.1 Main principle

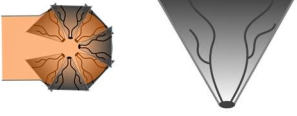
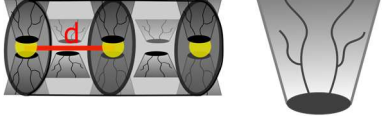
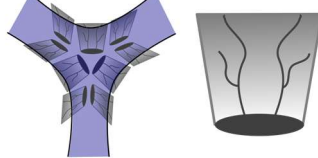
In the previous chapter, experimental observations were presented that indicate the existence of small cylinder-shaped units that organize themselves in a mesoscopic structure. Within these cylinders, alternating uranyl-nitrate-uranyl chains are embodied. One could speak of a one-dimensional ionic liquid enclosed in a bottlebrush structure.^[224] The presence of a living network of fast relaxation time is also indicated. The cylinders are connected via junction points and can glide along the backbone of the skeleton. Furthermore, the packing parameter seems to play a significant role for the evolving structure as well as for the resulting viscosity. These factors are included in a “minimal” model at nanoscale.

Here, the term “minimal” means that this model functions with a minimum of necessary input parameters that are either measurable or have at least a precise definition and physical meaning. This model considers the chemical terms at the molecular scale, the physical terms at the meso-scale as well as the flow characteristics at the macroscale. It combines the concept of pseudo-phases introduced by Shinoda^[225] and Tanford^[44], the expression for the free energy of bending for surfactant films derived from the works of Ninham^[54], Hyde^[65,73] and Israelachvili^[46] as well as theories of viscosity calculation from nanostructure by Cates^[116,117,124], Lequeux^[135] and Khatory^[142]. These pioneering concepts are introduced in Chapter I.

The evolving structure in the organic phase can be seen as made of four different microphases in chemical equilibrium that arrange themselves into a colloidal structure: endcaps (EC), cylinders (cyl), junctions (J) and monomers. The fourth microphase, monomers, will not significantly contribute to the increase in viscosity. Consequently, its contribution is negligible and will only be considered in the context of this model by decreasing the number of molecules participating in the decisive structure. Corresponding to each of these microphases, an effective packing parameter can be defined (*cf.* **Table 14**). It has to be noted that these values are estimated from a simplified transfer of the aqueous phase and probably do not represent the exact limits. The following model and chosen values are rather used to demonstrate and explain the viscosity increase than to obtain quantitative results. Especially the estimation of the value for junctions is difficult. To our knowledge, the only indication of the packing parameter of junctions was found as follows: “*The packing of the amphiphiles in a Y-junction is, on average, intermediate between that in a bilayer and a cylindrical micelle. This is because the junction may be, approximately, regarded as consisting of a small central bilayer-like region*”

surrounded by three semi-toroidal sections.” (Sylvio May in ^[122]). Since a junction will later be defined only as the unit that allows a threefold connection on a hexagonal grid (*cf.* Annex, Chapter VII.7.1), the cylindrical part of a junction is considered to be small. Therefore, the effective packing parameter of a junction unit is set to 1.2. This value is closer to that of a structure with a small average curvature, since it can be assumed as a saddle-like curvature.

Table 14. Overview of the three viscosity-determining microphases in chemical equilibrium and the corresponding effective packing parameter.

Spherical endcaps	Bottlebrush cylinder units surrounding alternating uranyl- nitrate-uranyl chains	Junctions with a saddle-like structure with an average curvature of $H \approx 0$
$P_{EC} = 3$	$P_{cyl} = 2$	$P_J \approx 1.2$
		

When the spontaneous packing parameter (*cf.* Chapter I.2.4) is close to one of these values, the corresponding microphase will be predominantly formed.

III.1.2 Microphase distribution

According to the concept of pseudo-phases, the chemical potential μ of a single extractant i in the diluent is equal to the chemical potential of i inside a microphase.^[44,225]

$$\mu_{i,\text{endcaps}} = \mu_{i,\text{cylinders}} = \mu_{i,\text{junction}} = \mu_{i,\text{monomer}} \quad (57)$$

The chemical potential μ_i of one extractant inside one of the microphases can be split into a standard reference potential μ_i^0 and a concentration-dependent term $RT \ln a_i$, where a_i is the activity.

$$\mu_{i,\text{endcaps}} = \mu_{i,\text{endcaps}}^0 + RT \ln a_{i,\text{endcaps}} \quad (58)$$

$$\mu_{i,\text{cylinder}} = \mu_{i,\text{cylinder}}^0 + RT \ln a_{i,\text{cylinder}} \quad (59)$$

$$\mu_{i,\text{junction}} = \mu_{i,\text{junction}}^0 + RT \ln a_{i,\text{junction}} \quad (60)$$

According to the concepts developed by Hyde and co-workers, the bending contribution to the free energy of the extractant in a given microphase can be expressed by a harmonic approximation as the deviation of the actual extractant geometry from the preferred one

multiplied with a bending constant κ^* .^[62,73]

$$F_{i,\text{bending}} = \frac{\kappa^*}{2} (P_{\text{microphase}} - P_0)^2 \quad (61)$$

with $P_{\text{microphase}} = (v/a \cdot l)$ and $P_0 = (v/a_0 \cdot l)$ denoting the effective packing parameter of a given microphase and the preferred, spontaneous one with v being the volume of the apolar moiety, a the area per extractant headgroup and l the mean surfactant chain length. The validity of this relation does *not* depend on the thickness of the layer to be bent. In the case of extractants, the bending modulus κ^* lies in the order of 1-2 kT per chain.^[226,227]

In a next step, the evolving structure is considered as built from cylindrical building blocks in dynamic equilibrium with endcaps and junctions as defects. Therefore, the standard reference potential of cylinders is defined as a reference state. As a result, the cost in free energy $\Delta\mu^0$ to transform cylinders (cyl) into endcaps (EC) or junctions (J) can be calculated from the differences in bending energy between each microphase of a certain aggregation number N_{agg} .

$$\mu_{i,\text{EC}}^0 - \mu_{i,\text{cyl}}^0 = \frac{\kappa^*}{2} \cdot \left[N_{\text{agg,EC}} (P_{\text{EC}} - P_0(x))^2 - N_{\text{agg,cyl}} (P_{\text{cyl}} - P_0(x))^2 \right] \quad (62)$$

$$\mu_{i,\text{J}}^0 - \mu_{i,\text{cyl}}^0 = \frac{\kappa^*}{2} \cdot \left[N_{\text{agg,J}} (P_{\text{J}} - P_0(x))^2 - N_{\text{agg,cyl}} (P_{\text{cyl}} - P_0(x))^2 \right] \quad (63)$$

The spontaneous packing parameter P_0 is varying with the relative uranyl content $x = [\text{uranyl}]/[\text{extractant}]$. Therefore, also the standard reference chemical potentials are dependent on the concentration of complexed uranyl in the organic phase. The uranyl content x varies from $x = 0$ (no uranyl ions in the organic phase) to $x = 0.45$, the approximate experimental stoichiometry of $[\text{Dialkylamide}]/[\text{UO}_2^{2+}] \approx 2.3$ ^[187,191]. At this value, the organic phase has reached the maximal possible concentration of uranyl.

The cost in free energy to convert a cylinder microphase into an endcap or respectively into junction unit gives the relative probability of occurrence of each microphase. Combination of equations (58) - (60) and (62) - (63) allows to calculate the relative concentration of extractants in each microphase.

$$\exp\left(\frac{\mu_{i,\text{endcap}}^0 - \mu_{i,\text{cylinder}}^0}{RT}\right) = \frac{c_{i,\text{cylinder}} \cdot \gamma_{i,\text{cylinder}}}{c_{i,\text{endcap}} \cdot \gamma_{i,\text{endcap}}} \quad (64)$$

$$\exp\left(\frac{\mu_{i,\text{junction}}^0 - \mu_{i,\text{cylinder}}^0}{RT}\right) = \frac{c_{i,\text{cylinder}} \cdot \gamma_{i,\text{cylinder}}}{c_{i,\text{junction}} \cdot \gamma_{i,\text{junction}}} \quad (65)$$

Since the micelles in the external pseudo-phase containing the monomers are considered to be a distinct “phase” dispersed in the “phase” containing four to hundred (N) molecules, the free energy of its formation corresponds to the assembly of N molecules. Therefore, the chemical potential of the individual molecules assembled in one pseudo-phase is the free energy of formation of the pseudo-phase divided by the number of molecules forming it. Therefore, the necessary ratio of activity coefficients γ_i can be estimated in a first approximation from the number of extractants per microphase N_{agg} as $\gamma_{i, \text{microphase}} \sim 1/N_{\text{agg, microphase}}$. The estimation of the aggregation numbers from the molar volumes are explained in the Annex, Chapter VII.7.

Respecting mass conservation, the total concentration of endcap, cylinder and junction units can be calculated from the relative concentrations $c_{\text{cyl}}/c_{\text{EC}}$ and $c_{\text{cyl}}/c_{\text{J}}$ and the total concentration of extractants c_{Ex} in solution. The total number of extractant molecules c_{Ex} is composed of the numbers of extractant N_{agg} per cylinder, endcaps and junctions:

$$N_{\text{agg,cyl}} \cdot c_{\text{cyl}} + N_{\text{agg,EC}} \cdot c_{\text{EC}} + N_{\text{agg,J}} \cdot c_{\text{J}} + (c_{\text{monomers}}) = c_{\text{Ex}} \quad (66)$$

$$c_{\text{cyl}} = \frac{c_{\text{Ex}}}{N_{\text{agg,cyl}} + \frac{N_{\text{agg,EC}}}{c_{\text{cyl}}/c_{\text{EC}}} + \frac{N_{\text{agg,J}}}{c_{\text{cyl}}/c_{\text{J}}}} \quad (67)$$

$$c_{\text{EC}} = \frac{c_{\text{cyl}}}{c_{\text{cyl}}/c_{\text{EC}}} \quad (68)$$

$$c_{\text{J}} = \frac{c_{\text{cyl}}}{c_{\text{cyl}}/c_{\text{J}}} \quad (69)$$

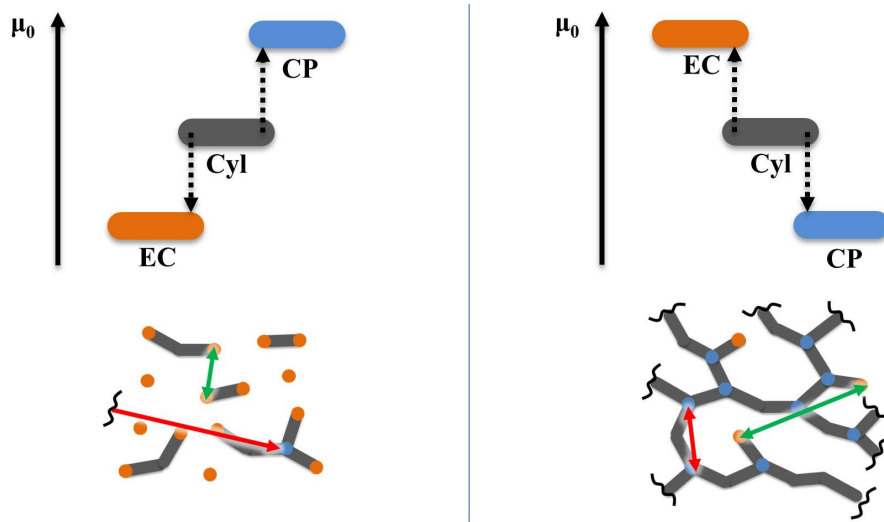


Figure 59. Schematic representation of the two extreme cases. **Left:** high concentration of endcaps, low concentration of junctions. **Right:** network formation due to high population of junction units and absence of endcaps. The corresponding standard reference potential of endcaps (orange), cylinders (grey) and junctions (blue) are represented above.

Consequently, if the standard reference chemical potential of endcaps is low, the resulting population of endcaps is high. If the standard reference chemical potential of endcaps is high, the formation of endcaps is unfavorable and the resulting concentration is expected to be low (*cf.* Figure 59.).

III.1.3 Modification for the presence of a second extractant

Keeping in mind the third objective of this work, to propose formulation approaches to solve this problem of viscosity increase, the presence of a second extractant should be included in the model. In presence of a second extractant, the spontaneous packing parameter $P_0(x)$ of equations (62) and (63) has to be replaced by a mixed spontaneous packing parameter $P_{\text{mix}}(x)$. In a first approximation, the value of the mixed spontaneous packing parameter is defined by the molar ratio between the two assuming ideal mixing.^[205]

Moreover, an entropic contribution $T\Delta S$ has to be added due to the possibility of permutations of extractant molecules at each microphase (*cf.* Eq. (72) and (74)).^[52] For the implementation of this contribution in the program interface, the gamma-function was used (*cf.* Chapter VII.7.2).

$$P_{\text{mix}}(x) = x_{\text{Ex1}} \cdot P_0(x)_{\text{Ex1}} + (1 - x_{\text{Ex1}}) \cdot P_0(x)_{\text{Ex2}} \quad (70)$$

$$\mu_{\text{EC}}^0 - \mu_{\text{cyl}}^0 = \frac{\kappa^*}{2} \cdot \left[N_{\text{agg,EC}} (P_{\text{EC}} - P_{\text{mix}}(x))^2 - N_{\text{agg,cyl}} (P_{\text{cyl}} - P_{\text{mix}}(x))^2 \right] - T\Delta S_{\text{EC}} \quad (71)$$

$$T\Delta S_{\text{EC}} = k_{\text{B}}T \cdot \left[\ln \frac{N_{\text{agg,EC}}!}{(x_{\text{Ex1}}N_{\text{agg,EC}})!(x_{\text{Ex2}}N_{\text{agg,EC}})!} - \ln \frac{N_{\text{agg,cyl}}!}{(x_{\text{Ex1}}N_{\text{agg,cyl}})!(x_{\text{Ex2}}N_{\text{agg,cyl}})!} \right] \quad (72)$$

$$\mu_{\text{J}}^0 - \mu_{\text{cyl}}^0 = \frac{\kappa^*}{2} \cdot \left[N_{\text{agg,J}} (P_{\text{J}} - P_{\text{mix}}(x))^2 - N_{\text{agg,cyl}} (P_{\text{cyl}} - P_{\text{mix}}(x))^2 \right] - T\Delta S_{\text{J}} \quad (73)$$

$$T\Delta S_{\text{J}} = k_{\text{B}}T \cdot \left[\ln \frac{N_{\text{agg,J}}!}{(x_{\text{Ex1}}N_{\text{agg,J}})!(x_{\text{Ex2}}N_{\text{agg,J}})!} - \ln \frac{N_{\text{agg,cyl}}!}{(x_{\text{Ex1}}N_{\text{agg,cyl}})!(x_{\text{Ex2}}N_{\text{agg,cyl}})!} \right] \quad (74)$$

III.1.4 Towards an intuition-driving image of the organic phase in 2D – Monte-Carlo-like simulation

In the previous subchapters, a minimal thermodynamic model was presented that allows to estimate the number concentration distribution of endcaps, cylinders and junctions for a given extractant and uranyl concentration. From these images, the evolving structure can be roughly imagined. However, a method is needed that allows to get a qualitative picture at the nanoscale. With that help, conclusions on the origin of the viscosity increase can be drawn, as well as a

method to solve the problem of viscosity-control.

The method of choice is a Monte-Carlo-like simulation that is based on the minimization of the frustration energy of each microphase. This approach is explained in the following text.

A simple way to do this is to transfer this problem into a 2-dimensional, hexagonal grid. A hexagonal grid was chosen because 6 neighbors are closer to nature than 8 neighbors in case of a square grid. The chosen grid possesses continuous boundary conditions. That means a hexagon at the end of the grid is (imaginary) the neighbor of the hexagon at the beginning of the grid in the same row/column. A single hexagon has approximately the size of one single microphase, *e.g.* two endcaps, one junction or one cylinder unit of the length of one uranyl-uranyl distance (*cf.* Annex, Chapter VII.7.1). In a first step, the hexagonal grid is filled randomly with colors, representing either diluent (white), endcap (orange), cylinder (grey) or junction (blue). The number distribution of these colors corresponds to the number distribution of microphases derived from the model.

In step two, a Monte-Carlo-like simulation is carried out. That means, the following steps are carried out one after another:

1. Two hexagons are picked randomly
2. The “frustration” of both hexagons is determined
3. These two hexagons are swapped and the resulting new “frustration” of these hexagons is determined
4. If the sum of frustration before the swap is higher than the sum of frustration after the swap, or equal, the swap is accepted. Otherwise the swap is undone.
5. Steps 1-4 are repeated, until no microphase/hexagon is frustrated any more or a minimum is reached

The “frustration” of each microphase is determined as follows. One can imagine them as elements with one (endcaps), two (cylinders) and three (junctions) open sides. These elements are non-frustrated when they are closed.

- An endcap is non-frustrated (frustration = 0), when only one further microphase is in the surrounding 6 hexagons. When there are more or less, the frustration is calculated by

$$F_{\text{frust}} = |N_{\text{EC}} + N_{\text{cyl}} + N_J - 1| \quad (75)$$

with N_{EC} , N_{cyl} and N_J being the number of direct adjacent endcaps, cylinders and branching points respectively.

An exemption is made for the possibility of bridging endcaps, that are expected to result in positive wetting energy and entropy gain by fluctuating uranyl ions. In that case, an endcap is allowed to exhibit two neighboring microphases.

- A cylinder is non-frustrated, when two further microphases adjoin. Furthermore, a steric requirement has to be fulfilled. We decided that at least one solvent unit has to separate the two microphases. Otherwise, the formation of triangles of three cylinder units would be promoted, which seems quite unlikely. If the cylinder has more or less neighbors, it is frustrated, and its frustration can be calculated via:

$$F_{frust} = |N_{EC} + N_{cyl} + N_J - 2| \quad (76)$$

- A junction has zero-frustration, when exactly three microphases are in the neighboring three hexagons. Moreover, also for junctions, steric conditions have to be fulfilled, leading to an 120° -angle between each microphase. We have considered, if a junction-junction interaction is favorable or not. We decided that this may be the case in our simplified simulation, especially at higher extractant and junction concentration. Making this interaction unfavorable did not lead to structures of low frustration. In addition, it is indicated in the literature that there is an attractive force between junctions that can lead to phase separation.^[144,228] This picture was recently completed with the proof of presence of nanocapillarity.^[148] Therefore, the frustration can be calculated in the following way. However, in the code (access described in Chapter VII.7.2), it is also indicated, how the change has to be altered to avoid junction-junction interactions.

$$F_{frust} = |N_{EC} + N_{cyl} + N_J - 3| \quad (77)$$

An overview of the main steps of the procedure as well as a table with the allowed structures is given in **Figure 60**. The energy and Monte-Carlo-like steps are decoupled. The energy already determines the relative numbers of endcaps, junctions and cylindrical segments. The 2 D lattice provides then structural parameters using neighbor information, but no energies.

The reason, why only a Monte-Carlo-like procedure and not a real Monte-Carlo simulation was chosen is the difficult estimation of frustration energy. A rough estimation of the frustration energy from the difference in interfacial tension between aqueous and organic phase shows that the order of magnitude of the frustration energy of one single microphase is significantly higher

than kT at room temperature ($\sim 4.1 \cdot 10^{-21}$ J):

$$\Delta F_{\text{frust}} \approx A \cdot \Delta\gamma \approx 1 \text{ nm}^2 \cdot 40 \frac{\text{mN}}{\text{m}} \approx 4 \cdot 10^{-20} \text{ J} \quad (78)$$

According to the Metropolis algorithm of simulated annealing commonly used for Monte-Carlo simulations^[229], the probability to accept an increase in frustration is proportional to $\exp\left(\frac{\Delta F}{kT}\right)$.

This value is expected to be very low. Therefore, the code could be simplified and swaps are only accepted if the frustration stays constant or decreases.

A detailed explanation of the principle and structure of the code as well as a description how to access the JavaScript Code can be found in Annex, Chapter VII.7.2.

Figure 61 shows an exemplary result of this simple simulation pointing out the three microphases in chemical equilibrium.

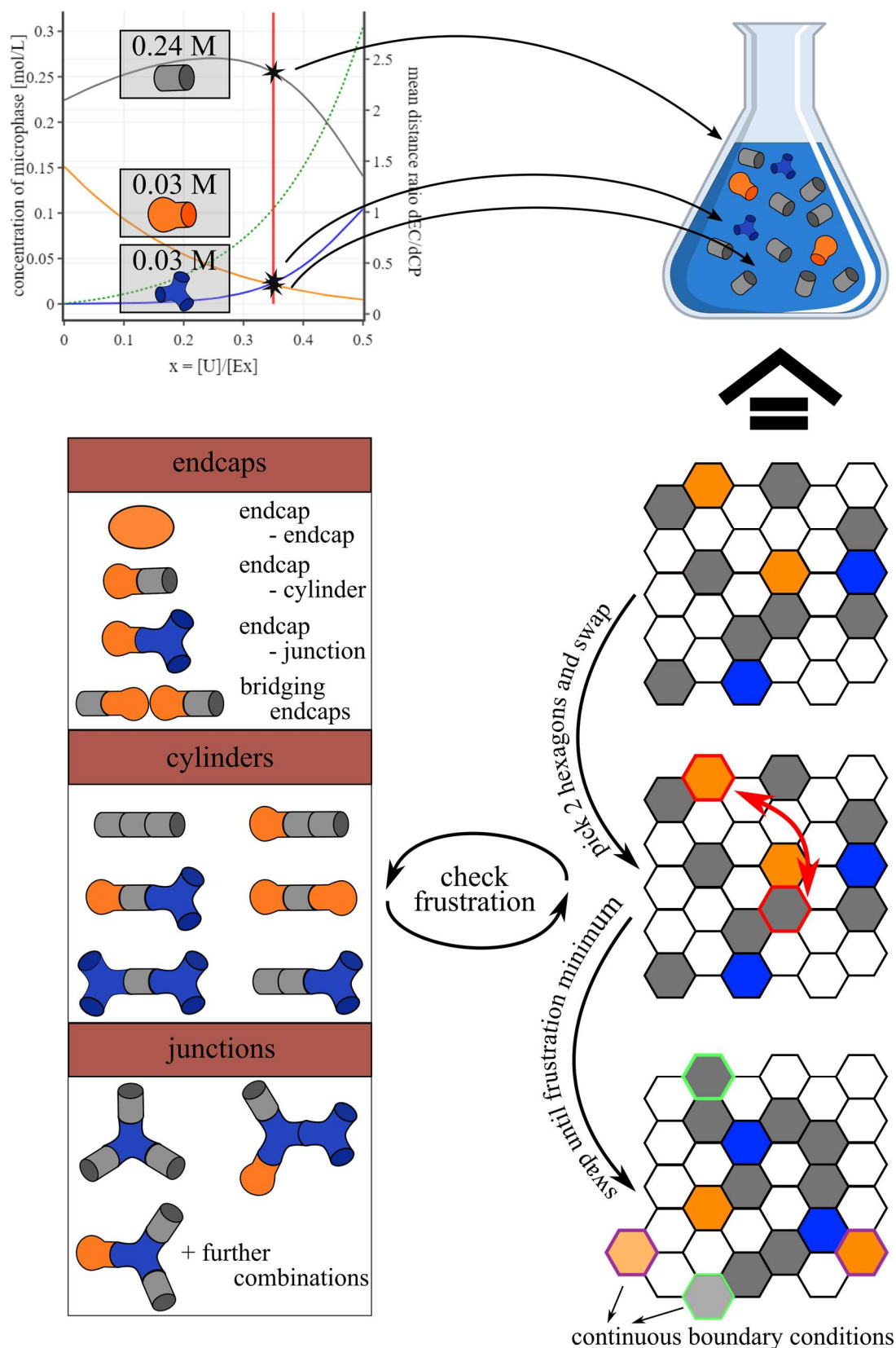


Figure 60. Scheme describing the Monte-Carlo-like simulation. The number concentration of each microphase derived from the chemical potential are transferred to a hexagon of a given size representing the distribution. After that, 2 hexagons are chosen and the frustration of the systems is compared before and after the swap. This step is repeated until a structure is found with a minimal frustration.

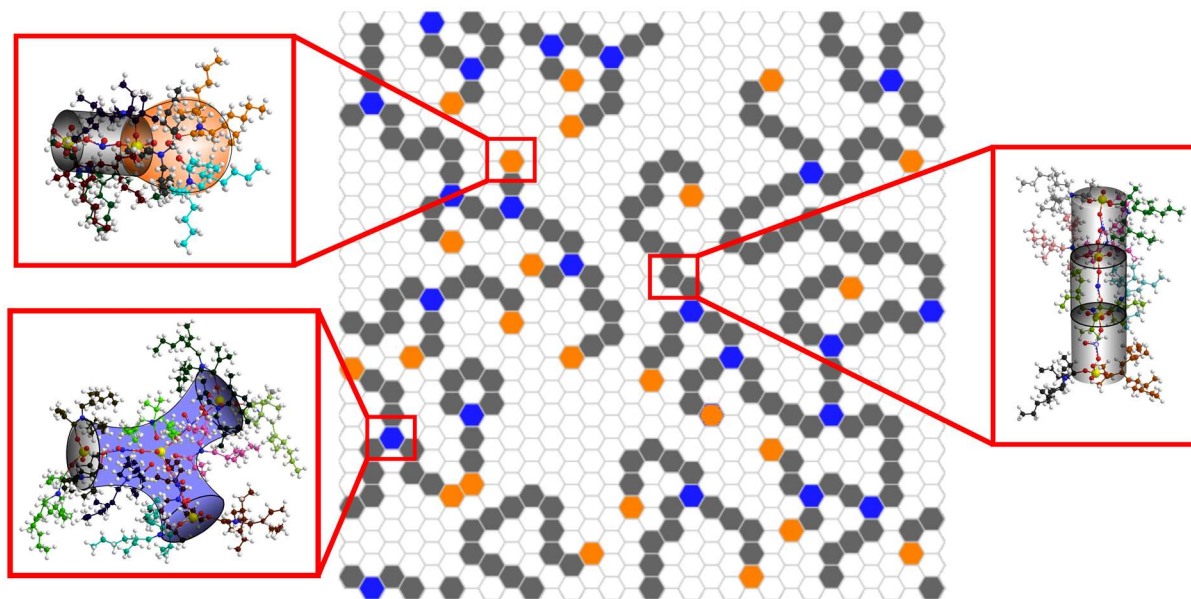


Figure 61. An exemplary result of the 2D simulation after minimization of the frustration energy.

III.1.5 Microphase equilibrium controlling the viscosity

The resulting intuition-driving picture of the organic phase in two dimensions (*cf.* **Figure 61**) gives a first idea of the origin of the viscosity increase. The more delicate point is now to transfer the evolution of the microphase distribution into a viscosity curve.

As was introduced in Chapter I.2.5, the theories of Lequeux, Cates and Khatory point out that the viscosity depends on different characteristic micellar lengths between endcaps and junction units (*cf.* equations (21), (24), (26)). It is difficult to obtain these lengths just from the microphase distribution without further information.

One way to do this, would be to analyze the 2-D image derived from the Monte-Carlo-like simulations of the organic phase to get characteristic lengths. This was implemented in the model (*cf.* Chapter III.2), but is also not very efficient due to the following reasons. First, the reduction from 3 dimensions to 2 dimensions is accompanied by several approximations and dimensional changes, resulting in lengths that are not representative any more for the three-dimensional case. Second, the calculations for a grid that is big enough to obtain a representative length distribution would take relatively long (about one day, with the existing code and on the personal computer). Since one image only represents the situation for one uranyl concentration, it would take weeks of calculation to obtain a semi-quantitative viscosity curve and even longer if statistical averaging is intended. Third, and more importantly (*cf.* Chapter I), viscosity is a macroscopic property that depends on the dynamical properties of the system. Since we do not have much information on the dynamic properties of this system, the

results would be only semi-quantitative from this investigation.

The most promising approach is to use directly the microphase distribution. The microphase distribution that is given by the evolution of the spontaneous packing parameter provides the number of endcaps, cylinders and junctions at a given metal concentration thereby defining the microstructure of the evolving living network. Based on this distribution we can now make the link to macroscopic properties of the system, in particular to viscosity. According to Cates, the following relationship for reptating chains can be applied.^[117]

$$\eta \sim L_{\text{eff}}^3 \quad (79)$$

where η is the zero-shear viscosity of an entangled solution of giant micelles and L is the mean contour length of the micelles. In the case of fast micellar breaking the scaling exponent is supposed to approach unity (*cf.* Chapter I.2.5). This is the case for some systems around the viscosity maximum.^[126] However, the calculated microphase distribution does not provide us with information about time scales and dynamic aspects of micellar breaking and recombination, and relaxation regimes of the system cannot be predicted. Therefore, we must rely primarily on geometrical aspects and length scales. Khatory *et al.* investigated the structure of entangled and branched wormlike micelles.^[142] Especially the presence of junctions required an evaluation of the contour length L (endcap to endcap distance in linear micelles without junctions) as an effective length L_{eff} , which was defined as the “*harmonic mean between the average distance from one point along the micelle to the first cross-link and the average distance from that point to the first endcap, or equivalently, the ratio of the total length over the concentration of endcaps plus twice that of connections*”^[142]. Especially the second part is interesting for the present purpose. The total length per volume of the structure-forming extractants is given by the sum of the single lengths of the microphases multiplied with their corresponding concentration. The single length of a microphase is determined by the length of the chosen hexagon l_{hexagon} (*cf.* Annex, Chapter VII.7.1), whereby one endcap (half a sphere) only counts as half a hexagon. Applying this method of estimation to the distribution of microstructures resulting from frustration differences between pseudo-phases, the averaged total length L_{eff} per volume of the structure forming surfactants is given by the sum of the respective lengths l_i of the single micro-phase units multiplied with their corresponding concentration.

$$L_{\text{eff}} = \frac{(c_{\text{EC}}/2 + c_{\text{cyl}} + c_{\text{J}}) \cdot l_{\text{hexagon}}}{c_{\text{EC}} + 2c_{\text{J}}} \quad (80)$$

with c_i being the concentration of the corresponding microphase.

This assumption is quite probable in that case, since the uranyl-ligand interaction is expected to be strong and this criterion is approximately true up to the viscosity maximum^[126], the scission-breakage mechanism can be neglected in the first order and would not change qualitative trends.

This proportionality is referring to the relative viscosity increase. Therefore, this L^3 factor has to be scaled with a scaling factor that is considered to be independent of uranyl and extractant concentration, as well as with the concentration dependent zero viscosity of the organic solvent composed of the extractant diluted in the diluent with viscosity η_{dil} . At a first approximation, this viscosity is dependent on the volume fraction of the extractant ϕ_{ext} according to Einstein's formula^[26]:

$$\eta_0 \approx A \cdot \eta_{\text{dil}}(1 + 2.5\phi_{\text{ext}}) \quad (81)$$

with A being a scaling factor. In this example, this scaling factor has chosen to be 1/12 [mPa·s] to fit the experimental viscosity curve. However, this value could also be measured or calculated in a more detailed way as indicated in Chapter I and in ^[26], in order to obtain better results.

A graphical overview on the main steps of the model is given in **Figure 62**.

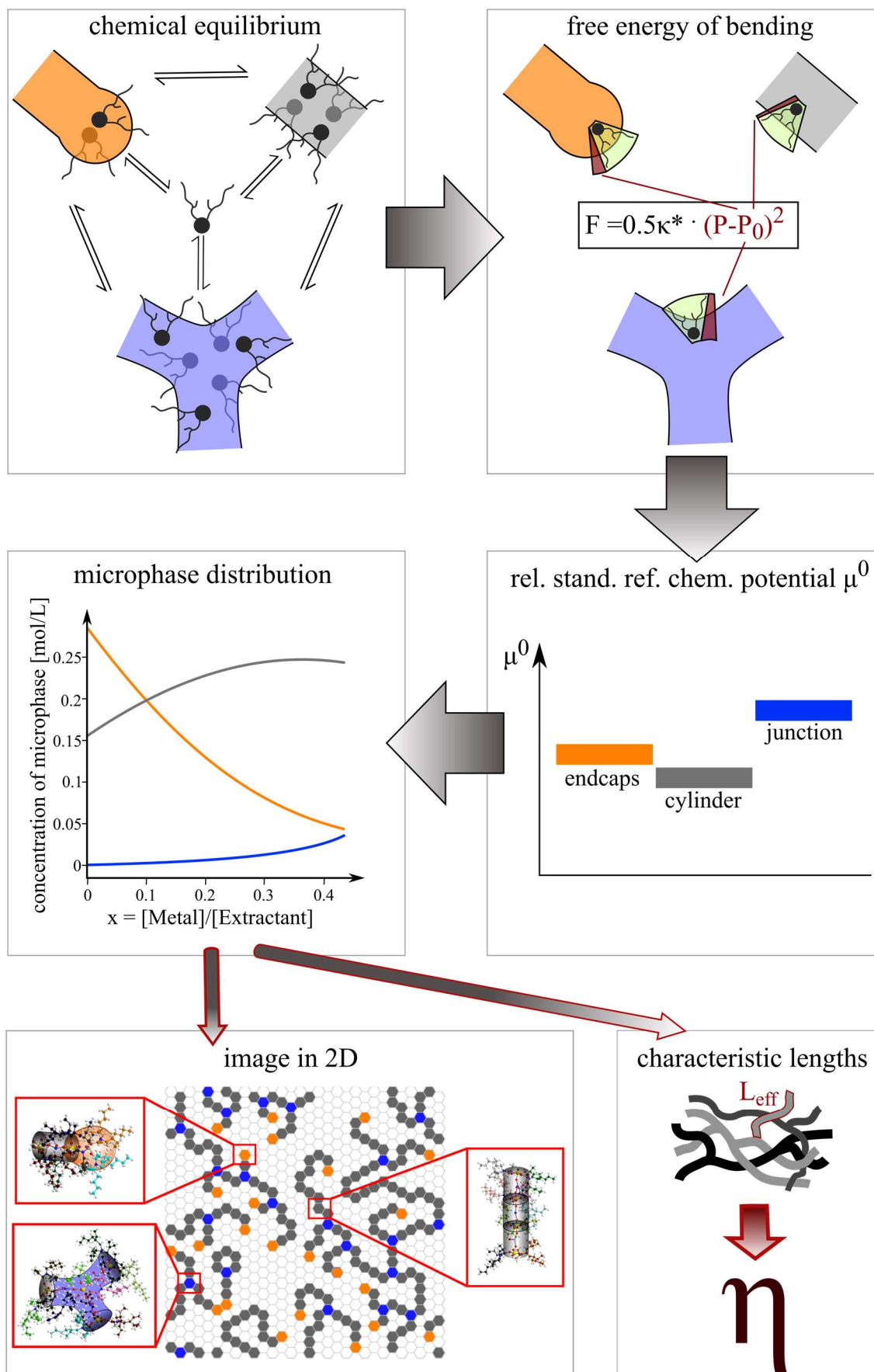


Figure 62. Schematic overview of the main steps of the model.

III.2 Implementation in a user-friendly interface

The main goal of this work is to understand the origin and the structures leading to this exponential viscosity increase. Therefore, the main terms and equations were implemented in a user-friendly interface that allows to vary different parameters easily. It has to be kept in mind that this model is a consciously simple model, whose main goal it is not to provide analytical and quantitative results. The goal is rather to develop a small tool, that helps to explain and understand the viscosity increase of monoamides and other physically gelling systems as well as to predict the response of the system to parameter changes. The possibility to “play” with the program by yourself is a good way to understand the origin of the resulting structures. This understanding will help to propose knowledge-based formulations to solve the problem. Therefore, I would recommend to everyone studying this work to use the program that can be executed online via the following address

www.vyrix.de/sim

or the following QR code:



Figure 63. QR code to access the model interface online

That is why JavaScript was chosen as the programming language, allowing both the fast calculation and presentation of the model results as well as the implementation in a HTML-based document which can be executed by every interested person without the need of an additional program.

The rough structure of the program is explained in the following. Detailed information on the calculations and on the programming are given in the Annex, Chapter VII.7. The how to access the complete code including explanatory comments can be found in the Annex, Chapter VII.7.2.

The interface of the program is shown in **Figure 64**. The general system (organic/aqueous phase) or the menu for a Monte-Carlo-like simulation can be chosen via the top line by clicking on one of the colored tabs.

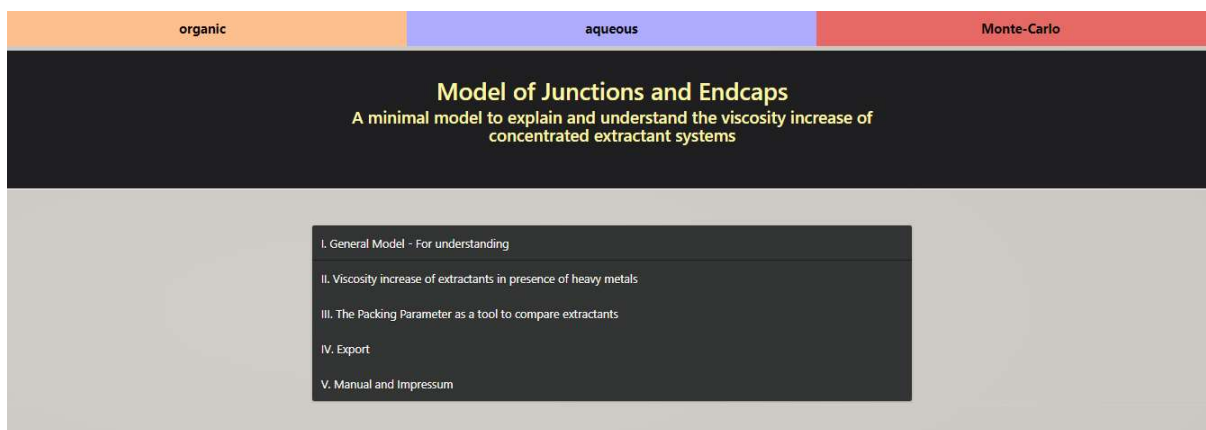


Figure 64. Screenshot of the model-interface. In the top line, the general system (organic/ aqueous) or the menu for the Monte-Carlo-like simulation can be chosen. By clicking on one of the titles (in black), an accordion opens to carry out the corresponding simulation.

After that, one can choose what one wants to do. By clicking on one of the titles, an accordion opens. Some accordions are described in detail in the following chapters. A short overview is given in the following:

Organic:

I. General Model – for understanding

This accordion was mainly created to understand the model. The difference in standard reference chemical potential, the corresponding microphase distribution as well as the resulting estimated viscosity can be calculated depending on different parameters. Furthermore, a metal concentration can be chosen in order to carry out a Monte-Carlo-like simulation at this composition.

II. Viscosity increase of extractant solutions in the presence of heavy metals

This accordion is more related to the experimental observations. Experimental viscosity curves can be chosen via a pop-up menu. The difference in standard reference chemical potential, the corresponding microphase distribution as well as the resulting estimated viscosity can be adjusted and compared to the experimental values. Also, in this accordion, a uranyl content x can be chosen in order to carry out a Monte-Carlo-like simulation at this composition. Effects such as variation of the diluent with different penetration power or changing the extractant molecule can be simulated.

III. The spontaneous packing parameter as a tool to compare amphiphiles

This section allows to calculate the spontaneous packing parameter depending on the values of v , a_0 and l as well as to calculate the apolar volume and chain length of amphiphiles. Furthermore, the schematic geometry of an amphiphile with a certain P_0 is plotted as a truncated cone with a ground area a_0 , a length l and a volume v . The plot is updated each time a slider is moved (cf. **Figure 65**).



Figure 65. Screenshot of the interface of Accordion III showing the schematic representation of the packing geometry.

The representation of P_0 as a truncated cone is calculated as follows. The volume of a truncated cone is given by

$$V_{tr.cone} = \frac{1}{3}\pi(r_1^2 + r_1r_2 + r_2^2)h \quad (82)$$

with r_1 and r_2 being the radii of the lower and upper circular areas and h the height of the truncated cone.

The radius r_1 of the lower (polar) circular area is given as

$$r_1 = \sqrt{\frac{a_0}{\pi}} \quad (83)$$

with a_0 denoting the area per headgroup used in the equation for the spontaneous packing parameter $P_0 = v/(a_0 \cdot l)$. Solving the equation for the volume for r_2 results in

$$r_2 = \frac{1}{2} \left[\frac{\sqrt{\frac{3}{\pi}} \cdot \sqrt{-h(\pi r_1^2 h - 4V_{tr.cone})}}{h} - r_1 \right] \quad (84)$$

Approximation of the height of the truncated cone with the chain length l allows to calculate the radii r_1 and r_2 of the circular areas that form the truncated cone. The

amphiphile shape can then be displayed in a next step by plotting the mesh formed by these two circles in a distance l .

Furthermore, the apolar volume as well as the chain length of an amphiphile can also be estimated by the program by using Tanford's formula^[72] and the table of Fedors^[206].

IV. Export

This accordion allows to export the created images as well as all relevant parameters and vectors of this tab.

V. Manual

In this section, the accordions as well as the parameters that can be varied are shortly described.

Aqueous:

VI. Anionic Surfactants in the presence of NaCl and Fragrances

Under this section, the viscosity curve of the anionic surfactant SLES with increasing NaCl concentration as well as the influence of model fragrances can be simulated.

VII. Anionic Surfactants in the presence of different salts

In this accordion, the influence of different salts on the viscosity curve of SLES can be related to the Collins principle of matching affinities.

VIII. Two homologous series of solutes

In this simulation, the influence of further model fragrances can be investigated. These model fragrances represent two homologous series of molecules, in order to investigate the effect of the apolar part or the logP value, respectively.

IX. Relative standard reference chemical potential and choice for Monte-Carlo-like simulation

Under this section, the relative distribution of the corresponding standard reference chemical potentials dependent on the salt concentration can be investigated. Moreover, a certain salt content can be chosen for a Monte-Carlo-like simulation under section XII.

X. Export

This accordion allows to export the created images as well as all relevant parameters and vectors of this tab.

XI. Manual

In this section, the accordions as well as the parameters that can be varied are shortly described.

Monte-Carlo:

XII. Monte-Carlo-like Simulation

This section allows to execute a Monte-Carlo-like simulation in order to obtain a representative image of the microstructure in 2D. The input concentration of endcaps, cylinders and junctions as well as the volume fraction of extractant can be either taken from Accordion I, II and IX or adjusted manually.

XIII. MC-Analysis

The resulting image of the simulation can be analyzed under this section. The distribution of the longest chains as well as the distribution of the single segments is displayed as well as the mean values.

XIV. Export

This accordion allows to export the created images as well as all relevant parameters and vectors of this tab.

XV. Manual

In this section, the accordions as well as the parameters that can be varied are shortly described.

In most of the accordions, the input values can be chosen via sliders. The results are recalculated and replotted each time one of the sliders moves, so that the investigation of the influence of one specific parameter is particularly easy.

In the following, general results of the model regarding the organic phase are presented.

III.3 General results of the model

The following text is mainly based on the first accordion ‘I. General Model – for understanding’ as well as the tab ‘XII. Monte-Carlo-like -Simulation’. The goal of the following sections is to describe the qualitative tendencies of the model in order to demonstrate with which parameters one could play in order to control the viscosity of such systems. Therefore, the accordion was implemented in a simplified manner. In the following subchapter, this accordion and its functions are presented more in detail. After that, some of the parameters are varied and the consequences demonstrated. In order to follow the discussion, the reader can look at the figures, but is also invited to use the slider oneself.

III.3.1 Presentation of Accordion I: ‘General model – for understanding’

This accordion was created to explain the model and to investigate the influence of the different input parameters. For this calculation, the extractant-specific parameters such as the density, molar volume and molar mass were taken from the extractant DEHiBA.

The following parameters can be adjusted by sliders:

- The initial packing parameter P_{init} represents the spontaneous packing parameter in absence of uranyl.
- The **metal response** defines the change in packing parameter from $x = 0$ to $x = 0.43$, therefore also the minimal spontaneous packing parameter P_{min} at maximal loading of the organic phase. In order to facilitate this investigation, it is assumed in this calculation that the spontaneous packing parameter P_0 varies linearly from P_{init} to P_{min} due to uranyl addition.
- The values P_{Ex2} and x_{Ex2} are only relevant if a second extractant is present. In that case, P_{Ex2} represents the initial packing parameter of Extractant 2 and x_{Ex2} describes the mole ratio between Extractant 1 and Extractant 2. By default, the value of x_{Ex2} is set to 0, indicating that only Extractant 1 is present in the organic phase.
- The slider value of c_{Ex} represents the total extractant concentration in mol/L. In case of $x_{\text{Ex2}} = 0$, the value corresponds to the concentration of Extractant 1
- κ^* represents the value of the bending constant in kT used in equation (61). For extractants, its value lies between 1-2 kT per extractant chain.^[52,80,230,231]
- With the slider for $x = [\text{U}]/[\text{Ex}]$ one can choose the uranyl content, at which the relative

standard reference potential for each microphase is displayed. By clicking on the button ‘Choose for MC’, one can transfer the resulting microphase distribution at position x to Accordion XII and perform a Monte-Carlo-like simulation.

A screenshot of the interface of Accordion I is shown in **Figure 66**. The two plot windows on top of the interface show the evolution of the calculated microphase distribution of endcaps (orange), junctions (blue) and cylinders (grey) as well as the estimated resulting viscosity curve (green dotted). On the right, the corresponding evolution of the standard reference potential is displayed. Below, a certain relative uranyl concentration can be chosen. The corresponding relative standard reference chemical potentials are displayed. The resulting microphase distribution at this position can be represented in two dimensions by performing a Monte-Carlo-like simulation.

For this purpose, Accordion XII has to be opened. A screenshot of this accordion is represented in **Figure 67**.

In the following subchapters, different input parameters are varied in order to demonstrate the respective influence.

I. General Model - For understanding

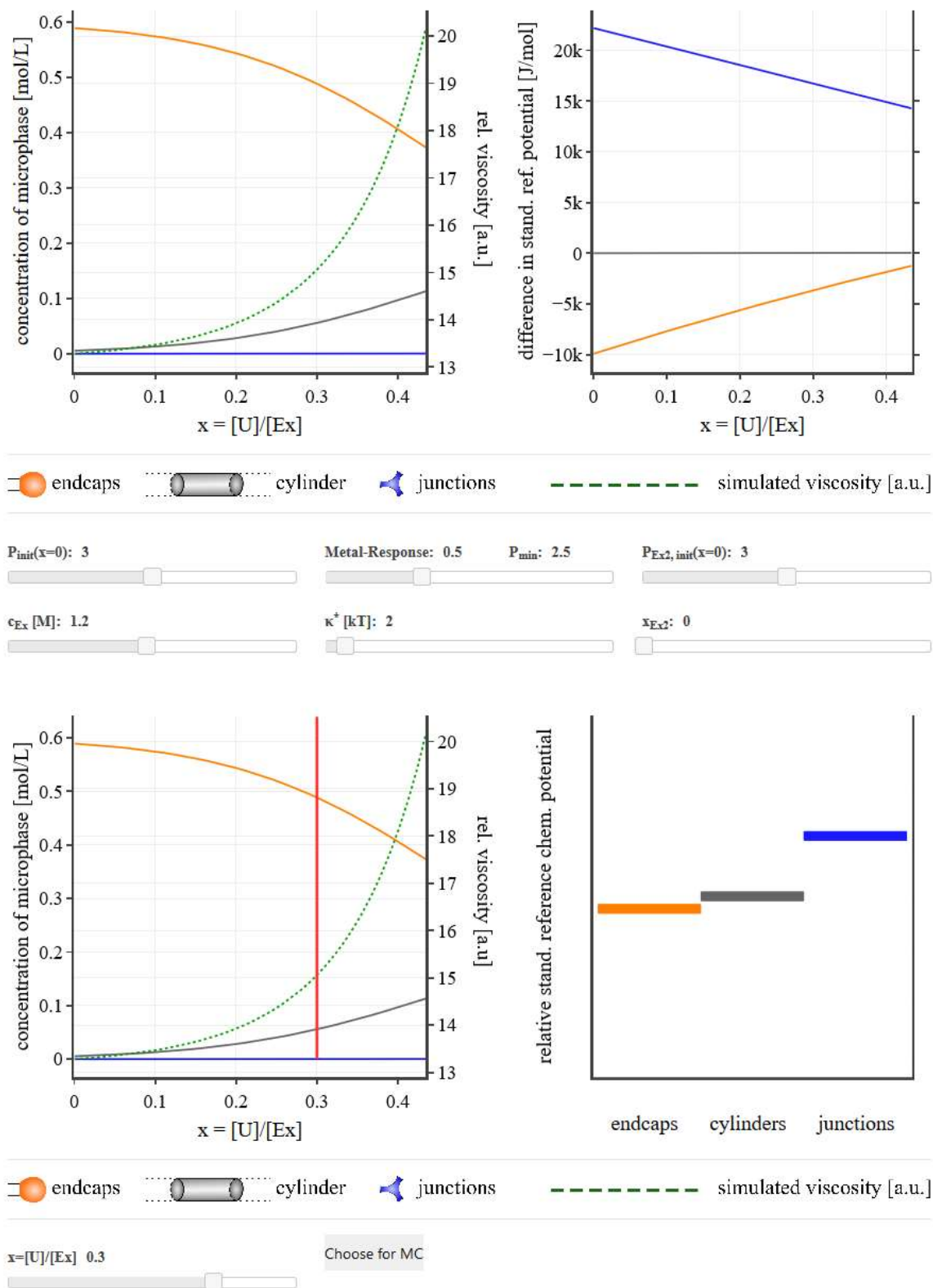


Figure 66. Screenshot of the interface of Accordion I. The input parameters can be chosen via sliders, the microphase distribution and the corresponding standard reference chemical potentials are recalculated and updated each time a slider moves.

XII. Monte-Carlo-like Simulation

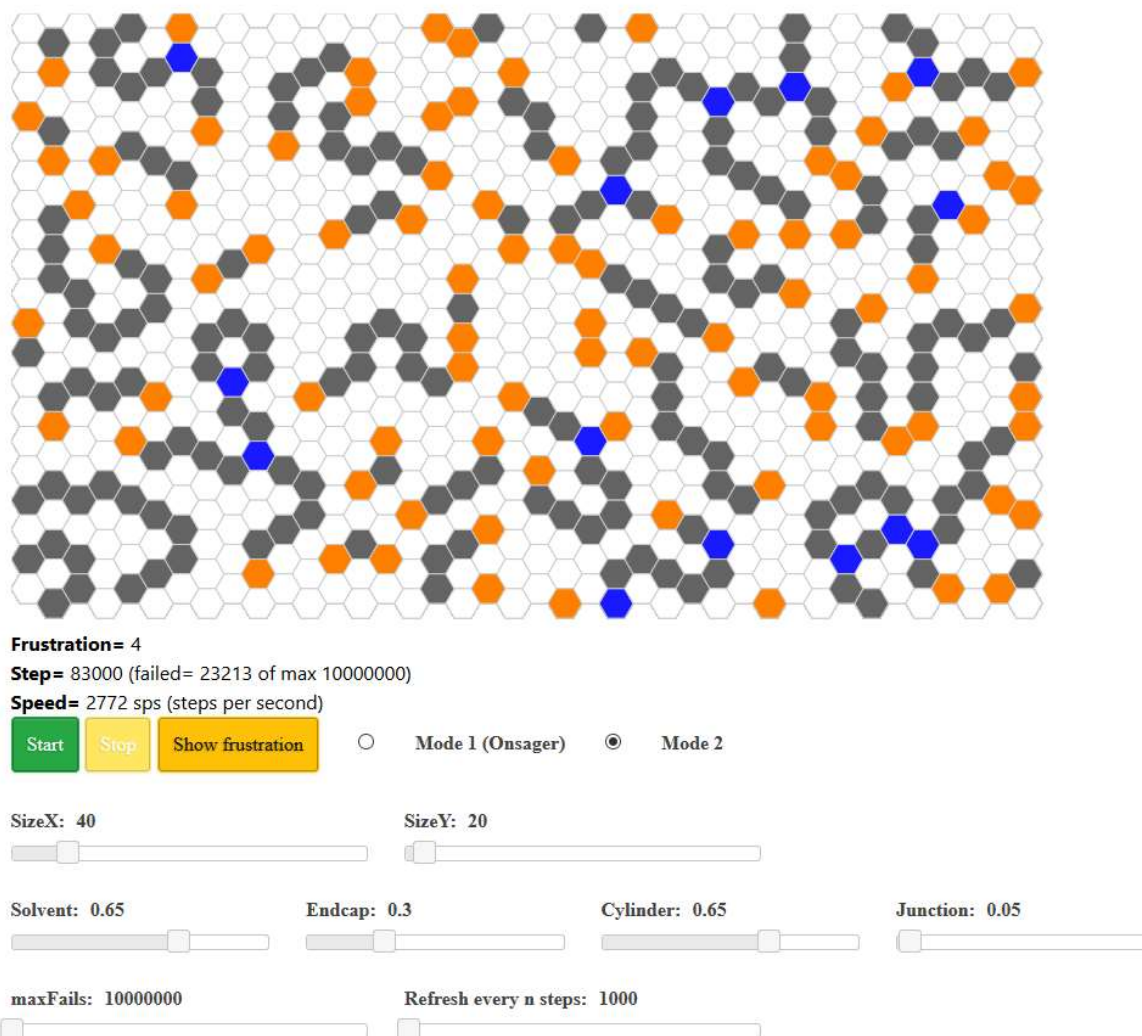


Figure 67. Screenshot of the interface of Accordion XII - Monte-Carlo-like simulation. The input parameters such as the volume fraction of diluent, as well as the concentration of the microphases endcap, cylinder and junction can be either taken from the calculated microphase distributions or chosen via sliders. Furthermore, the size of the hexagonal grid can be adjusted by 'SizeX' and 'SizeY', as well as the number of 'maximal fails', before the simulation is terminated. The slider 'Refresh every n steps' determines the frequency of image updates. The simulation can be started and stopped by the buttons 'Start' and 'Stop' as well as in case of a still frustrated microstructure, the frustration can be highlighted. The user can choose between two modes: Mode 1, which is mainly introduced for very high amphiphile concentration ($\phi > 0.55$) and where the total frustration is minimized based on a minimization of the number of frustrated microphases and therefore facilitates coalescence of microphases. Mode 2, which is recommended for most of the simulations, minimizes the total frustration energy.

III.3.2 Variation of the spontaneous packing parameter

In the first exemplary calculation, three different extractant molecules that have a certain spontaneous packing parameter P_{init} without the presence of uranyl are investigated. It is assumed that the spontaneous packing parameter changes for each of the molecules by a constant value of 0.7 from $x = 0$ to $x = 0.42$, the value of maximal loading of the organic phase. The total extractant concentration was chosen to be 1.2 M. That value is consciously chosen to

be less than that of most experimental investigations ($c = 1.5$ M), in order to take into account a certain concentration of mono- and dimeric extractant aggregates, that do not strongly contribute to the viscosity increase as well as in order keep a better overview in the Monte-Carlo-like simulation. The bending constant was set to $2 kT$, a common value for extractant molecules.^[52] The resulting evolution of the microphase distribution and the corresponding differences in standard reference chemical potential respective to cylinders (cf. equations (62) and (63)) are shown in **Figure 68**.

For each initial packing parameter, the concentration of endcaps decreases with increasing uranyl content, as well as the concentration of cylinder units. The concentration of junction units also increases, but stays low for realistic values of initial packing parameter P_{init} and metal response.

For a highly curved extractant ($P_{\text{init}} = 3.5$), endcaps always stay the dominant species over the whole uranyl range. The corresponding standard reference chemical potential is always lower than the one of cylinders and junctions. Consequently, the predominant structure are spherical aggregates formed by two endcaps (cf. **Figure 69**). The resulting calculated viscosity is consequently expected to be low.

When the chosen extractant is less curved ($P_{\text{init}} = 3.0$), the concentration of endcaps significantly decreases with uranyl concentration. Above a certain uranyl content, the standard reference chemical potential of endcaps becomes higher than that of cylinder units, and a sphere-to-cylinder transition can be observed. The predominance of more elongated aggregates is also visible in the corresponding two-dimensional image in **Figure 69**. Consequently, the viscosity starts to increase slightly.

For a very low curved extractant ($P_{\text{init}} = 2.6$), additionally to the sphere-to-cylinder transition, first branching of the elongated chains can be observed. As can be seen, the viscosity drastically increases. The number concentration of junction points is not yet enough to induce a decrease in viscosity.

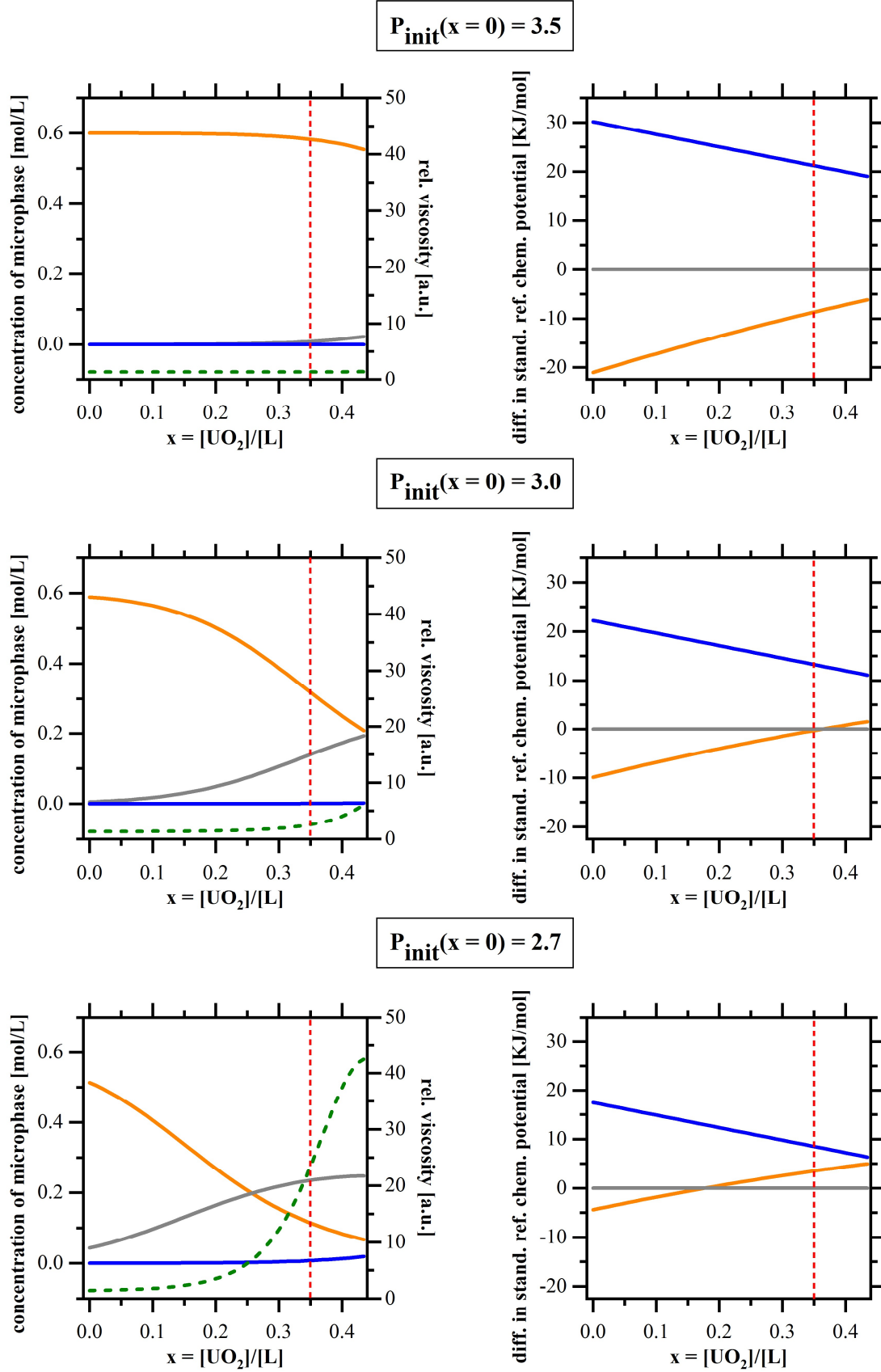


Figure 68. Calculated microphase distribution of endcaps (orange), cylinders (grey) and junctions (blue) as well as the corresponding differences in standard reference chemical potential respective to cylinders dependent on the initial spontaneous packing parameter P_{init} and the uranyl content x . The calculated viscosity curve is shown in as dashed green line. Metal response was set to 0.7, k^* to 2 kT and the total extractant concentration is 1.2 M. The position of the Monte-Carlo-like simulation shown in **Figure 69** is indicated by a red dashed line.

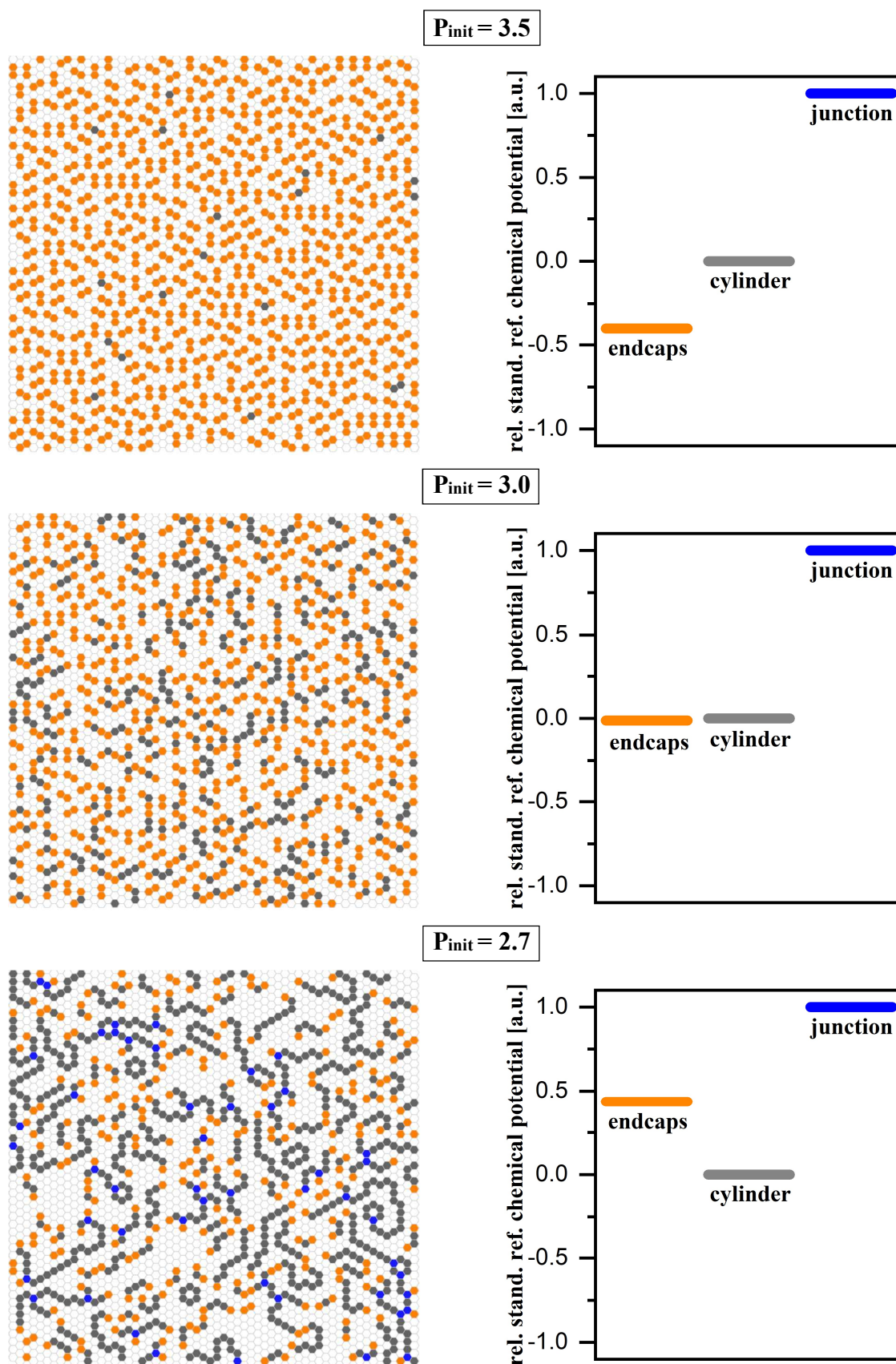


Figure 69. Two-dimensional image of the organic phase and rel. standard reference chemical potential at same uranyl content with different initial spontaneous packing parameters P_{init} . The structural composition and the corresponding microphase distribution are shown in **Figure 68**.

III.3.3 Addition of a second extractant

In a second investigation, the less curved extractant ($P_{\text{init}} = 2.6$) is stepwise replaced by a second, more curved extractant ($P_{\text{init}} = 3.2$). The other parameters stay the same as described in the subchapter before. The evolution of the microphase distribution as well as the corresponding differences in standard reference chemical potential respective to cylinder units are shown in **Figure 71**. Without the presence of a second extractant, the number concentration of endcaps decreases significantly with uranyl addition and at approximately $x_{\text{Ex2}} = 0.25$, cylinders become the dominant microphase. The viscosity increases drastically.

Addition of a second, more curved extractant, leads to a stepwise increase of the mixed spontaneous packing parameter (*cf.* equation (70)). The decrease in endcap concentration becomes less pronounced, a sphere-to-cylinder can be avoided. Consequently, the resulting viscosity is reduced.

Further, there seems to be a slight minimum in calculated viscosity for a mol ratio of approximately $x_{\text{Ex2}} = 0.8$. The calculated viscosity is lower in the range of $x_{\text{Ex2}} = 0.6-0.8$, demonstrating that the entropical term cannot be neglected. The entropic contribution due to the possibility of permutation leads to a higher concentration of endcaps. A similar effect is observed in the field of extraction. The distribution coefficient of a mixture of two extractants can be higher than the sum of distribution coefficients of the two extractants separately. This effect is called synergism (*cf.* Chapter I.2.4.2).^[52]

This insight is also important for Chapter IV, where the solution to the viscosity problem is presented. The knowledge that mixing two extractants may have two positive effects could help to develop formulation techniques. By the addition of a more curved extractant, first, the mean effective packing parameter is increased. Second, an entropical contribution is created that decreases the endcap energy. Both effects lead to a higher concentration of endcaps, thus a decrease in viscosity.

One could also imagine the effect of the addition of the higher curved extractant as follows. Before addition, a network of cylinder-shaped and saddle-like microphases is formed. The driving force is to minimize the frustration of the extractant and to avoid the formation of endcaps of high energy. The addition a second extractant that favors endcaps, changes the situation. The network is disintegrating stepwise. The first extractant stays in its favored tube-like geometry. Endcaps are formed and stabilized by the second extractant (*cf.* **Figure 70**).

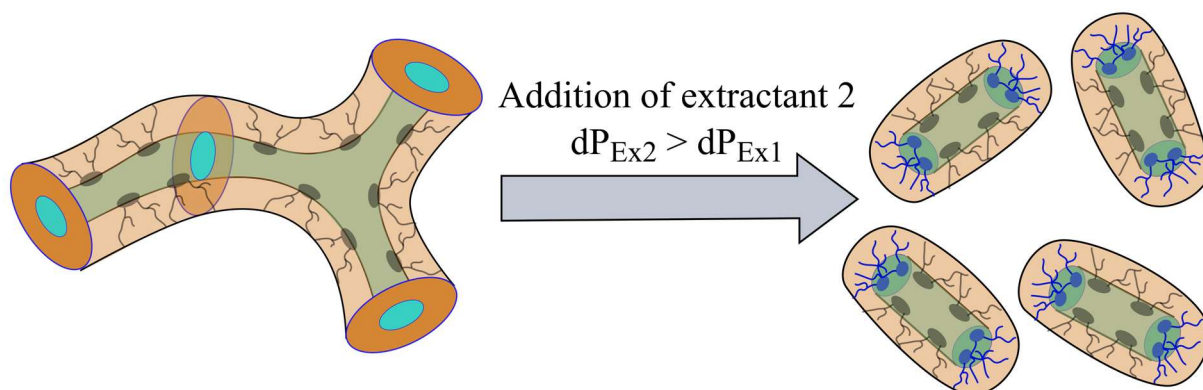


Figure 70. Schematic representation of the effect of addition of a more curved extractant

It is not compulsory that the second molecule with the packing parameter dP_{Ex2} is an extractant. It is also thinkable to add so-called “lipotropes”^[163] – short-chain alcohols – or other amphiphilic molecules. These will also have an influence on the mixed spontaneous packing parameter and create entropic effects.

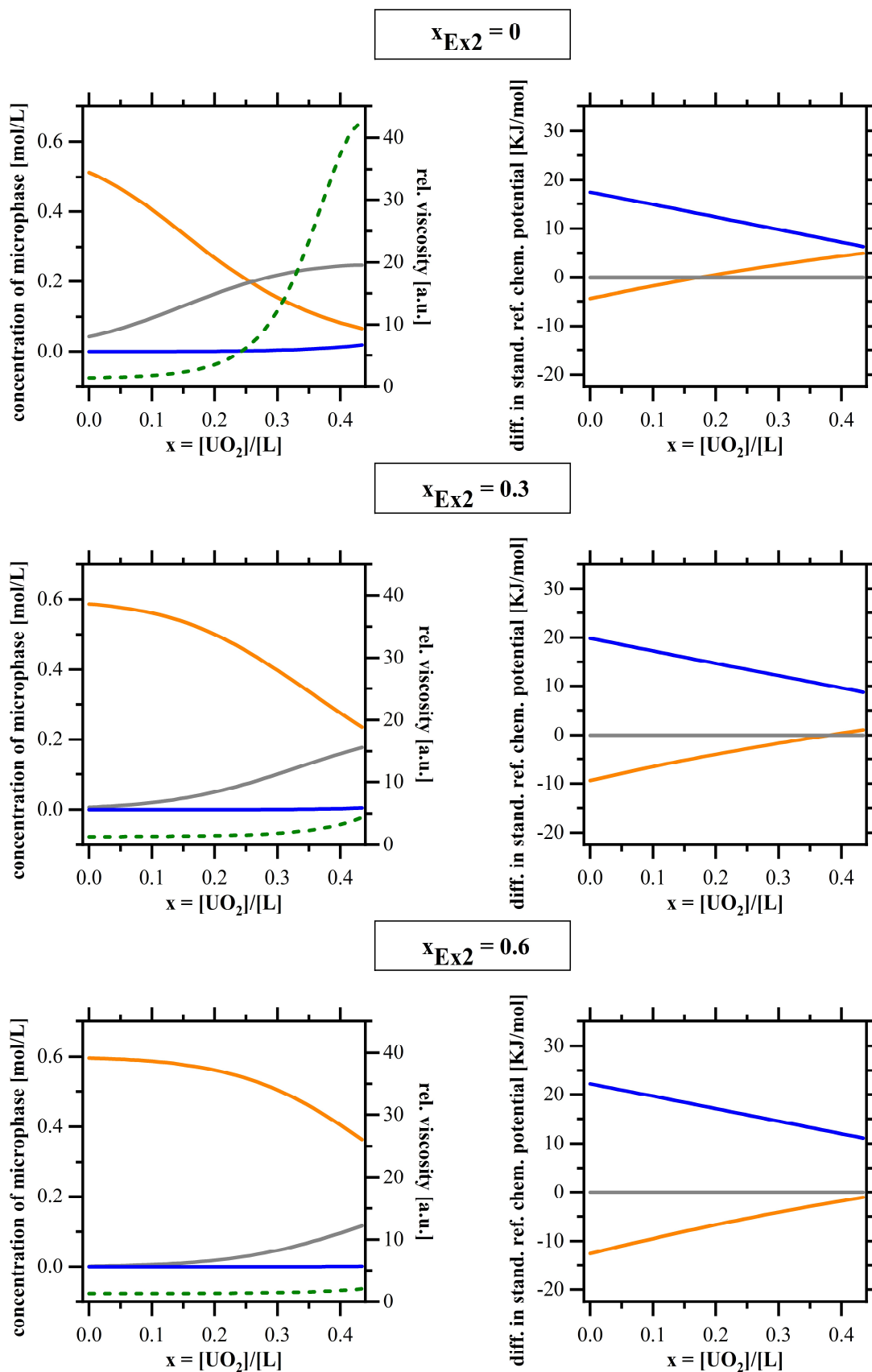


Figure 71. Calculated microphase distribution of endcaps (orange), cylinders (grey) and junctions (blue) as well as the corresponding standard reference chemical potential dependent on the mol ratio between an extractant 1 ($P_{init} = 2.7$) and an extractant 2 ($P_{init} = 3.2$). The calculated viscosity curve is shown in as dashed green line. Metal response was set to 0.7, κ^* to 2 kT and the total extractant concentration is 1.2 M.

III.3.4 Metal response

In this demonstration, the influence of the extracted metal ion on the spontaneous packing parameter is modeled. This effect is determined by the size and charge of the extracted ion. The larger the extracted ion, the larger will be its effect on the area per extractant that is used to calculate the spontaneous packing parameter. Complexed metal ions and the co-extracted counterions increase the polar core and the size of the radii of the resulting aggregates. That leads to a decrease in curvature and consequently to a decrease in packing parameter.

In the following investigation, an extractant with an initial spontaneous packing parameter $P_{\text{init}} = 3$ is considered extracting various ions and counterions that have a different effect on the minimal spontaneous packing parameter at maximal loading of the organic phase. This maximal increase from $x = 0$ to maximal loading is called the “*metal response*” in the following. The microphase distribution and the two-dimensional image of the Monte-Carlo-like simulation is shown in **Figure 71** and **Figure 72**.

First, a small metal response of 0.4 is considered. The spontaneous packing parameter does not change much with uranyl content. Consequently, endcaps are always the predominant microphase and even at uranyl content of $x = 0.35$, as can be seen in the simulation. The resulting viscosity will not increase much.

When the metal response is increased to higher values, a sphere-to-rod transition can be observed. The viscosity increase becomes more pronounced. For a case that the spontaneous packing parameter changes by a value of 1.2, a sphere-to-rod transition already occurs at half maximum loading of the organic phase ($x = 0.25$) and the presence of junctions becomes more important. In this example (metal response = 1.2), close to maximal uranyl loading, the number of junctions is even high enough to create a decrease in viscosity due to the additional relaxation mechanism of gliding connection points that is now possible.

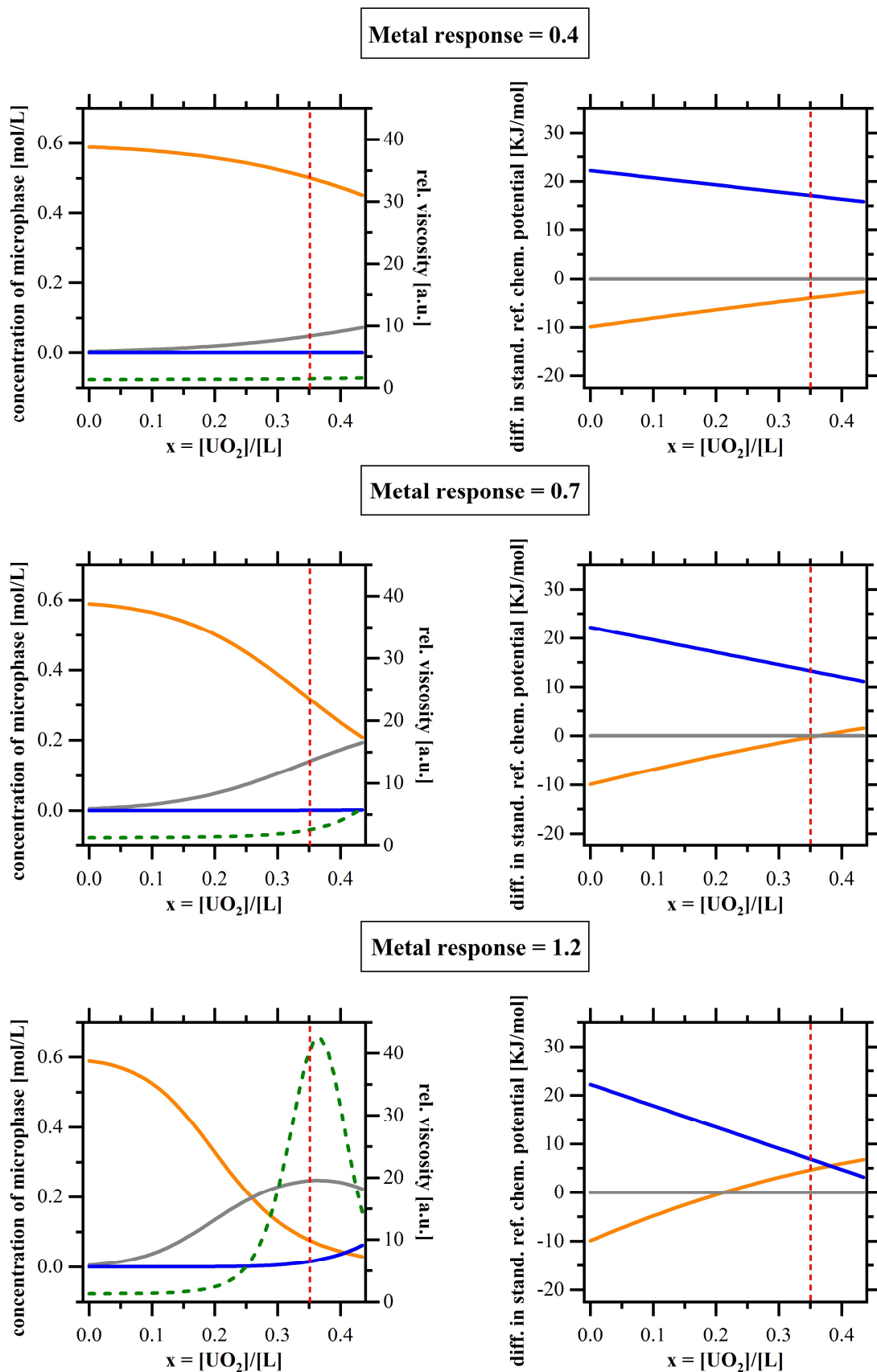


Figure 72. Calculated microphase distribution of endcaps (orange), cylinders (grey) and junctions (blue) as well as the corresponding standard reference chemical potential mol ratio dependent on the metal response on an extractant 1 with $P_{\text{init}} = 3$. The calculated viscosity curve is shown in as dashed green line. κ^* was set to $2 kT$ and the total extractant concentration is $1.2 M$.

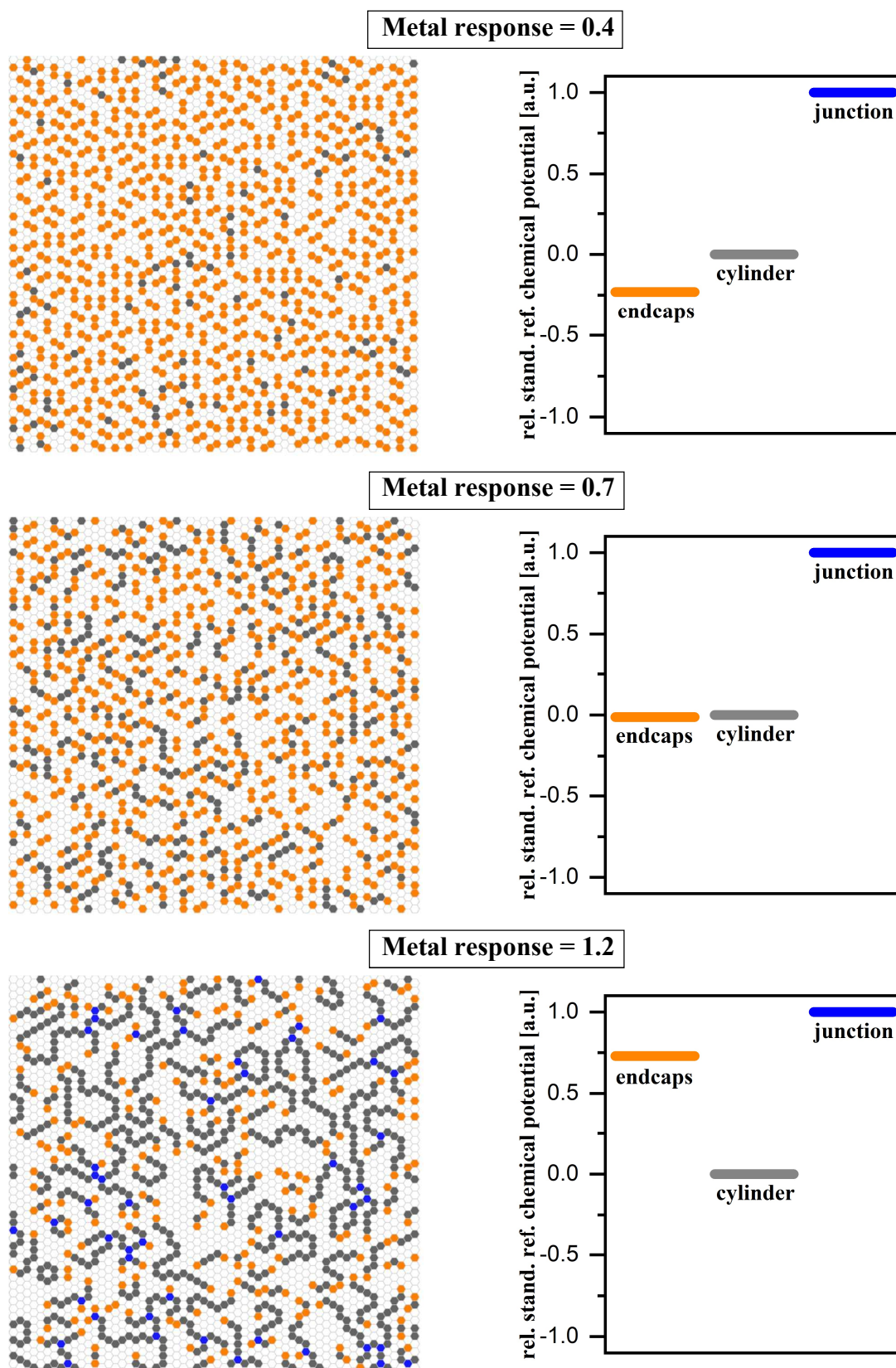


Figure 73. Two-dimensional image of the organic phase and rel. standard reference chemical potential of the same initial spontaneous packing parameters P_{init} with different metal response. The structural composition and the corresponding microphase distribution are shown in **Figure 72**.

III.3.5 Bending constant

Another important parameter that determines the evolution of the standard reference chemical potential and the microphase distribution is the bending constant. Its value determines the slope of the evolution of the difference in standard reference chemical potential of endcaps and junctions with respect to that of cylinders (*cf.* equation (62) and (63)). The results of the exemplary investigation are shown in **Figure 74**.

In general, one can say, that an increase of κ^* makes the curve of the standard reference chemical potential difference steeper. Consequently, a small change in uranyl concentration can have a bigger effect and the sphere-to-cylinder as well as the cylinder-to-branch transition occurs in a more defined concentration range and the change occurs less gradually and more abruptly.

As a result, at high bending constants, the viscosity will stay approximately constant longer before it increases drastically at a certain metal content. For more flexible molecules, the viscosity will increase more gradually. In other words, if an amphiphilic molecule is flexible, it will cost less energy to integrate that molecule in all three microphases than a rigid molecule that prefers to be in the microphase with the effective packing parameter that is closest to the spontaneous one. As a consequence, flexible molecules will always have a broader distribution of endcaps, cylinders and junctions than rigid molecules.

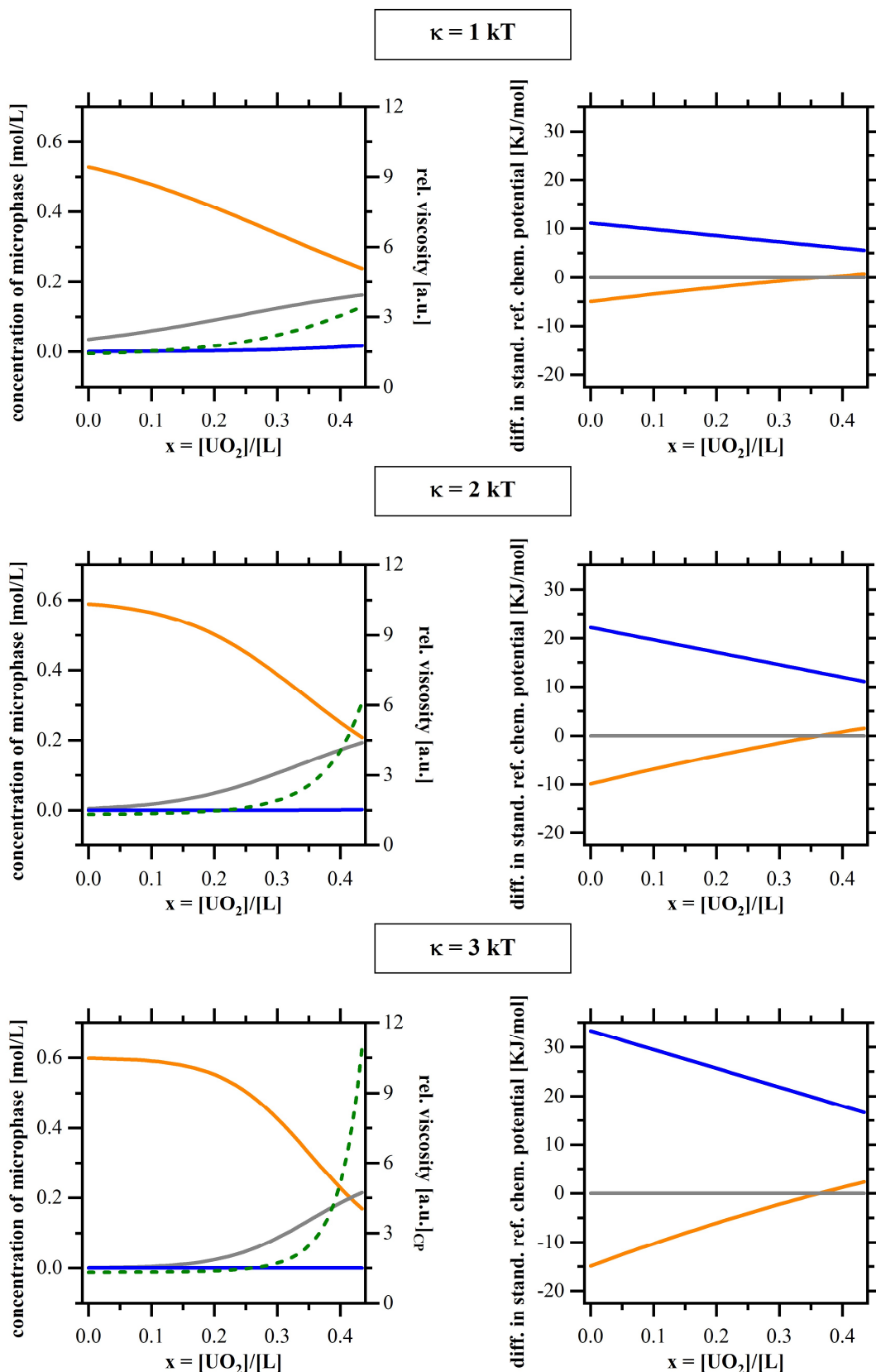


Figure 74. Calculated microphase distribution of endcaps (orange), cylinders (grey) and junctions (blue) as well as the corresponding standard reference chemical potential mol ratio dependent on the metal response on an extractant 1 with $P_{\text{init}} = 3$. The calculated viscosity curve is shown in as dashed green line. κ^* was set to 2 kT and the total extractant concentration is 1.2 M.

III.3.6 Concentration dependence and Onsager transition

Another parameter that plays a significant role for the viscosity is the concentration of extractant. One has to consider that according to the model, the extractant concentration does not have an influence on the evolving structures, only on the number density of the aggregates. This is only half the truth. This would be the case if one considers that the packing parameter is independent on the extractant concentration. However, it can be estimated that by increasing the amphiphilic concentration in a solution, the polarity and consequently the interaction between the total solvent and a single extractant will change. This will have an effect on the spontaneous packing parameter and therefore on the evolving structure as was already indicated by molecular dynamic simulations.^[196]

Figure 75 shows the structural evolution dependent on spontaneous packing parameter and volume fraction of extractant. One can see a tendency of structural change with concentration and the resulting viscosity. First, with increasing volume fraction of aggregated extractants, the aggregates are closer and the interaction as well as the collision of the resulting aggregates is more frequent. Second, one can also see that the probability of ‘*bridging endcaps*’ (cf. Chapters II.2.5 and III.1.4) and scattered larger aggregates seems to increase – especially when cylinders and junctions are present.

Moreover, **Figure 75** also indicates that at elevated extractant concentration, it is more difficult for the system to form a microstructure in which a minimum of frustrated microphases is present. For the two-dimensional investigation, this transition starts above approximately 50 volume percent of aggregated extractant. For the three-dimensional case, this value can differ since a three-dimensional arrangement can offer more structural possibilities. If this limiting volume fraction is reached, the microstructure must split up into regions with high frustration (marked in red in **Figure 75**) and regions without frustration in order to minimize the frustration energy.^[144,156,228] In order to point out this phase separation, the resulting microstructure was optimized for the case of a relatively low curved extractant ($P_{\text{init}} = 2.6$) in two ways. In the left figure, the total frustration energy of the system is minimized as it was done for the Monte-Carlo-like simulations before. In the right figure, the microstructure was optimized in a way that the number of frustrated microphases was minimized. For this case, the resulting ‘*clouds*’ of frustrated microphases are more visible and the term ‘*nanocrystals*’ (cf. Chapter I.2.5.3) is becomes more reasonable. As was pointed out in Chapter I.2.5.3, attraction between parallel cylinders is larger than between spheres. Therefore, the formation of nanocrystals is facilitated in the case of a less curved extractant favoring cylindrical units. If

these ‘clouds’ are small enough, the organic phase appears as a macroscopic homogeneous phase. This state is called the ‘*Onsager regime*’ (*cf.* Chapter I). If the ‘clouds’ grow big enough, macroscopic phase separation within the organic phase into an extractant-rich and an extractant-poor phase will occur. Therefore, this mechanism can be seen as a second mechanism leading to the third phase (*cf.* Chapter I.2.5.4).^[40] One can imagine the microstructure as a sponge formed by a living network that traps the diluent within its microstructure. If the network becomes too dense, the diluent is ‘squeezed out’ and two phases are created.

Both, the presence of ‘nanocrystals’ (*cf.* Chapter II.2.6.4) as well as the third phase formation (*cf.* Chapter II.2.5.6) were indicated experimentally. An increase at low q was observed in neutron scattering experiments indicating the presence of larger structures. During the preparation of the third phase, it was observed that the third phase does not structurally differ from the microstructure of the dilute organic phase in presence of uranyl. In contrast to the system HDEHP/Isane IP175, where the third phase forms a thin hexagonal phase^[232], the third phase of monoamides is dominant respective to the organic volume and only a thin diluent film is squeezed out at very high uranyl and acid content. This thin diluent film could be the amount of solvent that cannot be trapped any more in the dense structure of living network.

A more detailed comparison between the experimental observations and the results of the model will be carried out in Chapter III.5. In the following subchapter, the model will be applied to the investigated systems more in detail and the calculated viscosity will be related to the viscosity experimentally observed.

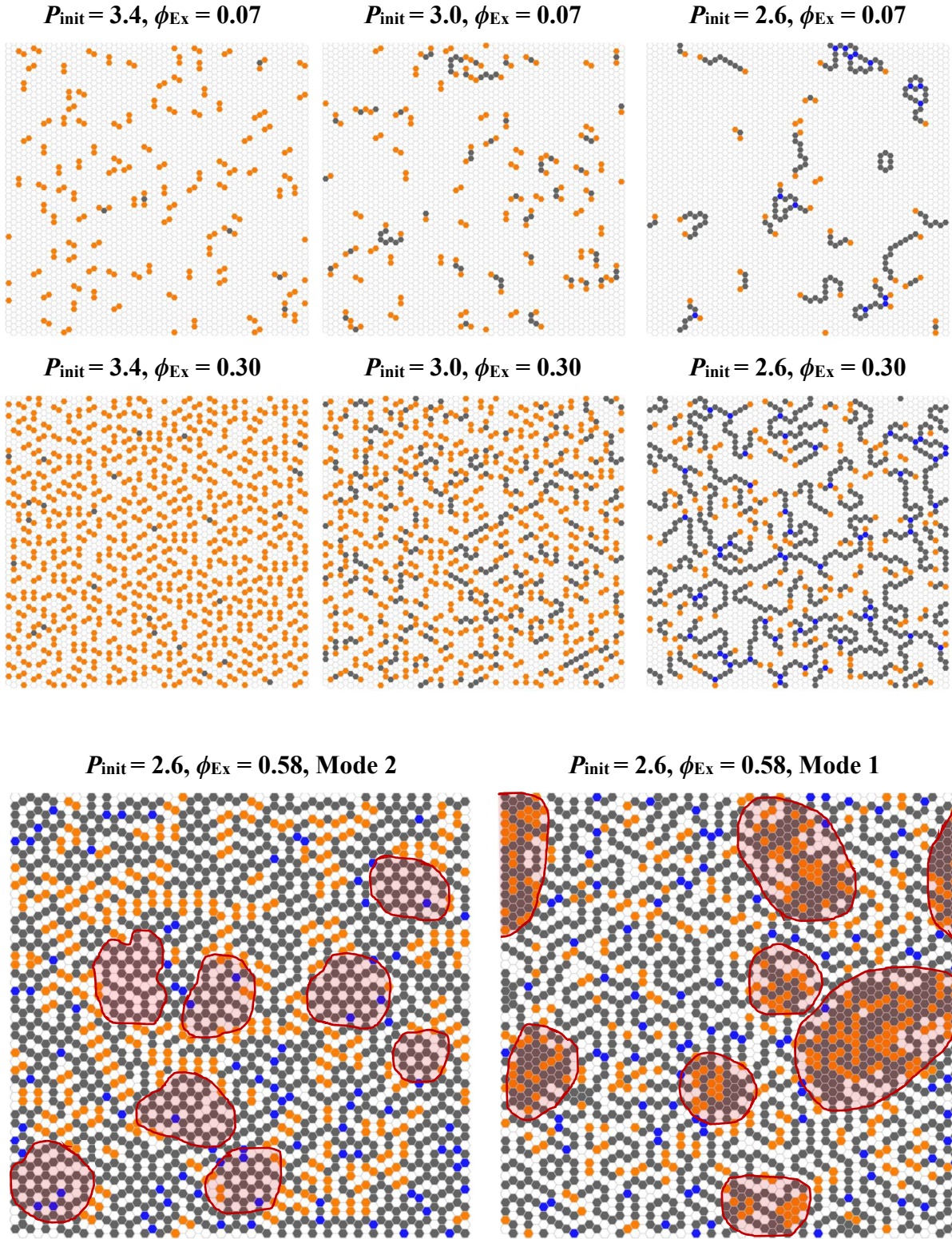


Figure 75. Two-dimensional image derived from Monte-Carlo-like simulation dependent on the initial packing parameter and the volume fraction of aggregated extractant. Calculations were carried out at $x = [U]/[Ex] = 0.35$ and the bending constant was set to $\kappa^* = 2 \text{ kT}$. Below, the simulation was carried out in two different ways to point out the Onsager transition. Mode 2 describes the general procedure used in simulations above, where the total frustration of the system is minimized. Minimization by Mode 1 minimizes the number of frustrated microphases.

III.4 Application of the model on the specific system

III.4.1 Presentation of Accordion II

Accordion II – ‘Viscosity increase of extractants in the presence of heavy metals is more specific. In this accordion, one can choose the extractant. Its apolar chain volume as well as the chain length is calculated according to the table of Fedors^[206] and Tanford’s formula^[72]. This procedure is further described in Chapter II.1.7. The polar surface area per extractant molecule that is needed to estimate the spontaneous packing parameter can be chosen via sliders for the case of an organic phase with no metals present (a_{\min}) and at the point of maximal loading (a_{\max}). It is assumed that the surface area increases gradually with increasing uranyl content since each uranyl ion that is added to the organic phase is directly complexed and must partly be counted to the effective polar moiety of the extractant.

Moreover, the solvent penetration can be simulated by variation of the corresponding slider. Its value describes the increase of the apolar volume relative to the apolar volume calculated from the table of Fedors.

As in the accordion before, the effective extractant concentration as well as the estimated bending constant can be varied. Furthermore, a scaling factor must be chosen to fit the relative viscosity increase from theory to the experimental values.

As in the example above, a certain uranyl content x can be chosen, in order to display the corresponding relative standard reference chemical potentials. Furthermore, the input values can be “sent” to Accordion XII, in order to carry out a Monte-Carlo-like simulation.

Additionally, one can choose between experimental values that were measured and compare them with the simulated curve (*cf.* **Figure 76**).

II. Viscosity increase of extractants in presence of heavy metals

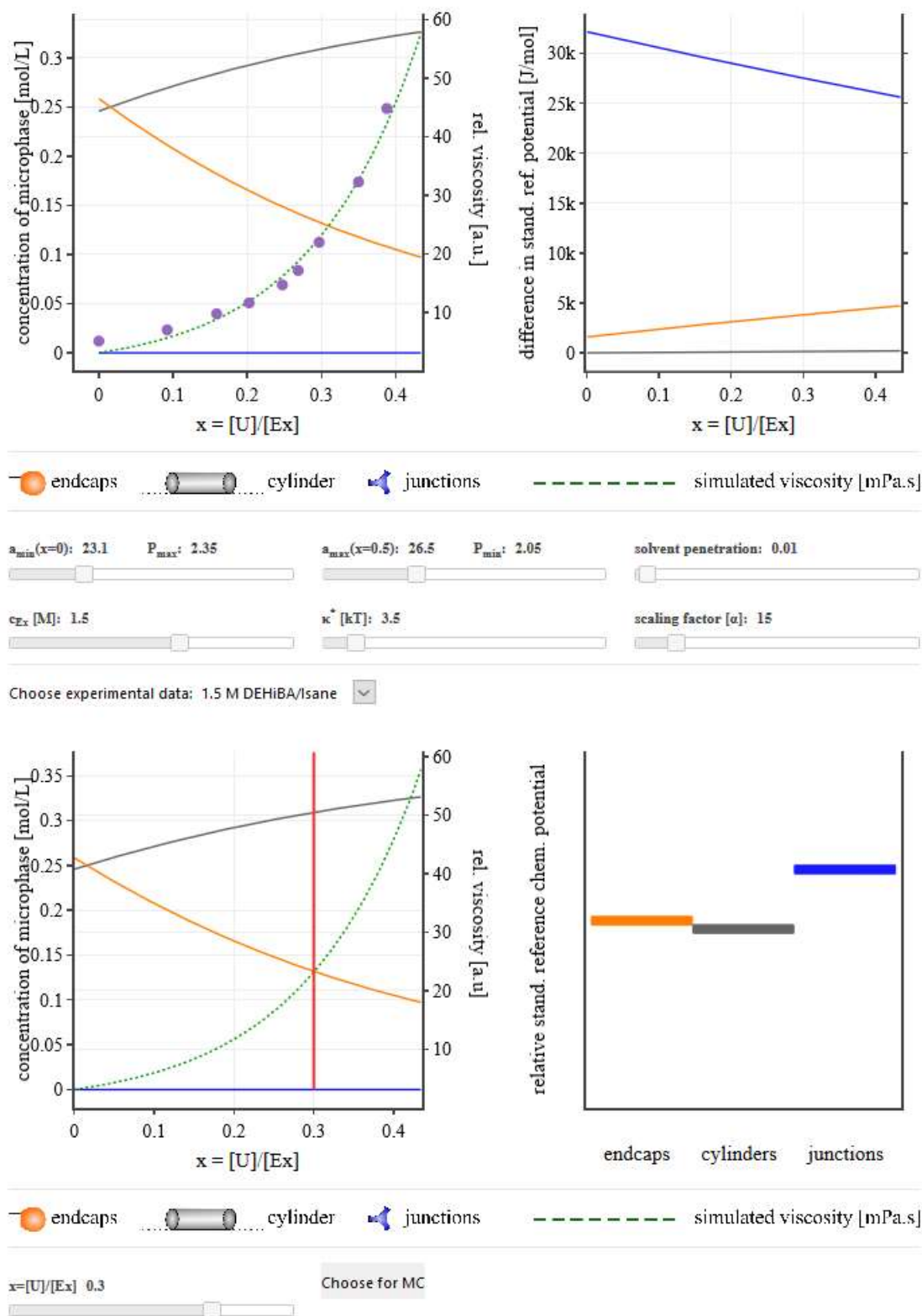


Figure 76. Screenshot of Accordion II of the model interface. The input parameters can be chosen via sliders, the microphase distribution and the corresponding standard reference chemical potentials are recalculated and updated each time a slider moves. The experimental viscosity values can be chosen via a pop-up menu and are displayed as purple circles

III.4.2 Estimation of the packing parameter and fitting of the experimental values

Figure 77 shows the experimentally observed viscosity curve for the system 1.5 M DEHiBA in Isane IP 175. The initial spontaneous packing parameter and the spontaneous packing parameter at maximum loading were set to the values estimated in Chapter II.1.7.2 assuming an octahedral geometry of the polar core. The viscosity curve derived from the microphase distribution and the effective length was multiplied with the factor $(1/15)(1 + 2.5\phi_{\text{Ex}})$ in order to estimate the intrinsic viscosity of the pure solvent and to fit the viscosity curve to the experimental values. The bending constant was chosen to be $3.5 kT$ per extractant molecule.

The curve is reproduced with a minimum of adjustable parameters.

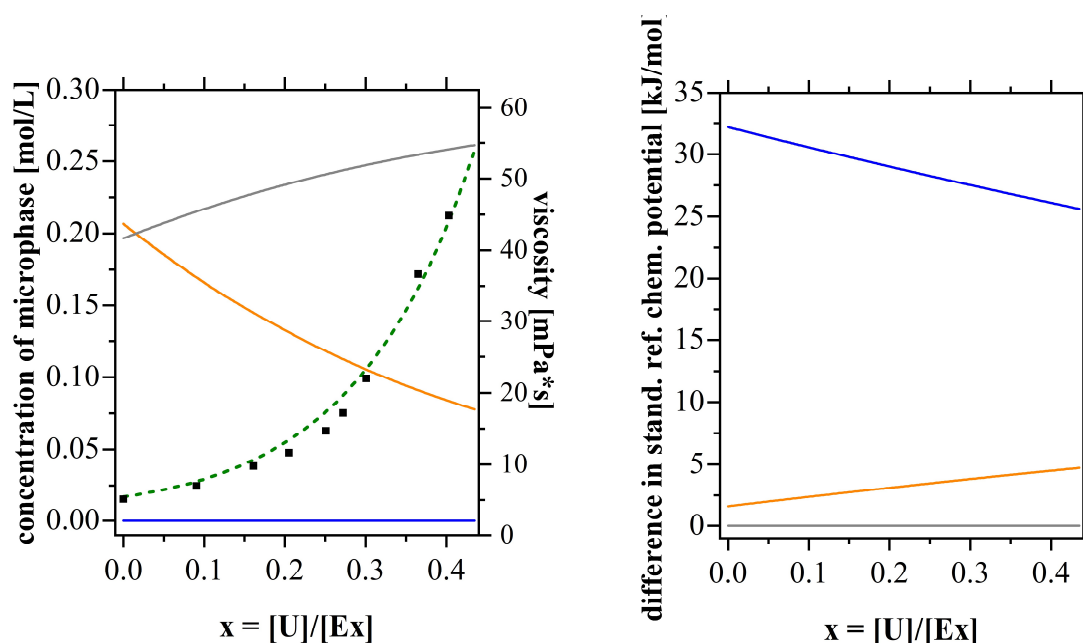


Figure 77. Comparison of the simulated viscosity values with the experimental ones. Input parameters: $a_{\min} = 23.1 \text{ \AA}^2$, $a_{\max} = 26.5 \text{ \AA}^2$, solvent penetration = 0.01, $\kappa^* = 3.5 kT$, scaling factor = 1/15.

As can be seen in **Table 6**, the polar area of the extractant DEHBA is generally smaller than a_0 of DEHiBA. In contrast hereto, DEHDMBA exhibits a larger a_0 . These trends are also visible by interfacial tension measurements at the dodecane/water interface (*cf.* Annex, **Suppl. Figure 21**). However, the values measured differ strongly from the geometrically estimated ones. On one hand, the estimation by geometry has its limitations and is only suitable for qualitative conclusions. On the other hand, interfacial tension measurements give access to the area per extractant at a macroscopic flat interface. These values can strongly differ from the actual area of the extractant inside a strongly curved and swollen aggregate. The area per molecule at a macroscopic flat interface is expected to be more influenced by the apolar extractant chains

than at a curved interface, as is indicated in a very simplified way in **Figure 78**.

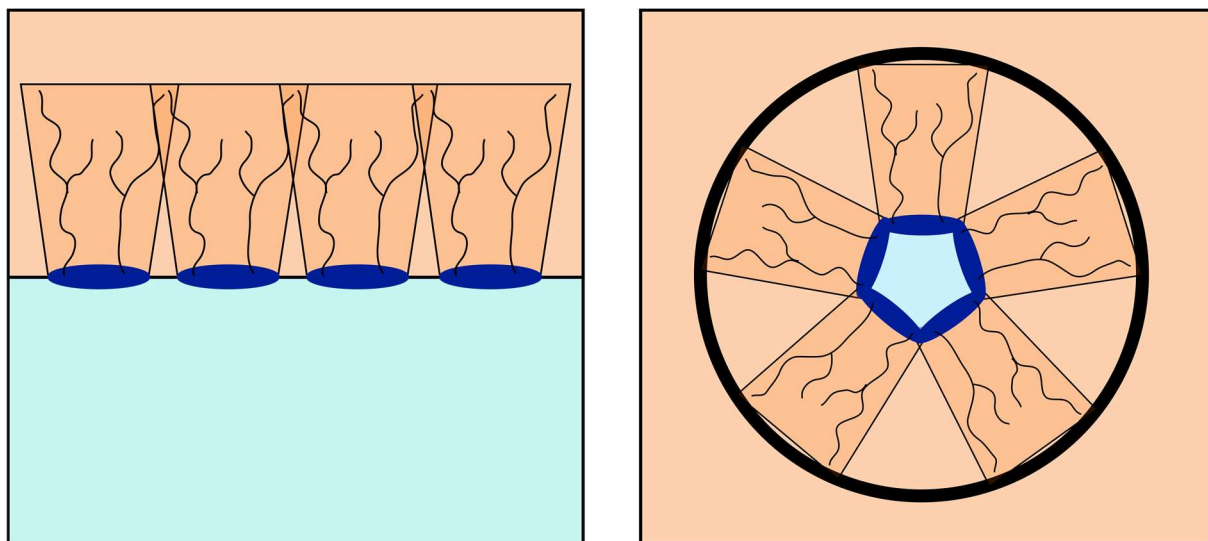


Figure 78. Schematic representation extractants at a macroscopic flat interface (left) and a curved interface of an aggregate (right)

As can be seen in **Figure 79**, changing the minimal and the maximal value of a_0 strongly influences the evolution of the viscosity curve. The qualitative trends observed experimentally are reflected. However, the exact experimental values observed for the extractants DEHBA and DEHDMBA cannot be simulated using the geometrical assumption from **Table 6** and with the input parameters (bending constant, scaling factor) needed to reproduce the viscosity curve of DEHiBA (*cf.* **Figure 77**). There are many reasons that could explain the deviation. First, the bending constant could differ from extractant to extractant. Second, the geometrical assumptions are very simplified, for example the small alkyl chain bound to the carboxylic group was counted to the polar volume, as was also done in Ref. [205]. The influence of this group can also be seen in interfacial tension measurements (*cf.* Annex, **Suppl. Figure 21**). However, it is not sure, if this part has to be added completely to the polar volume, or if a percentage affects also the apolar volume and chain length. Third, it is also not certain, if the scaling factor A is completely independent of the type of extractant.

The perspectives and limitations of this model approach are reviewed in detail in Chapter III.5.1.

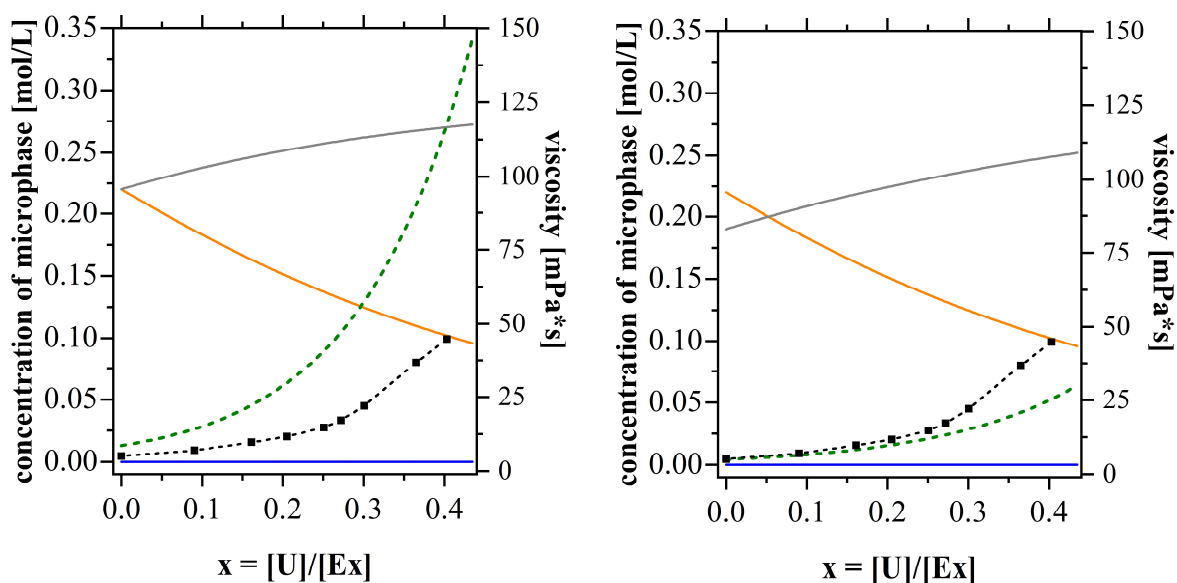


Figure 79. Evolution of the microphase distribution and simulated viscosity, by small changes of the area per headgroup evolution. Left: Decrease of area per headgroup: $a_{min} = 23.5 \text{ \AA}^2$ (black dashed), $a_{max} = 25.9 \text{ \AA}^2$ (green dashed). Right: Increase of area per headgroup: $a_{min} = 23.5 \text{ \AA}^2$ (black dashed), $a_{max} = 27.2 \text{ \AA}^2$ (green dashed). All other parameters were kept such as written in **Figure 77**. Color code: orange: endcaps, grey: cylinders, blue: junctions, black: experimental values.

III.4.3 Diluent dependence and solvent penetration

In the program, there is also a slider integrated that can simulate the influence of solvent penetration. **Figure 80** shows the influence on the viscosity curve of increasing solvent penetration. The apolar volume is stepwise increased, as a consequence the extractant becomes more curved, endcaps are favored. The resulting viscosity decreases.

These observations are consistent with the experimental observation (*cf.* Chapter II.2.4). The viscosity decreases with increasing solvent penetration.

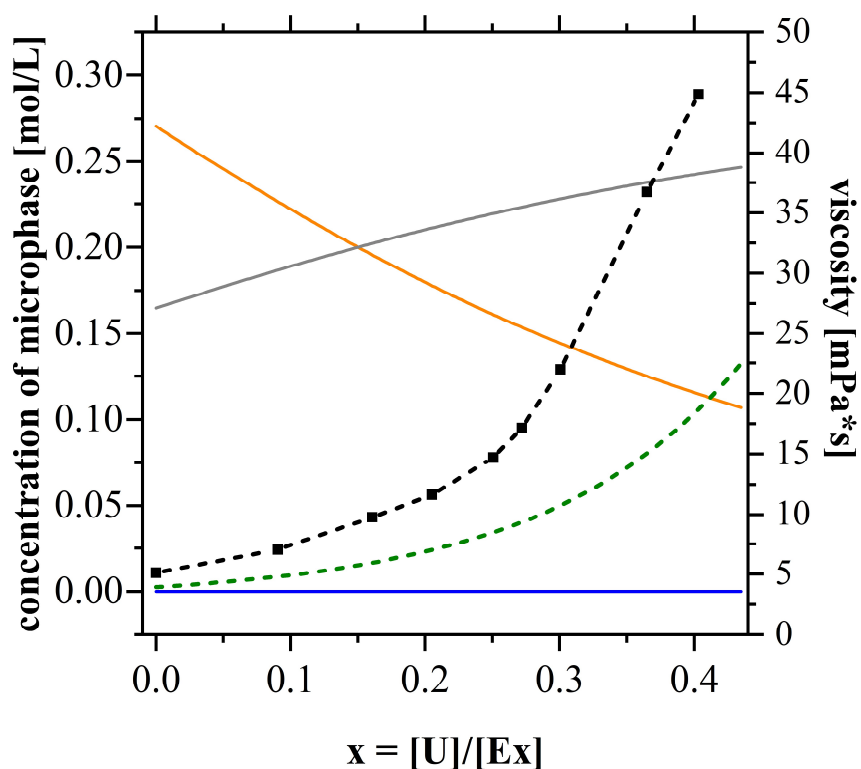


Figure 80. Evolution of the microphase distribution and simulated viscosity, with increased penetration power of the diluent (0.03, green dashed). All other parameters were kept such as indicated in **Figure 77**. Color code: orange: endcaps, grey: cylinders, blue: junctions, black experimental values.

III.5 Conclusion and remarks

III.5.1 Summary of the model and critical remarks

In the subchapters above, a minimal model was developed and presented to explain and understand the viscosity increase of monoamides. It helps to interpret the experimental differences in viscosity between the different extractants by the use of the difference in spontaneous and effective packing. Also, the impact of the diluent can be explained by the model. The viscosity curve can be reproduced by adjusting a minimum of parameters.

The model is based on three important concepts in colloidal chemistry and considers the chemical terms at the molecular scale, the physical terms at the meso-scale as well as the flow characteristics at the macroscale. It combines the concept of pseudo-phases, the expression for the free energy of bending for surfactant films as well as common fluid theories from the 90s. Assuming chemical equilibrium between monomers and the three microphases endcaps, cylinders and junctions, the standard reference chemical potentials and the corresponding microphase distribution as functions of the uranyl content can be derived.

A Monte-Carlo-like simulation allows to translate the microphase distribution in an intuition-driving image in two dimensions of the microstructure in the organic phase.

Introducing an effective length allows to break down the dynamic and static properties of the living network to a static property and to translate the microphase distribution directly into viscosity.

An interactive interface was created that facilitates to change input parameters easily and contributes to a better understanding of the problem. Moreover, this interface allows to compare the experimental results with the simulated ones. Furthermore, the Monte-Carlo-like simulation can be directly carried out for a freely chosen uranyl content.

However, there are some points that could be refined in future.

First, the estimation of the packing parameter was only done geometrically. With this method, qualitative trends can be established. However, for a more quantitative determination, it is necessary to estimate or measure the evolution of the spontaneous packing parameter exactly and to determine the effective parameter in each microphase more precisely.

The concentration of monomers was estimated as a constant value close to the *cac*. However, the monomer concentration is likely to change with ion concentration. Consequently, the total concentration of extractants participating in self-assembly should not be seen as constant, as it was done in this approach to keep the model ‘minimal’. The relative microphase distribution is

not affected by the number of monomers, but the absolute distribution of micophases.

Furthermore, the concentration dependence is currently only taken into account by a gradual decrease of the number density of each microphase as well as by a different intrinsic viscosity estimated by Einstein's formula. However, with increasing extractant concentration, further parameters change. First, the activity coefficients of the microphases can change with extractant increase. Even if the single concentrations of the microphases are relatively low, an effect is expected. Moreover, with increasing extractant concentration, the polarity of the medium and therefore the intra- and intermolecular interactions may change with addition of extractant. That there is an effect of total extractant concentration was seen by Ferru *et al.*^[194,196] and in the Small-Angle Neutron Scattering experiments (*cf.* **Figure 56**, Chapter II.2.6.2). According to their simulations by molecular dynamics, the aggregates tend to form smaller aggregates at higher extractant concentration.

In order to obtain certain input parameters and values that are necessary for the calculations, a number of simple geometrical calculations were carried out (*cf.* Annex, Chapter VII.7.1). The validity of the sum of these approximations is also in question. But these assumptions should not change the qualitative trends, only the absolute values. Since this model never claimed to deliver quantitative results, these approximations are a reasonable compromise.

One of the crucial steps to obtain the value of simulated viscosity is to reduce the dynamic properties of this living network to one single characteristic effective length – as was proposed by Khatory *et al.*^[137]. Certainly, this reduction seems to be too simple. Admittedly, it is in question, if it is really sufficient to connect the complicated and complex value of viscosity to a single characteristic length. There are other parameters that could influence the absolute value of the viscosity like the persistence length of the resulting polymers or the solvent “goodness” of the diluent for the polymer network.^[233] However, without knowledge of the dominant relaxation mechanism and relaxation times, this is a good compromise for the requirements of a “minimal” model. The approximations made in this model seem to be sufficient to predict the microstructure and its effects on the viscosity in a qualitative way.

As a conclusion, the model is consciously kept simple. The assumptions are sufficient to explain and understand the viscosity increase of monoamides in presence of uranyl. The model helps to predict the influence of certain parameters and to develop formulation approaches to avoid the viscosity problem. These formulation approaches are described in Chapter I.

III.5.2 Compatibility with a COSMO-RS approach

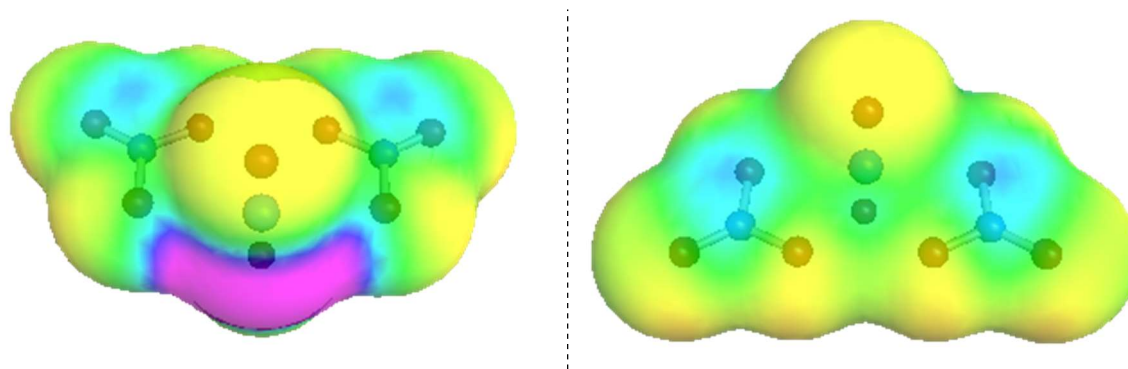
The model proposes a network-like structure formed by alternating uranyl nitrate molecules that arrange in chains. Furthermore, the possibility of junctions is not excluded. Since the formation of such chains is not obvious and was to our knowledge only mentioned once in literature for organic systems^[196], this phenomenon is shortly discussed in terms of possible uranyl nitrate conformers and its COSMO-RS surfaces.

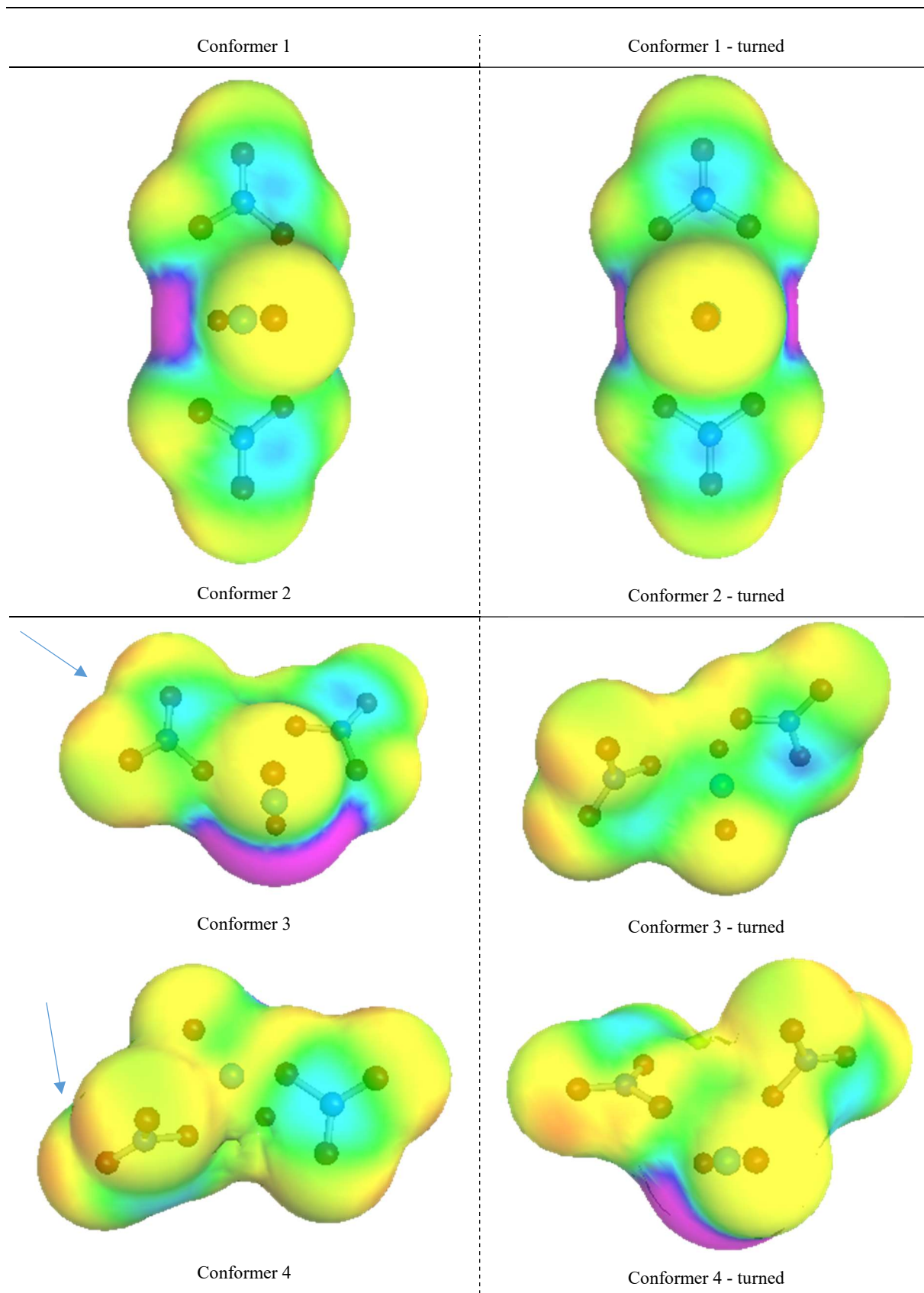
Table 15 shows the five most probable conformers of uranyl nitrate complexes and their corresponding σ -surfaces calculated by Maximilian Hahn. A short introduction to COSMO-RS and the surfaces is given in Annex, Chapter VII.4. As a rough principle, COSMO-RS describes the interaction of molecules as locally interacting molecular surfaces of a certain surface charge density σ .^[234] Therefore, local molecular surfaces with a more red color shade have a so-called negative screening charges and will preferentially interact with a surface with more bluish color shade having positive charge screening.

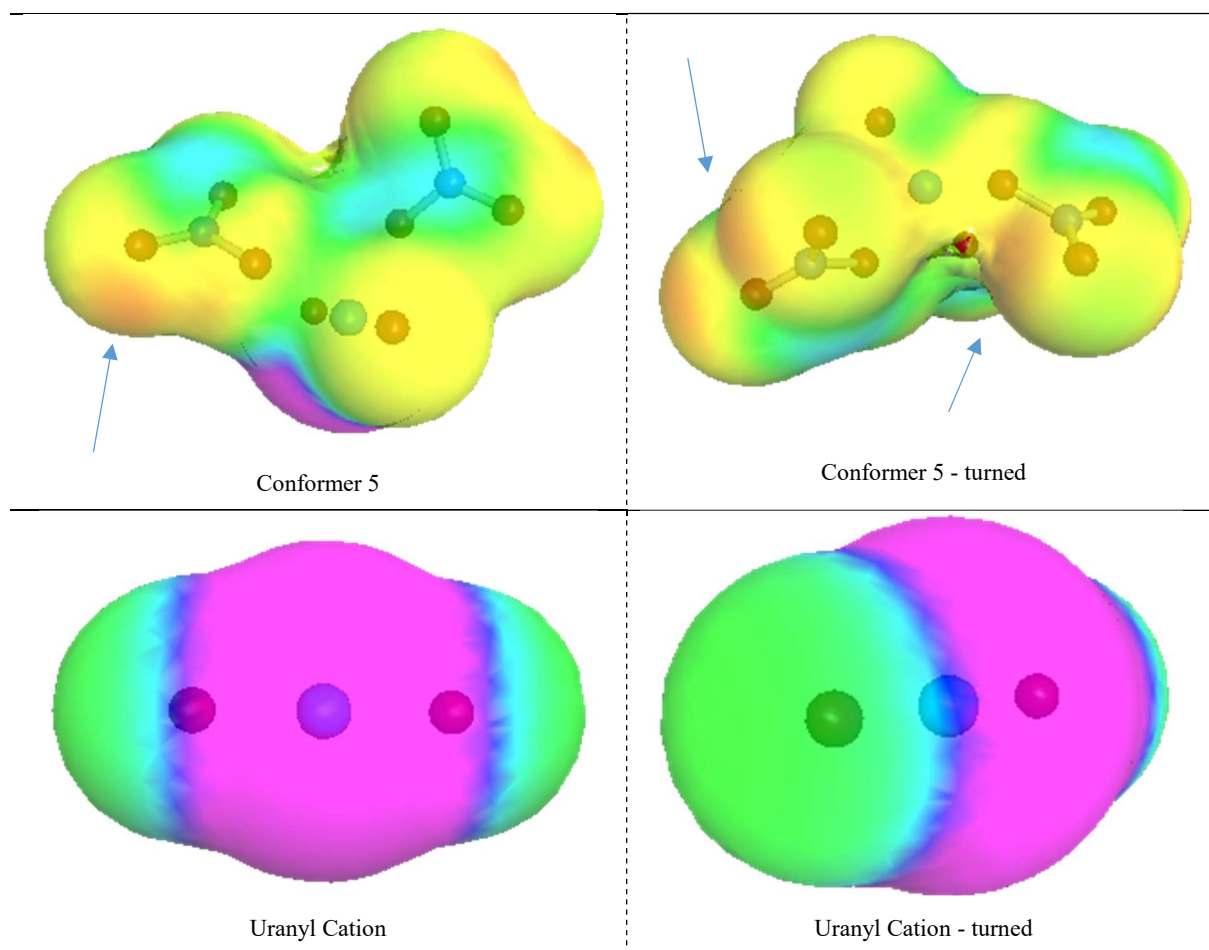
In the conformers 1 and 2, the nitrates interact via two oxygen each with the uranyl cation. The result is a complex with one or two strongly negative surface areas and apart from that neutral screened surfaces. These two configurations will preferentially interact with the polar part of extractant molecules and will mainly form aggregates or complexes with one uranyl ion inside.

Looking at the conformers 3, 4 and 5, one can see that the uranyl cation is mainly coordinated by one oxygen per nitrate. The results are positive surface charge densities on the nitrates (indicated by arrows in **Table 15**). Therefore, an interaction of such red surfaces with a purple interface of uranyl (negative surface charge density) is possible and favorable. This interaction can lead to chains as well as to branching points. Therefore, from a COSMO-RS approach point of view, chains and branching points formed by alternating uranyl-nitrate chains are possible.

Table 15. The five most probable conformers for a uranyl nitrate complex. Conformers are optimized using TURBOMOLE on TZVPD level. The configurations are listed with increasing energy from top to bottom. Bottom row: Uranyl cation optimized on TZVP level.







III.5.3 Conclusion and propositions for the solution of the viscosity problem

In this chapter, a minimal model at the nanoscale was developed and presented to describe a living branched network of a one-dimensional ionic liquid enclosed in a bottlebrush structure of extractant chains. The main idea of the model is the presence of three microphases in chemical equilibrium. The microphase distribution is given by the difference in standard reference chemical potential. The resulting viscosity is obtained by introducing a characteristic length L_{eff} that reduces the viscosity to a static property at a first approximation.

Even though if the model is kept simple, it allows to understand experimental observations, to get a qualitative image in two dimensions as well as develop formulation principles in order to reduce the viscosity.

Having analyzed different parameters, the spontaneous packing parameter was determined as the decisive parameter to control viscosity. It was demonstrated that a higher spontaneous packing parameter of the extractant leads to higher curved microphases, particularly endcaps.

These reduce the mean effective aggregate length and consequently the viscosity.

As was indicated in II.2.1 and Chapter III.3.2, the viscosity can be modified by changing the extractant geometry. If the spontaneous packing parameter for a certain condition is unknown, the approach explained in Chapter II.1.7 can be used to compare extractants qualitatively. An increase in packing parameter can be induced by introduction of hydrophobic chains that are bulkier or simply more chains, polar headgroups that are smaller or chains that are shorter. It should be noted that increasing the apolar volume is not an easy task. The di-ethylhexyl chains of the three monoamides that were investigated already are already quite bulky. The introduction of dissymmetry – the use of two different extractant chains – could be a promising approach. It was demonstrated for gemini extractants that decreasing the symmetry by two different chains results in larger spontaneous curvature allowing to assess stronger curved microphases.^[235] Decreasing the chain length would also be possible, but the disadvantage of this approach is that one risks to promote the formation of the third phase. Reducing the chain length means to reducing the sterical repulsion between two aggregates. The attractive interaction would lead then to third phase formation (*cf.* Chapter I.2.5.4).^[40]

As implied in Chapter II.2.5.4 and III.4.3, the diluent and solvent penetration can be used to control viscosity. Penetrating diluents increase the apolar volume and consequently the spontaneous packing parameter. The resulting viscosity is decreased. However, it has to be noted, even if the use of penetrating diluents can be a simple and powerful approach, it will be difficult to realize in industrial applications. Most of the penetrating diluents have non-negligible disadvantages like for example the danger of explosion in the case of isooctane or the poor chemical stability of aromatic compounds against nitric media.

It is also conceivable, that additives with a cosolvent effect can have a positive effect. The addition of a cosolvent such as lipotropes^[163], short- and long chain alcohols or bulky hydrotropes, has two effects. First, the headgroup of for example alcohols are smaller than amide groups. Therefore, the mean area per headgroup is reduced leading to an increase in spontaneous packing parameter. A parallel effect is expected on the apolar chain volume and on the mean chain length. One could also argue with the flexibility. Addition of a cosolvent can increase the flexibility of the outer chain shell. Consequently, curvatures can be more easily compensated without frustration of the extractant. Therefore, endcaps can be more easily formed. Furthermore, the addition of an alcohol can lead to a reduction of the bending constants^[231,236] resulting in a slower increase in viscosity (*cf.* Chapter III.3.5).

Furthermore, as was indicated in Chapter III.3.3, also a second extractant could have a viscosity decreasing effect. The addition can have two effects. First, the addition of a more strongly curved extractant changes the mean curvature. Second, the addition of a second effect can lead to a positive configurational entropic contribution, that lowers the endcap energy.^[52,80] It can be also assumed that the more strongly curved extractant accumulates at the more curved regions and stabilizes endcaps.

The four possibilities to control viscosity are summarized in **Figure 81**. All approaches have their advantages and disadvantages, especially regarding industrial application. Besides viscosity, other parameters such as density difference, security, interfacial tension and extraction behavior are important and a compromise between them has to be found.

In the following chapter, the validity of this concept is investigated.

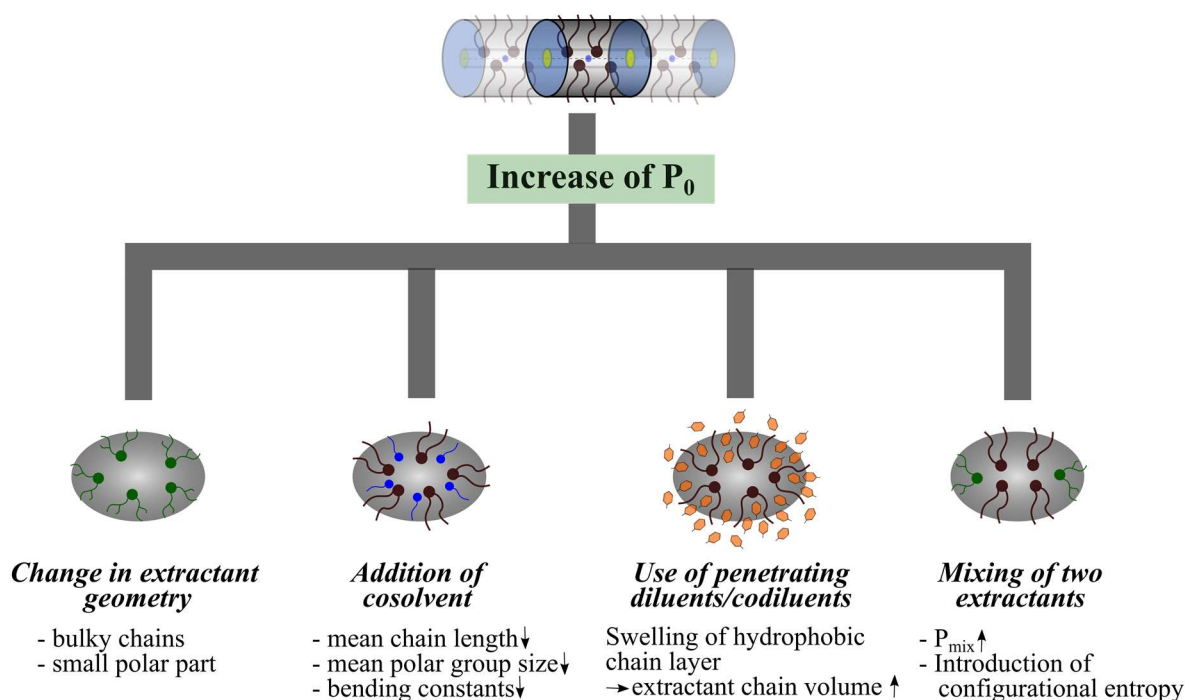


Figure 81. Possible approaches to reduce the viscosity resulting from the model. To simplify the overview, the resulting structures are plotted as ellipsoids. In the same way, they could represent endcaps in a smaller network structure.

IV FORMULATION STRATEGIES TO SOLVE THE PROBLEM

In the following chapter, the concept of the model introduced in Chapter III will be tested. Since viscosity is not the only parameter that is important, the concepts will only briefly be investigated. The optimization of a possible solvent for the industrial uranyl/plutonium extraction taking into account all crucial parameters (*cf.* Chapter I.2.2.4) is far beyond the scope of this thesis.

IV.1 Changing the extractant geometry

The most efficient and simplest way to tackle the viscosity increase is to change the extractant geometry. To demonstrate this approach, a new molecule was tested from a group of extractants that were patented in 2017 for their excellent extraction properties.^[237]

N-methyl-*N*-octyl-2-ethylhexylamide (MOEHA, *cf.* **Figure 82**) belongs to the group of dissymmetric *N,N*,-dialkylamides and combines the advantages of symmetric dialkylamides (*cf.* Chapter I.2.6) with further advantages such as a better extraction of plutonium at high acidity which is important for the design of reactors of future generations.^[237]

The term ‘*dissymmetric*’ implies that the two long chains are not bound to the nitrogen as in the case of ‘*symmetric*’ ones, but one branched chain is bound to the carbonyl group and one linear chain to the amino group.

The third alkyl chain is a small methyl group. The influence of this methyl group on the area per extractant is expected to be smaller than in the case of the three monoamides studies in Chapter II, whose small alkyl chains are 3 to 4 times larger than a methyl group. Moreover, the fact that the two long chains that contribute to the apolar volume are separated by a rigid spacer, a carboxyamide with delocalized electrons, strengthens the expectations that the apolar volume should be increased compared to two ethylhexyl chains bound to the same nitrogen. The combination of a linear with a branched chain is likely to be less compatible to each other than two ethylhexyl chains. The presence of a spacer as well as two different chains leads to a larger apolar volume compared to the three monoamides investigated in the previous chapters. The structure evokes the structure of gemini surfactants. For these, Oda *et al.* have shown that decreasing the symmetry by two different chains results in larger spontaneous curvature allowing to assess stronger curved microphases.^[235] Furthermore, the investigated dissymmetric gemini surfactants were less viscous and had higher overlap concentrations than symmetric ones. Therefore, the resulting spontaneous packing parameter is expected to be higher than that of DEHiBA, DEHBA and DEHDMBA. That is also confirmed by calculation of the pseudo-packing parameter introduced in Chapter II.1.7 (*cf.* **Table 16**)

Table 16. Calculation of the minimal packing parameter and the spontaneous packing parameter of MOEHA assuming a tetrahedral and an octahedral geometry, in order to compare the extractant geometry with the geometry of TBP, DEHBA, DEHiBA and DEHDMBA.

Formula	C ₁₇ H ₃₅ NO	Minimal packing parameter	
Molar mass [g/mol]	269.47	R_{core} [Å]	3.011
Molar volume [Å ³ /molecule]	521.5	R_{tot} [Å]	5.154
l_{chain} [Å]	10.3	$P_{0,\text{min}}$	1.88
V_{apolar} [Å ³]	459.2	Spontaneous packing parameter P_0' at $x = [\text{U}]/[\text{Ex}] = 0$ and 0.43 assuming a tetrahedral arrangement of the extractant headgroups around the core	
V_{polar} [Å ³]	62.2	$b_{\text{tetrahedron}}$ at $x = 0$ [Å]	7.172
$V_{\text{pol.core}}$ [Å ³] at $x = 0$	355	$b_{\text{tetrahedron}}$ at $x = 0.43$ [Å]	7.978
$V_{\text{pol.core}}$ [Å ³] at $x = 0.43$	488	$a_{0,\text{tet}}$ at $x = 0$ [Å ²]	22.3
		$a_{0,\text{tet}}$ at $x = 0.43$ [Å ²]	27.6
		P_0' at $x = 0$	2.00
		P_0' at $x = 0.43$	1.61
		Spontaneous packing parameter P_0' at $x = [\text{U}]/[\text{Ex}] = 0$ and 0.43 assuming an octahedral arrangement of the extractant headgroups around the core	
		$b_{\text{octahedron}}$ at $x = 0$ [Å]	6.21
		$b_{\text{octahedron}}$ at $x = 0.43$ [Å]	6.91
		$a_{0,\text{oct}}$ at $x = 0$ [Å ²]	16.71
		$a_{0,\text{oct}}$ at $x = 0.43$ [Å ²]	20.67
		P_0' at $x=0$	2.66
		P_0' at $x=0.43$	2.15

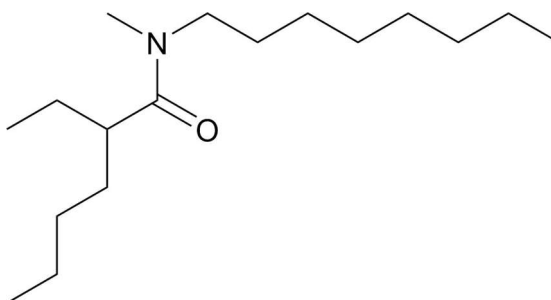


Figure 82. Structure of MOEHA

According to the calculations of the spontaneous and the minimal packing parameter, the curvature of the extractant MOEHA lies between the curvature of TBP and DEHBA.

This is also observed experimentally. As can be seen in **Figure 83**, the viscosity curve of 1.5 M

MOEHA lies between the curve of TBP and DEHBA. At a uranyl/extractant ratio of around 0.5, a third phase is produced. But even the viscosity of the third phase is relatively low (30 mPa·s). This strengthens the theory that the third phase in the case of the monoamides investigated is a consequence of the structure that evolves with increasing uranyl content. The living network becomes denser, until the expendable diluent is squeezed out and separated from this structure. This theory is supported by the scattering spectra investigated in Chapter II.2.5.6, that have shown that the microstructure is not a condensed crystalline phase, but exhibits a scattering spectrum close to the monophasic organic phase.

The result observed is quite satisfying. At a uranyl concentration between 80-100 g/L that is typically used in industry, the viscosity is below 10 mPa·s. This value is a good basis for further investigations. If this value is not sufficient, this viscosity can further be reduced by decreasing the extractant concentration, increasing the temperature, changing the diluent or adding a co-extractant or co-solvent.

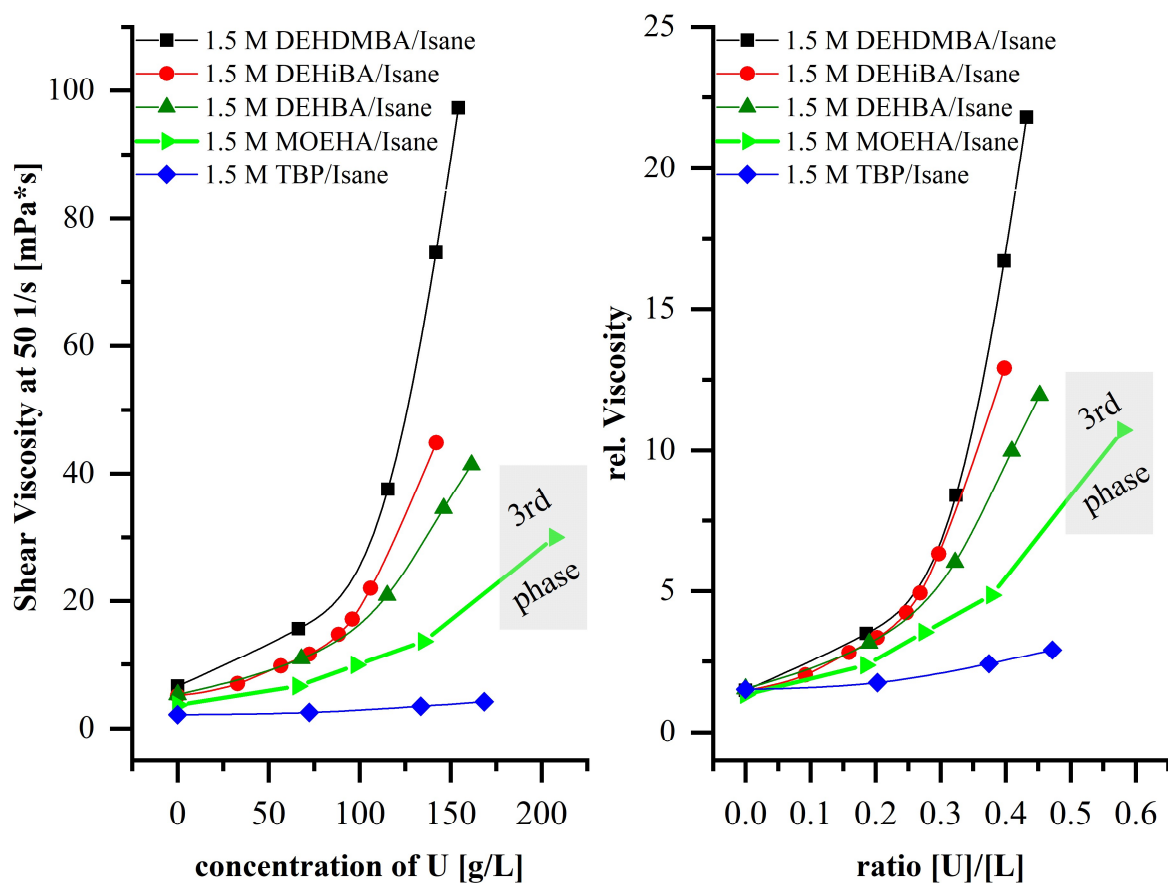


Figure 83. Viscosity increase due to increasing uranyl concentration in the organic phase for different extractants at 25 °C. Left: Apparent viscosity at a shear rate of 50 1/s. Right: Relative viscosity normalized by the viscosity of the non-contacted extractant/diluent mixtures ■ 1.5 M DEHDMBA ● 1.5 M DEHiBA ▲ 1.5 M DEHBA ► 1.5 M MOEHA ◆ 1.5 M TBP diluted in Isane IP 175 versus the molar ratio uranyl/extractant.

IV.2 Changing the diluent by additives

In Chapter II.2.4 as well as by the model it was indicated that there is a significant effect of the diluent on the spontaneous packing parameter and consequently on the viscosity. Penetrating diluents such as toluene increase the extractant curvature and can decrease the viscosity. However, due to safety and stability reasons (*cf.* Chapter I.2.6.3) toluene or isooctane is not relevant for industrial application. Therefore, penetrating and safe diluents must be found to improve the important factor viscosity. One possible approach could be the use of diluent mixtures that contain both aliphatic and aromatic compounds such as some kinds of kerosene that are already used in extraction processes in several countries, or aromatic industrial diluents such as Solvesso^[238]. However, a lot of other parameters such as density difference, distribution coefficient or interfacial tension play a role and must be evaluated in detail. Therefore, this effect is not redemonstrated.

In this chapter, additives are tested in order to reduce the viscosity. The first idea was to increase the hydrophobic volume by the addition of so-called Guerbet alcohols. These 2-alkyl-1-alkanols are strongly branched and one could have expected that the presence of these alcohols affects the viscosity. Therefore, three different Guerbet alcohols of the Trademark Isofol by Sasol^[239] were investigated for the system 1.5 M DEHBA/Isane (*cf.* **Figure 84**). The added concentration was 0.5 M of alcohol, leading to a mol ratio of 1:3 between additive and extractant. This ratio was expected to be high enough to see an effect. The terms ‘Isofol 12, 16 and 24’ stand for the mean total chain length of the branched Guerbet alcohol. The main compound of Isofol 12 is 2-butyloctanol, for example. The exact compositions can be found in Ref [239].

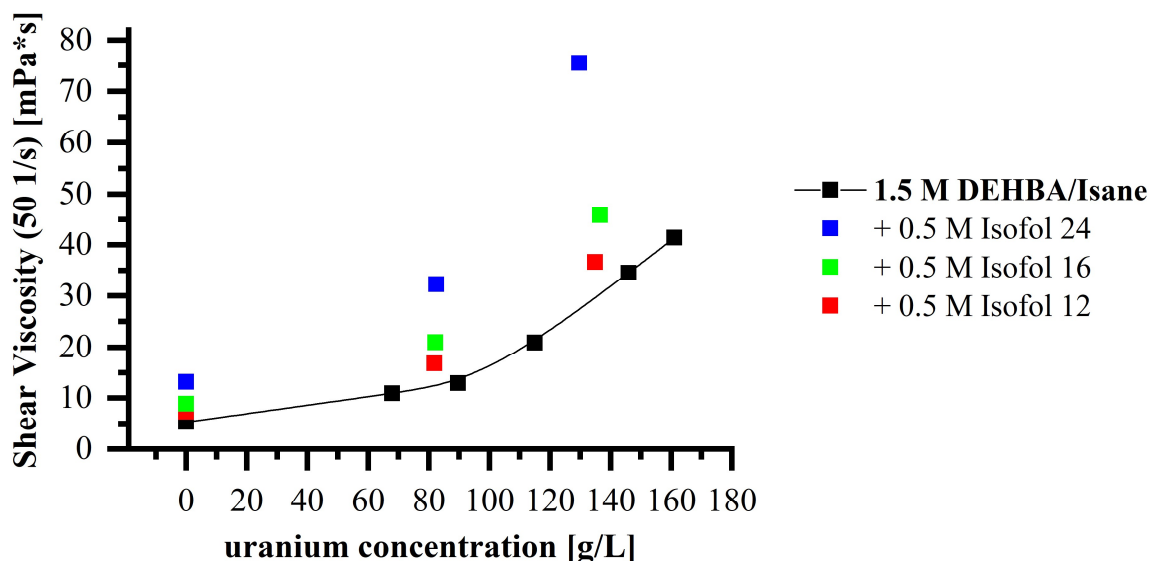


Figure 84. Viscosity increase due to increasing uranyl concentration in the organic phase for 1.5 DEHBA in presence of different Guerbet alcohols at 25 °C. The corresponding uranyl concentrations in the organic phase result from the contact of the organic phase with aqueous stock solutions of 3 M nitric acidity containing 0, 125 or 240 g/L uranyl.

As can be seen, the viscosity is significantly increased in the presence of Guerbet alcohols. The longer the alcohol chains, the higher the viscosity. This can have two reasons. First, especially the longer chained alcohols are quite hydrophobic. It is not certain that they will go to the polar micellar interface and affect the interfacial film. Staying in the continuous phase as monomers increases the viscosity of the diluent/extractant mixture without uranyl, as can be seen by the first points of the curve. This intrinsic viscosity affects the whole curve. Second, Guerbet alcohols are quite long, longer than the mean extractant chain length. Even if the apolar volume is increased by the presence of the Guerbet alcohols and the polar area is decreased, the chain length is also increased and seems to be the dominant term.

As a conclusion, the additive chosen should be short. The increase in curvature or respectively in apolar volume should be achieved by small bulky additives and not long ones. This was tried in the second investigation of additives (*cf.* **Figure 85**). Toluene and octane were tested as representatives of penetrating hydrocarbons, butanol and octanol as representatives for short-chain alcohols. Moreover, it was tested, if the viscosity can be changed more by increasing the octanol concentration.

For a mol ratio of 1:3, all four additives reduce the viscosity. Octane and toluene seem to be more efficient than octanol and butanol. However, in the range of uncertainty for the measured uranyl concentrations, these trends are difficult to verify.

Increasing of the concentration of octanol induces an increase in viscosity. However, this effect

seems to be rather attributable to an increase in solvent viscosity than to a change of microstructure.

Overall, it can be concluded that the viscosity can be decreased by the presence of small molecules such as short-chain aliphatic compounds or small-chain alcohols. However, the decrease is not large, but visible. It seems that the uranyl-extractant interaction is the dominant term for the decrease in spontaneous packing parameter and the increase in viscosity. This interaction is necessary for the extraction of metals and can only partly be compensated by the presence of additives.

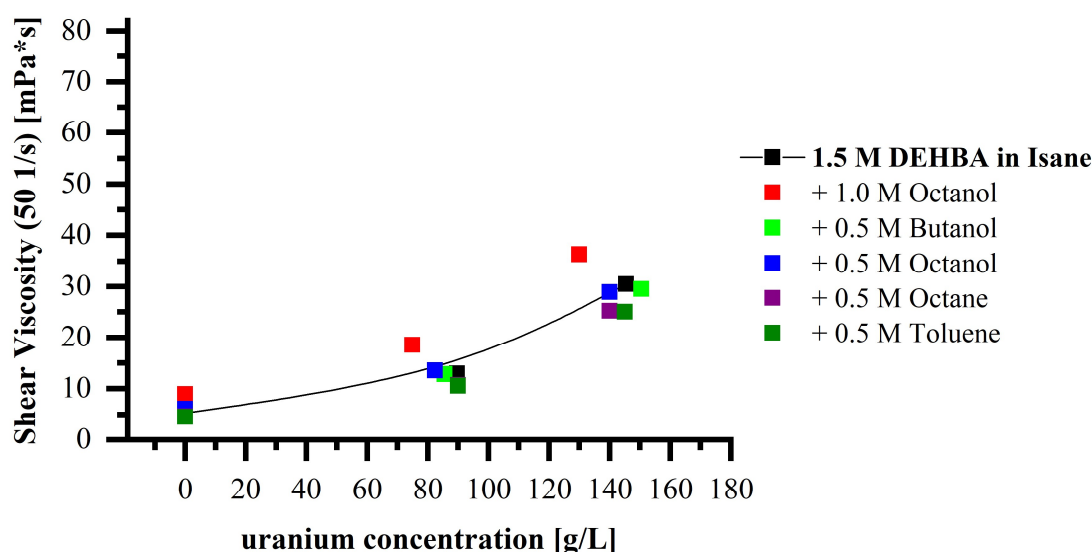


Figure 85. Viscosity increase due to increasing uranyl concentration in the organic phase for 1.5 DEHBA in presence of different additives at 25 °C. The corresponding uranyl concentrations in the organic phase result from the contact of the organic phase with aqueous stock solutions of 3 M nitric acidity containing 0, 125 or 240 g/L uranyl.

Further additives were tested for the system 1.5 M DEHiBA in Isane. The intention for this investigation was to use bulky additives. The bulkiness should be induced by the presence of rings. Moreover, tert-butanol was tested. From the series of these molecules, the effect at low uranyl content seems to be very low or even negative. Only for 2-methyltetrahydrofuran, the effect was significant. The other effects lie in the range of uncertainty. This molecule is also efficient in reducing the viscosity of 1.5 M DEHDMBA in Isane IP 175 (*cf.* **Figure 87**). The other molecules are either not efficient enough or too large.

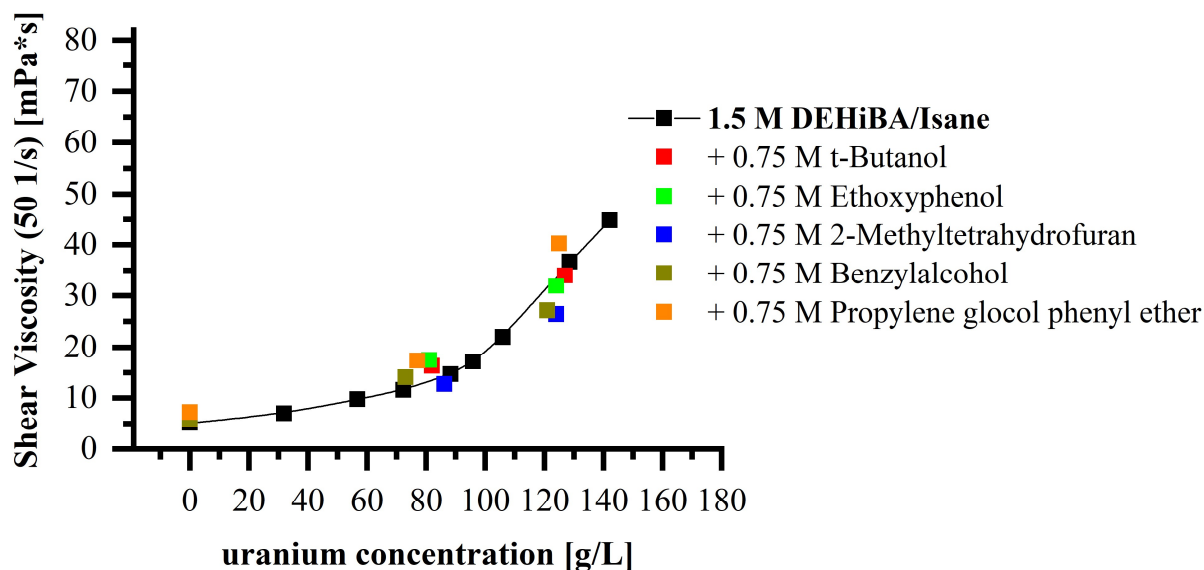


Figure 86. Viscosity increase due to increasing uranyl concentration in the organic phase for 1.5 DEHiBA in presence of different additives at 25 °C. The corresponding uranyl concentrations in the organic phase result from the contact of the organic phase with aqueous stock solutions of 3 M nitric acidity containing 0, 125 or 240 g/L uranyl.

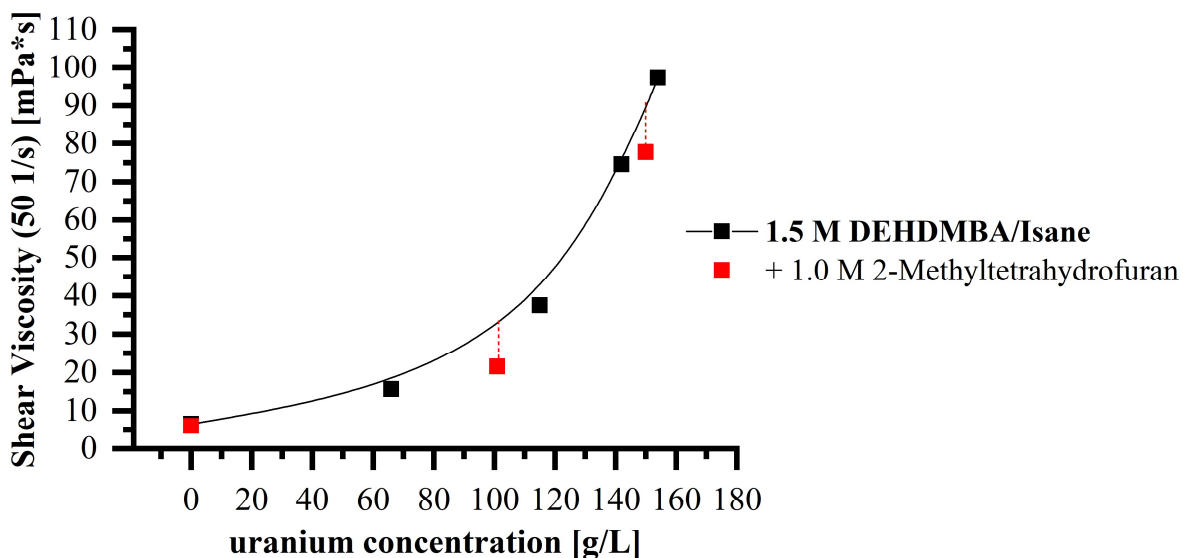


Figure 87. Viscosity increase due to increasing uranyl concentration in the organic phase for 1.5 DEHDMBA in presence of 1 M 2-methyltetrahydrofuran at 25 °C. The corresponding uranyl concentrations in the organic phase result from the contact of the organic phase with aqueous stock solutions of 3 M nitric acidity containing 0, 125 or 240 g/L uranyl.

As a conclusion, additives can contribute to reduce the viscosity. They should fulfill the following criteria. The additives should be small enough to be able to penetrate the protruding extractant chains and not to affect the intrinsic viscosity of the diluent/extractant mixture. Furthermore, they should be bulky to increase the apolar volume. The effect on the polar area per extractant is assumed to be small, since the extractant-metal interaction seems to be the dominant term. This could be also the reason why the reduction of viscosity is not elevated.

The most efficient additives tested have reached a reduction of viscosity of approximately 30 percent. A much higher reduction of the viscosity by additives seems to be unlikely, because the increase in headgroup area by heavy metals will be dominant over a possible moderate change of the apolar moiety.

IV.3 Mixing two extractants

The last approach proposed in Chapter III.5.3 was to mix two extractants. Different mixtures of DEHBA and DEHiBA were chosen. As can be seen in **Figure 88**, the viscosity depends on the DEHiBA/DEHBA mol ratio. As was demonstrated in Chapter II.2.1, the viscosity of the organic phase containing DEHBA is lower than containing DEHiBA at the same uranyl content. This result was correlated with a smaller spontaneous packing parameter of DEHBA. Gradual exchange of DEHiBA by DEHBA molecules leads to a gradual decrease of viscosity at the same uranyl content. This effect can be contributed to a gradual decrease in mixed packing parameter. However, there is no minimum in viscosity observable indicating an endcap-favoring mixing entropical contribution. This could be either explained by the high similarity of these extractants or a negligible entropic contribution.

Since there was no synergistic effect observed neither in distribution coefficient nor in viscosity, the idea of mixing two extractants was not further followed up. Moreover, changing the geometry of the extractant to a more curved one seems to be more promising. Furthermore, for the targeted extraction process, one single molecule would be easier to handle than an extractant mixture. Due to the strong radiation and acidity, a different degradation behavior can lead to a change in viscosity and extraction behavior with time.

It could be possible that a stronger effect is visible by mixing a monoamide extractant with a strongly curved one such as TBP. However, mixing a monoamide with an organophosphorus extractant implies further disadvantages such the loss of complete incinerability or the introduction of problematic degradation products. Since this investigation is not relevant for application, also this approach was not further followed up.

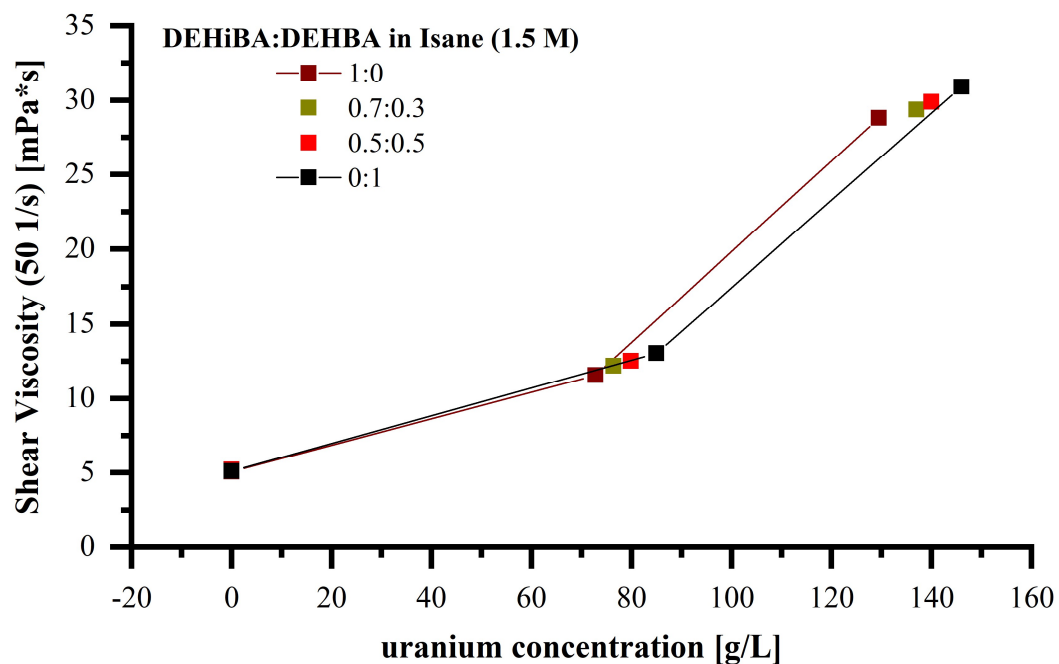


Figure 88. Viscosity increase due to increasing uranyl concentration in the organic phase for different DEHiBA/DEHBA mol ratios at 25 °C. The total extractant concentration was kept constant at 1.5 M. The solid lines are only added for better overview and do not represent the viscosity curve. The corresponding uranyl concentrations in the organic phase result from the contact of the organic phase with aqueous stock solutions of 3 M nitric acidity containing 0, 125 or 240 g/L uranyl.

IV.4 Conclusion

In this chapter, the different formulation strategies proposed in Chapter III were briefly tested. A detailed investigation was not attempted, since besides viscosity a number of further parameters have to be considered, which would have gone beyond the scope of this thesis.

Changing the extractant to a one that is as curved as possible one was identified as the most promising approach. The suitability of the molecule MOEHA could be predicted, confirmed and explained by the use of the spontaneous packing parameter derived from geometry and concepts of gemini surfactants. Supplementary addition of bulky and small additives such as 2-methyl-tetrahydrofuran, toluene or octane as well as changing the diluent into a more penetrating one can contribute to further decrease the viscosity of extractant systems.

In contrast hereto, the mixing of two monoamide extractants that show similarity was identified as less promising. The entropic contribution for these systems seems to be small, whereby the viscosity is determined by the mol ratio between the two extractant. Therefore, the viscosity has its minimum in presence of the diluted pure extractant with the higher spontaneous packing parameter.

V APPLICATION OF THE MODEL TO AQUEOUS SYSTEMS

The model described in Chapter III is a model and based on principles that are generally valid. Therefore, its application is not limited to extractant systems. It can also be adjusted for use in surfactant systems in aqueous media.

In the following chapter, its wider validity is demonstrated by applying the model to anionic surfactant solutions in presence of salt and model solutes. This system is relevant for several industrial applications, particularly of perfume formulation for cosmetic applications.

Below, this topic is briefly introduced and the theoretical background briefly revised. After that, known experimental observations and the context behind is elucidated. Then, the theoretical modifications necessary to adapt the model to this specific system are presented. Finally, the results are discussed and compared with the experimental observations.

Parts of this Chapter are used for the following Publication:

M. PLEINES, W. KUNZ, T. ZEMB, D. BENCZÉDI, W. FIEBER, Molecular Factors governing the Viscosity Peak of Giant Micelles in Presence of Salt and Fragrances, *submitted to Journal of Colloid and Interface Science* **2018**.

V.1 Introduction

Viscosity and viscoelasticity play an important role in industry. The rheology of the product has a great importance for the producer and the consumer.^[122, pp.453–545]

In food industry, for example, the rheology of a product affects amongst others the production, the texture and smoothness of a product, but also the long-term stability.^[240] In paint and coating industry, optimal viscosity and viscoelasticity are needed to ensure homogeneous leveling and avoid sagging. Furthermore, the viscosity controls also the sedimentation of color pigments and consequently the long-term stability.^[241] For household cleaners, viscosity affects the residence time on vertical surfaces and therefore the cleaning and reaction time. Moreover, higher viscosity avoids splashing of the dangerous alkaline or acidic products.^[122, pp.515–541] As a last example, from the industry for personal care products and cosmetics, shower gels should easily flow from the container, but should have a pleasant appearance and have a strong gel character giving the impression of a high-quality product and facilitating the application onto the body.^[122, pp.493–515]

Giant micelles can form gel-like structures with particular properties that make them indispensable for such consumer and industry products.^[122,242,243] Their rheological properties are the consequence of a complex interplay between different micellar length and time scales, which are significantly influenced by temperature, the molecular structure and the concentration of surfactants, co-surfactants and other additives. The viscoelastic property of entangled giant micelles has been the subject of numerous studies providing a wealth of insights on mechanistic aspects at molecular and supramolecular levels.^[130,244–246] Particularly interesting are surfactants with charged headgroups that show a strong response to the presence of counterions and where the addition of small amounts of salt can lead to an increase of the viscosity by several orders of magnitude. As indicated in Chapter I, these interactions result in a non-monotonic trend as the ionic concentration is increased, referred to as the “*salt curve*” by application scientists, and characterized by a viscosity increasing from values that are close to that of water to a pronounced viscosity peak, followed by a subsequent decrease. This characteristic behavior can be explained by a continuous topological transformation of the micelles from spherical, to elongated, to entangled wormlike ones and finally to branched cylinders decorated by endcaps. On a nanometer-scale, these effects are the consequence of the increasing charge screening of the surfactant headgroups by the added electrolytes.^[135,138,141,142,247–249] Testing the effect of adding a chaotropic, kosmotropic or antagonistic salt represents thus a convenient formulation tool in the field of personal care

applications and beyond, where NaCl is routinely used to thicken aqueous surfactant solutions.

One of the most widely used surfactants in consumer products for body care, such as shower gels, liquid hand soap or shampoos is sodium lauryl ether sulfate (SLES) ^[250]. This sodium salt of coconut oil fatty alcohols (12-14 C-atoms) with a degree of ethoxylation of 2-3, exhibits good cleaning and foaming properties and also possesses good solubility in hard water.^[251]

The delicate balance of such formulations can be disrupted, however, by the simple addition of further ingredients, such as fragrance oils for example, making the macroscopic behavior such as viscosity or viscoelasticity difficult to predict.^[252,253] This influence was investigated by several groups and is generally estimated based on experience.^[254–257] In this chapter, the minimal model presented in Chapter III is applied to the system of SLES in water in the presence of different salts and fragrances.

In the past, only a few studies have tried to develop models for the growth of giant micelles. Two recent studies based on coarse grained dissipative particle dynamics (DPD) simulations were able to predict radial distributions within a micelle^[258] or to calculate scission free energy that determines the micellar length^[259] in the presence and absence of fragrances. Kralchevsky and co-workers recently presented a self-consistent, quantitative model for the growth of wormlike micelles for non-ionic surfactants.^{319]} The model is based on an accurate description of the different contributions to the micelle free energy, namely the interfacial tension, the steric repulsion of headgroups, as well as the conformational free energy of the surfactant hydrocarbon chains in the micellar core. An excellent agreement between the expectation from theory at meso-scale and experimental values has been achieved. Nevertheless, to our knowledge, no quantitative predictive model exists that translates molecular organization at nano-scale of charged surfactant molecules forming giant micelles into macroscopic properties such as the viscoelasticity.

This model presented in the following is based on different theories in the fields of colloidal chemistry and polymer physics and therefore represents a new promising thermodynamic model. It combines the concepts of molecular packing parameters, supramolecular curvature and elasticity of the surfactant film, and polymer physics extended to “living polymer” in the case of giant micelles, respectively. Emphasis will be placed on the prediction of the salt curve of SLES. A quantitative approach to predict both the position and the amplitude of the viscosity peak of giant micelles will be shown. In addition, the influence of additives such as salts and single fragrance raw materials will be modeled and compared to experimental data.

V.2 The “salt curve” in presence of model solutes and fragrances

The influence of fragrance molecules on the salt curve of SLES in water was investigated in detail by A.Parker and W.Fieber by rheology.^[126] These results are shortly summarized in the following.

The salt curve of 10 wt% of SLES in the presence of NaCl as well as a schematic evolution of the microstructure is shown in **Figure 89**.

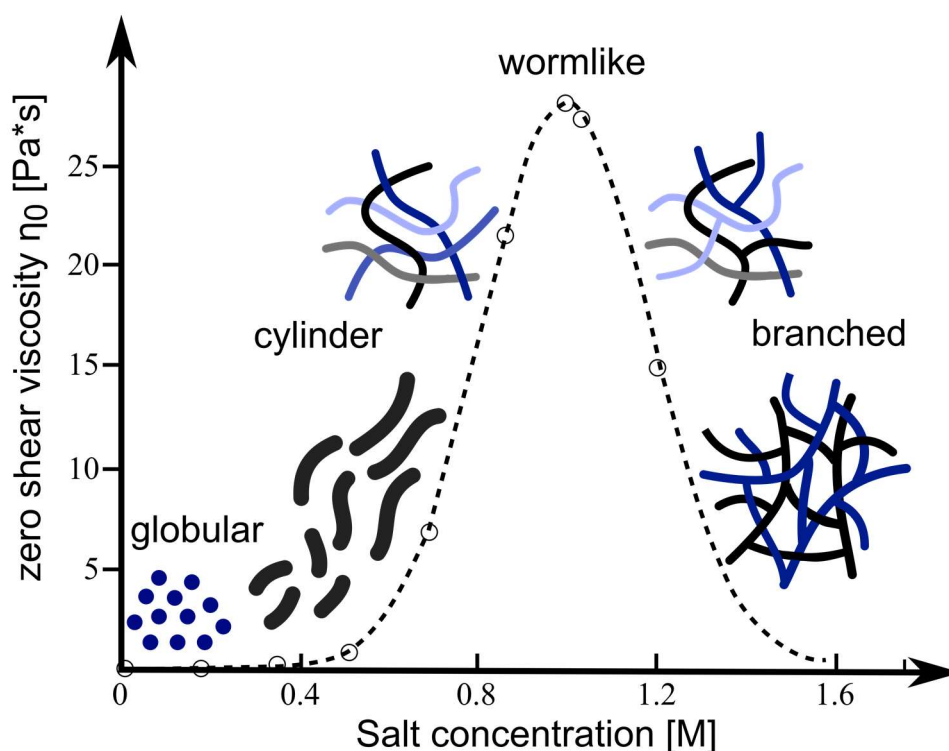


Figure 89. Salt curve of 10 wt% SLES in water in presence of NaCl and the schematic evolution of the microstructure. Experimental values taken with permission from [126].

In presence of fragrances, the viscosity curve can change. **Figure 90** shows the influence of the four model perfume molecules vanillin, limonene, linalool and citronellol compared to the viscosity curve of pure SLES diluted in water.

The general Gaussian curve is preserved for all four molecules. Parker *et al.* could distinguish between two independent mechanisms that affect the position and the amplitude of the salt curve: a co-surfactant and a co-solvent type of effect, where the studied fragrance molecules typically showed characteristics that were a linear combination of the two effects.^[126] First, a shift of the viscosity maximum to lower salt concentration can occur. That is the case for the perfume molecules linalool and citronellol. This effect was attributed to a co-surfactant effect.

Fragrance molecules are typically amphiphilic and insert into the surfactant film. The resulting interface flattening leads to a transition from spheres to cylinders at lower salt content.^[126]

A second effect that can occur is a decrease in maximum viscosity. This effect is seen for all perfume molecules investigated except limonene and is most pronounced for the most hydrophilic molecule – vanillin. The effect of reduction of overall viscosity was referred to have its origin in a film softening effect of the perfume molecules and could be related to the hydrophilicity of the corresponding fragrances. This effect was further declared to be independent and uncoupled of the co-surfactant effect that leads to a shift of the curve.^[126]

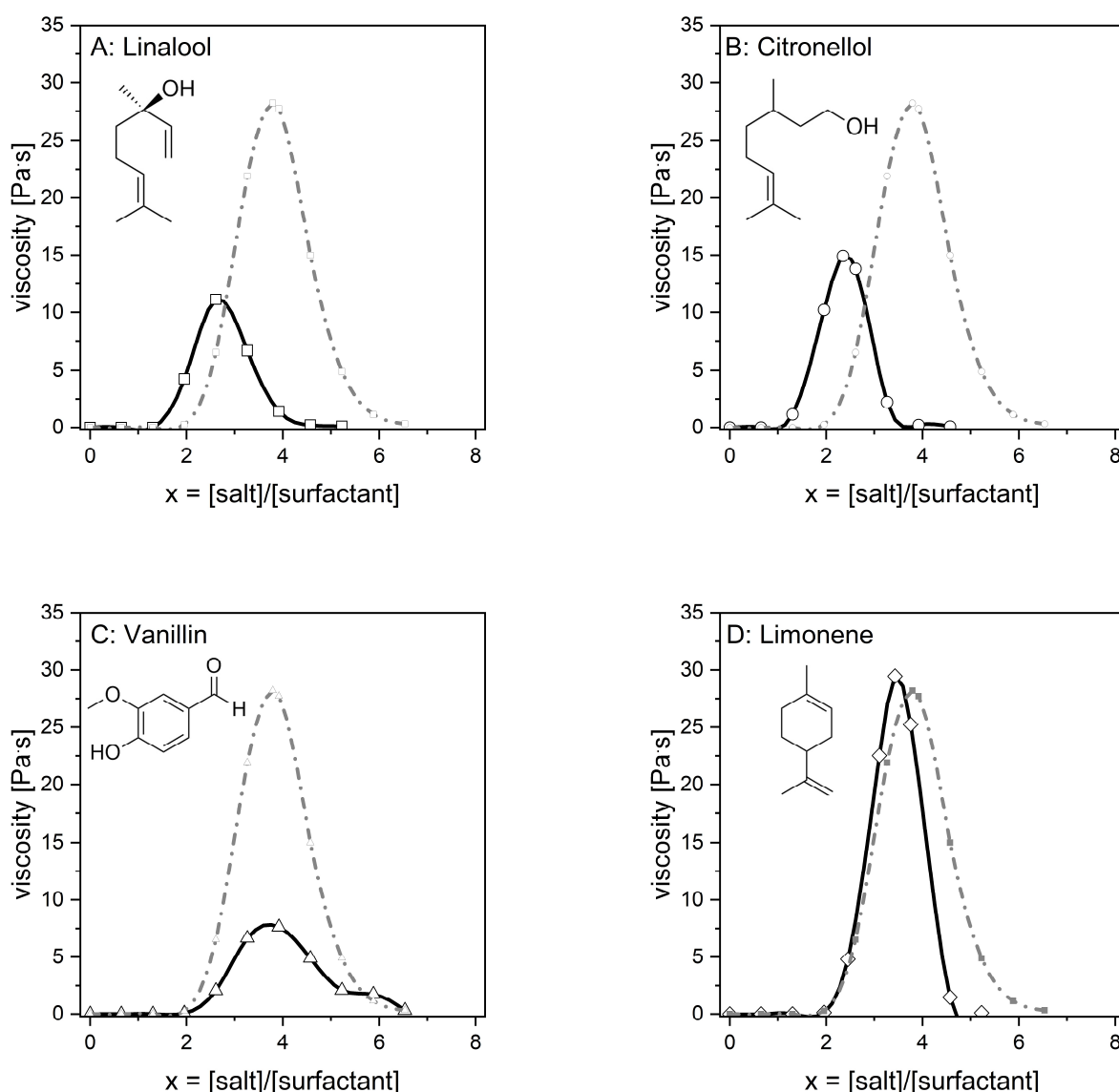
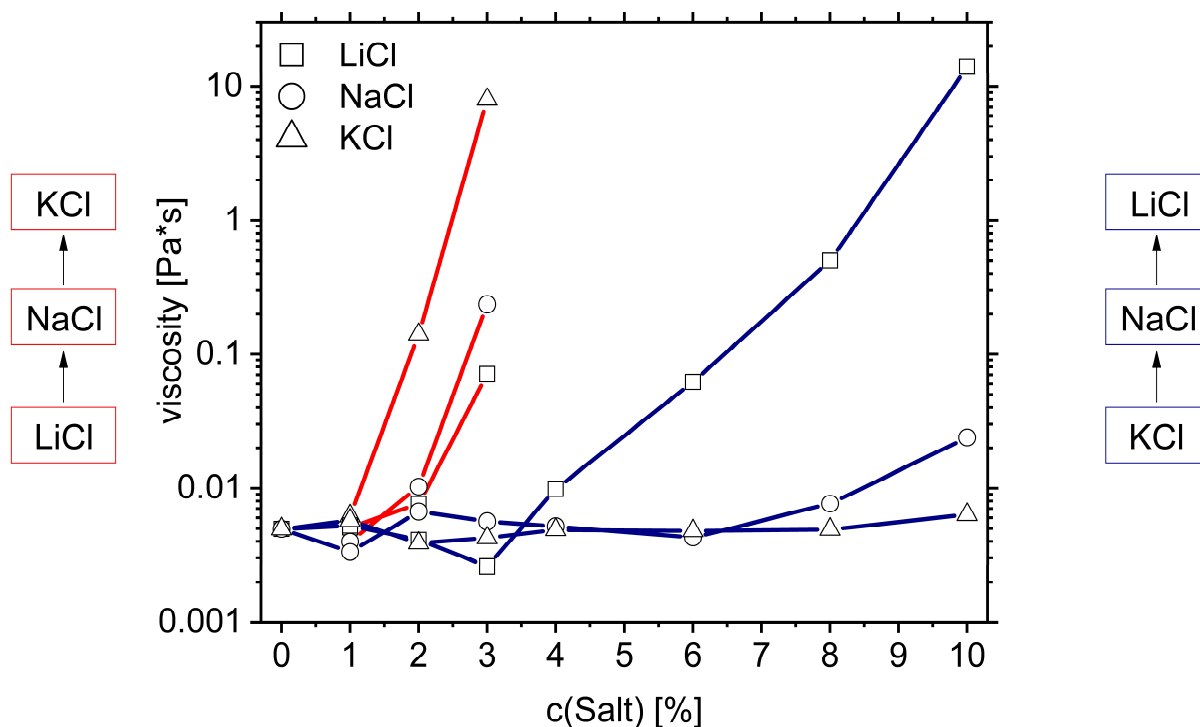
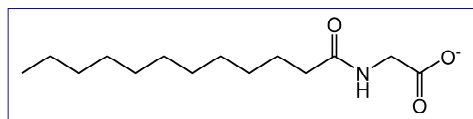


Figure 90. Salt curves of 10 wt% SLES in presence of salt and 0.5 wt% of different perfume molecules. The viscosity curve of SLES in absence of perfume molecules is shown for each of the four examples in grey. Experimental values taken with permission from [126].



Hofmeister has investigated in his highly quoted work “Zur Lehre von der Wirkung der Salze”^[260,261] more than one century ago the effect of salt on proteins. His main conclusion – the Hofmeister series – was to correlate the effectiveness of protein denaturation of several salts with their “water ordering capacity”, later related to hydration.^[262,263] This concept was later extended to the “concept of matching affinities” in order to understand ion pair formation in aqueous solution.^[262,264] The concept is based on the idea that contact ion pairs of oppositely charged ions are only formed spontaneously when they have similar water affinities.^[264] As a consequence, small and ‘*hard*’ anions interact preferentially with small and ‘*hard*’ cations and big and ‘*soft*’ anions with big and ‘*soft*’ cations. This idea can be imagined as follows. Two small and hard oppositely charged ions (also called *kosmotropes*) are strongly hydrated, but their reciprocal attraction is strong enough to expel the hydration shells between them. In contrast hereto, two oppositely charged ‘*soft*’ ions (also called *chaotropes*) are weakly hydrated

and the electrostatic interaction between them is also less pronounced than in the case of two kosmotropes. However, this interaction is strong enough to expel the weakly bound hydration sphere and to form an ion pair. For the combination of a kosmotropic and a chaotropic ion, the reciprocal interaction does not suffice to make the ‘*hard*’ ion lose his hydration water. Therefore, the ions stay separated by hydration water and do not form ion pairs.^[265]

For SLES, possessing a sulfate group which is classified as a ‘soft’ functional group according to the concept of matching affinities, the viscosity increase starts at lower salt concentration if potassium chloride is used as salt. For the ‘harder’ ions Na^+ and Li^+ , the steep viscosity increase occurs at higher salt concentration.

In contrast hereto, if a carboxylic surfactant such as sodium lauryl glycinate is used as surfactant, the salt response is inverse. The sphere-to-rod transition in presence of lithium chloride occurs at lower salt concentration, while the transition occurs at much higher salt content in case of sodium and potassium chloride.

The viscosity increase seems to be related to the concept of matching affinities according to the Hofmeister series. Strong ion pair formation between a soft headgroup and a soft metal ion or respectively a hard anionic headgroup and a hard cation leads to a stronger screening of the electrostatic repulsion of the surfactant headgroups reducing the spontaneous curvature of the surfactant (*cf.* **Figure 92**).

The observations described in this chapter will be tried to be explained and implemented in a predictive way in the model. The theoretical background will be explained in detail in the next subchapter.

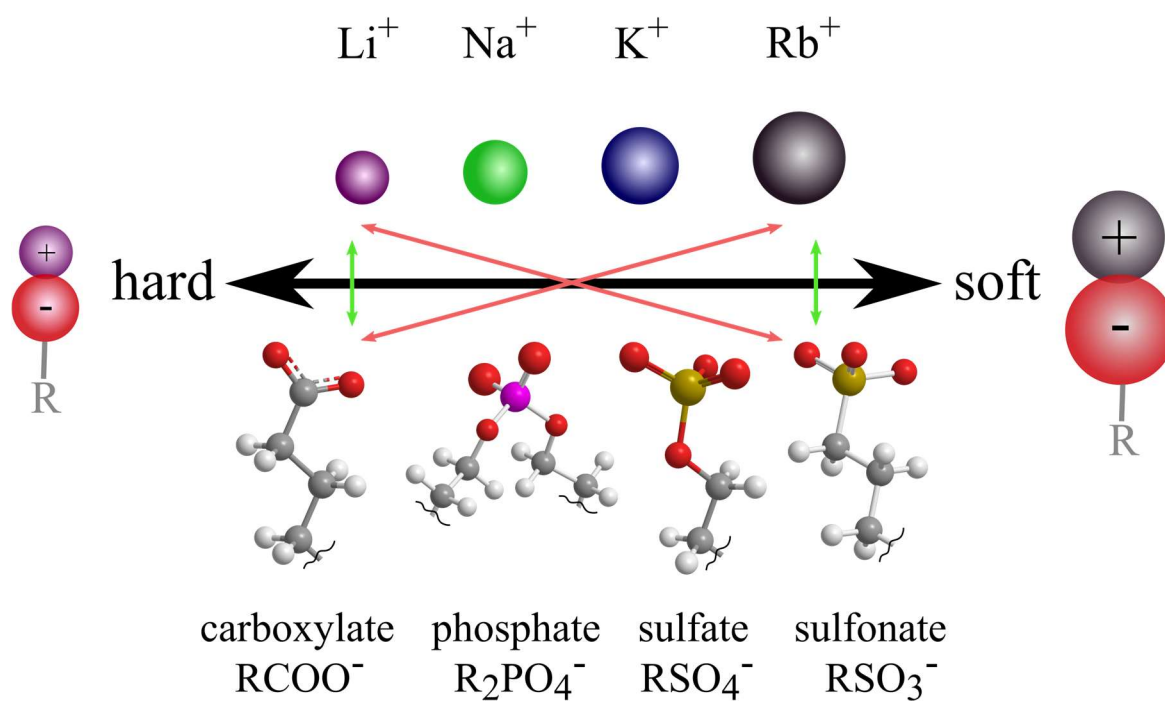


Figure 92. Schematic representation of the concept of matching affinities according to the Hofmeister series. Replotted and adjusted from [266].

V.3 Adapting the model to the aqueous case

The main principle of the model stays the same. However, in order to repeat the model, to recapitulate the main idea and to clarify the transfer in the aqueous case, in the following the main steps are explained in detail. Furthermore, the modifications necessary to adapt the model to the case of anionic surfactants in the presence of salt and model solutes are presented.

V.3.1 General Theory for the calculation of the Microphase Distribution and Viscosity

As in the organic phase, the model is based on three well-established key elements derived from chemistry, physics and chemical engineering. It combines

- the concept of pseudo-phases introduced by Shinoda^[225] and generalized by Tanford^[44],
- the expression for the free energy of bending for surfactant films derived from the concept works of Ninham^[54], Hyde^[65,73] and Israelachvili^[46], further generalized by taking into account the whole surfactant molecule and not only the hydrocarbon chain length (see below for a detailed description). With this modification, our coarse grain approach avoids unnecessary details about the location of solutes in “core”, “palisade” and other layers for which bending is difficult to determine.
- as well as classical theories in polymer physics, translated to “living polymer” or “connected wormlike micelles” by Cates^[116,117,124], Lequeux^[135] and quantified by Candau and Khatory^[142].

The micellar structure in aqueous solution is described as the combination of four different microphases – endcaps, cylinders, junctions (or equivalently, branching points) and monomers – in thermodynamic equilibrium with each other. Except for monomers, for each of these pseudo-phases, an effective packing parameter P can be precisely defined (*cf.* **Figure 93**) Provided that not only hydrocarbon chains, but the whole hydrated micelle is considered, P is well-defined for endcaps considered as half-spheres (1/3) and long cylinders, flexible or not (1/2)^[46]. For junctions, the value of P is intermediate between the one of cylinders and the one of bilayers, respectively, since they can be regarded as a central bilayer-like region surrounded by three semi-toroidal sections.^[267] Therefore, the approximate value of P for junctions formed by SLES molecules was set to 0.8 assuming a slightly higher influence of the bilayer part. A direct effect of the monomers in water on the viscosity evolution is negligible, since the surfactant concentrations used in this study of around 260 mM (10% w/w) are several orders of magnitude higher than the *cmc* of the surfactant considered (~ 0.7 mM).

The relative quantities of the present pseudo-phases are given in terms of chemical potentials originating in “frustration”, *i.e.* differences between effective and spontaneous packing. Therefore, the change of the spontaneous packing parameter subsequent to an addition of electrolyte and the resulting changes in the effective packing parameters are the basis of the calculation of the microphase distribution for any sample compositions.

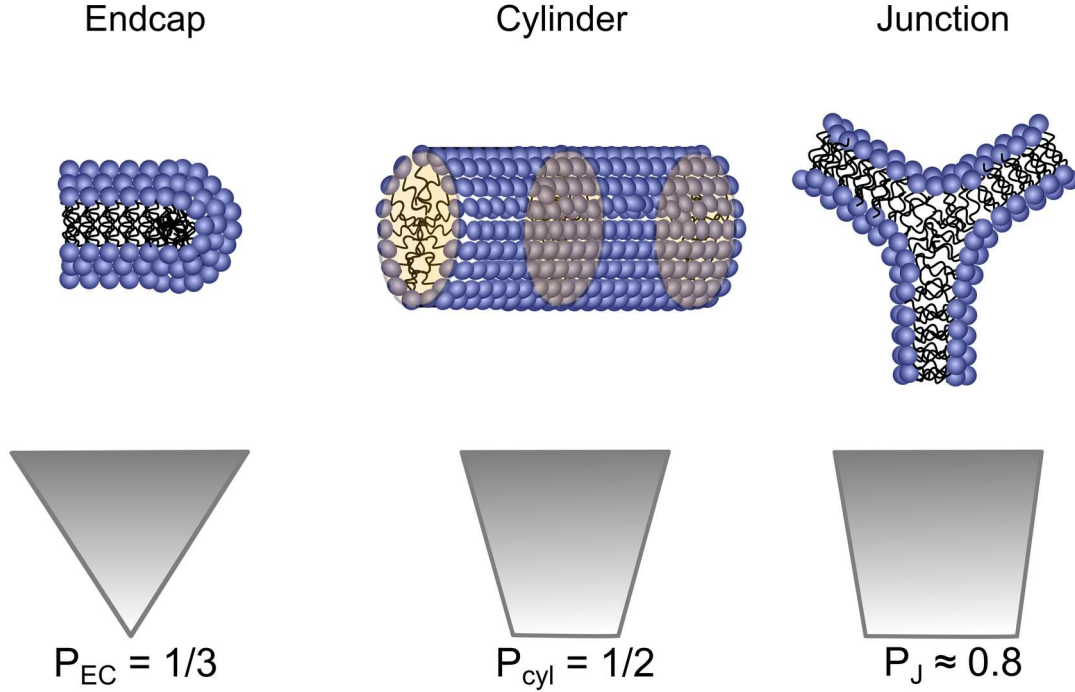


Figure 93. The three viscosity-determining microphases in chemical equilibrium: endcaps, cylinders and junctions

V.3.1.1 Microphase distribution

According to the concept of pseudo-phases, the chemical potential μ of a single surfactant i in water is equal to the chemical potential of i inside a microphase.^[44,225]

$$\mu_{i,\text{endcaps}} = \mu_{i,\text{cylinders}} = \mu_{i,\text{junction}} = \mu_{i,\text{monomer}} \quad (85)$$

The chemical potential μ_i of one surfactant inside one of the microphases can be split into a standard reference potential μ_i^0 and a concentration-dependent term $RT \ln a_i$, where a_i is the activity.

$$\mu_{i,\text{endcaps}} = \mu_{i,\text{endcaps}}^0 + RT \ln a_{i,\text{endcaps}} \quad (86)$$

$$\mu_{i,\text{cylinder}} = \mu_{i,\text{cylinder}}^0 + RT \ln a_{i,\text{cylinder}} \quad (87)$$

$$\mu_{i,\text{junction}} = \mu_{i,\text{junction}}^0 + RT \ln a_{i,\text{junction}} \quad (88)$$

According to the concepts developed by Hyde and co-workers^[62], the bending contribution to the free energy of the surfactant can be expressed by a harmonic approximation, as the deviation of the actual surfactant geometry from the preferred one multiplied with a bending constant κ^* .^[73]

$$F_{\text{bending}} = \frac{\kappa^*}{2} (P - P_0)^2 \quad (89)$$

The validity of this relation does not depend on the thickness of the layer to be bent. In classical works adapted to micelles with flexible headgroups and well-defined linear hydrocarbon chains, $P = (v/a \cdot l)$ and $P_0 = (v/a_0 \cdot l)$ are the effective and the spontaneous packing parameters, respectively, with v being the volume of the nonpolar moiety, a and a_0 the corresponding area per surfactant headgroup and l the mean surfactant chain length. In the case of alkyl sulfates, the bending modulus κ^* lies in the order of 2-3 $k_B T$ per molecule *i.e.* of the order of 5 kJ/mole.^[226,227,268]

The classical approach to micellar packing, taking into account the hydrocarbon chain lengths as the only length to be considered, has opened the field of predictive modeling of non-ionic and ionic micelles. The packing parameter, a scalar number, stands as “apolar volume” divided by an area multiplied by an average “length”^[46], all three values taken at the scale of one molecule belonging to an “untearable” film made of surfactants. Since entropy dominates chain conformations, the average length does not depend on the presence of solutes. However, it requires determining whether organic solutes are in the core or in the palisade layer, as well as estimating the neutral plane variation in the presence of added electrolytes. In order to avoid introducing parameters linked to the palisade/core equilibrium^[269,270], we use here an alternative definition of the respective spontaneous packing parameters. Since the value of length is a matter of definition, we now use the full length of a surfactant molecule including the headgroup. To be consistent, the volume of the water molecules bound to the headgroup must be taken into account in the molecular volume. Also, the area per molecule has to be taken at the water/hydrated surfactant interface, and not at the interface between chains and headgroups. This definition reduces the number of parameters, because the location of the solute in headgroup “palisade” region or in the “core” of micelle need no more to be specified.

$$P_0 = \frac{v_{SLES}}{a_I \cdot \langle l_{C+I} \rangle} \quad (90)$$

with v_{SLES} representing the effective molar volume of SLES including hydrophobic tail and

polar headgroup as well as hydration water. a_l is the respective area per surfactant at the water-micelle interface (and not at the head to hydrocarbon interface) and $\langle l_{c+l} \rangle$ the mean surfactant length including the interface thickness d_l . This alternative definition of P_0 is self-consistent taking into account Gauss' theorem of differential geometry, and is shown in **Figure 94**.

In the next step, the evolving structure of linear surfactant micelles is considered as built from cylindrical building blocks in dynamic equilibrium with endcaps and junctions as defects. Therefore, the standard reference potential of cylinders is defined as the reference state. As a result, the difference in the standard reference chemical potentials of endcaps and junctions relative to the chemical potential of cylinders can be calculated from the differences in free energy of bending.

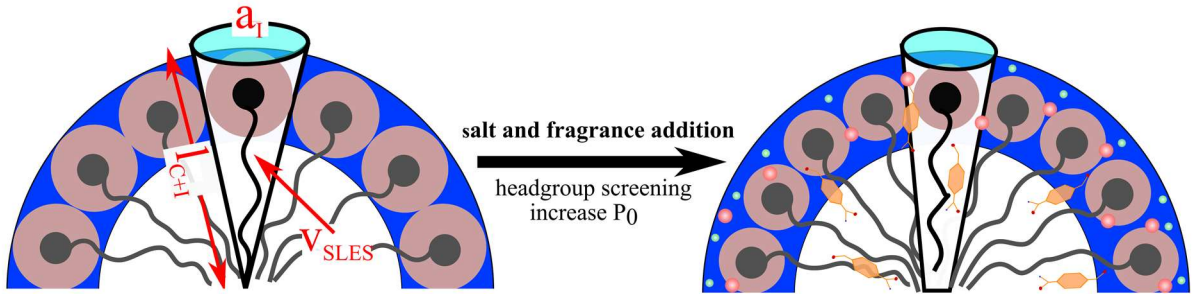


Figure 94. Schematic description of the alternative definition of the spontaneous packing parameter

$$\mu_{i,EC}^0 - \mu_{i,cyl}^0 = \frac{\kappa^*}{2} \cdot \left[N_{agg,EC} (P_{EC} - P_0(x))^2 - N_{agg,cyl} (P_{cyl} - P_0(x))^2 \right] \quad (91)$$

$$\mu_{i,J}^0 - \mu_{i,cyl}^0 = \frac{\kappa^*}{2} \cdot \left[N_{agg,J} (P_J - P_0(x))^2 - N_{agg,cyl} (P_{cyl} - P_0(x))^2 \right] \quad (92)$$

The spontaneous packing parameter is varying with the salt content expressed as the excess mole fraction $x = [\text{salt}]/[\text{surfactant}]$. The scaling of this variation is explained later. Therefore, also the standard reference chemical potentials are dependent on the amount of additionally added salt. The cost in free energy to convert a cylinder microphase into an endcap or respectively into junction units gives the relative probability of occurrence of each microphase. Combining equations (86) - (88) and (89) - (90) leads to an expression for the relative concentration of surfactants in each microphase.

$$\exp \left(\frac{\mu_{i,endcap}^0 - \mu_{i,cylinder}^0}{RT} \right) = \frac{c_{i,cylinder} \cdot \gamma_{i,cylinder}}{c_{i,endcap} \cdot \gamma_{i,endcap}} \quad (93)$$

$$\exp \left(\frac{\mu_{i,junction}^0 - \mu_{i,cylinder}^0}{RT} \right) = \frac{c_{i,cylinder} \cdot \gamma_{i,cylinder}}{c_{i,junction} \cdot \gamma_{i,junction}} \quad (94)$$

The ratio of activity coefficients γ_i can be estimated in a first approximation from the number of surfactants per microphase N_{agg} as $\gamma_{i,microphase} \sim 1/N_{agg, microphase}$. Respecting mass conservation, the total concentration of endcap, cylinder and junction units can be calculated from the relative proportions c_{cyl}/c_{EC} and c_{cyl}/c_J and the total concentration of surfactants c_S in solution. The result is the microphase distribution of endcaps, cylinders and junctions dependent on the salt content.

$$N_{agg,cyl} \cdot c_{cyl} + N_{agg,EC} \cdot c_{EC} + N_{agg,J} \cdot c_J + (c_{monomers}) = c_S \quad (95)$$

$$c_{cyl} = \frac{c_S}{N_{agg,cyl} + \frac{N_{agg,EC}}{c_{cyl}/c_{EC}} + \frac{N_{agg,J}}{c_{cyl}/c_J}} \quad (96)$$

$$c_{EC} = \frac{c_{cyl}}{c_{cyl}/c_{EC}} \quad (97)$$

$$c_J = \frac{c_{cyl}}{c_{cyl}/c_J} \quad (98)$$

with $c_{cylinder}$, c_{endcap} and $c_{junction}$ representing the concentration of each microphase and $N_{agg,cyl}$, $N_{agg,EC}$ and $N_{agg,J}$ being the estimated aggregation number of the corresponding microphases. As a result, the evolution of the distribution of microphases can be estimated from the evolution of the spontaneous packing parameter with the excess salt to surfactant ratio - in the following denoted as the excess salt content x .

V.3.1.2 Microphase equilibrium controlling the viscosity

The microphase distribution that is given by the evolution of the spontaneous packing parameter provides the number of endcaps, cylinders and junctions at a given salt concentration thereby defining the network structure of the giant micelles. Based on this distribution it is now crucial to make the link to macroscopic properties of the system, in particular to viscosity. According to Cates the following relationship for reptating chains can be applied^[117]:

$$\eta \sim L^3 \quad (99)$$

where η is the zero-shear viscosity of an entangled solution of giant micelles and L is the mean contour length of the micelles. In the case of fast micellar breaking the scaling exponent is supposed to approach unity, which is the case for the present system^[126] around the viscosity maximum of the salt curve of SLES. However, our current model does not provide us with any information about time scales and dynamic aspects of micellar breaking and recombination, and relaxation regimes of the system cannot be predicted. Therefore, we will rely primarily on

purely geometrical aspects and length scales. Khatory *et al.* investigated the structure of entangled and branched wormlike micelles.^[142] Especially the presence of junctions necessitated a new definition of the contour length L (endcap to endcap distance in purely linear micelles without junction) as an effective length L_{eff} , which is defined as the “*harmonic mean between the average distance from one point along the micelle to the first cross-link and the average distance from that point to the first endcap, or equivalently, the ratio of the total length over the concentration of endcaps plus twice that of connections*”^[142]. Applying this method of estimation to the distribution of microstructures resulting from frustration differences between pseudo-phases, which is the bases of our model, the averaged total length L_{eff} per volume of the structure forming surfactants is given by the sum of the respective lengths l_i of the single microphase units multiplied with their corresponding concentration.

$$L_{eff} = \frac{c_{EC} \cdot l_{EC} + c_{cyl} \cdot l_{cyl} + c_J \cdot l_J}{c_{EC} + 2c_J} \quad (100)$$

Consequently, L_{eff} will be used in Eq. (99) to calculate the macroscopic zero-shear viscosity. The scaling constant in the Cates model needs to be optimized to match the calculated values with the experimental data. In this work, this constant was set to a value of 1/12 [Pa·s/nm³].

V.3.2 Evolution of the spontaneous packing parameter

The excess salt content x determines the lateral electrostatic repulsion between the anionic headgroups^[69], and consequently the spontaneous packing parameter increases with increasing salt concentration, while the spontaneous curvature of the surfactant film decreases. In order to simulate the microphase distribution as a function of x , the evolution of the area per headgroup or respectively the evolution of the spontaneous packing parameter must be determined. In a first approximation, v_{SLES} , representing the effective molar volume of SLES including the hydration water of the polar moiety, and $\langle l_{C+I} \rangle$, the mean surfactant length including the interface thickness d_I , are assumed to be salt-independent. The effective molar volume of SLES was derived from its known density of 1.1 g/cm³ yielding 577 Å³ per molecule^[126]. The mean chain length of the molecule can be estimated by Tanford's formula to be 16.7 Å^[72]. The degree of hydration as well as the interfacial area per molecule were determined by Clancy *et al.* to be close to 4.5 Å including 3-4 molecules of water per headgroup.^[271] The latter is consistent with a high resolution neutron scattering (data up to 6 nm⁻¹ in q -space) determined by Cabane *et al.* who found the “interfacial thickness” defined as the minimal distance to travel from a pure hydrocarbon to an aqueous headgroup domain of SDS micelles in water to be “*well below 5 Å*”^[272]. Consequently, the evolution of the spontaneous packing parameter is mainly

influenced by the evolution of the area per molecule at the water-micellar interface.

The concentration range of salt to be considered is defined by two limiting cases. First, the starting point of the investigation is the case without added salt, where the concentration of counterion solely comes from the sodium salt of the surfactant. The spontaneous packing parameter can be derived from Clancy *et. al*^[271], who have determined the interfacial area at the headgroup to solvent interface per surfactant of SLES in water by light scattering and SAXS to be 100.5 \AA^2 (referred to a_{\max}). This is clearly different from the well-known area per headgroup at the nonpolar core to headgroup interface considered with earlier definitions of bending at the hydrocarbon core interface.

Second, the end-point of the titration was chosen to be the point of macroscopic phase separation. The origin of this phase separation can be related to a predominance of junction units.^[144,228] For the case of 10 wt% of SLES in water, the phase separation starts at a NaCl concentration of around 12 wt%, corresponding to an excess salt content $x \approx 8$. No evidence for the existence of liquid crystals has been observed. Therefore, at this concentration, the spontaneous packing parameter resulting from a steady decrease of the interfacial area per molecule should approach the effective packing parameter of 0.8, chosen for junction microphases as shown above, corresponding to a minimal area per surfactant of 40 \AA^2 (a_{\min}).

In order to calculate the spontaneous packing parameter P_0 at a given excess salt content x , the evolution of the area per headgroup was extrapolated according to an association-dissociation process.



$$K_d = \frac{[Na^+][SLES^-]}{[Na^+SLES^-]} \quad (102)$$

$$[Na^+SLES^-] = \frac{[Na^+]_0[SLES^-]}{K_d + [SLES^-]} = \frac{[Na^+]_0\{[SLES^-]_0 - [Na^+SLES^-]\}}{K_d + \{[SLES^-]_0 - [Na^+SLES^-]\}} \quad (103)$$

$$\begin{aligned} [Na^+SLES^-]\{K_d + [SLES^-]_0 - [Na^+SLES^-]\} \\ = [Na^+]_0\{[SLES^-]_0 - [Na^+SLES^-]\} \end{aligned} \quad (104)$$

$$\begin{aligned} -[Na^+SLES^-]^2 + [Na^+SLES^-] \cdot \{K_d + [Na^+]_0 + [SLES^-]_0\} \\ - [Na^+]_0[SLES^-]_0 = 0 \end{aligned} \quad (105)$$

$$[Na^+SLES^-] = \frac{1}{2} \left(\pm \sqrt{[Na^+]_0^2 - 2[Na^+]_0 \{[SLES^-]_0 - K_d\} + \{[SLES^-]_0 + K_d\}^2} + [Na^+]_0 + [SLES^-]_0 + K_d \right) \quad (106)$$

with K_d being an empirical excess dissociation constant describing the local binding of excess ions, and $[Na^+]$, $[SLES^-]$ and $[Na^+SLES^-]$ being the analytical concentrations of free sodium ions, the dissociated, negatively charged form of SLES, and the associated ion pair, respectively. $[Na^+]_0$ and $[SLES^-]_0$ are the total concentration of added sodium ions and the total concentration of SLES molecules in solution, respectively. The ratio $[NaSLES]/[SLES]_0$ is referred to as the degree of excess counterion association α . In the literature, the dissociation of sodium and micelles of alkyl sulfates in absence of excess ions are found to be approximately 0.25.^[271,273–275] Assuming two limiting cases, a_{max} and a_{min} , the area per surfactant at a given excess salt content x can be accessed:

$$a_l(x) = \frac{[Na^+SLES^-]}{[SLES]_0} a_{min} + \left(1 - \frac{[Na^+SLES^-]}{[SLES]_0} \right) a_{max} \quad (107)$$

The value for K_d is difficult to determine experimentally because it has to be seen as a general dissociation constant that is averaged over all possible microphases. For the calculations in this work, an excess dissociation constant of $K_d(Na^+SLES^-) = 0.26 \text{ M}^{-1}$ was used due to better agreement with the experimental data.

V.3.3 Co-solvent effect of fragrance molecules

In order to simulate the co-surfactant effect of certain fragrance molecules^[126], the spontaneous packing parameter of the surfactant has to be modified to the spontaneous packing parameter P_0 in the presence of a solute. This represents the preferred geometry of the surfactant in the presence of fragrance molecules. The solubilization of the nonpolar solutes within the micelles has to be considered which increases the effective micellar volume. Additionally, their presence will also affect the cross-section at the micelle-water interface.

Contrary to previously published models to accommodate for interfacial solubilization of hydrophobic solutes in non-ionic surfactant microemulsions (CIT model^[276]), the situation is different in the case of charged surfactants. As has been recently shown for charged surfactants the contributions of additives to the charge density and charge screening, respectively, has to

be taken into account.^[277] The penetration of uncharged additives into the hydrophobic part of the micelle can diminish the charge repulsions between headgroups, which will get closer to each other, thereby decreasing the effective cross section area a . Similar effects can be expected for nonpolar additives with amphiphilic character such as terpene alcohols, that can act as co-surfactant and insert into the palisade layer.^[253,254,278] We propose to take into account self-consistently both contributions of a nonpolar additive to a surfactant micelle, namely the increase of hydrophobic volume and charge screening:

$$P_{mix} = \frac{v_{SLES} + x_F \beta v_F}{a_I \left[1 - A \cdot \lambda \cdot \left(\frac{a_F}{a_I} \right) \right]} \quad (108)$$

with x_F being the mole fraction of fragrance/surfactant in the solution, v_F the molar volume of the fragrance molecule derived by density measurements^[279], and a_F the excess area brought in at the solvent-micelle interface per fragrance molecule.^[276] There, a_F was obtained by fitting experimental data from microemulsion phase diagrams to the CIT model. In the absence of such data available we alternatively calculated a_F as the circular area with the radius of a sphere that corresponds to the molecular volume of the individual solute. Since this approach does not take into account the molecular shape it only gives an approximation. λ is the excess solubilization as the mole fraction of additive molecules in the surfactant interface per mole of surfactant, defined in Ref. [280]. λ was shown to be proportional to a reduction of the micellar curvature^[281], which would correspond to a shift of the viscosity maximum to the left in our case. β represents the factor that takes into account the portion of molecules that is dissolved in the aqueous solvent and *not* in the micelle. This factor is approximated by considering that the micellar partition coefficient of the solutes in SLES micelles is related to the octanol-water partition coefficient of individual fragrance molecules P_{OW} .^[282]

$$\beta = \frac{10^{\log P_{OW}} \cdot \phi_{SLES}}{1 + 10^{\log P_{OW}} \cdot \phi_{SLES}} \quad (109)$$

with the volume fraction ϕ_{SLES} of SLES, estimated at 9.1 %. The scaling constant A comprises the reduction of the dielectric constant between two negatively charged headgroups from unscreened (~ 80) to screened (~ 30).

V.3.4 Interface softening effect

A further phenomenon that has to be considered is the effect of the fragrance molecules on the interfacial rigidity constant κ^* . It was observed previously^[126] that some fragrance molecules

reduced the amplitude of the salt curve, which we attributed to a co-solvent effect taking place at the micelle-water interface. As a consequence, this leads to a softening of the interface, which was empirically related to the hydrophilicity of the fragrance and thus to its concentration in the water phase of the surfactant microemulsions. In the present model, we consider also that the distribution of the fragrance molecules between water and micelle depends, in first approximation, on the hydrophilicity of the fragrance. Consequently, it can be described by its $\log P_{ow}$ value. More precisely, with the micellar partition coefficient of SLES being equal to the octanol-water partition coefficient $P_{ow}^{[282]}$, the concentration of solutes in the water phase is inversely proportional to their $\log P_{ow}$ value. Therefore, following the empirically established relationship from [126], we suggest a model equation that describes the influence of the presence of fragrance molecules in the water phase on the film bending constant κ_p^* :

$$\kappa_p^* = \kappa_0^* \cdot \exp\left(\frac{-B \cdot x_p}{\log P_{ow}}\right) \quad (110)$$

with B being a scaling constant.

To our knowledge, interface softening was only hardly investigated in literature. Safinya and Roux have studied the decrease of bending energy of membranes and SDS in presence of pentanol^[236,283] and found a softening of the same order of magnitude as supposed here.

V.4 Results of the model

V.4.1 10% SLES pure in water

In the following, simulations according to the model described above are made assuming an anionic surfactant system of 10 wt% SLES in aqueous solution with the addition of excess amounts of salt. **Figure 95** shows the evolution of the percentage of headgroup associated sodium ions with increasing NaCl concentration. An excess dissociation constant K_d of 0.26 M^{-1} was used in the calculations, which fitted best to experimental data points (see below). The degree of counterion association α increases asymptotically from zero to one thereby approaching complete neutralization of SLES^- anions with Na^+ cations at high salt concentration.

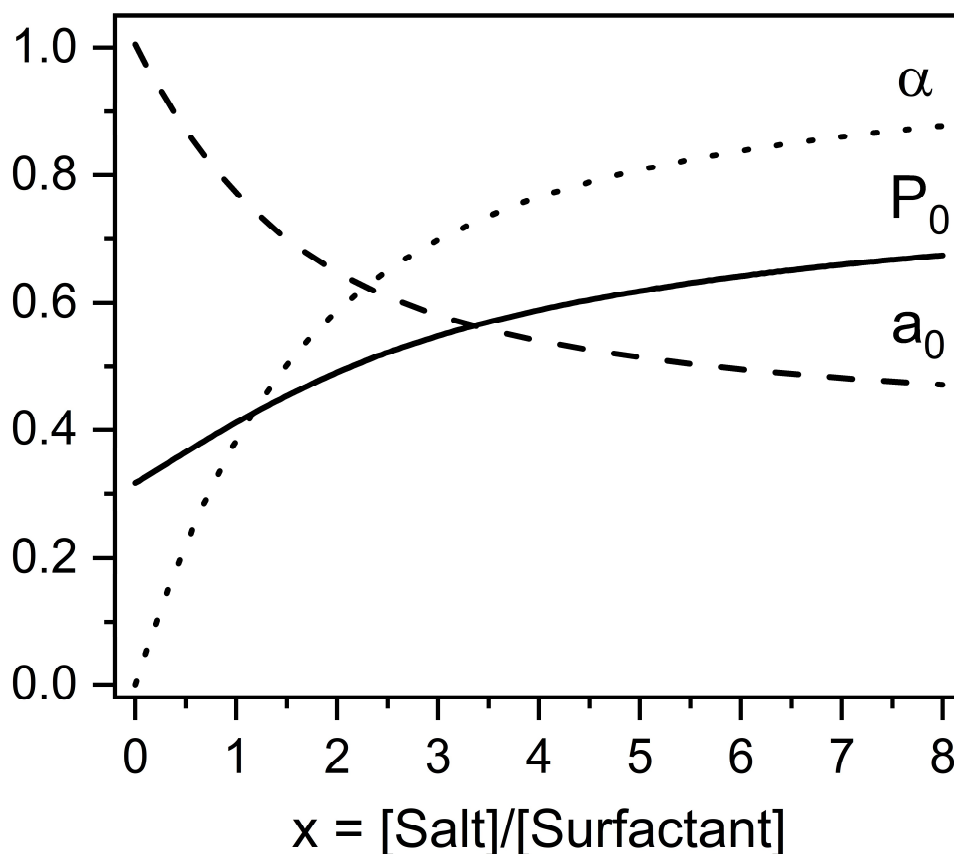


Figure 95. Simulated evolution of the percentage of sulfate headgroups of SLES associated with a sodium counterion, $\alpha = [\text{NaSLES}]/[\text{SLES}]_0$ (dotted line), the area per headgroup a_0 (dashed line) and the resulting evolution of the spontaneous packing parameter P_0 (solid line) as a function of the excess salt content x . K_d was set to 0.26 M^{-1} in this example.

With increasing ion adsorption at the micellar interface, the headgroup repulsion is screened and the area per headgroup decreases from 1.0 nm^2 without the addition of NaCl and levelling off at about 0.47 nm^2 . As a consequence, assuming that the evolution of the spontaneous

packing parameter is dominated by the headgroup size, P_0 increases with excess salt content x , according to Eq.(90). The spontaneous packing at $x = 8$, the concentration of macroscopic phase separation, is close to 0.7, confirming works of Zilman *et al.* proposing that a predominance of junctions can induce phase separation.^[144,228]

The resulting evolution of P_0 was used to calculate the cost in free energy to form endcaps or junctions from cylinders defined here as the reference state. The result is shown in **Figure 96, left**. Three different regimes can be observed. At low salt concentration, the energetically most favorable microphase is formed of endcaps, whereas there are predominantly cylinders at medium and junctions at high salt concentration, respectively. The cost in free energy of junctions vs. cylinders decreases continuously. Endcaps on the other hand become less favorable than cylinders, but the difference levels off at high salt concentration. This evolution of the energy of formation of the microphases is compatible with the findings of Tlustý and Safran, who evaluated in reduced units the relative curvature energy of endcaps and junctions.^[284] The cost in free energy allows the calculation of the probability of occurrence of each microphase (*cf.* Eq. (93) - (94)). The resulting evolution of microphase distribution with increasing NaCl concentration is shown in **Figure 96, right**. The concentration of endcaps decreases with excess salt content x while the concentration of junction units increases. The concentration of cylinder units increases and goes through a broad maximum at approximately $x = 4$, before cylinder units merge to junctions and the concentration decreases. This microphase distribution is consistent with the expected structural transition from spheres (predominance endcaps) to linear wormlike micelles (predominance cylinders) to a branched network (predominance junctions).^[249]

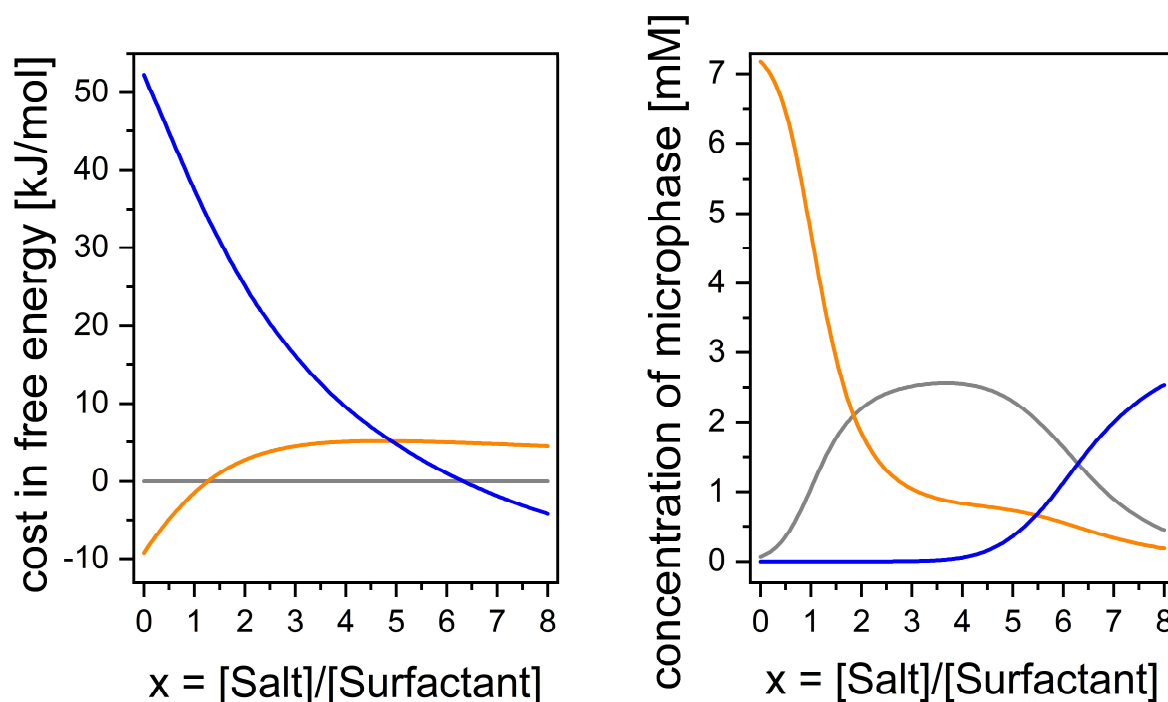


Figure 96. Left: Simulated evolution of the difference in standard reference chemical potential of endcaps (orange) and junctions (blue) respective to cylinder microphases with varying excess salt content x . Right: Microphase distribution of endcaps (orange), cylinders (grey) and junctions (blue) as a function of x .

Subsequently, effective micellar length and calculated macroscopic viscosity were obtained according to Eq. (99) and (100) (cf. **Figure 97**). Interestingly, both curves show a symmetric Gauss-shaped profile with a maximum around $x = 3.75$. The third power dependence of the viscosity on the effective micellar length narrows the peak width but does not shift the position. Finally, the calculated salt curve is compared to the experimental values of measured zero-shear viscosity of a 10% SLES solution with increasing concentrations of NaCl (taken from Ref. [126]) (cf. **Figure 98**). For a better understanding, the microphase distribution that governs the predicted viscosity curve is also displayed in this figure. The schematic evolution of the different energy levels is also displayed for three concentrations. Only two physical values are needed to adjust the predicted curve to the experimental one:

- a (vertical) scaling factor, which is an integral part of the Cates equation (Eq. (22)) to match the experimentally obtained values with the model,
- the excess dissociation constant K_d of the ionic headgroup which is the term that controls the horizontal position of the salt curve. It can be approximately accessed by electrical conductivity measurements, as well as scattering studies^[285,286]. We used a value of $K_d = 0.26 \text{ M}^{-1}$ for which the asymptotic evolution of the area per headgroup as well of the spontaneous packing parameter was in agreement with the criterium of

macroscopic phase separation at $x = 8$ and the experimental values were best reproduced. With these two scaling factors, a perfect match with the experimental data points is achieved. It should be mentioned that absolutely no scaling parameter was used to adjust the width of the Gauss-shaped curve of the calculated viscosity.

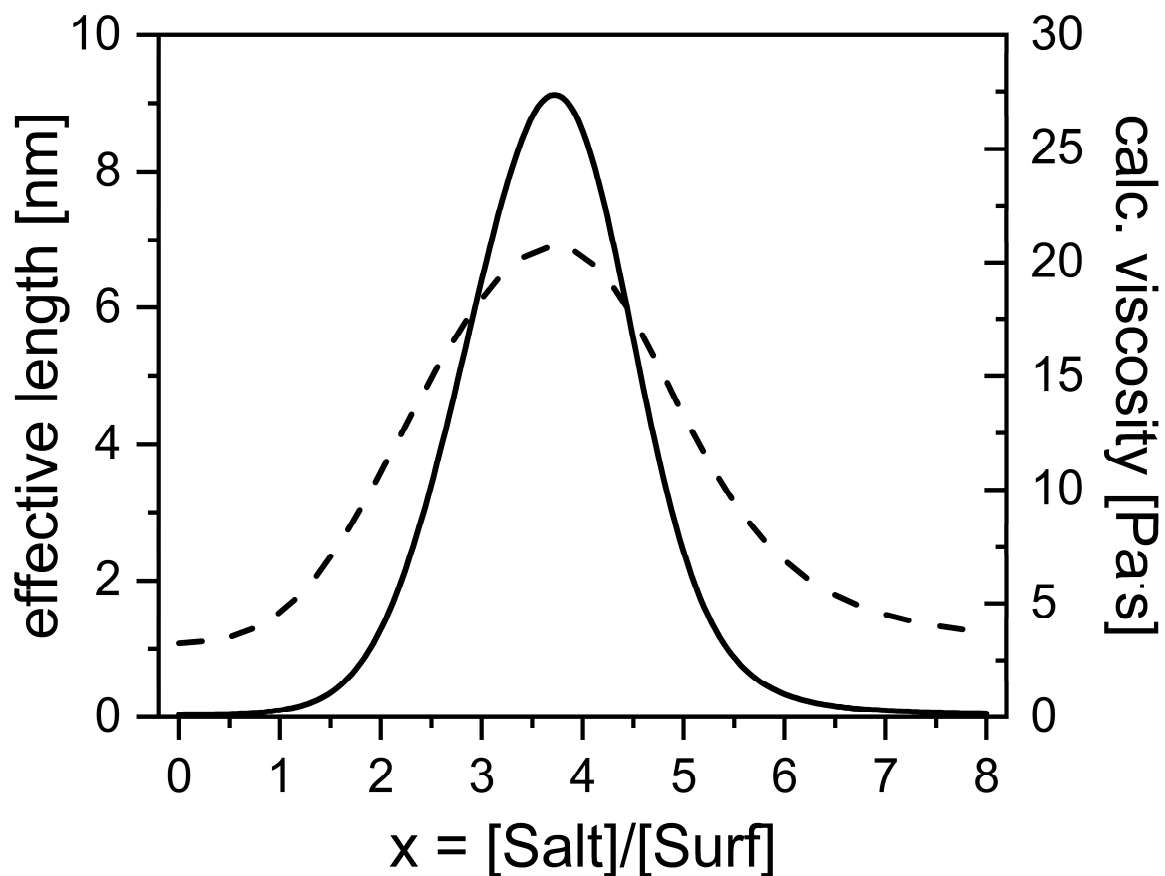


Figure 97. Evolution of the effective micellar length L_{eff} (dashed line) and the calculated viscosity resulting from the microphase distribution (solid line) as a function of excess salt content x

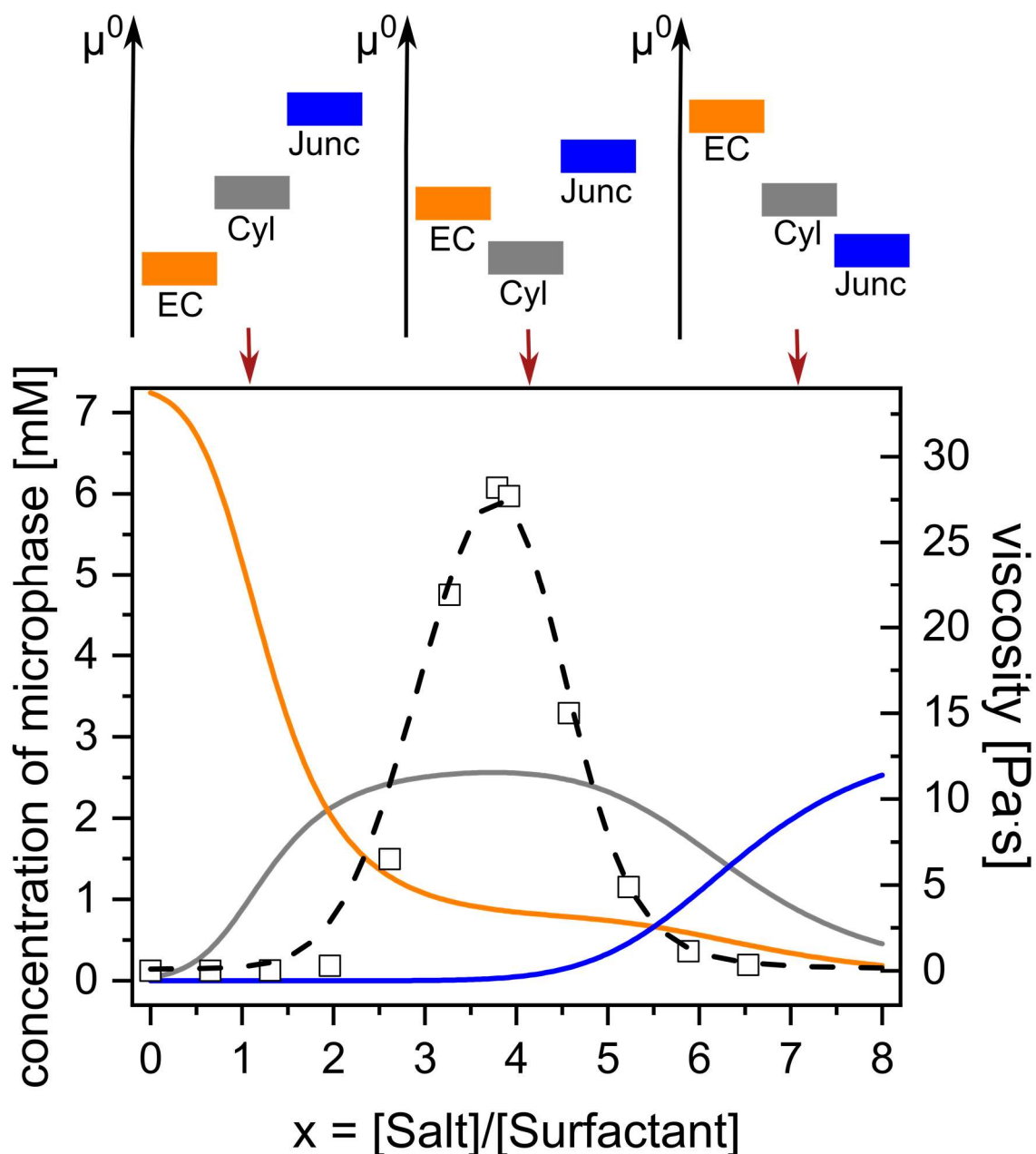


Figure 98. Comparison of the simulated viscosity curve of 10 wt% SLES in water (dashed black line) with the experimental values from Ref. [126] (squares). Additionally: The corresponding evolution of endcaps (orange), cylinders (grey) and junctions (blue) as a function of excess salt content x . Above, the corresponding relative states in standard reference chemical potential of each microphase are shown schematically.

V.4.2 Influence of added electrolytes on the viscosity curve

Variations of the salt curve can take place in two ways, namely a shift of the position of the maximum, and a change in the amplitude of the viscosity peak (value at the maximum). We first probed the effect of different types of salt. **Figure 99** shows the measured salt curves of 10% SLES solutions in the presence of KCl, NaCl and LiCl. Both effects described above could be observed to various extents. First, the position of the viscosity peak shifts to higher salt concentration in the order $\text{KCl} < \text{NaCl} < \text{LiCl}$. Second, the maximal viscosity at the peak

increases in the order $\text{KCl} < \text{NaCl} < \text{LiCl}$. Both observations can be reproduced by the model.

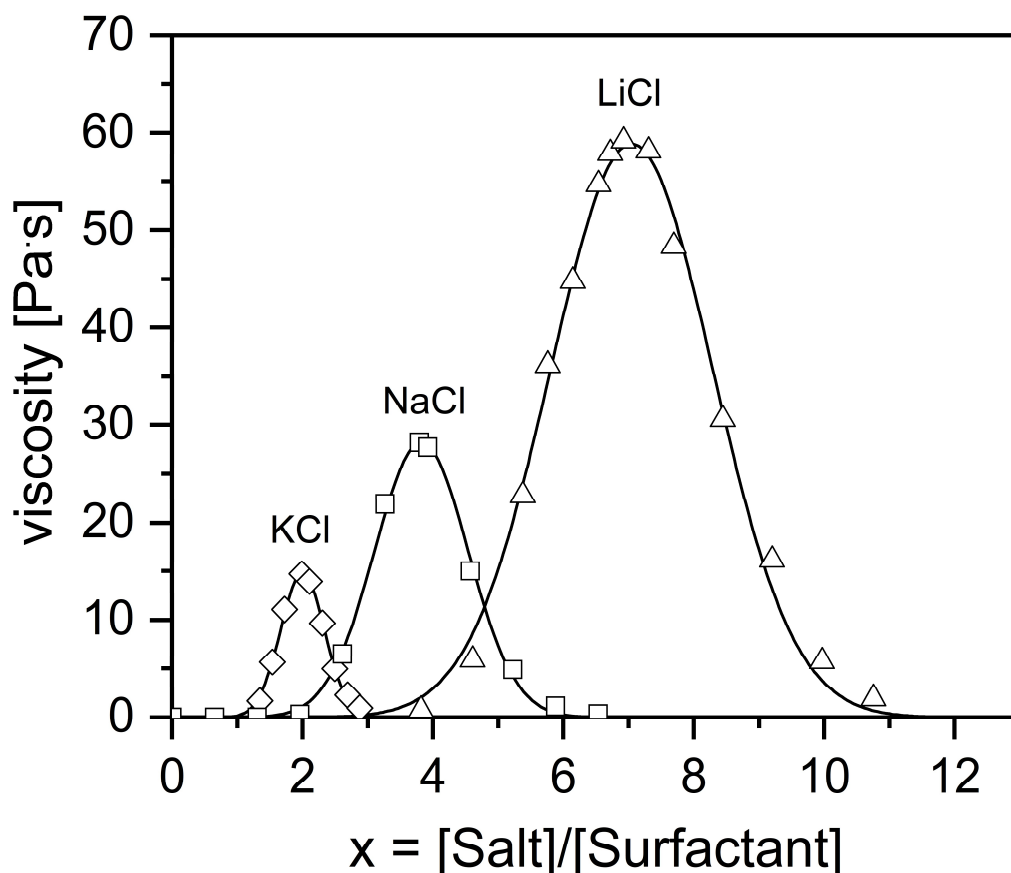


Figure 99. Salt curves of 10 wt% SLES for different salts. Salts: KCl (\diamond), NaCl (\square), LiCl (\triangle). Solid lines represent the fit of the experimental data to a Gaussian function. Experimental values received from Lydia Zahnweh and Vincent Joly, Universität Regensburg.

The position of the viscosity peak strongly depends on the evolution of the spontaneous packing parameter P_0 and therefore on the ability of the ions to screen the electrostatic repulsion between headgroups.^[260,262–264] The headgroup-ion interaction is expressed by the excess dissociation constant K_d and follows the Hofmeister series (*cf.* Chapter V.2). The “hardness” of the cation increases in the order $\text{KCl} < \text{NaCl} < \text{LiCl}$. For an alkyl ether sulfate such as SLES that is considered as “soft”, the interaction with a potassium ion will therefore be strong, resulting in a low dissociation constant. Consequently, the degree of counterion association α increases more rapidly with added KCl, which directly affects the evolution of a_0 and P_0 , respectively (*cf.* Equations (90), (102)-(106)). Therefore, the sphere-to-rod transition also occurs at lower salt concentration and the viscosity peak is shifted to a lower excess salt content. The opposite is true for the lithium counterion considered as “hard” and having a higher dissociation constant with the SLES anion. As a consequence, the viscosity maximum is shifted to higher salt concentrations.^[262] Similar results have also been reported previously for cationic surfactants

and anionic counterions.^[287] **Figure 100** shows the simulated salt curves in comparison with the experimental values, for different dissociation constants. Best results are obtained for $K_d(K^+SLES) = 0.11$, $K_d(Na^+SLES) = 0.26$ and $K_d(Li^+SLES) = 0.53$.

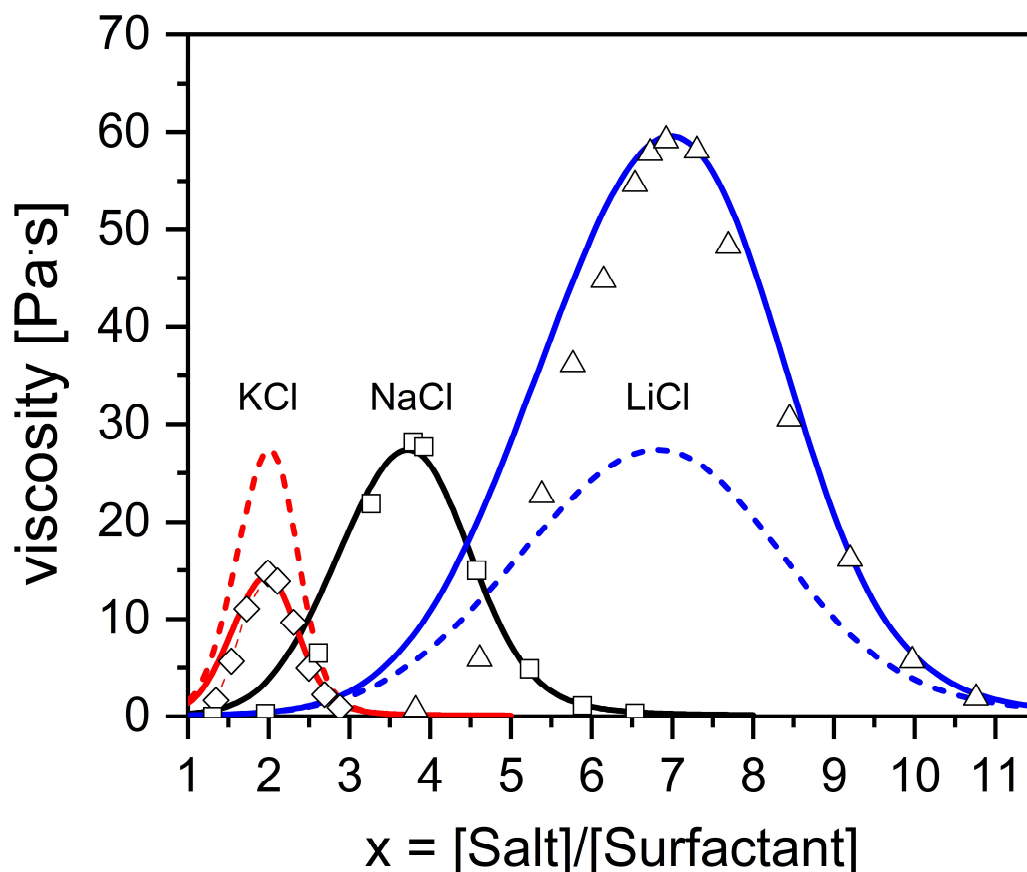


Figure 100. Comparison of simulated salt curves with experimental viscosity values. Symbols: Experimental values for KCl (\diamond), NaCl (\square), LiCl (\triangle). Dashed lines show the simulated viscosity curves without bending correction for different dissociation constants K_d : 0.11 (red), 0.25 (black), 0.53 (blue); solid lines show the simulated viscosities with bending correction for κ^* : 2.2 kT (red), 2.5 kT (black), 2.85 kT (blue). Influence of added fragrances on the viscosity curve

The experimental data not only reveal a horizontal shift of the SLES salt curve, but also the amplitudes vary significantly in the order $K^+ < Na^+ < Li^+$. This surprising observation is not reflected in the simulated salt curves using only different values of K_d . We hypothesize that in addition to the binding affinity to the SLES anion, the positively charged cation also has an effect on the bending constant κ^* . This may be linked to the ion penetration into the hydration layer of the micelle-water interface. K^+ is the less strongly hydrated and therefore smallest cation in the series and probably penetrates deeper than Na^+ or Li^+ ^[288], with the consequence of a softening of the interface resulting in a decrease of κ^* . A similar influence of the type of salt on the maximum viscosity of charged, giant micelles was shown for CTAB by Oelschlaeger *et al.*^[289]. In the series of non-penetrating inorganic salts (as opposed to the penetrating organic

counterions such as salicylate salts), the shift of the viscosity maximum to higher salt concentration was proportional to the amplitude of the respective salt curves, in the order $\text{ClO}_3^- < \text{NO}_3^- < \text{Cl}^-$.

For our study, it can be assumed that K^+ as a chaotropic ion possesses the weakest and smallest hydration shell resulting in the smallest hydration diameter.^[290] Therefore, the penetration power of the potassium ion into the interfacial layer is expected to be the highest of the three investigated ions. As a consequence, the bending constant κ^* in presence of KCl (hydration radius $r_H = 0.212$ nm) must be reduced and the bending constant in presence of LiCl ($r_H = 0.241$ nm) must be increased with respect to NaCl ($r_H = 0.218$ nm).^[290] The dashed lines in **Figure 100** indicate the simulated curves with varying K_d after bending correction. Satisfying accordance to the experimental data was found for a decrease in bending constant of 12% in case of KCl and an increase in κ^* of 14% in case of LiCl, compared to NaCl.

In a previous study^[126], Parker *et al.* have measured the effect of fragrance molecules added as solutes on the position and amplitude of the salt curve. A shift to lower salt concentrations was observed for molecules that possess an amphiphilic structure, which was qualitatively attributed to an interfacial flattening due to the insertion of the molecules as co-surfactants into the interfacial layer. Moreover, a decrease of the maximum viscosity occurred for some of the molecules, where the magnitude scales with the hydrophilicity of the molecules. This co-solvent type effect is supposed to be independent of the co-surfactant effect, and molecules can show both effects individually at various extents. For example, the very hydrophilic vanillin without a pronounced amphiphilicity decreases the viscosity maximum the most but does not shift the position of the curve. In contrast, the amphiphilic compound citronellol shifts the curve by more than 2 wt% of NaCl, but the viscosity is much less decreased.

Figure 101 shows the evolution of the microphase distribution of 10 wt% SLES in presence of 0.5 wt% fragrance with increasing NaCl concentrations. For the calculation, the modifications described by Eq. (108) on P_0 and by Eq. (110) on κ^* , respectively, were applied on these four representative fragrances that are very common in formulations: linalol, citronellol, vanillin and limonene. Two physical values must be known in order to predict the viscosity in the presence of a solute: the $\log P$ value (octanol-water partition coefficient), and the excess solubilization λ (described in Ref. [280]). $\log P$ values were determined experimentally by HPLC (Dr. Christine Vuilleumier, Firmenich SA) and used in the calculations for vanillin (0.72), linalol (2.94), citronellol (3.37), limonene (5.40). λ values for linalol and limonene were taken from [281]. Additionally, λ for citronellol was estimated from the experimentally

determined PIT in nonionic microemulsions (data not shown). According to [276] and [281], λ is high for surface active molecules, and values of limonene (0.07), linalol (0.16), and citronellol (0.38) reflect well the order of the shift of the salt curve to lower salt concentrations. Vanillin on the other hand did not give rise to a measurable shift of the salt curve^[126] and we attributed therefore a value of zero to vanillin.

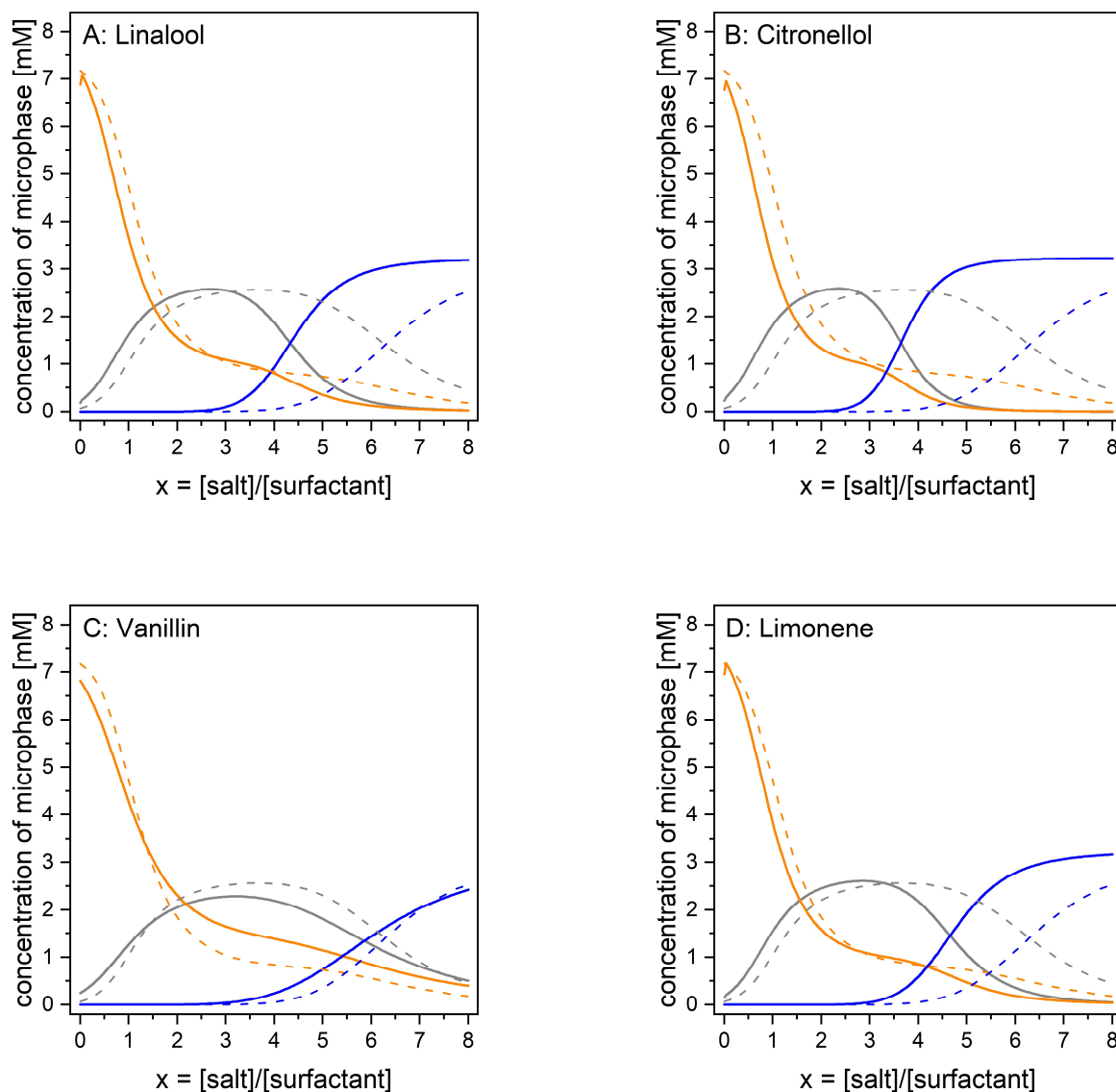


Figure 101. Simulated microphase distributions for 10 wt% SLES in water in presence of 0.5 wt% of fragrance as a function of the excess salt content x . A: Linalol, B: Citronellol; C: Vanillin; D: Limonene. Dashed lines indicate the evolution of the microphase distribution of pure SLES in water.

Comparing the microphase evolution of pure SLES (*cf.* **Figure 98**) shows that the presence of fragrance molecules has a significant influence on the evolution of the microphase distribution. Linalol and citronellol show the same tendencies with respect to pure SLES in water. The presence of fragrances leads to an increase in P_0 at $x = 0$ compared to the system in absence of

fragrances, namely by a value of 0.05 for citronellol and 0.03 for linalol. For both cases, the salt concentration range in which the cylinder microphase is dominant is significantly narrowed. Further, the decrease in endcap concentration at lower excess salt content x and the increase in junction concentration at elevated x is steeper compared to pure SLES. As a consequence, the sphere-to-cylinder transition as well as the transition to a branched network occurs at lower excess salt content x , resulting in a shift of the viscosity maximum to the left. Since the difference in P_0 compared the pure SLES is larger for citronellol, this shift to lower salt concentration is more elevated than for linalol.

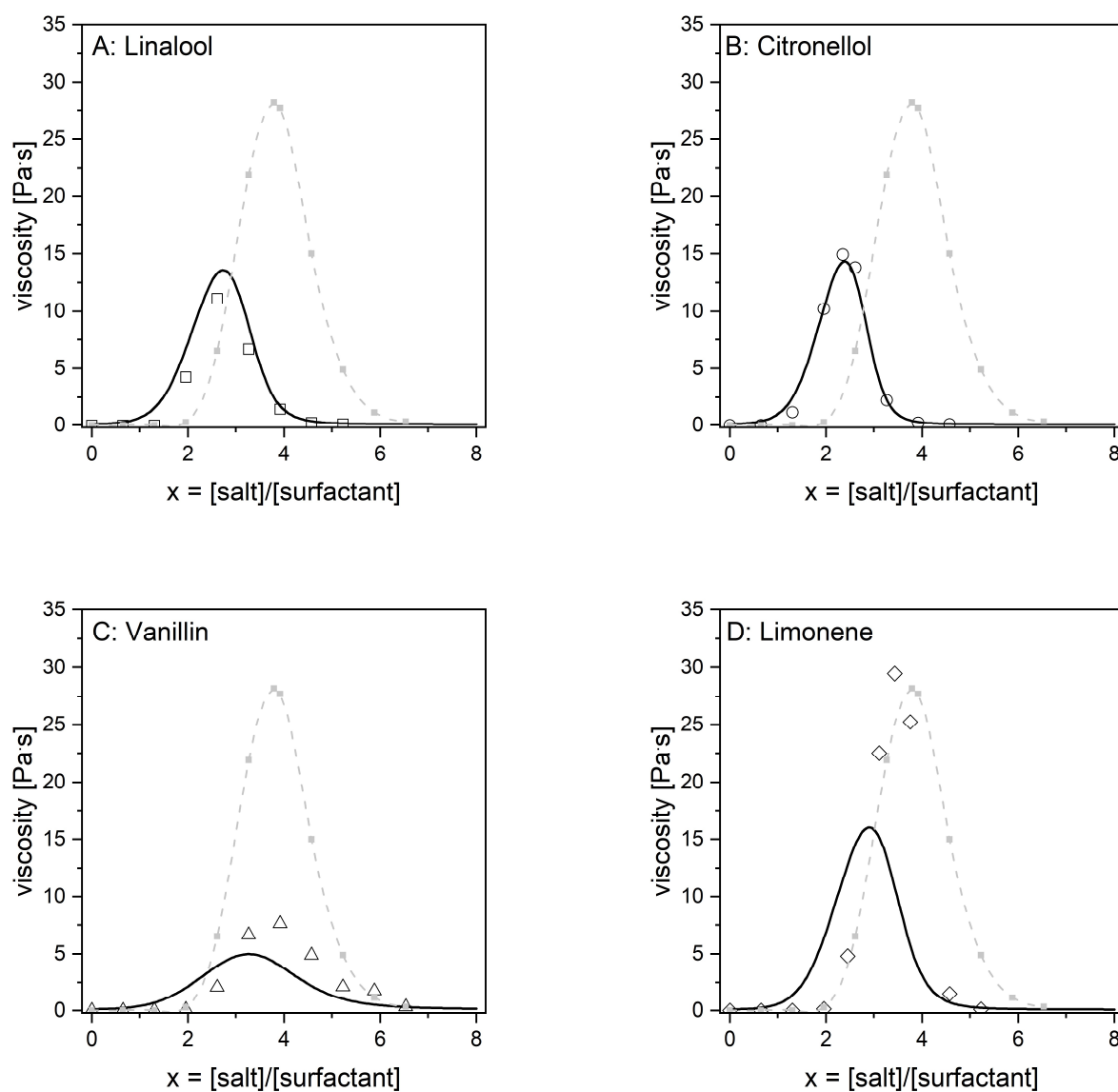


Figure 102. Comparison of simulated viscosity curves with experimental values for 10 wt% SLES in presence of 0.5 wt% fragrance. Experimental values are shown as empty symbols, the simulated curves are solid black lines. As guideline, the experimental curve of 10 wt% SLES is shown as dotted grey line.

Figure 102 compares the simulated viscosity curves with the experimental data, reproduced from [126]. An excellent agreement is obtained for citronellol and linalol. Peak position, maximum viscosity as well as peak width of the Gaussian-shaped curve show an almost perfect match with the experimental data. Note that these curves have been obtained based on the model for pure SLES with two modifications to take into account of co-solvent and co-surfactant type effects of the fragrances (Eq. (108) and Eq. (110)), with $\log P$ and λ as experimental input parameters.

Apart from the scaling parameter that is necessary to weight the influence of $\log P$ (constant A, bending constant, vertical shift) and λ (constant B, packing parameter, horizontal shift) and a semi-empirical excess dissociation constant, respectively, no additional, empiric factors or constants were utilized in predicting the viscosity curves. This is direct consequence of our approach to consider the whole surfactant length and not only the hydrocarbon chain in the evaluation of packing: there is no need to consider the distribution of added solute in the “core” or in the “palisade” layer. This distribution can be obtained in some cases by NMR relaxation or the optical properties of the solute, but this is done indirectly and is very time consuming. Applying our model does not require this extra experimental information or a set of parameters. Constants A (Eq. (108)) and B (Eq. (110)) were adjusted to 0.18 and 2.5, respectively, and employed for all four fragrance materials.

For vanillin and, a bit less, for limonene, the position of the salt curve is well reproduced, and with the current model and the overall parameter settings, the general trend of the amplitude of the salt curve with the $\log P$ is maintained. However, absolute values of the maximum viscosity for the two fragrances are underestimated. There may well be other parameters or structural descriptors than $\log P$ that have an effect on the bending constant of the surfactant interface and hence on the viscosity of gels of giant micelles. For example, molecular size may have an impact on how deep the fragrance molecules penetrate into the layer of headgroups or into the micellar core, respectively. The geometry of the molecules (rings, branches) may lead to a gain in entropy compared to their linear homologues and therefore reduce the entropy penalty when mixing into the surfactant interface. In any case, a larger number of fragrance molecules with a broader structural variation will be necessary to dissect these differential effects and fine tune the present model, but this is outside the scope of this work.

V.5 Conclusion

In this chapter, the model developed in Chapter III was transferred to the aqueous phase by use of a special definition of the packing parameter. With this model, the position, maximal intensity as well as the width of the bell-shaped viscosity curve of 10 wt% SLES in water in the presence of varying excess NaCl content could be reproduced with excellent agreement.

Cosurfactant effects as well as interface softening effects that occur when perfume molecules are added to the formulation were also implied in the model. The shift in viscosity peak position as well as the decrease in maximal viscosity could be reproduced for the most part with almost perfect conformity. Only in the case of vanillin and limonene, a deviation is observed regarding the maximal viscosity which can be attributed to specific or structural effects.

All terms implemented are *a priori* linear. Therefore, it can be expected that this model can be useful for the prediction of the macroscopic behavior of surfactant gels for industrial formulations containing electrolytes as well as fragrances thus reducing the amount of necessary experiments for complex multi-component formulations.

Moreover, this model can explain and predict the influence of the type of added electrolyte. The position of the viscosity maximum could be calculated by input of the dissociation constant of the charged headgroup and the counterion. By this, even specific ion effects according to the Hofmeister series are considered. The position of the viscosity peak can be predicted. We observed that the amplitude, however, also depends on the electrolyte. We have hypothesized that the positively charged cation also has an effect on the bending constant κ^* , maybe linked to the ion penetration into the hydration layer of the micelle-water interface. This is a still unresolved question, since to our knowledge there is no predictive model, that describes the softening of the bending constant as induced by chaotropic, kosmotropic or penetrating ions.

It has to be noted that mixed counterion effects are usually not linear and mixed electrolyte systems would require further approximations and calculations, such as detailed described by Parsegian and co-workers in the case of mixed competing anions.^[291]

Figure 103 sums up the evolution of microphase distribution, standard reference chemical potential, microstructure as well of the resulting viscosity. The understanding due to this model allows also to make propositions how the cosolvent and the interface softening can be avoided or counteracted. The cosolvent effect could be antagonized by either adjusting the salt content or by inducing a competition between two salts with different dissociation constants. The

interface softening effect is more difficult to counteract. For this purpose, the interface must be made more rigid by an additive. Rigidity can be often induced by a high charge density such it is the case for polyelectrolytes.^[292] Therefore, the “viscosity booster” that is commercially added to enhance the rheological properties of aqueous solutions of SLES in presence of salt - cocamidopropyl betaine – could be a good solution.^[293] Besides the cosurfactant effect, also a higher bending constant is expected. Furthermore, also other additives such as longer-chain alcohols ($C > 7$) can induce higher rigidity.^[294–296]

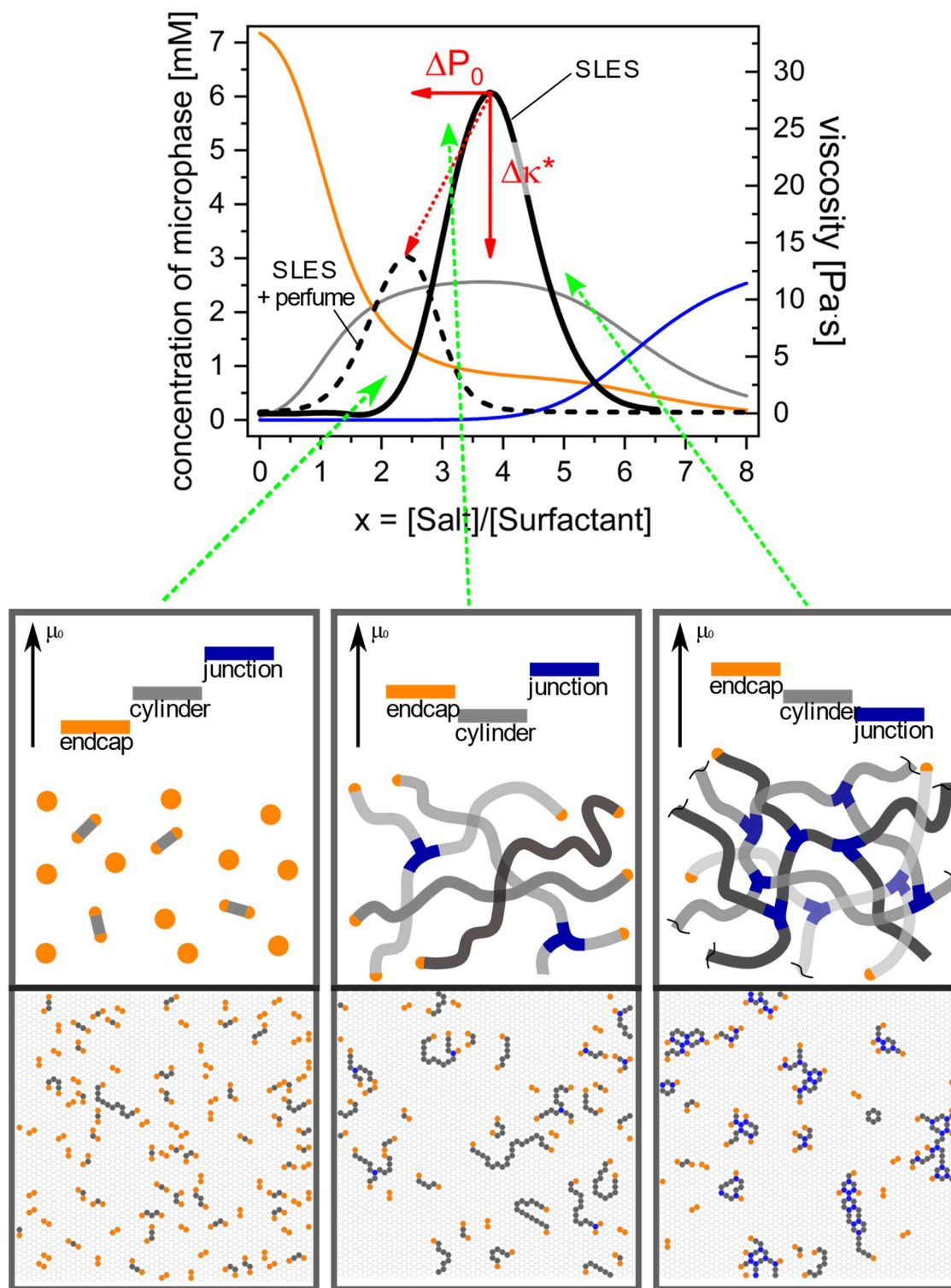


Figure 103. *Top:* Microphase distribution of 10 wt% SLES in water with salt addition and resulting experimental and calculated viscosity. *Bottom:* The corresponding standard reference chemical potential as well as the resulting structure are shown a) schematically and b) by a Monte-Carlo-like simulation in two dimensions.

VI GENERAL CONCLUSION AND OUTLOOK

Parts of this Chapter are used for the following Publication:

M. PLEINES, W. KUNZ, T. ZEMB, Understanding and Prediction of the Clouding Phenomenon by Spontaneous and Effective Packing Concepts, *submitted to Journal of Surfactants and Detergents* **2018**.

VI.1 Summary and general conclusion

In this work, we have focused on viscosity since it is an essential property in any application such as industrial extraction processes or omnipresent product formulations. It is a measure for the internal resistance to flow or shear. This macroscopic property originates from molecular as well as mesoscopic properties. The prediction of the evolution of the viscosity with changing parameters is crucial for several applications, amongst others for liquid-liquid extraction processes and for formulation of aqueous surfactant systems. Its importance ranges from fundamental research to large-scale industrial application in several industrial areas.

In this work, a “minimal” model taking into account the relevant free energies was developed that helps to understand, control and predict the evolution of the viscosity of microemulsions in the presence of solutes. The term “minimal” means in that context that this model is based on a minimal set of parameters that are all either measurable and have at least a physical meaning, thus avoiding input of any adjustable parameter. This model that considers the chemical terms at molecular scale, the physical terms at meso-scale as well as the flow characteristics at macroscale was applied on water-poor extracting microemulsions as well as on aqueous anionic surfactant systems.

Liquid-liquid extraction is the central technology in metal recycling. The extraction is always driven by oil-soluble surfactant molecules. TBP (Tributyl phosphate) is one of those widely used extracting surfactants, in short extractants. This molecule allows selective extraction of actinides in the framework of the nuclear fuel cycle as well as lanthanides for the life-cycle of electronic devices.^[8] Emulsification and demulsification processes in extraction devices are only efficient when the difference in viscosity between organic and aqueous phase is small, typically smaller than 5. Even if the processes using TBP as selective extractant are known since world-war II, economic and technical reasons motivate the research for alternative extractants. One promising approach is the use of *N,N*-dialkylamides which also have good extraction properties and significant advantages over TBP (*cf.* Chapter I.2.6.3). The main disadvantage of *N,N*-dialkylamides is the viscosity of the organic phase which increases exponentially when processes are intensified by increasing heavy metal and extractant concentration. Approaches to tackle the problem and to optimize formulations are based on experimental investigations along ‘experimental design’. To our knowledge, a predictive model that explains the viscosity increase of extractants and the influence on certain parameters did not exist previously in literature.

In a first step, experimental indications were collected in order to identify the origin of the viscosity increase of different monoamides in presence of uranyl (*cf.* Chapter II).

The viscosity rises in the order TBP < DEHBA < DEHiBA < DEHDMBA. The evaluation of a spontaneous packing parameter calculated from geometry that helps to compare the extractant geometries qualitatively allows to correlate the viscosity increase with the molecular structure or respectively, with the extractant curvature. Higher spontaneous curvature reduces the viscosity increase.

This observation is also consistent with the observation that increasing the penetration power of the diluent can also reduce the viscosity by swelling of the apolar chain volume. These observations are supported by COSMO-RS evaluations of chain wetting by solvent solubility. The temperature dependence is consistent with the Arrhenius model and it was shown that the activation energy for shearing increases with uranyl concentration by typically 50%.

Small- and wide-angle x-ray scattering experiments show a characteristic correlation “hump” corresponding to a correlation distance of approximately 1 nm. We use the term “hump” instead of the classical broad peak to stress that it is larger at full-width maximum than any peak observed in liquid crystals. This indicates that the uranyl ions are not distributed homogeneously in the solution. There seems to be rather an ill-defined average distance between them and alternating uranyl-nitrate chains are expected. This indication is also consistent with observations obtained from molecular dynamics.^[196] Furthermore, the broadness of the peak as well as the flat scattering at lower q indicate a strong polydispersity of the evolving structures as well as a dynamic equilibrium between different topologies formed by neighboring uranyl-nitrate-extractant aggregates.

Small-Angle Neutron Scattering experiments also indicate the presence of anisotropic particles with local cylindrical geometry. However, the high-volume fraction of extractants makes it difficult to evaluate the spectra quantitatively, since there is no convenient analytical structure factor describing concentrated anisotropic effects. An increase of scattering intensity at low q values for some samples indicates the presence of large, but finite structures.

In brief, the experimental observations indicate the formation of a loose living network with different topologies formed by a one-dimensional ionic liquid of alternating uranyl-nitrate chains embodied in a ‘bottlebrush’ structure of extractants.^[224] This microstructure is stronger developed for extractants with a small spontaneous packing parameter and/or diluted in non-penetrating oils. As a consequence, the viscosity increase is higher than for extractants with a higher spontaneous packing parameter and/or that are diluted in penetrating oil.

This picture of the evolving microstructure in the organic phase was transferred into a minimal

model at nanoscale (*cf.* Chapter III). The model is based on three well-established concepts in the field of colloids and molecular self-assembly:

1. the concept of pseudo-phases proposed by Shinoda and developed Tanford,
2. the expression for the free energy of bending for surfactant films by Ninham, Hyde and Israelachvili
3. as well as common fluid theories for living polymers from the 90s by Cates, Candau, Lequeux and Khatory.

Assuming chemical equilibrium between monomers and the three microphases endcaps, cylinders and junctions, the cost in free energy to convert a cylinder microphase into an endcap or respectively into junction units can be calculated and gives the relative probability of occurrence of each microphase.

A Monte-Carlo-like simulation on a hexagonal grid allows to translate the microphase distribution in an intuition-driving image in two dimensions of the microstructure in the organic phase.

Introducing an effective length L_{eff} allows to break down the dynamic property ‘viscosity’ to a static one and to translate the microphase distribution directly into viscosity.

An interactive interface was created that allows to change input parameters and conditions easily and contributes to a better understanding of the problem. Moreover, this interface allows to compare the experimental results with the simulated ones. Furthermore, the Monte-Carlo-like simulation can be directly carried out for a freely chosen uranyl content and system.

Analyzing the model proposes different approaches to decrease the viscosity of extractants in the organic phase.

The spontaneous packing parameter was determined as the decisive parameter to control viscosity of systems involving amphiphile self-assembly. It was demonstrated that a higher spontaneous packing parameter of the extractant leads to higher curved microphases, particularly endcaps. These reduce the mean aggregate length and consequently the viscosity. Four approaches are conceivable. The spontaneous packing parameter can be increased by either changing the extractant geometry, by using a penetrating diluent, by addition of an additive with cosolvent effect or by addition of a second, higher curved extractant. The possibilities were evaluated with respect to their applicability in industrial extraction processes. Changing the extractant structure by minimizing the polar area and maximizing the bulkiness of the apolar chains was determined as the most effective approach (*cf.* Chapter IV). Other approaches were considered either as not powerful enough or as introducing problematic

changes in security, stability or other hydrodynamical parameters.

In Chapter V, the model developed in the framework of this thesis was transferred to aqueous systems. Giant wormlike micelles formed by anionic surfactants in aqueous solution exhibit interesting rheological properties with high impact on industrial applications, especially in home and personal care products. Their structural and consequently their viscoelastic properties change during salt addition. Usually, the addition of a few percent of salt leads to an increase of the zero-shear viscosity by several orders of magnitude up to a viscosity peak. Further salt addition leads to a decrease in viscosity which was explained by the presence of more and more branching points that serve as stress relaxation points allowing micellar chains to slide along the micellar contour. The position and intensity of the viscosity peak changes by addition of solutes or fragrances and varies also with the type of salt added. We show that this general model can be adjusted for the aqueous case and allows to reproduce the Gaussian shaped viscosity curve of an anionic surfactant in presence of salt with excellent agreement. Furthermore, the influence of the type of salt as well as of added perfumes could be predicted and understood. Cosurfactant effects as well as interface softening effects that occur when perfume molecules are added to the formulation are considered in this model.

Moreover, this model can explain and predict the influence of the type of added electrolyte. The excess salt content of the viscosity maximum could be calculated by input of the dissociation constant of the charged headgroup and the counterion. Therefore, even specific ion effects according to the concept of matching affinities can be considered in this calculation. The position of the viscosity peak can be predicted, while the amplitude was shown to depend also on the electrolyte. We have hypothesized that the positively charged cation also has an effect on the molecular bending constant κ^* , maybe linked to the ion penetration into the hydration layer of the micelle-water interface.

As a conclusion, the model developed in this thesis is a useful tool to obtain a basic understanding of the viscosity evolution for several kinds of microemulsions involving amphiphilic self-assembly. Due to its intuitive and easy interface, crucial parameters that determine the viscosity can be identified and understood.

Furthermore, the model allows to predict changes of the system at least qualitatively and could serve as a useful tool to start the optimization of a given formulation.

In the following, possible future perspectives of this approach are described.

VI.2 Strategies for refinement

Considering the link between chemical equilibrium, a harmonic expression of the frustration free energy of coexisting pseudo-phases and the effective length as nanoscale has allowed us to rationalize the effect of added electrolytes in W/O as well as O/W giant connected micelles. There are some approximations made inherently and the generality of the concept as well as the predictive power of the model could be improved and would require further investigations.

The following proposed improvements and refinements apply to the organic system of *N*, *N*-dialkylamide extractant systems.

First, the estimations of the packing parameters and the aggregation numbers of the specific microphases were only done geometrically. With this method, qualitative trends can be found out and allow an ordering of the extractant geometry. However, for a more quantitative determination, it would be necessary to determine the evolution of spontaneous and effective packing in each microphase precisely for several uranyl concentrations, extractant molecules and diluents. Further combined x-ray and neutron scattering experiments coupled with molecular dynamic simulations would be a promising approach. However, this investigation would be very time consuming and could be difficult due to the high extractant and uranyl concentration. Furthermore, protons cannot be simulated by molecular dynamic simulations and longer chain diluents such as dodecane increase the calculation time. In total, this investigation would take much longer than to measure viscosity curves. Therefore, it should be estimated first, if this effort would bring enough additional benefit. Cryo-TEM measurements could give more insight of the structure in the organic phase.^[120,297,298] This experiment was actually planned in the framework of this work at the Israel Institute of Technology in Haifa, but could not be realized due to administrative difficulties. A microscopic image of the organic phase could on one hand identify the Onsager regime and on the other hand prove the presence of junction points, if the resolution is sufficient. The contrast of such images would be excellent due to the high electron density of uranyl ions.

Second, the concentration dependence is currently only taken into account by a gradual decrease of the number density of each microphase as well as by a different intrinsic viscosity estimated by Einstein's formula. However, in literature, further scaling factors and concentration dependencies, especially on the life time of a micelle and the scission-recombination mechanism, can be found.^[299,300] The implementation of such dependencies could lead to more quantitative results. Moreover, as was indicated in Chapters II.2.6.4 and III.3.6, a higher concentration of amphiphiles can lead to partial coalescence of the microstructures and the

formation of dense aggregate ‘clouds’. This phenomenon can be referred to an Onsager transition^[154,156] or an effect similar to jamming known in aqueous salt solutions^[209]. Such a transition is indicated in the 2-dimensional Monte-Carlo-like simulation, but not in viscosity calculation. The implementation of suitable van-der-Waals potentials that result in a preference of cylinder-cylinder attraction rather than sphere-sphere would allow to obtain a more realistic image of the Onsager-transition. Also, for the direct transfer of microphase distribution to viscosity, an approach has to be developed that correlates the transition point from a homogeneous into a microphase separated system with the packing abilities of the evolving microstructure. Additionally, it should be considered that further parameters can change with elevated extractant concentration. However, we do not know if the model would have improved predictive properties if these refinements were implemented. First, the activity coefficients of the microphases can change with increase in extractant concentration. Moreover, with increasing extractant concentration, the polarity of the medium and therefore the intra- and intermolecular interactions may change. This effect was already observed by Ferru *et al.*^[194,196]. According to their simulations by molecular dynamics, the aggregates tend to smaller aggregates at higher extractant concentration. This effect is not predicted by the model.

Moreover, one of the crucial steps to obtain the value of simulated viscosity is to reduce the dynamic properties of this living network to one single geometrical effective length as was proposed by Khatory *et al.*^[137]. This reduction allows on one hand a fast and easy transfer of the microphase distribution to viscosity, but certainly induces inaccuracies. Other parameters that could influence the absolute value of the viscosity are the persistence length of the resulting polymers or the solvent “goodness” of the diluent for a polymer network.^[233] However, without knowledge of the dominant relaxation mechanism and the dominant relaxation times, this seems to be a good solution – especially for the requirements of a minimal model. An alternative way to derive the viscosity would be to use the resulting image of the Monte-Carlo-like simulation to derive characteristic lengths. This is already implemented in the user interface under the accordion “Analysis”, where characteristic lengths can be calculated. However, in order to derive the distances that are representative for the system, the Monte-Carlo-like simulation should be carried out in three dimensions.

Further, the different approaches to optimize the viscosity control of extractant solutions in presence of uranyl should be further investigated. As most promising, changing the extractant geometry was identified. The use of dissymmetric extractants seems to be the most efficient way to induce curvature.^[235,237] Further molecules should be tested as well the choice of the diluent optimized to swell the apolar volume. In parallel, other important parameters such as

interfacial tension as well as separation coefficients must be considered.

The application of the new model in aqueous systems can also be improved. The calculation of the spontaneous packing parameter as well as of the aggregation numbers per microphase could be done more accurately by scattering experiments and microscopic investigations.

Moreover, the implementation of the two effects interface softening as well as the cosolvent effect by perfume molecules should be investigated more in detail and tested on large series of model solutes. Especially the case of charged surfactants in the presence of salt and model fragrances is certainly worth to investigate more in detail. For a further reconfirmation of the potential of the model and more detailed understanding one should carry out at least the following experiments and correlate the results with the model:

- Measurement of the viscosity curves for at least three different surfactant molecules with increasing headgroup softness (*e.g.* a carboxylate, a phosphate and a sulfate) and similar apolar chains for at least three different salts each with increasing headgroup softness (*e.g.* LiCl, NaCl and KCl). This would allow to confirm or improve, respectively, the hypothesis about the correlation of the viscosity peak position with the concept of matching affinities as well as the link between hydrodynamic ion radius, ion penetration and the amplitude of the salt curve.
- Determination of the dissociation constants for each system by conductivity measurements.^[274] Further, in the model, we have chosen the simplest model available to describe the effect of counter-ions on the area per molecule. Much more refined models linking the area per head-group as lateral equations of state have been developed in the case of lipids by E. Leontidis *et al.*^[301]. Maybe these models could be reformulated for the case of anionic surfactants and bring more precise predictions of experimental observations.
- Combined Small-Angle X-Ray and Neutron scattering to determine a) the morphology of the microemulsion and b) the spontaneous packing parameter of the surfactant in presence of at least three salt concentrations each.^[204] This would help to confirm the calculated microphase distribution as well as the approximated evolution of the spontaneous packing parameter.
- Measurement of the bending constant per molecule for each system at least three salt concentrations to verify the assumed concentration independence or to evaluate its evolution. Bending constants can be accessed from Small-Angle Neutron Scattering and neutron spin-echo spectroscopy.^[302]

- Investigation of at least two homologous series of fragrance molecules with the same headgroup, but different apolar part in order to evaluate the effects of $\log P$ and excess solubilization λ (that must also be determined by UV absorption, see Ref. [303]). This series of salt curves would allow to confirm or improve, respectively, the Eq. (108) for the cosolvent effect as well as Eq. (110) for the interface softening effect. In the ideal case, the bending modulus should be also determined for each system.
- Testing of the additivity of the fragrance effect. For this purpose, the viscosity curve of a chosen system should be measured a) with increased concentration of one added fragrance raw material and b) with stepwise addition of 2-3 different fragrances. These experiments would allow to confirm the assumed linearity of the terms used Eq. (108) to calculate the effect of fragrances on the spontaneous packing parameter.

This series of experiments can result in two possible conclusions. Either the model is confirmed as it is, or some refinements in the calculations must be implemented to get a “ready-to-use” tool in formulation industry for suppliers as well as for intermediary consumers.

VI.3 Further applications

VI.3.1 Prediction of the cloud point

VI.3.1.1 The mechanism behind the cloud point phenomenon

Since the model developed in this work is valid generally, it can be adapted for further applications that involve macroscopic phenomena linked to a continuous change in spontaneous packing.

Another important phenomenon that has importance in several applications is the phase separation of fluids at a given temperature - the so-called cloud point. Above this characteristic temperature, complex fluids formed by nonionic surfactants become turbid and separate into an amphiphile-rich and an amphiphile-poor phase. The cloud point observed for nonionic surfactants and rarely for ionic surfactants^[304,305] can probably also be explained by an adjusted version of the model. The origin of the cloud point is still under discussion amongst researchers and can be referred to four main mechanisms^[305]:

- *Sphere-to-rod transition*: Starting in the early 1980's, the first researchers investigating the mechanism of the cloud point have attributed the origin of the phase separation to a sphere-to-rod transition induced by a decrease in surfactant area per headgroup with temperature. The increase in aggregate size was indicated by light scattering, NMR self-diffusion^[306] and small-angle neutron scattering^[307].
- *Attractive interaction*: Others such as Corti *et al.*^[308–310] have argued that the increase in scattering intensity close to the cloud point should rather be attributed to critical opalescence and the origin of the cloud point phenomena is mainly attributed to attractive interactions between aggregates. Zulauf and co-workers^[311,312] even have excluded a change in shape and size explicitly and have explained the phase separation as a result of increasing attraction between spherical micelles with temperature.
- *Micellar growth and attractive interaction*: Others, such as Cebula and Ottewill^[313] as well as Glatter and co-workers^[314] have concluded that micellar growth and attractive interaction do not exclude each other and have found evidence for both mechanisms. Approaching the cloud point temperature a sphere-to-rod transition comes into play and strengthens attractive interactions^[314] Indeed, as already mentioned in Chapter I.2.5.3, van-der-Waals attraction is inefficient between spheres and significantly more efficient between cylinders.^[153, pp.1–37] Therefore, every sphere-to-rod transition induces stronger interparticle attraction.

That point of view is formally equivalent to the classical modelization of the origin of the cloud point that the micelles formed by non-ionic surfactants may interact via an attractive potential well whose depth increases with temperature.^[305] Ruppert has described the cloud point phenomena by a Flory-Huggins approach by taking into account a temperature dependent interaction parameter and the molecular structure of the non-ionic surfactant. He was the first who considered both contributions from ethylene oxide headgroups and the apolar chains. He concluded that clouding results from the balance between the hydrophobic and hydrophilic interactions of the micelle with its surroundings.^[315]

- *Self-assembling networks and branched structures*: In the late 1990's a further step was made since cryogenic transmission electron microscopy (cryo-TEM) has shown direct evidence of the existence of connections points close to the cloud point of C₁₂E₅ in aqueous solution.^[316] Similar results were found for oil-swollen aggregates for the system C₁₂E₅/water/*n*-octane^[317] The results from cryo-TEM show a gradual transition from disconnected polymer-like micelles to a connected micellar network. Zilman and co-workers^[145,147,318] have developed a general thermodynamic formulation combined with experimental results that explains the separation with the temperature dependence of spontaneous curvature of the surfactant. When a critical density of junctions is reached, the attraction is strong enough to separate the solution into two phases. Within the two phase region a concentrated and a dilute network of interconnected O/W cylinders coexists.^[316]

VI.3.1.2 Using the model to explain and predict the cloud point

The adjustment of the model presented in Chapter III and V would allow to describe the phenomenon both on the molecular as well as on the mesoscale. With the new definition of the spontaneous packing parameter as described in Chapter V, P_0 can be calculated from the effective molar volume v_{eff} of the surfactant including hydrophobic tail and polar headgroup as well as hydration water, a_I - the respective area per surfactant at the water-micelle interface (and not at the head to hydrocarbon interface) - and $\langle l_{C+I} \rangle$, the mean surfactant length including the interfacial thickness d_I . In a first approximation, $\langle l_{C+I} \rangle$ can be considered as temperature-independent. v_{eff} as well as a_I should mainly depend on the hydration or dehydration, respectively, of the ethylene oxide (EO) groups.

- The evolution of a_I was shown by Danov *et al.*^[319] to decrease almost linearly from approximately 1.1 nm² to 0.6 nm² from 25°C to 70°C for several C_iEO_j surfactants. The

effect of the molecular structure on this evolution must be tested if this approach is further followed up. However, for the simple demonstration of the principle, this evolution is considered as independent from the molecular structure.

- For the decrease in v_{eff} one could expect a linear dehydration of a certain number of H₂O molecules per ethylene oxide group within a defined temperature range. Nilsson and Lindman^[320] have shown by measuring the self-diffusion coefficient of D₂O in several systems that the hydration of the EO groups seems to be independent of the system and mainly depends on the temperature and composition of the system. Shikata and co-workers^[321] have investigated the temperature-dependent hydration/dehydration behavior of different Poly(ethylene oxide)s. They have found for different PEOs that the hydration number per ethylene oxide unit m_{EO} seems to be independent of the molar mass and is around 4 in a temperature range below 30°C. Above this temperature, m_{EO} decreases gradually until a value of 2 at a temperature of 70°C. For the following exemplary calculation, we have assumed a similar behavior for nonionic surfactants with a smaller number of ethylenoxide groups.
- $\langle l_{C+I} \rangle$ is approximated as the sum of the length of the 80% of a fully extended chain length according to Tanford's formula (*cf.* Chapter V) and the interfacial thickness d_I . This value is considered as mainly dependent on the number of EO groups and a value of 0.2 nm per EO group was estimated. For branched chains, 80% of the longest fully extended chain is used.

Having approximated the evolution of a_I , v_{eff} and $\langle l_{C+I} \rangle$ with temperature, the evolution of the spontaneous packing parameter $P_0 = v_{\text{eff}}/(a_I \cdot \langle l_{C+I} \rangle)$ can be estimated. From that, the procedure described in detail in this work to calculate the cost in free energy and the microphase distribution can be applied.

We illustrate this idea of comparing a branched and a linear ethoxylated alcohol. G. Smith has compared branched Guerbet alcohol ethoxylates with linear ones and has shown that branching lowers the cloud point of alcohol ethoxylates in water.^[322]

Let us consider two nonionic surfactants with four ethylene oxide groups. Molecule *L* (for linear) has a dodecyl chain, Molecule *B* (for branched) has a 2-butyl-octyl chain. Consequently, both molecules have the same molar mass and it can be assumed that also the temperature dependence respective to the area per headgroup and dehydration is similar. The only significant difference is the length $\langle l_{C+I} \rangle$ which is significantly shorter for the branched molecule.

Applying the above assumptions allows to calculate the microphase distribution for the molecules L and B (cf. **Figure 104**).

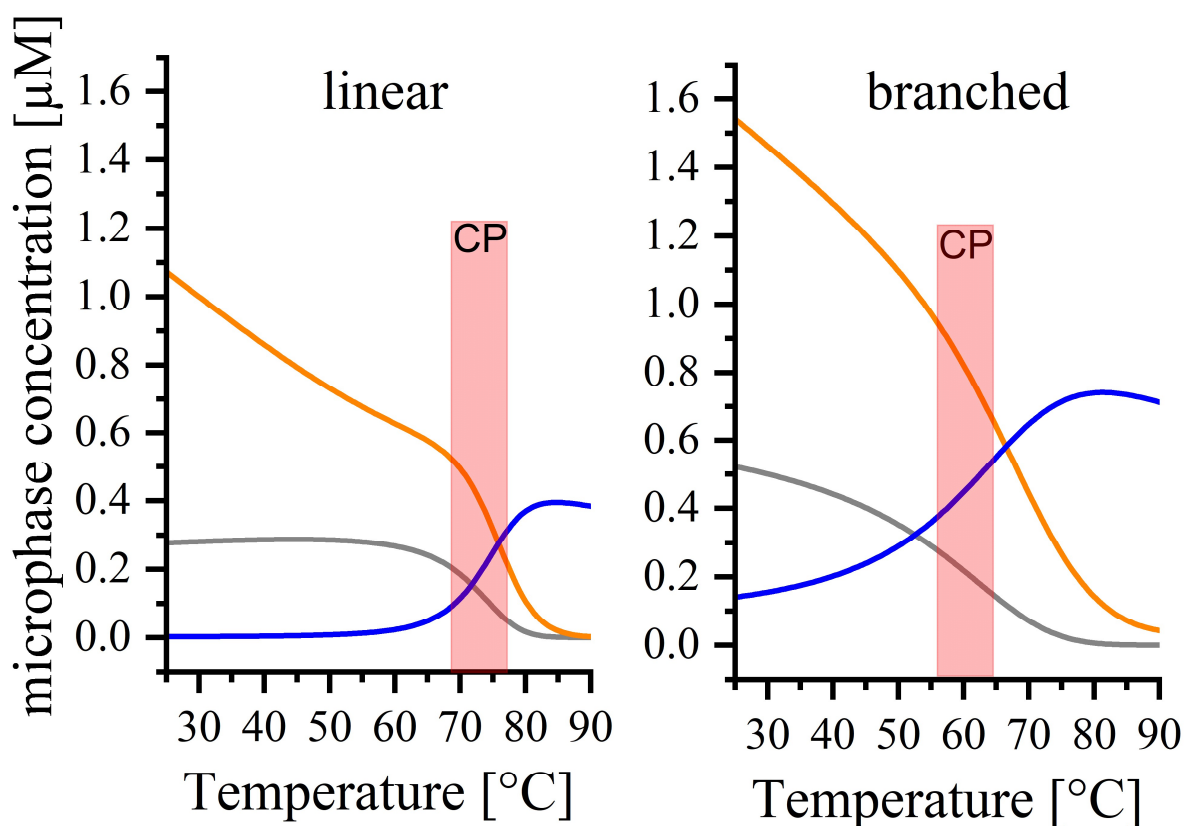


Figure 104. Exemplary calculation of the microphase distribution of a linear (left) and a branched (right) ethoxylated surfactant applying a bending constant of 1.5 kT. Endcaps are plotted in orange, cylinders in grey and junctions in blue. The most probable temperature range of the cloud point is indicated in red.

As can be seen, the microphase distribution of both molecules is different and the branched molecule B has already at lower temperatures a higher tendency to form cylindrical micelles. As described above, the cloud point can be either attributed to attraction between elongated aggregates or a dominant concentration of junctions. Attraction would become maximal, when cylindrical units are parallel.^[153] For this case, the probability of clouding is high, when the cylinder concentration is high, and the endcap concentration is low (endcaps shorten the micellar length). Regarding the mechanism of attracting junction points, the cloud point should be situated approximately at the point when the junctions become dominant. This is either the case when the curve of junctions (blue) and endcaps (orange) or the curve of junctions and cylinders (grey) cross. The endcap concentration stays high for a broad temperature range since it is expected that only one third of the number of molecules is needed to form an endcap compared to a cylinder unit. Due to the two main possible mechanisms, only a temperature range for the cloud point position can be indicated by this model without knowing the decisive criterion. The cloud point is either induced by a dominance of junctions over cylinders or over

endcaps. However, with this criterion, a clear difference between branched and linear molecules can be shown and allows to explain the ordering of different series of nonionic surfactants. In this example, the cloud point for the linear molecule L is expected to be situated between 70 and 75 °C, while the branched molecule B is modeled to lie between 55 and 65°C. The order of magnitude (decrease of around 10 °C due to branching) is in agreement with values from literature that locate the cloud point of L between 67-70°C (MARLOWET BL) and of a branched $C_{12}E_4$ molecule (LIALET 123-4) between 61-63°C.^[323] For these values, one has to consider that these products are industrial products with a certain distribution in composition.

As a conclusion, our minimal model also shows a great potential to describe the cloud point. Due to the new definition of the spontaneous packing parameter, this potential also includes the explanation and prediction of effects of model solutes such as fragrances.

VI.3.2 Parallelism to the HLD-NAC concept

In the 1970's, a useful advancement of older concepts such as the HLB value (1949, Griffin)^[324], the R-ratio (1954, Winsor)^[325] or the PIT technique (Shinoda, 1964)^[326] was developed - the hydrophilic lipophilic deviation (HLD) concept. It is based on determining the “*optimal formulation*”. At the optimum formulation composition of a water/surfactant/oil system, the surfactant has the same affinity to the polar and apolar pseudo-phase resulting in a triphasic system (oil/microemulsion/water) with a minimum in interfacial tension. The HLD is a normalized semi-empirical expression for the change in chemical potential when a surfactant molecule is transferred from the oil phase into the aqueous phase and can be calculated by a linear combination of different formulation variables for both ionic surfactants (Eq. (119)) and non-ionic surfactants (Eq. (120)).^[327–329] Under the conditions of the optimum formulation, the HLD is zero. A positive HLD means that the surfactant is hydrophobic under the given conditions. As a consequence, the surfactant prefers a negative curvature and W/O (micro-) emulsions (Type II microemulsions) are favored. In contrast hereto, a negative HLD indicates that the surfactant is hydrophilic under the given conditions and favors O/W (micro-)emulsions.

The HLD can be calculated via the following semi-empirical expression:

$$HLD = \frac{\mu_W^S - \mu_O^S}{RT} = Cc + \ln(S) - k \cdot EACN - t(T - T_{ref}) + f(A) \quad (111)$$

$$HLD = \frac{\mu_W^S - \mu_O^S}{RT} = Ccn + b \cdot S - k \cdot EACN + t(T - T_{ref}) + \phi(A) \quad (112)$$

with the following contributions:^[328,329]

- Cc and Ccn denote the characteristic curvature of the surfactant describing the intrinsic properties of the surfactant such as the hydrophilic/lipophilic nature of the surfactant. In the case of non-ionic surfactants this value can be split into α , a term that is characteristic for the molecular structure of the hydrophobic tail and EON denoting the number of ethylene oxide groups. A higher characteristic curvature means that the surfactant is more hydrophobic under the given conditions. Increasing the number of ethylene oxide groups decreases the characteristic curvature and the HLD .
- The terms $+\ln(S)$ for ionic surfactants and $+b \cdot S$ for non-ionic surfactants account for the effect of salt on the surfactant. In the case of ionic surfactants, the factor describes the charge screening effect decreasing the repulsion between the charged headgroups. For non-ionic surfactants, salt typically has a “salting out” effect indicated by an increase of the HLD with salt concentration S (in wt%). All characteristic parameters (b , k , t) are positive by convention.
- The term $-k \cdot EACN$ accounts for the surfactant-oil interaction and describes the nature of the oil phase. $EACN$ stands for the “equivalent alkane carbon number”^[328]. The higher the $EACN$, the more ‘hydrophobic’ is the oil and as a consequence, the more ‘hydrophilic’ is the surfactant (HLD decreases).
- The terms $-t(T - T_{ref})$ and $+t(T - T_{ref})$ describe the temperature influence on the HLD with T being the temperature of the system and T_{ref} being the reference temperature, usually 25°C. In the case of ionic surfactants, temperature mainly influences the water-water hydrogen bonds resulting in a decrease of the HLD and the ‘hydrophobicity’ of the surfactant. For non-ionic surfactants, the behavior is reverse. The dominant effect of temperature is the weakening of the water-EO group interaction. Therefore, the surfactant becomes more ‘hydrophobic’ with temperature and the HLD increases.

The HLD concept is therefore a useful, semi-empirical tool to determine the formulation conditions for bicontinuous microemulsions ($HLD = 0$, Type III or IV systems) and to predict the preference of the surfactant to form Type I or Type II microemulsions. Furthermore, the HLD value gives good predictions for emulsion stability.^[24]

However, the HLD concept cannot predict properties of microemulsions such as solubilization capacity, interfacial tension, specific phase transitions or phase volumes.^[329] In an attempt to gain in predictive power, Acosta *et al.* has introduced the NAC concept. The basic idea of this concept is to use the “net curvature” H_n as thermodynamic property and use the HLD as scaling

variable.^[329] The net curvature is a mathematical formulation to express whether the curvature of surfactant film at the oil/water interface is either negative (convex towards the oil-reverse micelle interface), positive (concave towards the oil-micelle interface) or zero (the so-called critical point). H_n is defined as the difference between two coexisting hypothetical spherical aggregates of oil and water characterized by the radii R_o and R_w and can be expressed by the HLD :^[329]

$$H_n = \left| \frac{1}{R_o} \right| - \left| \frac{1}{R_w} \right| = -\frac{HLD}{L} \quad (113)$$

where L is a length scaling parameter that has to be found to be proportional to the extended length of the surfactant tail. Further detailed information on the definition of R_o and R_w are given in Ref. ^[329,330].

Approaching the optimal formulation, a $HLD = 0$ would predict either R_o (for Type I) or R_w (for Type II) approaches infinity. However, in reality, aggregates can only grow to a characteristic length ξ as defined by de Gennes and Taupin.^[331] This length depends on the volume fractions of oil and water as well as the total surfactant interfacial area and can be determined by SANS measurements.^[329] Therefore, besides the net curvature H_n (*cf.* Eq. (121)) also the average curvature H_a has to be considered (*cf.* Eq. (114)) and both equations have to be solved simultaneously.

$$H_a = \frac{1}{2} \left(\left| \frac{1}{R_o} \right| + \left| \frac{1}{R_w} \right| \right) \geq \frac{1}{\xi} \quad (114)$$

The NAC concept was successfully applied to predict “fish” phase diagrams^[329] and cloud points of alkyl ethoxylates.^[332] Moreover, by using a shape-based NAC model that relates H_n and H_a to the length and radius of microemulsion aggregates composed of a cylindrical core with hemispherical endcaps, Kiran and Acosta could predict the morphology and the viscosity of microemulsions.^[333]

As was pointed out by Kunz *et al.*, there is a correlation between the concepts of HLD , spontaneous curvature and spontaneous packing parameter.^[64] Indeed, the spontaneous packing parameter P_0 must be equal to 1 in the case of the optimal formulation ($HLD = 0$), since there is no preference that the surfactant bends towards oil or water. In Chapter I.2.4.2, we have seen that the spontaneous packing parameter can be expressed in terms of average and Gaussian curvatures as

$$P_0 = 1 + \langle H_0 \rangle l + \frac{1}{2} \langle K_0 \rangle l^2 \quad (115)$$

One should note that the net curvature $H_n^{[329]}$ as well as the modified net curvature $H_n'^{[333]}$ scale to the HLD as

$$H_n' = \frac{H_n}{2} = -\frac{HLD}{2L} \quad (116)$$

Comparing equations (115) and (116) with $P_0 = HLD + 1$ at the optimal composition, one can see that the concept of net curvature does not consider the spontaneous Gaussian curvature K_0 contribution sufficiently. This contribution may be negligible for some cases (*e.g.* cylinders), but important for others, especially in bicontinuous structures.^[334]

A link or a well-defined correspondence between these two concepts would allow to use both in parallel, have easier access to microstructure and free energy contributions but also to the huge databases of HLD values in industry (*cf.* **Figure 105**).

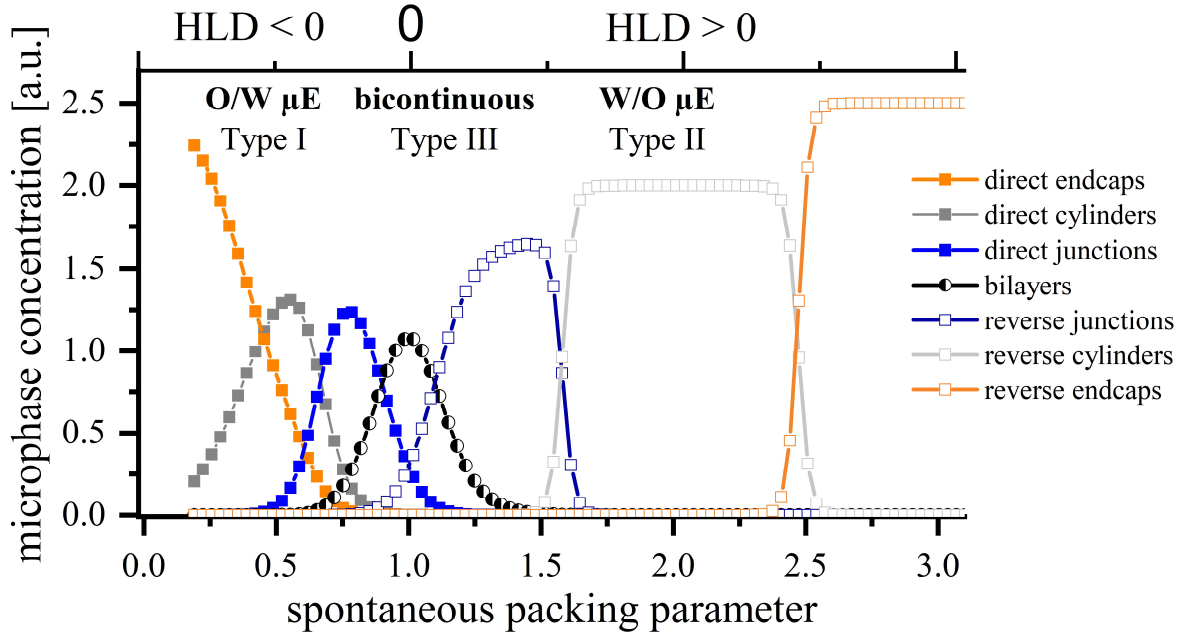


Figure 105. Schematic representation of a possible extension of the model to the whole range of curvature. Results of an exemplary calculation assuming a linear variation of the spontaneous packing parameter also indicated by a transition from a negative HLD value to a positive one.

One starting point for this approach would be the separate determination of mean and Gaussian bending constants for several systems as was demonstrated by Hellweg *et al.* combining dynamic light scattering and neutron spin-echo spectroscopy^[78,335] as well as the corresponding mean and Gaussian curvatures. The most promising link between *HLD-NAC* and spontaneous packing is probably only possible by going back to the basic equation for free energy of

bending. While our model considers the spontaneous packing parameter P_0 to describe the surfactant shape and the frustration energy for certain microphases, the HLD-NAC concept uses net average curvature H_n related to the *HLD* and a limiting length ξ . The net average curvature has similarities to the concept of spontaneous and effective packing, as was already mentioned above. Moreover, Equation (114) introduces a limitation for the size (maximal frustration) of the microstructure. This relation could have a relation to the free energy of bending and allow to introduce a correspondence between the free energy of bending and the average curvature dependent on ξ . However, the exact way to make both concepts consistent stays an open question.

VII ANNEX

VII.1 List of Abbreviations

cac critical aggregation concentration

cf. compare

cmc critical micelle concentration

DEHBA *N,N*-(2-ethylhexyl)butyramide

DEHDMBA *N,N*-(2-ethylhexyl)dimethylbutyramide

DEHiBA *N,N*-(2-ethylhexyl)isobutyramide

DIAMEX *DIAMide EXtraction*

e.g. for example

EU *European Union*

GANEX *Group ActiNide EXtraction*

HDEHP *Di*-(2-ethylhexyl) phosphoric acid

HSAB *Hard and Soft Acids and Bases*

MOX *Mixed oxide fuel*

NMR-DOSY *Diffusion-ordered nuclear magnetic resonance spectroscopy*

O/W *oil-in-water microemulsion*

PEO *Poly(ethylen oxide)*

PUREX *Plutonium Uranium Redox Extraction*

SANEX *Selective ActiNide EXtraction*

TALSPEAK *Trivalent Actinide - Lanthanide Separation by Phosphorous Extraction from Aqueous Komplexes*

TBP *Tributylphosphate*

TOA *tri-octylamine*

TOPO *Trioctylphosphine oxide*

VPO *Vapor pressure osmometry*

W/O *water-in-oil microemulsion*

VII.2 Table of Figures and Tables

Figures - Short titles

FIGURE 1: ENDANGERED ELEMENTS ACCORDING TO A RESEARCH CONDUCTED BY THE CHEMICAL INNOVATION KNOWLEDGE TRANSFER NETWORK.....	12
FIGURE 2. SCHEMATIC REPRESENTATION OF A HYDROMETALLURGICAL PROCESS STARTING FROM “LEACHING” OVER “SOLVENT EXTRACTION” TO “STRIPPING”.....	14
FIGURE 3. TOP:SCHEMATIC REPRESENTATION OF A MIXER-SETTLER. BOTTOM: MIXER-SETTLER IN A COUNTERCURRENT ARRANGEMENT.....	16
FIGURE 4. SCHEMATIC REPRESENTATION OF A CENTRIFUGAL EXTRACTOR.....	16
FIGURE 5. SCHEMATIC REPRESENTATION OF A PULSED COLUMN. A TYPICAL EXTRACTION OF URANYL BY A PULSED COLUMN IS SHOWN. THE ORGANIC PHASE IS LOADED WITH URANYL DURING THE EXTRACTION.....	17
FIGURE 6. SCHEMATIC EVOLUTION OF THE CRITICAL CAPILLARY NUMBER AS A FUNCTION OF THE VISCOSITY RATIO.	20
FIGURE 7: SCHEMATIC REPRESENTATION OF SIMPLE SHEAR OF A LIQUID FILM.....	21
FIGURE 8. SIMPLE PICTURE OF THE ORIGIN OF VISCOSITY	26
FIGURE 9. QUALITATIVE EVOLUTION OF THE INTERFACIAL TENSION OF A MACROSCOPIC WATER-OIL INTERFACE IN PRESENCE OF AN AMPHIPHILIC MOLECULE AND THE CORRESPONDING MESOSTRUCTURAL EVOLUTION.	29
FIGURE 10. SCHEMATIC OVERVIEW OVER THE THREE MAIN MECHANISMS OF METAL EXTRACTION	31
FIGURE 11. LEFT: SCHEMATIC VIEW OF A DIRECT MICELLE WITH A HYDROCARBON INTERIOR IN FLUID STATE. HEADGROUP REPULSION AND INTERFACIAL ATTRACTION DETERMINE THE OPTIMUM HEADGROUP AREA A_0	33
FIGURE 12. SCHEMATIC REPRESENTATION OF THE PRINCIPAL CURVATURES C_1 AND C_2 OF A SADDLE-LIKE GEOMETRY.	34
FIGURE 13. THE SPONTANEOUS AND THE EFFECTIVE PACKING PARAMETER IN AQUEOUS AND ORGANIC MEDIA	37

FIGURE 14. OVERVIEW OF POSSIBLE STRUCTURES DEPENDENT ON CURVATURE AND PACKING PARAMETER.....	38
FIGURE 15. THE FOUR ORGANIZED MICROSTRUCTURES DESCRIBED BY TESTARD ET AL.	39
FIGURE 16. SCHEMATIC PHASE BEHAVIOR OF MALONAMIDES IN PRESENCE OF SOLUTES/IONS IN THE ORGANIC PHASE.	40
FIGURE 17. POSSIBLE PHASE DIAGRAM OF STRUCTURES IN AN EXTRACTING ORGANIC PHASE DEPENDENT ON EXTRACTANT CONCENTRATION AND NORMALIZED METAL CONTENT C_s/C	43
FIGURE 18. REVERSE WORMLIKE MICELLES IN THE DILUTE (LEFT) AND THE SEMI-DILUTE (RIGHT) REGIME. A POLAR CORE IS ENCLOSED IN A BOTTLEBRUSH STRUCTURE OF EXTRACTANT CHAINS	46
FIGURE 19. SCHEMATIC REPRESENTATION OF SHEAR THINNING AND NEWTONIAN VISCOSITY BEHAVIOR.....	47
FIGURE 20. THE CHARACTERISTIC LENGTH-SCALES OF WORMLIKE MICELLES: THE RADIUS OF GYRATION, THE CONTOUR LENGTH, THE PERSISTENCE LENGTH AND THE CROSS SECTION .	47
FIGURE 21. SCHEMATIC EVOLUTION OF VISCOSITY AND STRUCTURE DEPENDENT ON SALT CONCENTRATION.	49
FIGURE 22. THE THREE MECHANISMS OF STRESS RELAXATION FOR WORM-LIKE MICELLES	49
FIGURE 23. SCHEMATIC REPRESENTATION OF A CONNECTED NETWORK OF REVERSE WORMLIKE MICELLES.	51
FIGURE 24. LOCALLY CONDENSED NANOCRYSTALS COEXISTING WITH A DILUTE SOLUTION	53
FIGURE 25. STICKY ELLIPSOIDS FORMING A CHAIN BRACELET.	55
FIGURE 26. SIMPLIFIED SCHEME OF THE PUREX PROCESS.	58
FIGURE 27. RELATIVE RADIOACTIVITY OF SPENT NUCLEAR FUEL WITH A BURN-UP OF 38 MWd/kg U.	58
FIGURE 28. STRUCTURE OF TRIBUTYL PHOSPHATE (LEFT) AND GENERAL MONOAMIDE STRUCTURE (RIGHT)	60
FIGURE 29. MESOMERIC STRUCTURES OF MONOAMIDES INDICATING A PARTIAL NEGATIVE CHARGE ON THE OXYGEN ATOM	61

FIGURE 30. POLARIZATION CHARGE DENSITY (Σ) SURFACE OF LEFT: DEHiBA AND RIGHT: URANYL NITRATE CALCULATED BY COSMO-RS.	61
FIGURE 31. VISCOSITY OF ORGANIC PHASE (RED DASHED) AND PHASE SEPARATION TIME (BLUE SOLID) WITH INCREASING URANIUM LOADING AT AMBIENT TEMPERATURE.	62
FIGURE 32. STRUCTURES OF THE MONOAMIDES DEHiBA (LEFT), DEHBA (MIDDLE) AND DEHDMBA (RIGHT).....	63
FIGURE 33. MD SIMULATION SNAPSHOTS TAKEN FROM [196]	64
FIGURE 34. SCHEMATIC REPRESENTATION OF BABINET’S PRINCIPLE.	72
FIGURE 35. LEFT: CORE (R_2) AND SHELL (R_1) RADIUS OF THE MODEL AGGREGATE. RIGHT: MINIMUM HYDROPHILIC HEAD CORE RADIUS R_2'	75
FIGURE 36. SCHEMATIC EVOLUTION OF THE AREA PER HEADGROUP PER EXTRACTANT DUE TO VOLUME INCREASE OF THE POLAR CORE.....	75
FIGURE 37. ESTIMATION OF THE INTERFACIAL AREA PER EXTRACTANT TO CALCULATE THE PSEUDO SPONTANEOUS PACKING PARAMETER.	76
FIGURE 38. VISCOSITY INCREASE DUE TO INCREASING URANYL CONCENTRATION IN THE ORGANIC PHASE FOR DIFFERENT EXTRACTANTS AT 25 °C.	80
FIGURE 39. CORRELATION BETWEEN THE ESTIMATED SPONTANEOUS PACKING PARAMETERS BY THREE METHODS (TABLE 5) AND THE OBSERVED VISCOSITY CURVE (IN GREY).	81
FIGURE 40. VISCOSITY INCREASE DUE TO INCREASING URANYL CONCENTRATION IN THE ORGANIC PHASE FOR DIFFERENT EXTRACTANT CONCENTRATIONS AT 25 °C.	82
FIGURE 41. VISCOSITY INCREASE DUE TO INCREASING URANYL CONCENTRATION IN THE ORGANIC PHASE FOR DIFFERENT EXTRACTANT CONCENTRATIONS AT 25 °C.	83
FIGURE 42. TEMPERATURE DEPENDENCE OF SHEAR VISCOSITIES (200 1/s) OF ORGANIC PHASES DEPENDING ON URANYL AND EXTRACTANT CONCENTRATION.	85
FIGURE 43. LEFT: LINEAR FITS USING EQUATION (55) FOR 1.5 M DEHiBA DILUTED IN ISANE IP 175 CHARGED WITH URANYL. RIGHT: RESULTING FIT PARAMETER FROM ARRHENIUS FITS.	87
FIGURE 44. APPARENT VISCOSITIES (LEFT) AND SHEAR STRESSES (RIGHT) DEPENDING ON THE SHEAR RATE.	90

FIGURE 45. LEFT: SHEAR VISCOSITIES AT 25 °C DEPENDENT ON DILUENT AND URANYL CONCENTRATION. RIGHT: APPROXIMATE VISCOSITY INCREASE FROM CONTACT WITH NITRIC ACID (0 M) TO 2/3 LOADING OF THE ORGANIC PHASE (0.5 M URANYL).....	91
FIGURE 46. SAXS SPECTRA OF ORGANIC PHASES CONTAINING DEHiBA DISSOLVED IN ISANE IP 175 AND CONTACTED WITH AQUEOUS PHASE. .	96
FIGURE 47. SAXS SPECTRA OF ORGANIC PHASES CONTAINING 1.5 M DEHiBA DISSOLVED IN ISANE IP 175 AND CHARGED WITH URANYL BY CONTACT WITH AQUEOUS PHASES. .	97
FIGURE 48. TOP: SCHEMATIC REPRESENTATION OF POSSIBLE VACANCIES WITHIN A URANYL-NITRATE-URANYL CHAIN. .	98
FIGURE 49. SAXS SPECTRA OF ORGANIC PHASES CONTAINING DEHiBA IN DIFFERENT CONCENTRATIONS DISSOLVED IN ISANE IP 175 AND CHARGED WITH DIFFERENT CONCENTRATIONS OF URANYL. .	101
FIGURE 50. SCHEMATIC INTERPRETATION OF THE SAXS EXPERIMENT WITH INCREASEASING EXTRACTANT CONCENTRATION AT LEFT: CONSTANT URANYL CONTENT AND RIGHT CONSTANT URANYL EXTRACTANT RATIO ..	102
FIGURE 51. SAXS SPECTRA OF ORGANIC PHASES CONTAINING 1.5 M MONOAMIDE EXTRACTANT DISSOLVED IN LEFT: DODECANE AND RIGHT: TOLUENE AND BOTH CHARGED WITH 0.5 ± 0.05 M URANYL. .	103
FIGURE 52. SAXS SPECTRA OF ORGANIC PHASES CONTAINING 1.5 M DEHiBA DISSOLVED IN LEFT: DODECANE AND RIGHT: XYLENE AND BOTH CHARGED WITH INCREASING URANYL CONCENTRATION. ..	104
FIGURE 53. TEMPERATURE DEPENDENT SWAXS SPECTRA OF ORGANIC PHASES CONTAINING 1.5 M DEHiBA DISSOLVED IN ISANE IP 175 AND CHARGED WITH DIFFERENT CONCENTRATIONS OF URANYL. ..	105
FIGURE 54. SAXS SPECTRA OF CONCENTRATED ORGANIC PHASES CHARGED WITH URANYL. . .	106
FIGURE 55. SANS SPECTRA OF ORGANIC PHASES CONTAINING 1.5 M DEHiBA IN DEUTERATED DODECANE CHARGED WITH URANYL. .	107
FIGURE 56. SANS SPECTRA OF ORGANIC PHASES CONTAINING DIFFERENT CONCENTRATIONS OF DEHiBA IN DEUTERATED DODECANE CHARGED WITH A DEFINED MOL RATIO $[\text{URANYL}]/[\text{EXTRACTANT}]$ OF 0.25 ± 0.05 (HALF SATURATION..	110

FIGURE 57. SANS SPECTRA OF ORGANIC PHASES CONTAINING 1.5 M OF EXTRACTANT IN TWO DIFFERENT DEUTERATED DILUENTS.	111
FIGURE 58. EXAMPLE OF A RISE IN LOW Q AS SEEN FOR SOME OF THE SAMPLES.	114
FIGURE 59. SCHEMATIC REPRESENTATION OF THE TWO EXTREME CASES. ..	121
FIGURE 60. SCHEME DESCRIBING THE MONTE-CARLO-LIKE SIMULATION. ..	126
FIGURE 61. AN EXEMPLARY RESULT OF THE 2D SIMULATION AFTER MINIMIZATION OF THE FRUSTRATION ENERGY.	127
FIGURE 62. SCHEMATIC OVERVIEW OF THE MAIN STEPS OF THE MODEL.	130
FIGURE 63. QR CODE TO ACCESS THE MODEL INTERFACE ONLINE	131
FIGURE 64. SCREENSHOT OF THE MODEL-INTERFACE. ..	132
FIGURE 65. SCREENSHOT OF THE INTERFACE OF ACCORDION III SHOWING THE SCHEMATIC REPRESENTATION OF THE PACKING GEOMETRY.	133
FIGURE 66. SCREENSHOT OF THE INTERFACE OF ACCORDION I.	138
FIGURE 67. SCREENSHOT OF THE INTERFACE OF ACCORDION XII - MONTE-CARLO-LIKE SIMULATION. ...	139
FIGURE 68. CALCULATED MICROPHASE DISTRIBUTION AS WELL AS THE CORRESPONDING DIFFERENCES IN STANDARD REFERENCE CHEMICAL POTENTIAL RESPECTIVE TO CYLINDERS DEPENDENT ON THE INITIAL SPONTANEOUS PACKING PARAMETER P_{INIT} AND THE URANYL CONTENT X. ...	141
FIGURE 69. TWO-DIMENSIONAL IMAGE OF THE ORGANIC PHASE AND REL. STANDARD REFERENCE CHEMICAL POTENTIAL AT SAME URANYL CONTENT WITH DIFFERENT INITIAL SPONTANEOUS PACKING PARAMETERS P_{INIT}	142
FIGURE 70. SCHEMATIC REPRESENTATION OF THE EFFECT OF ADDITION OF A MORE CURVED EXTRACTANT.....	144
FIGURE 71. CALCULATED MICROPHASE DISTRIBUTION AS WELL AS THE CORRESPONDING STANDARD REFERENCE CHEMICAL POTENTIAL DEPENDENT ON THE MOL RATIO BETWEEN AN EXTRACTANT 1 ($P_{\text{INIT}} = 2.7$) AND AN EXTRACTANT 2 ($P_{\text{INIT}} = 3.2$).....	145
FIGURE 72. CALCULATED MICROPHASE DISTRIBUTION AS WELL AS THE CORRESPONDING STANDARD REFERENCE CHEMICAL POTENTIAL MOL RATIO DEPENDENT ON THE METAL RESPONSE ON AN EXTRACTANT 1 WITH $P_{\text{INIT}} = 3$	147

FIGURE 73. TWO-DIMENSIONAL IMAGE OF THE ORGANIC PHASE AND REL. STANDARD REFERENCE CHEMICAL POTENTIAL OF THE SAME INITIAL SPONTANEOUS PACKING PARAMETERS P_{INIT} WITH DIFFERENT METAL RESPONSE..	148
FIGURE 74. CALCULATED MICROPHASE DISTRIBUTION AS WELL AS THE CORRESPONDING STANDARD REFERENCE CHEMICAL POTENTIAL MOL RATIO DEPENDENT ON THE METAL RESPONSE ON AN EXTRACTANT 1 WITH $P_{\text{INIT}} = 3$.	150
FIGURE 75. TWO-DIMENSIONAL IMAGE DERIVED FROM MONTE-CARLO-LIKE SIMULATION DEPENDENT ON THE INITIAL PACKING PARAMETER AND THE VOLUME FRACTION OF AGGREGATED EXTRACTANT..	153
FIGURE 76. SCREENSHOT OF ACCORDION II OF THE MODEL INTERFACE.	155
FIGURE 77. COMPARISON OF THE SIMULATED VISCOSITY VALUES WITH THE EXPERIMENTAL ONES.....	156
FIGURE 78. SCHEMATIC REPRESENTATION EXTRACTANTS AT A MACROSCOPIC FLAT INTERFACE (LEFT) AND A CURVED INTERFACE OF AN AGGREGATE (RIGHT)	157
FIGURE 79. EVOLUTION OF THE MICROPHASE DISTRIBUTION AND SIMULATED VISCOSITY.....	158
FIGURE 80. EVOLUTION OF THE MICROPHASE DISTRIBUTION AND SIMULATED VISCOSITY, WITH INCREASED PENETRATION POWER OF THE DILUENT.	159
FIGURE 81. POSSIBLE APPROACHES TO REDUCE THE VISCOSITY RESULTING FROM THE MODEL.	166
FIGURE 82. STRUCTURE OF MOEHA	169
FIGURE 83. VISCOSITY INCREASE DUE TO INCREASING URANYL CONCENTRATION IN THE ORGANIC PHASE FOR DIFFERENT EXTRACTANTS AT 25 °C.....	171
FIGURE 84. VISCOSITY INCREASE DUE TO INCREASING URANYL CONCENTRATION IN THE ORGANIC PHASE FOR 1.5 DEHBA IN PRESENCE OF DIFFERENT GUERBET ALCOHOLS AT 25 °C.....	173
FIGURE 85. VISCOSITY INCREASE DUE TO INCREASING URANYL CONCENTRATION IN THE ORGANIC PHASE FOR 1.5 DEHBA IN PRESENCE OF DIFFERENT ADDITIVES AT 25 °C.....	174
FIGURE 86. VISCOSITY INCREASE DUE TO INCREASING URANYL CONCENTRATION IN THE ORGANIC PHASE FOR 1.5 DEHiBA IN PRESENCE OF DIFFERENT ADDITIVES AT 25 °C..	175

FIGURE 87. VISCOSITY INCREASE DUE TO INCREASING URANYL CONCENTRATION IN THE ORGANIC PHASE FOR 1.5 DEHDMBA IN PRESENCE OF 1 M 2-METHYLTETRAHYDROFURAN AT 25 °C..	175
FIGURE 88. VISCOSITY INCREASE DUE TO INCREASING URANYL CONCENTRATION IN THE ORGANIC PHASE FOR DIFFERENT DEHiBA/DEHBA MOL RATIOS AT 25 °C.....	178
FIGURE 89. SALT CURVE OF 10 WT% SLES IN WATER IN PRESENCE OF NaCl AND THE SCHEMATIC EVOLUTION OF THE MICROSTRUCTURE.	183
FIGURE 90. SALT CURVES OF 10 WT% SLES IN PRESENCE OF SALT AND 0.5 WT% OF DIFFERENT PERFUME MOLECULES.	184
FIGURE 91. VISCOSITY EVOLUTION OF 10 WT% SLES AND SODIUM LAURYL GLYCINATE IN WATER IN PRESENCE OF DIFFERENT SALTS.....	185
FIGURE 92. SCHEMATIC REPRESENTATION OF THE CONCEPT OF MATCHING AFFINITIES ACCORDING TO THE HOFMEISTER SERIES.	187
FIGURE 93. THE THREE VISCOSITY-DETERMINING MICROPHASES IN CHEMICAL EQUILIBRIUM: ENDCAPS, CYLINDERS AND JUNCTIONS	189
FIGURE 94. SCHEMATIC DESCRIPTION OF THE ALTERNATIVE DEFINITION OF THE SPONTANEOUS PACKING PARAMETER.....	191
FIGURE 95. SIMULATED EVOLUTION OF THE PERCENTAGE OF SULFATE HEADGROUPS OF SLES ASSOCIATED WITH A SODIUM COUNTERION, THE AREA PER HEADGROUP A_0 AND THE RESULTING EVOLUTION OF THE SPONTANEOUS PACKING PARAMETER P_0 AS A FUNCTION OF THE EXCESS SALT CONTENT X.....	198
FIGURE 96. LEFT: SIMULATED EVOLUTION OF THE DIFFERENCE IN STANDARD REFERENCE CHEMICAL POTENTIAL OF ENDCAPS (ORANGE) AND JUNCTIONS (BLUE) RESPECTIVE TO CYLINDER MICROPHASES WITH VARYING EXCESS SALT CONTENT X. RIGHT: MICROPHASE DISTRIBUTION OF ENDCAPS, CYLINDERS AND JUNCTIONS AS A FUNCTION OF X.....	200
FIGURE 97. EVOLUTION OF THE EFFECTIVE MICELLAR LENGTH $Leff$ AND THE CALCULATED VISCOSITY RESULTING FROM THE MICROPHASE DISTRIBUTION AS A FUNCTION OF EXCESS SALT CONTENT X	201
FIGURE 98. COMPARISON OF THE SIMULATED VISCOSITY CURVE OF 10 WT% SLES IN WATER WITH THE EXPERIMENTAL VALUES FROM REF.[126].	202
FIGURE 99. SALT CURVES OF 10 WT% SLES FOR DIFFERENT SALTS.	203

FIGURE 100. COMPARISON OF SIMULATED SALT CURVES WITH EXPERIMENTAL VISCOSITY VALUES.	204
FIGURE 101. SIMULATED MICROPHASE DISTRIBUTIONS FOR 10 WT% SLES IN WATER IN PRESENCE OF 0.5 WT% OF FRAGRANCE AS A FUNCTION OF THE EXCESS SALT CONTENT X.	206
FIGURE 102. COMPARISON OF SIMULATED VISCOSITY CURVES WITH EXPERIMENTAL VALUES FOR 10 WT% SLES IN PRESENCE OF 0.5 WT% FRAGRANCE.	207
FIGURE 103. TOP: MICROPHASE DISTRIBUTION OF 10 WT% SLES IN WATER WITH SALT ADDITION AND RESULTING EXPERIMENTAL AND CALCULATED VISCOSITY.....	211
FIGURE 104. EXEMPLARY CALCULATION OF THE MICROPHASE DISTRIBUTION OF A LINEAR (LEFT) AND A BRANCHED (RIGHT) ETHOXYLATED SURFACTANT APPLYING A BENDING CONSTANT OF 1.5 kT..	224
FIGURE 105. SCHEMATIC REPRESENTATION OF A POSSIBLE EXTENSION OF THE MODEL TO THE WHOLE RANGE OF CURVATURE.....	228

Tables

TABLE 1. LOCAL PRINCIPAL CURVATURES, MEAN AND GAUSSIAN CURVATURES AS WELL AS EFFECTIVE PACKING PARAMETERS FOR DIFFERENT AGGREGATE SHAPES	36
TABLE 2. SHORT OVERVIEW OF NON-SPHERICAL STRUCTURES OBSERVED FOR EXTRACTANTS IN LITERATURE	41
TABLE 3. SUMMARY OF THE MOST COMMON RECOVERY PROCESSES FOR SPENT FUEL	59
TABLE 4: CONFIGURATIONS USED FOR SANS MEASUREMENTS AT THE LLB.....	70
TABLE 5. CHARACTERISTIC PROPERTIES OF THE MAIN EXTRACTANTS INVESTIGATED	77
TABLE 6. THE MINIMAL PACKING PARAMETER AS WELL AS THE SPONTANEOUS PACKING PARAMETER ASSUMING A TETRAHEDRAL AND OCTAHEDRAL ARRANGEMENT CALCULATED FOR THE MAIN EXTRACTANTS INVESTIGATED	77
TABLE 7: RESULTS FROM FITTING THE TEMPERATURE DEPENDENCE OF VISCOSITY USING THE ARRHENIUS EQUATION.	87

TABLE 8. LOGP' VALUES ACCOMPLISHED BY COSMO-RS CALCULATION FOR DIFFERENT PHASE II/PHASE I COMBINATIONS DEMONSTRATING THE AFFINITY OF THE EXTRACTANT IN THE CORRESPONDING PHASES.....	92
TABLE 9. LOGP' VALUES ACCOMPLISHED BY COSMO-RS CALCULATION FOR DIFFERENT PHASE II/PHASE I COMBINATIONS DEMONSTRATING THE AFFINITY OF THE EXTRACTANT IN THE CORRESPONDING PHASES TRANSFERRED INTO FREE ENERGY OF TRANSFER $\Delta G_{TR} = RT \ln P$	93
TABLE 10. QUALITATIVE TREND OF AGGREGATE VOLUME OBTAINED FROM FORWARD SCATTERING	95
TABLE 11. FIT PARAMETER OBTAINED FROM FITS OF ORGANIC PHASES CHARGED WITH URANYL	108
TABLE 12. FIT PARAMETER OBTAINED FROM FITS OF ORGANIC PHASES CHARGED WITH URANYL	110
TABLE 13. FIT PARAMETER OBTAINED FROM FITS OF ORGANIC PHASES CHARGED WITH URANYL	112
TABLE 14. OVERVIEW OVER THE THREE VISCOSITY-DETERMINING MICROPHASES IN CHEMICAL EQUILIBRIUM AND THE CORRESPONDING EFFECTIVE PACKING PARAMETER.....	119
TABLE 15. THE FIVE MOST PROBABLE CONFORMERS FOR A URANYL NITRATE COMPLEX..	162
TABLE 16. CALCULATION OF THE MINIMAL PACKING PARAMETER AND THE SPONTANEOUS PACKING PARAMETER OF MOEHA ASSUMING A TETRAHEDRAL AND AN OCTAHEDRAL GEOMETRY	169

VII.3 Experimental Methods – chemicals and underlying theory

VII.3.1 List of chemicals used in this work

Suppl. Table 1. List of the main chemicals used in this work.

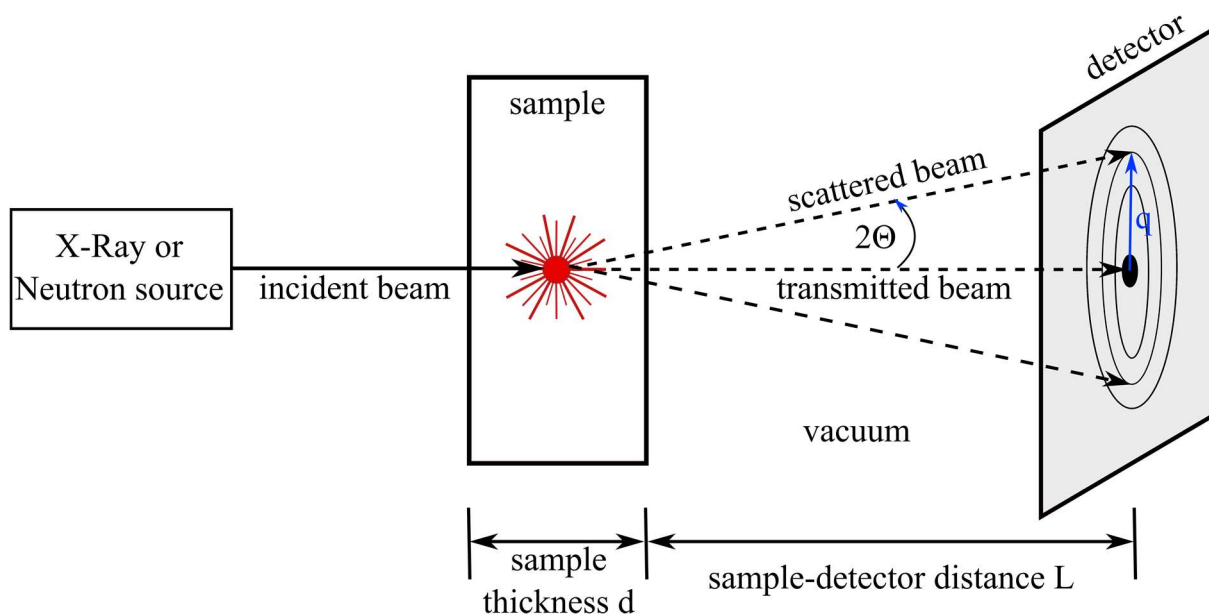
Chemical	Supplier	Purity
DEHiBA	Pharmasynthese (Lisses, FR)	> 99.5 %
DEHBA	Pharmasynthese (Lisses, FR)	> 99.5 %
DEHDMBA	Pharmasynthese (Lisses, FR)	> 99.5 %
TBP	Sigma Aldrich/Merck	> 99.5 %
MOEHA	Pharmasynthese (Lisses, FR)	> 99.5 %
Uranyl Stock solution, 373 g/L, 2 M HNO ₃	CEA Marcoule	-
Nitric acid, 69-70%	Fischer	> 99.5 %
Toluene	Sigma Aldrich/Merck	> 99.8 %
Xylene	Sigma Aldrich/Merck	> 98 %
Isane IP 175	Total	industrial
Composition: ~ 70% C10, ~ 20% C11, ~ 10% C9 ^[336]		
Dodecane	Sigma Aldrich/Merck	> 99 %
Isooctane	Sigma Aldrich/Merck	> 98 %
n-Octanol	Sigma Aldrich/Merck	> 99 %
D26-dodecane	Euroisotop	> 99 %
D8-toluene	Euroisotop	> 99 %
D18-isooctane	Euroisotop	> 99 %
D2O	Euroisotop	> 99 %
Tert-Butanol	Sigma Aldrich/Merck	> 99.5 %
Isofol 12	Sasol	industrial additive
Isofol 16	Sasol	industrial additive
Isofol 24	Sasol	industrial additive
2-MTHF	Sigma Aldrich/Merck	> 97 % + stabilzer
2-Ethoxyphenol	Sigma Aldrich/Merck	> 98 %
Benzylalcohol	Sigma Aldrich/Merck	> 99 %
Propylene glycol phenyl ether	Sigma Aldrich/Merck	> 93 %

VII.3.2 X-Ray and Neutron Scattering

Scattering of X-Rays and Neutrons is a powerful method to investigate the mesoscopic structure of colloids. Measurements at low scattering angles between 0.1 and 10° , are called Small Angle X-ray Scattering or Small Angle Neutron Scattering (SAXS or SANS for neutron). Depending on the set-up of the measurements and the wavelengths used, these scattering techniques allow to investigate structures between 1 nm and several hundred nm.

These techniques are often used complimentary. Since X-Rays are scattered at the electrons of the atomic shell, fluctuations in electron density of a sample compared to the solvent create the scattering contrast. Therefore, X-Ray scattering is especially sensitive to electron-rich scatterers. In contrast hereto, neutron radiation is scattered by the nuclei of atoms. The interaction of the neutron with a nucleus depends on the isotope and is expressed by the scattering length density (*SLD*) of each isotope. The crucial basis of this technique is the big difference in *SLD* values between hydrogen and deuterium ($SLD(^1\text{H}) = -0.374 \cdot 10^{-12}$ cm, $SLD(^2\text{H}) = 0.667 \cdot 10^{-12}$ cm). Using this feature allows to obtain a high scattering contrast when the hydrogenated extractant structures are formed in a deuterated diluent.

The basic principle of these two methods are the same. The incident wave interacts with the scattering centers. Each scatterer reemits a spherical wave. Theses waves interfere and the resulting pattern is detected behind the sample perpendicular to the direction of the incoming beam that initially hit the sample (*cf.* **Suppl. Figure 1**). The scattering pattern contains information on the structure of the sample.



Suppl. Figure 1. Scheme of a SAXS or SANS set-up

For colloidal structures in solution, the scattering pattern is a result of several contributions. The scattering intensity of the diluent $I(q)_{\text{dil}}$ and of monomers $I(q)_{\text{monomer}}$ must be considered as well as $I(q)_{\text{aggregate}}$, the intensity of aggregates. Uranyl ions can be excited to a state of higher energy by absorbing X-Rays. During relaxation to the ground state, photons can be emitted and fluorescence occurs. This fluorescence is difficult to subtract correctly at elevated uranyl concentration since the transmission of the samples becomes low and a calibration is difficult. However, it was determined experimentally, that the fluorescence I_F can be considered as q -independent and increases linear with uranyl concentration. Furthermore, it can be assumed at high q values ($> 10 \text{ nm}^{-1}$), that the solvent peak is independent of the concentration of uranyl in solution. Therefore, the heights of the solvent peaks must be approximately constant for different uranyl concentrations at same diluent and extractant concentration. Therefore, the corrected scattering intensity $I(q)$ caused by the scattering of monomers and aggregates can be determined from

$$I(q) = I(q)_{\text{aggregate}} + I(q)_{\text{monomer}} = I(q)_{\text{raw}} - \phi_{\text{dil}} I(q)_{\text{dil}} - I_F \quad (117)$$

With ϕ_{dil} being the volume fraction of the diluent and $I(q)_{\text{raw}}$ the measured scattering intensity at absolute scale.

The corrected scattering intensity $I(q)$ at absolute scale can be written as

$$I(q) = N \cdot V^2 \cdot \Delta SLD \cdot P(q) \cdot S(q) \quad (118)$$

with N being the number of scattering particles, V the volume of scatterers, ΔSLD the scattering contrast, $P(q)$ the form factor and $S(q)$ the structure factor. The form factor gives information about the particle size and shape while the structure factor indicates the interactions between the single particles.

The so-called forward scattering can give information on the particle volume. At low q values, the form factor $P(q)$ can be assumed as equal to 1 such as the structure factor $S(q)$ for very dilute systems. With $N \cdot V = \Phi$ being the volume fraction, one can derive an expression for the particle volume.

$$I(q)/S(q) = \Phi \cdot V \cdot \Delta SLD \quad (119)$$

If the volume fraction and scattering contrast are known, the volume of the particles can be obtained. However, this calculation as well as the extraction and fitting of the form factor is

only useful for very dilute systems. Since in this work, mainly concentrated systems were used and form factors and structure factors were tried to be fitted simultaneously, the informative value from quantitative analysis of such systems must be taken with care.

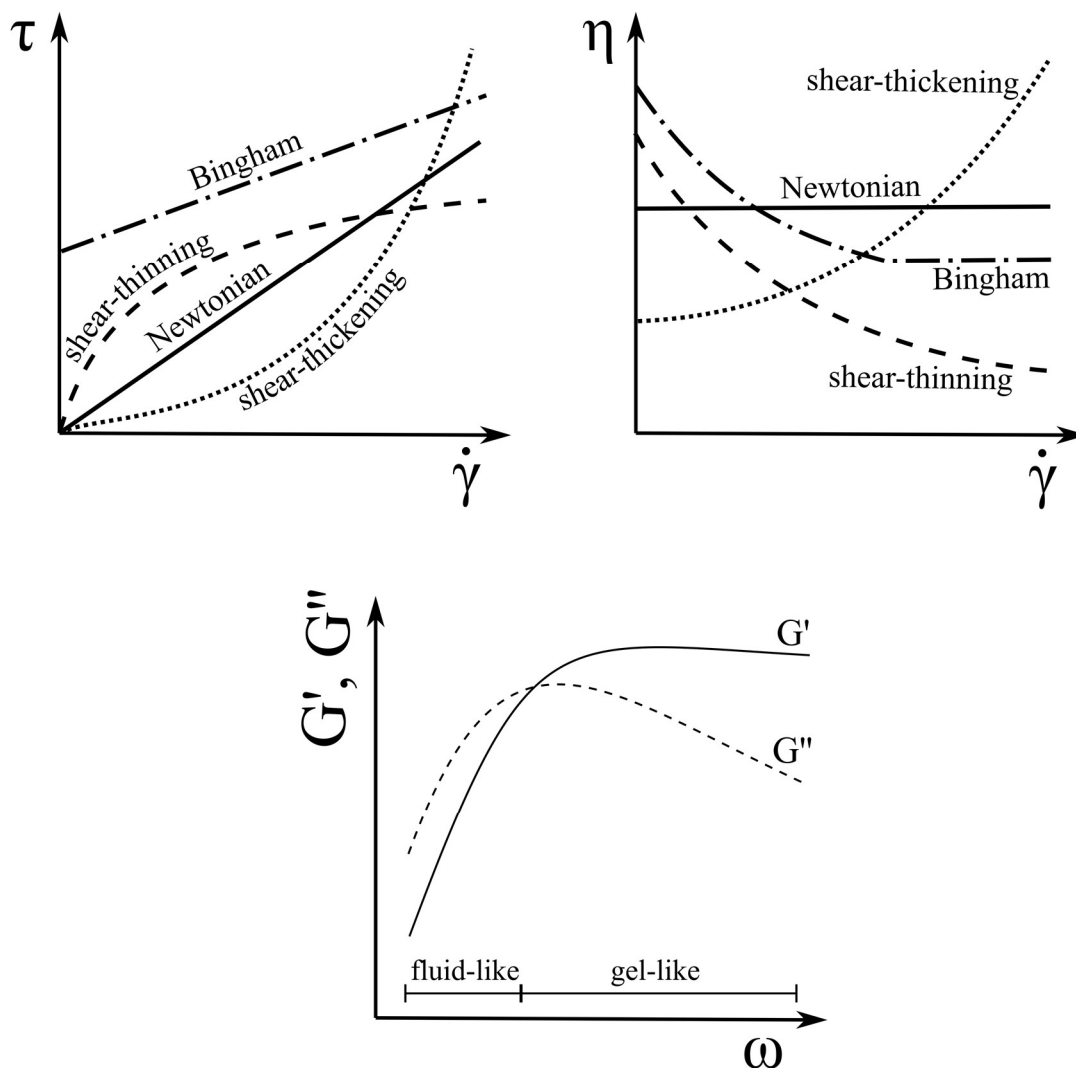
VII.3.3 Rheology^[130,337,338]

In the following, rheology is shortly explained and introduced. Since the structures in the organic phase described in this work seem to be too weak to induce significant viscoelasticity, only the basics that are needed for common understanding are presented.

Rheology is the study of the flow of matter. Rheology answers the question ‘How does the material respond to an applied force?’. This question is particularly important for complex structured materials with so-called viscoelastic behavior. The flow of such materials cannot be characterized by a single value of viscosity. The viscosity and flow behavior changes with changing conditions. Shaking of ketchup, for example, leads to a decrease in viscosity. This behavior is called ‘shear-thinning’ and is desired since this behavior facilitates the pouring out of the ketchup.

A sample can be classified according its flow behavior with varying shear rate. The viscosity of some materials is independent from the shear rate. Such liquids have a so called ‘Newtonian’ behavior. Other liquids are ‘non-Newtonian’ and become more viscous (shear-thickening) or less viscous (shear-thinning) with increasing shear rate. For other liquids, so-called ‘Bingham fluids’, first a ‘yield stress’ has to be overcome before the flow behavior becomes ‘Newtonian’ (*cf. Suppl. Figure 2*).

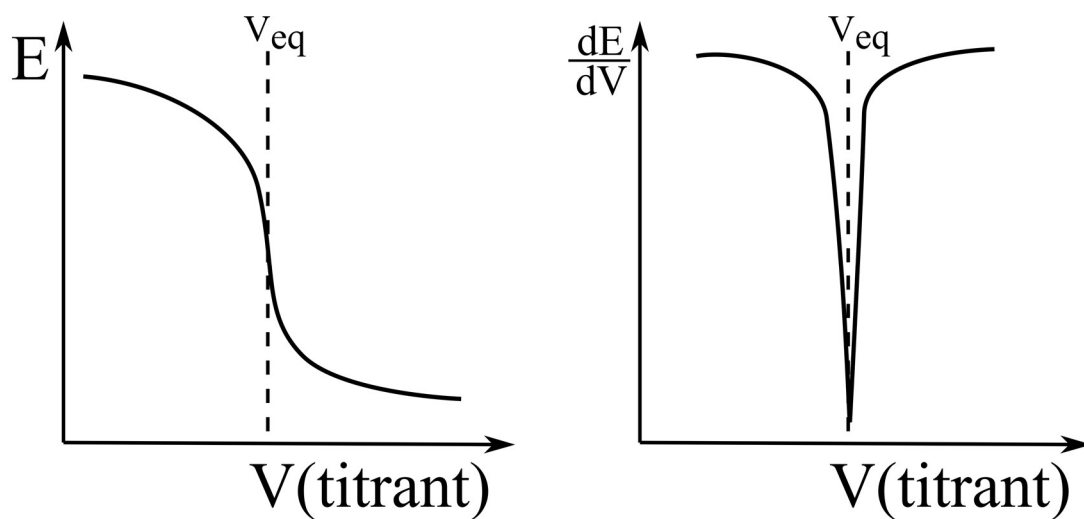
Another possibility to classify a sample is to carry out oscillatory shear measurements in the so-called linear viscoelastic range in which the storage modulus G' and the loss modulus G'' are independent from the strain amplitude. The storage modulus characterizes the elastic, solid-state properties of the liquid, while the loss modulus describes the viscous, fluid-like characteristics. The determination of these values with increasing oscillatory shear frequency allows to identify if the liquid behaves more gel-like ($G' > G''$) or more liquid-like ($G' < G''$) at a certain frequency.



Suppl. Figure 2. Schematic representation of classification of rheological properties of liquids into Newtonian, Bingham shear-thinning and shear-thickening as well as into fluid-like or gel-like.

VII.3.4 Potentiometric Titration

Potentiometric titration is a technique that is similar to a conventional direct titration of a redox titration. Instead of using an indicator, the potential across the analyt is measured. For this purpose, a metal indicator electrode and reference electrode are used of which each forms one half cell. The potential between these electrodes is measured after each addition of titrant. The potential of the indicator electrode varies with metal concentration. A typical curve of the potential against the volume of titrant added can be seen in **Suppl. Figure 3**. The midpoint in the steeply rising portion of the curve is estimated visually and taken as the end point.



Suppl. Figure 3. Schematic curve of a potentiometric titration. Left: Potential (typically in V) versus volume of titrant. Right: First derivative of the curve for better representation of the endpoint of the reaction.

VII.4 Short introduction to COSMO-RS^[234,339–341]

The calculations were carried out using the software COSMOtherm^[234]. The CONductor-like Screening MODEL for Realistic Solvation (COSMO-RS) theory combines quantum chemical calculations and statistical thermodynamics in order to predict chemical potentials and thermodynamic equilibrium properties of solutions.

The basis of this theory is the idea of locally interacting molecular surfaces. A preliminary task of COSMO-RS calculations is the creation of so-called COSMO-files by quantum chemical calculations and an iterative algorithm (QC-COSMO). These calculate the state of molecules embedded inside a conductor with a given dielectric constant. The underlying algorithm yields a self-consistent state describing the energy, the geometry of the molecule, the electron density and the polarization charge density in a virtual conductor. This state is stored in the COSMO-file and deals as reference state for molecules in the liquid phase. In a perfect conductor, all interactions are screened completely on the conductor interface by the conductor polarization charge density σ . Therefore, considering an ensemble of molecules, there are no intermolecular interactions and each molecule in the COSMO state can be treated individually. However, this is far from reality. Therefore, in order to simulate the liquid state, COSMO-RS introduces molecular contacts. As soon as two molecules are put in direct contact, the conductor between them is reduced by their contact area. This change in screened surface causes an energy change which can be split up in an electrostatic contribution and one arising from hydrogen bonding. The dispersive interactions are assumed to stay constant. The energy change is zero when the conductor polarizations on the contact surfaces of the two molecules are exactly opposite since the resulting screening charge stays zero. Therefore, molecules prefer to make contacts with polar surface pieces that are oppositely polarized.

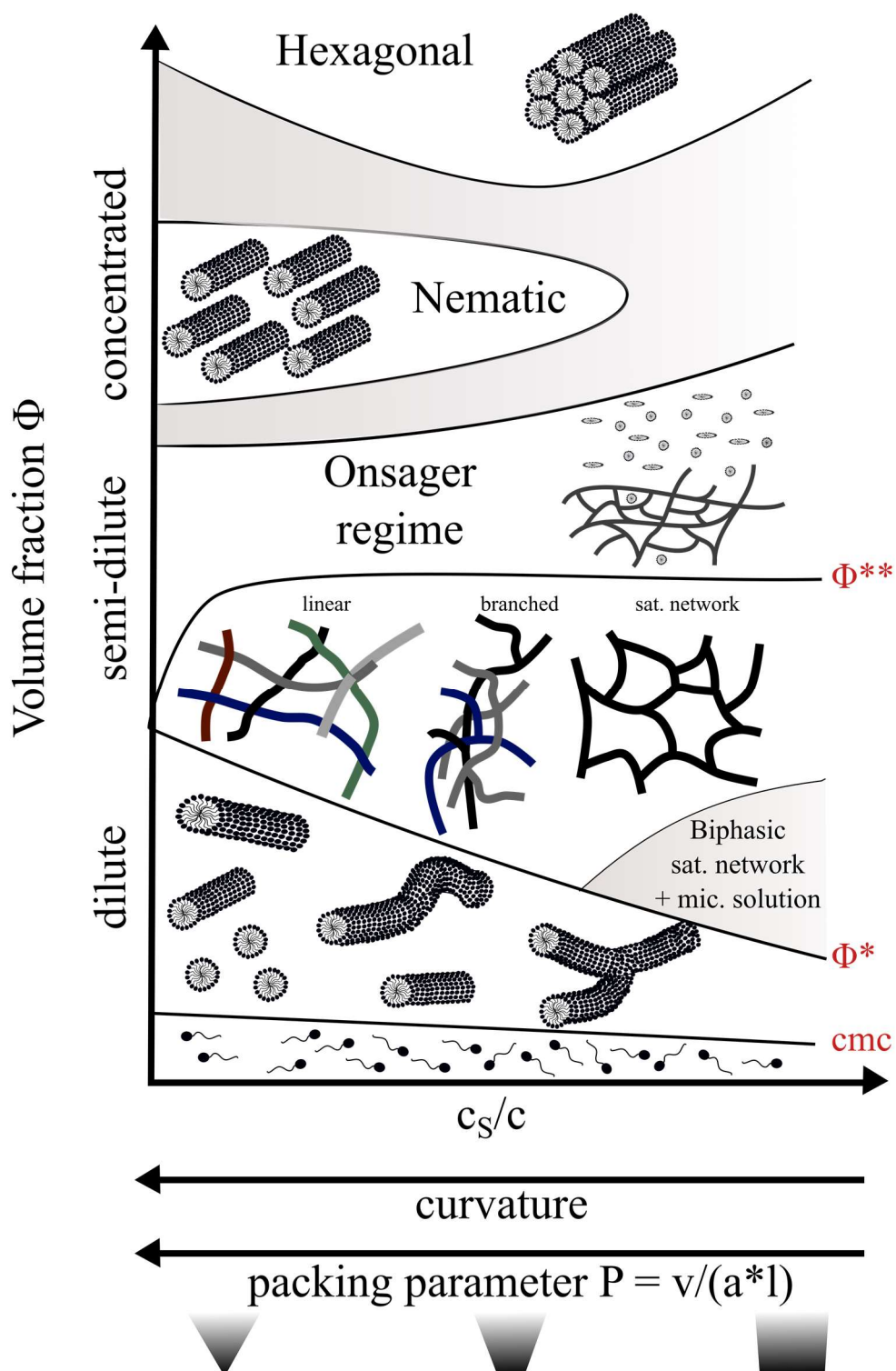
In order to obtain macroscopic thermodynamic properties of the liquid system, the local, pair-wise surface contact energies have to be summed up and thermodynamically averaged over all possible configuration of the liquid. This procedure is strongly facilitated since the problem in three dimensions is reduced to statistical thermodynamics of independently pair-wise interacting surface areas.

The σ -profile of a molecule is the histogram of the molecular COSMO surfaces respective to the its different polarization charge densities. The COSMO cavities (*cf.* **Figure 30** for an example of the COSMO cavities of certain extractants) are colored as follows. A deep blue surface area stands for a strongly negative polarization charge density, *i.e.* for parts of the

molecule that are strongly positively polarized. In contrast hereto, red COSMO surfaces indicate strongly negative molecular surface regions. Neutral surface parts are colored green.

COSMO-RS is a useful tool to calculate thermophysical properties and is widely used in process design and development for solvent and solubility screening, including ionic liquids. Also, pK_a estimation, partitioning predictions and similarity evaluations in drug design are possible.

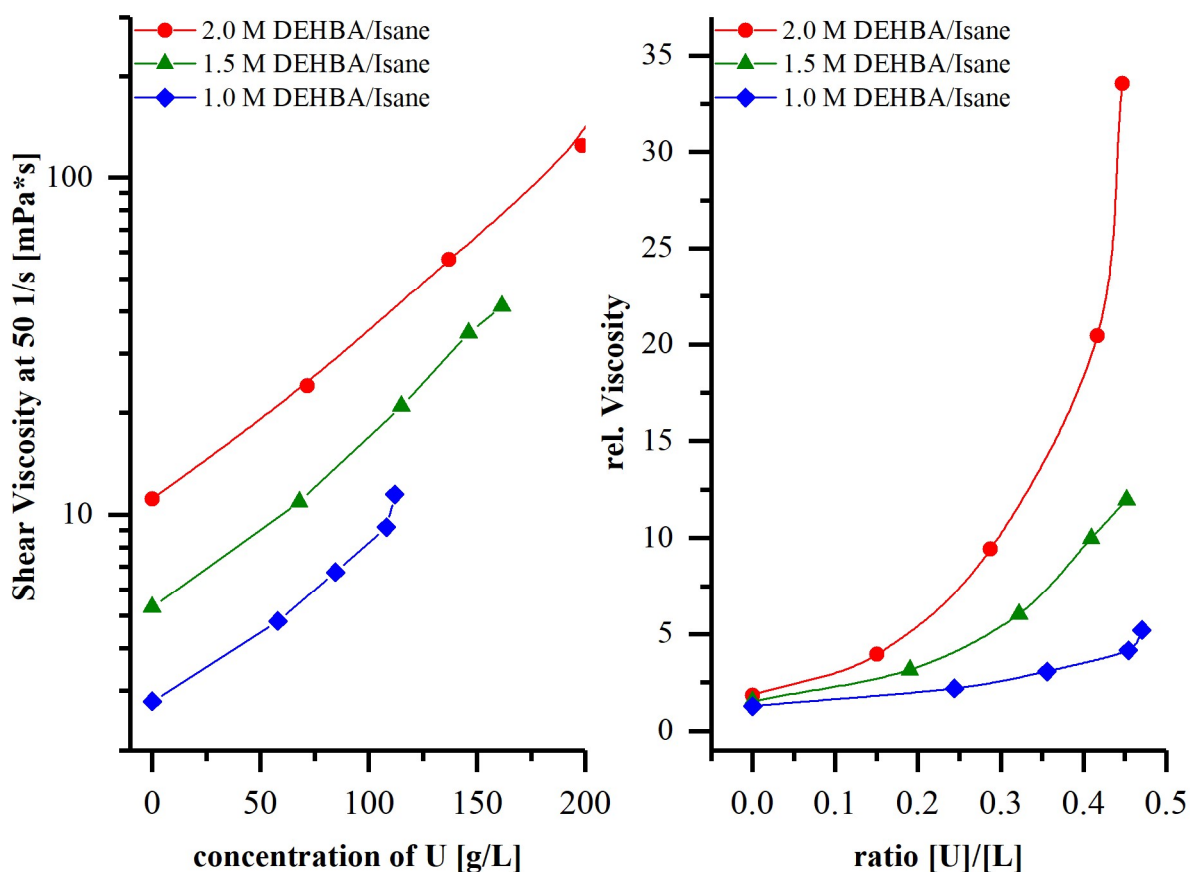
VII.5 Phase diagram of surfactant structures according to Cates



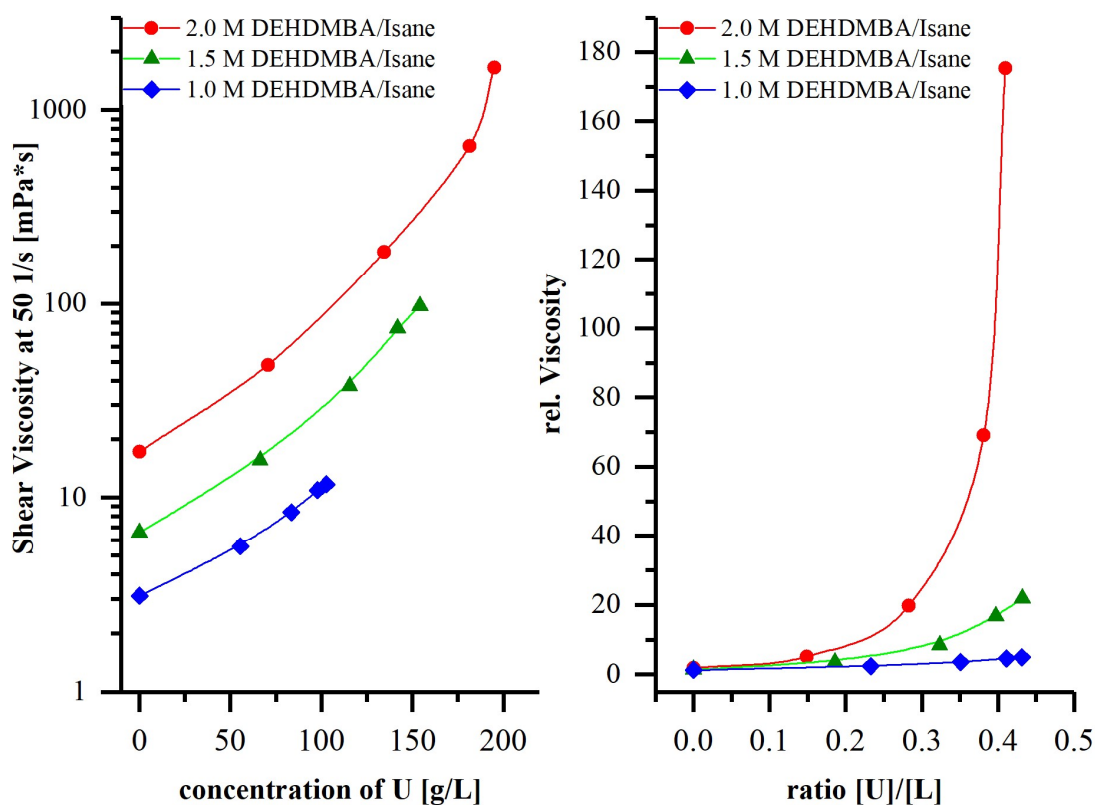
Suppl. Figure 4. Schematic phase diagram of surfactant self-assembly. Replotted and adjusted from^[116]

VII.6 Supplementary information to Chapter II.2

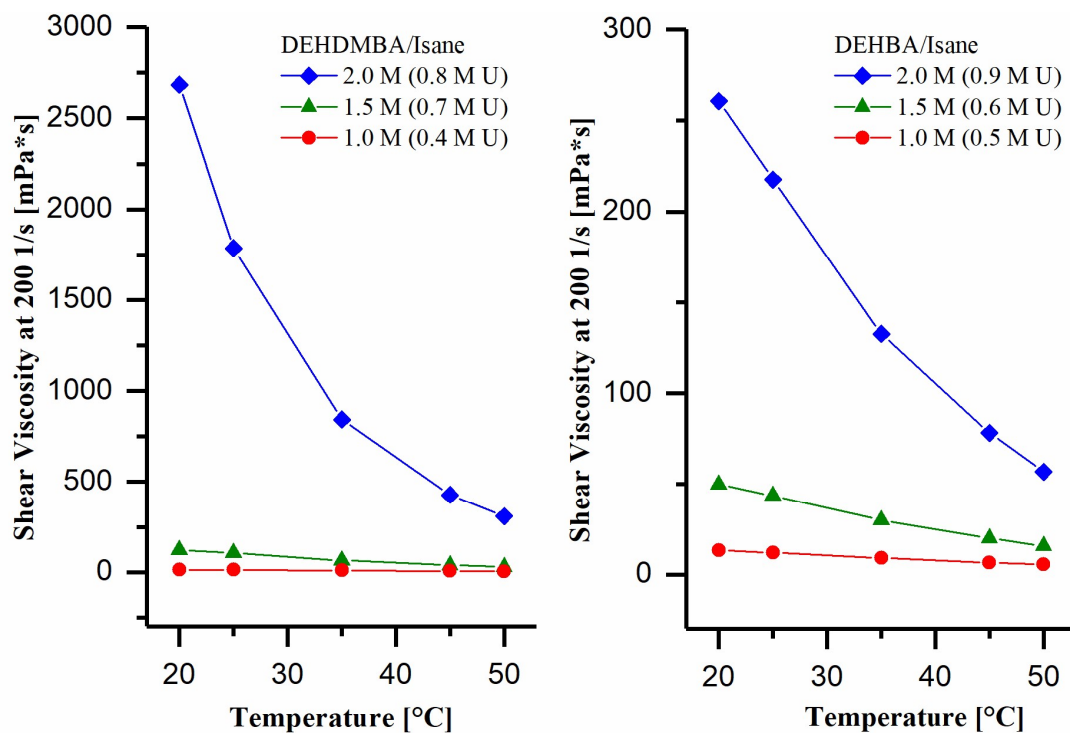
VII.6.1 Additional viscosity curves with variation of extractant concentration



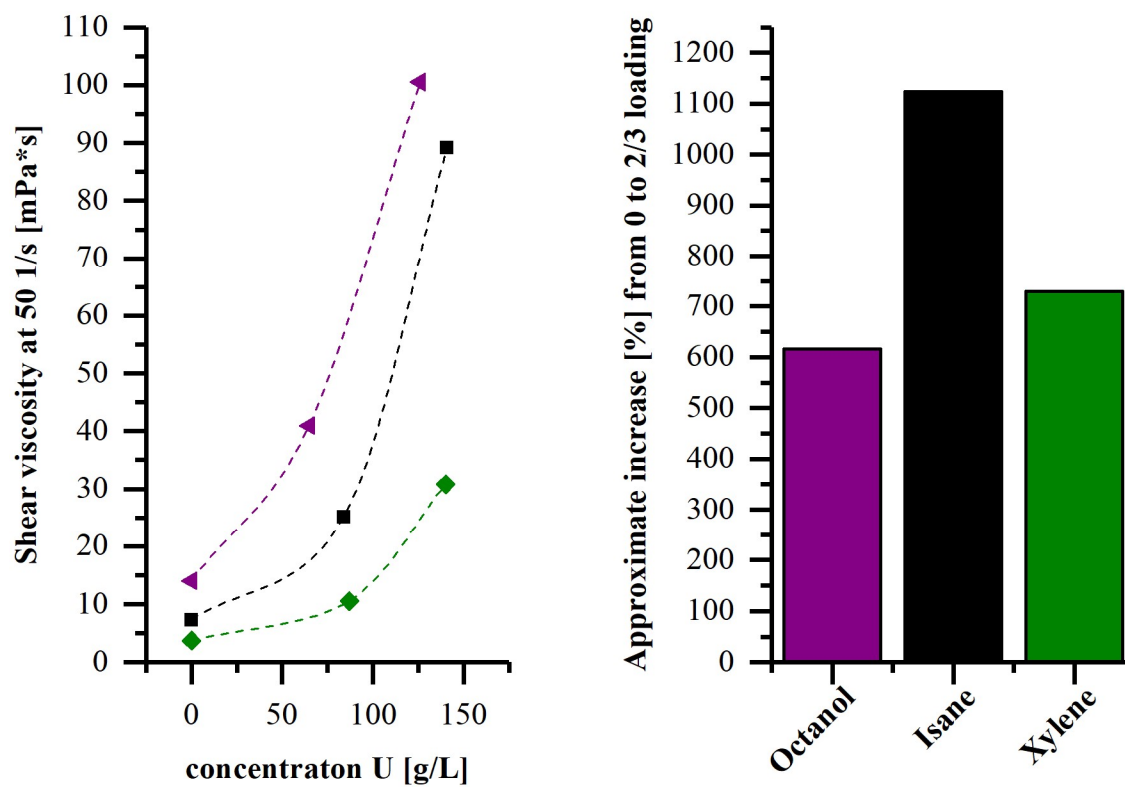
Suppl. Figure 5. Viscosity increase due to increasing uranyl concentration in the organic phase for different extractant concentrations at 25 °C. Left: Apparent viscosity at a shear rate of 501/s in linear scale. Right: Relative viscosity normalized by the viscosity of the non-contacted extractant/diluent mixtures \blacksquare 0.5 M \bullet 1.0 M \blacktriangle 1.5 M \blacklozenge 2.0 M DEHBA diluted in Isane IP 175 versus the molar ratio uranyl/extractant.



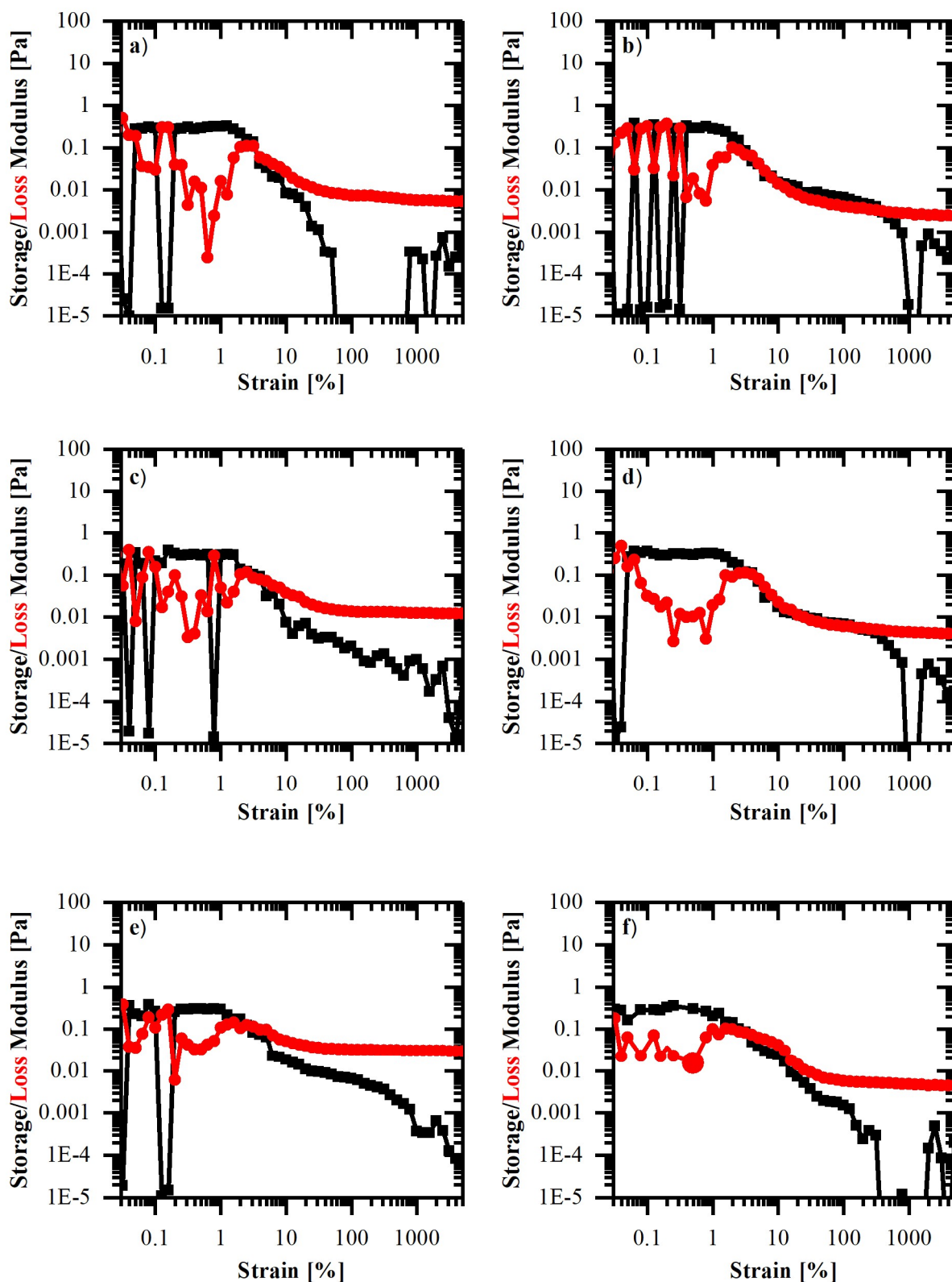
Suppl. Figure 6. Viscosity increase due to increasing uranyl concentration in the organic phase for different extractant concentrations at 25 °C. Left: Apparent viscosity at a shear rate of 501/s in linear scale. Right: Relative viscosity normalized by the viscosity of the non-contacted extractant/diluent mixtures \blacksquare 0.5 M \bullet 1.0 M \blacktriangle 1.5 M \blacklozenge 2.0 M DEHDMBA diluted in Isane IP 175 versus the molar ratio uranyl/extractant.



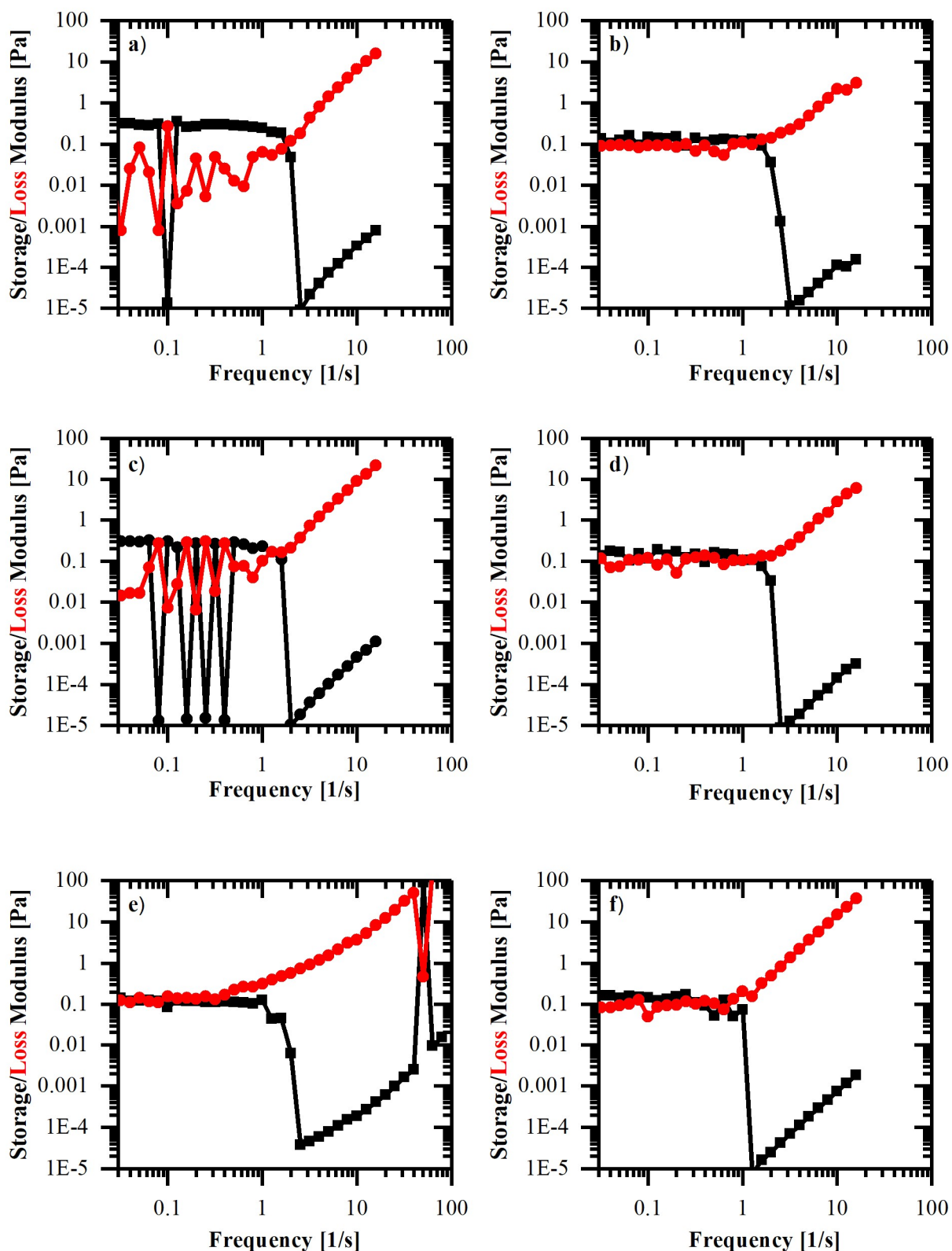
Suppl. Figure 7. Temperature dependence of shear viscosities (200 1/s) of organic phases depending on uranyl and extractant concentration. Left: 1 M, 1.5 M and 2 M DEHDMBABA diluted and Right: 1 M, 1.5 M and 2.0 M DEHBA in Isane and charged with different concentrations of uranyl



Suppl. Figure 8. Left: Shear viscosities at 25 °C dependent on diluent and uranyl concentration. Investigated system: 1.5 M DEHDMBA in different diluents contacted with different aqueous phases (uranyl nitrate dissolved in 3 M nitric acid). Right: Approximate viscosity increase from contact with nitric acid (0 M) to 2/3 loading of the organic phase (0.5 M uranyl)



Suppl. Figure 9. Amplitude sweeps at $f = 1$ 1/s of organic phases containing extractant (left: 1.5 M DEHiBA, right: 1.5 M TBP) diluted in Isane IP 175 after uranyl nitrate extraction. $[UO_2^{2+}]$ = a) 0 M b) 0 M c) 0.33 M d) 0.40 M e) 0.53 M f) 0.67 M



Suppl. Figure 10. Frequency sweeps at $\gamma = 0.2$ % of organic phases containing extractant (left: 1.5 M DEHiBA, right: 1.5 M TBP) diluted in Isane IP 175 after uranyl nitrate extraction. $[UO_2^{2+}] =$ a) 0 M b) 0 M c) 0.33 M d) 0.40 M e) 0.53 M f) 0.67 M

VII.6.2 Assumptions and input values for the geometrical calculation of the spontaneous packing parameter

Suppl. Table 2. Molar volumes used for the calculation of polar core volume in Chapter II.2.1

Molecule	Molar volume [cm ³ /mol]	Molar volume [Å ³ /molecule]	Referenz
H ₂ O	18.1	30.1	[342]
NO ₃ ⁻	35.4	58.8	[342]
UO ₂ (NO ₃) ₂	68.3	113.8	[343]

Assumed stoichiometry per Extractant of a spherical extractant aggregate:

Suppl. Table 3. Relative stoichiometries per extractant estimated from values of Ref.^[191,207] after contact with 3 M HNO₃.

	TBP	DEHiBA	DEHBA	DEHDMBA	MOEHA
Extractant	1	1	1	1	1
H ₂ O	0.2	0.1	0.1	0.1	0.1
NO ₃ ⁻	0.6	0.4	0.4	0.4	0.4
V(polar, $x = 0$) [Å ³ /molecule]	335	576	564	770	355

Suppl. Table 4. Relative stoichiometries per extractant estimated from values of Ref.^[191,207] after maximum loading with uranyl.

	TBP	DEHiBA	DEHBA	DEHDMBA	MOEHA
Extractant	1	1	1	1	1
H ₂ O	0.16	0.1	0.1	0.1	0.1
UO ₂ (NO ₃) ₂ ⁻	0.5	0.5	0.5	0.5	0.5
V(polar, $x = 0.5$) [Å ³ /molecule]	422	710	674	903	488

One should note, that these assumptions are as simplified as possible to make it general. Although these values can vary in reality, they are likely to show the relative trend.

VII.6.3 Tables of viscosity data and distribution coefficients

Suppl. Table 5. Shear viscosities and distribution coefficients of TBP diluted in Isane IP 175 in different concentrations and contacted with aqueous solutions containing 3 M nitric acid and uranyl in different concentrations

Extractant concentration	+ 343 g/L	+ 150 g/L	+ 75 g/L	+ 0 g/L
1.5 M				
Shear Visc. At 50 1/s (25°C) [mPa*s]	4.21	3.50	2.54	2.19
Shear Visc. At 200 1/s (25°C) [mPa*s]	4.33	3.90	2.78	2.08
Shear Visc. At 795 1/s (25°C) [mPa*s]	4.82	4.20	2.96	2.61
dynamic viscosity before contact	1.47			
viscosity increase due to uranium (0 to x)	92%	60%	16%	0%
viscosity increase due to uranium (0 _non contact to x)	186%	138%	73%	49%
[U] in organic phase [g/L]	168.5	133.7	72.4	0.0
[U] in organic phase [mol/L]	0.71	0.56	0.30	0.00
x = [U]/[Ex]	0.47	0.37	0.20	0.00
[U] in aqueous phase [g/L]	178.8	19.2	3.9	0.0
[U] in aqueous phase [mol/L]	0.75	0.08	0.02	0.00
distribution coefficient	0.94	6.97	18.68	

Extractant concentration	+ 343 g/L	+ 150 g/L	+ 75 g/L	+ 0 g/L
1.0 M				
Shear Visc. At 50 1/s (25°C) [mPa*s]	2.56	2.33	1.99	1.50
Shear Visc. At 200 1/s (25°C) [mPa*s]	2.75	2.65	2.34	1.84
Shear Visc. At 795 1/s (25°C) [mPa*s]	2.97	2.98	2.93	2.55
dynamic viscosity before contact	1.33			
viscosity increase due to uranium (0 to x)	70%	55%	32%	0%
viscosity increase due to uranium (0 _non contact to x)	93%	76%	50%	13%
[U] in organic phase [g/L]	114.9	99.7	68.5	0.0
[U] in organic phase [mol/L]	0.48	0.42	0.29	0.00
x = [U]/[Ex]	0.48	0.42	0.29	0.00
[U] in aqueous phase [g/L]	232.3	53.2	7.4	0.0
[U] in aqueous phase [mol/L]	0.98	0.22	0.03	0.00
distribution coefficient	0.49	1.87	9.20	

Extractant concentration	+ 343 g/L	+ 150 g/L	+ 75 g/L	+ 0 g/L
2.0 M				
Shear Visc. At 50 1/s (25°C) [mPa*s]	6.38	4.90	3.38	2.77
Shear Visc. At 200 1/s (25°C) [mPa*s]	6.78	4.78	3.56	2.70
Shear Visc. At 795 1/s (25°C) [mPa*s]	7.62	5.29	3.82	2.97
dynamic viscosity before contact	1.70			
viscosity increase due to uranium (0 to x)	131%	77%	22%	0%
viscosity increase due to (0 _non contact to x)	276%	189%	99%	63%
[U] in organic phase [g/L]	225.8	144.4	73.5	0.0
[U] in organic phase [mol/L]	0.95	0.61	0.31	0.00
x = [U]/[Ex]	0.47	0.30	0.15	0.00
[U] in aqueous phase [g/L]	121.5	8.3	2.5	0.0
[U] in aqueous phase [mol/L]	0.51	0.03	0.01	0.00
distribution coefficient	1.86	17.34	29.49	

Chapter VII - Annex

Suppl. Table 6. Shear viscosities and distribution coefficients of DEHiBA diluted in Isane IP 175 in different concentrations and contacted with aqueous solutions containing 3 M nitric acid and uranyl in different concentrations

Extractant concentration	+ 343 g/L	+ 240 g/L	+ 185 g/L	+ 150 g/L	+ 125 g/L	+ 100 g/L	+ 75 g/L	+ 40 g/L	+ 0 g/L
1.5 M									
Shear Visc. At 50 1/s (25°C) [mPa*s]	44.8	36.7	22.0	17.2	14.7	11.6	9.8	7.0	5.1
Shear Visc. At 200 1/s (25°C) [mPa*s]	44.6	36.9	22.1	17.3	14.9	11.7	9.9	7.1	5.1
Shear Visc. At 795 1/s (25°C) [mPa*s]	44.5	37.0	22.5	17.7	15.1	12.2	10.3	7.5	5.5
dynamic viscosity before contact [mPa*s]	3.47								
viscosity increase due to uranium (0 to x)	777%	618%	330%	235%	188%	128%	91%	37%	0%
viscosity increase due to uranium (0 non contact to x)	1191%	957%	533%	394%	324%	235%	181%	102%	47%
[U] in organic phase [g/L]	142.1	128.6	106.0	95.9	88.3	72.3	56.7	31.9	0.0
[U] in organic phase [mol/L]	0.60	0.54	0.45	0.40	0.37	0.30	0.24	0.13	0.00
x = [U]/[Ex]	0.40	0.36	0.30	0.27	0.25	0.20	0.16	0.09	0.00
[U] in aqueous phase [g/L]	205.1	113.4	79.2	57.0	42.7	29.5	19.2	9.7	0.0
[U] in aqueous phase [mol/L]	0.86	0.48	0.33	0.24	0.18	0.12	0.08	0.04	0.00
distribution coefficient	0.69	1.13	1.34	1.68	2.07	2.45	2.95	3.30	

Extractant concentration			+ 185 g/L		+ 125 g/L		+ 75 g/L		+ 0 g/L
0.5 M									
Shear Visc. At 50 1/s (25°C) [mPa*s]			2.4		2.3		1.9		1.6
Shear Visc. At 200 1/s (25°C) [mPa*s]			2.4		2.3		2.2		1.9
Shear Visc. At 795 1/s (25°C) [mPa*s]			2.7		2.5		2.5		2.4
dynamic viscosity before contact [mPa*s]	1.43								
viscosity increase due to uranium (0 to x)			51%		46%		20%		0%
viscosity increase due to uranium (0 non contact to x)			70%		63%		35%		12%
[U] in organic phase [g/L]			32.0		29.0		20.6		0.0
[U] in organic phase [mol/L]			0.13		0.12		0.09		0.00
x = [U]/[Ex]			0.27		0.24		0.17		0.00
[U] in aqueous phase [g/L]			153.0		96.0		54.4		0.0
[U] in aqueous phase [mol/L]			0.64		0.40		0.23		0.00
distribution coefficient			0.21		0.30		0.38		

Extractant concentration	+ 343 g/L	+ 240 g/L			+ 125 g/L	+ 100 g/L	+ 75 g/L		+ 0 g/L
1.0 M									
Shear Visc. At 50 1/s (25°C) [mPa*s]	10.6	9.4			5.5	4.9	4.2		2.9
Shear Visc. At 200 1/s (25°C) [mPa*s]	10.8	9.5			5.6	5.2	4.3		2.9
Shear Visc. At 795 1/s (25°C) [mPa*s]	11.3	9.9			5.9	5.0	4.7		3.3
dynamic viscosity before contact [mPa*s]	2.12								
viscosity increase due to uranium (0 to x)	267%	224%			89%	70%	46%		0%
viscosity increase due to uranium (0 non contact to x)	400%	341%			157%	131%	99%		36%
[U] in organic phase [g/L]	110.0	100.0			65.8	54.8	44.7		0.0
[U] in organic phase [mol/L]	0.46	0.42			0.28	0.23	0.19		0.00
x = [U]/[Ex]	0.46	0.42			0.28	0.23	0.19		0.00
[U] in aqueous phase [g/L]	233.0	140.0			42.7	29.5	19.2		0.0
[U] in aqueous phase [mol/L]	0.98	0.59			0.18	0.12	0.08		0.00
distribution coefficient	0.47	0.71			1.54	1.86	2.32		

Extractant concentration	+ 343 g/L	+ 240 g/L	+ 185 g/L	+ 150 g/L		+ 100 g/L		+ 40 g/L	+ 0 g/L
2.0 M									
Shear Visc. At 50 1/s (25°C) [mPa*s]	282.4	136.2	77.5	55.5		30.9		16.1	10.5
Shear Visc. At 200 1/s (25°C) [mPa*s]	282.0	133.7	77.6	55.5		30.9		16.2	10.5
Shear Visc. At 795 1/s (25°C) [mPa*s]	278.4	131.1	78.1	56.0		31.2		16.6	11.0
dynamic viscosity before contact [mPa*s]	6.39								
viscosity increase due to uranium (0 to x)	2595%	1200%	640%	430%		195%		54%	0%
viscosity increase due to uranium (0 non contact to x)	4318%	2031%	1112%	768%		383%		152%	64%
[U] in organic phase [g/L]	165.2	160.7	132.4	118.1		82.9		36.0	0.0
[U] in organic phase [mol/L]	0.69	0.68	0.56	0.50		0.35		0.15	0.00
x = [U]/[Ex]	0.35	0.34	0.28	0.25		0.17		0.08	0.00
[U] in aqueous phase [g/L]	182.1	82.2	52.9	34.8		18.9		5.6	0.0
[U] in aqueous phase [mol/L]	0.77	0.35	0.22	0.15		0.08		0.02	0.00
distribution coefficient	0.91	1.96	2.50	3.40		4.39		6.46	

Chapter VII - Annex

Suppl. Table 7. Shear viscosities and distribution coefficients of DEHBA diluted in Isane IP 175 in different concentrations and contacted with aqueous solutions containing 3 M nitric acid and uranyl in different concentrations

Extractant concentration	+ 343 g/L	+ 240 g/L	+ 150 g/L	+ 75 g/L	+ 0 g/L
1.5 M					
Shear Visc. At 50 1/s (25°C) [mPa*s]	41.4	34.5	20.9	10.9	5.3
Shear Visc. At 200 1/s (25°C) [mPa*s]	41.4	34.5	20.9	11.0	5.4
Shear Visc. At 795 1/s (25°C) [mPa*s]	41.6	35.0	21.3	11.4	5.7
dynamic viscosity before contact [mPa*s]	3.46				
viscosity increase due to uranium (0 to x)	683%	552%	295%	106%	0%
viscosity increase due to uranium (0 non contact to x)	1096%	897%	503%	215%	53%
[U] in organic phase [g/L]	161.5	146.2	115.1	67.9	0.0
[U] in organic phase [mol/L]	0.68	0.61	0.48	0.29	0.00
x = [U]/[Ex]	0.45	0.41	0.32	0.19	0.00
[U] in aqueous phase [g/L]	185.7	96.7	37.8	8.0	0.0
[U] in aqueous phase [mol/L]	0.78	0.41	0.16	0.03	0.00
distribution coefficient	0.87	1.51	3.05	8.44	

Extractant concentration	+ 343 g/L	+ 240 g/L	+ 150 g/L	+ 75 g/L	+ 0 g/L
1.0 M					
Shear Visc. At 50 1/s (25°C) [mPa*s]	11.5	9.2	6.8	4.8	2.8
Shear Visc. At 200 1/s (25°C) [mPa*s]	11.6	9.4	7.0	4.9	3.0
Shear Visc. At 795 1/s (25°C) [mPa*s]	12.1	9.7	7.3	5.2	3.3
dynamic viscosity before contact	2.21				
viscosity increase due to uranium (0 to x)	311%	229%	142%	73%	0%
viscosity increase due to uranium (0 non contact to x)	420%	316%	206%	119%	26%
[U] in organic phase [g/L]	111.9	108.1	84.7	58.1	0.0
[U] in organic phase [mol/L]	0.47	0.45	0.36	0.24	0.00
x = [U]/[Ex]	0.47	0.45	0.36	0.24	0.00
[U] in aqueous phase [g/L]	235.3	134.8	68.1	17.9	0.0
[U] in aqueous phase [mol/L]	0.99	0.57	0.29	0.08	0.00
distribution coefficient	0.48	0.80	1.24	3.25	

Extractant concentration	+ 343 g/L	+ 240 g/L	+ 150 g/L	+ 75 g/L	+ 0 g/L
2.0 M					
Shear Visc. At 50 1/s (25°C) [mPa*s]	203.6	124.2	57.2	24.0	11.1
Shear Visc. At 200 1/s (25°C) [mPa*s]	203.4	124.4	57.3	24.0	11.3
Shear Visc. At 795 1/s (25°C) [mPa*s]	202.8	124.8	57.4	24.4	11.7
dynamic viscosity before contact	6.07				
viscosity increase due to uranium (0 to x)	1728%	1014%	414%	115%	0%
viscosity increase due to uranium (0 non contact to x)	3253%	1945%	842%	295%	83%
[U] in organic phase [g/L]	212.8	198.5	137.0	71.7	0.0
[U] in organic phase [mol/L]	0.89	0.83	0.58	0.30	0.00
x = [U]/[Ex]	0.45	0.42	0.29	0.15	0.00
[U] in aqueous phase [g/L]	134.5	44.4	15.8	4.2	0.0
[U] in aqueous phase [mol/L]	0.57	0.19	0.07	0.02	0.00
distribution coefficient	1.58	4.47	8.66	17.11	

Chapter VII - Annex

Suppl. Table 8. Shear viscosities and distribution coefficients of DEHDMBA diluted in Isane IP 175 in different concentrations and contacted with aqueous solutions containing 3 M nitric acid and uranyl in different concentrations

Extractant concentration	+ 343 g/L	+ 240 g/L	+ 150 g/L	+ 100 g/L	+ 75 g/L	+ 0 g/L
1.5 M						
Shear Visc. At 50 1/s (25°C) [mPa*s]	97.3	74.5	37.5	25.1	15.6	6.6
Shear Visc. At 200 1/s (25°C) [mPa*s]	97.2	74.6	37.6	25.1	15.7	6.6
Shear Visc. At 795 1/s (25°C) [mPa*s]	97.4	74.8	37.9	25.6	16.1	7.0
dynamic viscosity before contact [mPa*s]	4.46					
viscosity increase due to uranium (0 to x)	1374%	1029%	468%	244%	137%	0%
viscosity increase due to uranium (0 non contact to x)	2079%	1570%	740%	463%	250%	48%
[U] in organic phase [g/L]	154.3	141.9	115.5	86.2	66.3	0.0
[U] in organic phase [mol/L]	0.65	0.60	0.49	0.36	0.28	0.00
x = [U]/[Ex]	0.43	0.40	0.32	0.24	0.19	0.00
[U] in aqueous phase [g/L]	192.9	101.0	37.3	15.8	9.6	0.0
[U] in aqueous phase [mol/L]	0.81	0.42	0.16	0.07	0.04	0.00
distribution coefficient	0.80	1.41	3.10	5.44	6.88	

Extractant concentration	+ 343 g/L	+ 240 g/L	+ 150 g/L		+ 75 g/L	+ 0 g/L
1.0 M						
Shear Visc. At 50 1/s (25°C) [mPa*s]	11.7	10.9	8.4		5.6	3.1
Shear Visc. At 200 1/s (25°C) [mPa*s]	11.8	11.0	8.4		5.6	3.1
Shear Visc. At 795 1/s (25°C) [mPa*s]	12.2	11.4	8.8		6.0	3.4
dynamic viscosity before contact [mPa*s]	2.35					
viscosity increase due to uranium (0 to x)	278%	252%	171%		80%	0%
viscosity increase due to uranium (0 non contact to x)	398%	364%	258%		137%	32%
[U] in organic phase [g/L]	102.7	97.9	83.5		55.4	0.0
[U] in organic phase [mol/L]	0.43	0.41	0.35		0.23	0.00
x = [U]/[Ex]	0.29	0.27	0.23		0.16	0.00
[U] in aqueous phase [g/L]	244.5	145.0	69.4		20.6	0.0
[U] in aqueous phase [mol/L]	1.03	0.61	0.29		0.09	0.00
distribution coefficient	0.42	0.68	1.20		2.69	

Extractant concentration	+ 343 g/L	+ 240 g/L	+ 150 g/L		+ 75 g/L	+ 0 g/L
2.0 M						
Shear Visc. At 50 1/s (25°C) [mPa*s]	1653.2	651.9	185.3		48.2	17.2
Shear Visc. At 200 1/s (25°C) [mPa*s]	1641.8	651.4	185.5		48.2	17.2
Shear Visc. At 795 1/s (25°C) [mPa*s]	1545.6	636.3	184.8		48.3	17.6
dynamic viscosity before contact [mPa*s]	9.43					
viscosity increase due to uranium (0 to x)	9508%	3688%	977%		180%	0%
viscosity increase due to uranium (0 non contact to x)	17431%	6812%	1865%		411%	82%
[U] in organic phase [g/L]	195.0	181.5	134.7		70.7	0.0
[U] in organic phase [mol/L]	0.82	0.76	0.57		0.30	0.00
x = [U]/[Ex]	0.55	0.51	0.38		0.20	0.00
[U] in aqueous phase [g/L]	152.3	61.5	18.2		5.2	0.0
[U] in aqueous phase [mol/L]	0.64	0.26	0.08		0.02	0.00
distribution coefficient	1.28	2.95	7.40		13.62	

Suppl. Table 9. Shear viscosities and distribution coefficients of DEHIBA diluted in Isane IP 175 in different concentrations and contacted with aqueous solutions containing 3 M nitric acid and uranyl in different concentrations. Viscosities were measured temperature dependent.

Extractant concentration	+ 343 g/L	+ 185 g/L		+ 125 g/L	+ 0 g/L
1.5 M					
Shear Visc. At 50 1/s (20°C) [mPa*s]	57.1	27.5		18.0	5.8
Shear Visc. At 50 1/s (25°C) [mPa*s]	46.6	24.9		16.2	5.5
Shear Visc. At 50 1/s (35°C) [mPa*s]	30.8	17.9		12.0	4.5
Shear Visc. At 50 1/s (45°C) [mPa*s]	20.41	12.29		8.6	3.44
Shear Visc. At 50 1/s (50°C) [mPa*s]	16.2	9.6		6.9	2.9
[U] in organic phase [g/L]	142.1	106.0		88.3	0.0
[U] in organic phase [mol/L]	0.60	0.45		0.37	0.00
x = [U]/[Ex]	0.40	0.30		0.25	0.00

Extractant concentration	+ 343 g/L			+ 125 g/L	+ 0 g/L
1.0 M					
Shear Visc. At 50 1/s (20°C) [mPa*s]	12.3			6.3	3.1
Shear Visc. At 50 1/s (25°C) [mPa*s]	11.3			5.5	2.9
Shear Visc. At 50 1/s (35°C) [mPa*s]	8.6			4.4	2.4
Shear Visc. At 50 1/s (45°C) [mPa*s]	6.31			3.3	1.95
Shear Visc. At 50 1/s (50°C) [mPa*s]	5.2			2.9	1.7
[U] in organic phase [g/L]	110.0			65.8	0.0
[U] in organic phase [mol/L]	0.46			0.28	0.00
x = [U]/[Ex]	0.46			0.28	0.00

Extractant concentration	+ 343 g/L	+ 185 g/L	+ 150 g/L		+ 0 g/L
2.0 M					
Shear Visc. At 50 1/s (20°C) [mPa*s]	204.0	99.4	70.4		11.6
Shear Visc. At 50 1/s (25°C) [mPa*s]	163.0	79.1	56.4		10.6
Shear Visc. At 50 1/s (35°C) [mPa*s]	100.0	50.8	37.0		8.0
Shear Visc. At 50 1/s (45°C) [mPa*s]	59.30	31.70	23.60		5.82
Shear Visc. At 50 1/s (50°C) [mPa*s]	43.1	24.1	18.2		4.7
[U] in organic phase [g/L]	165.2	132.4	118.1		0.0
[U] in organic phase [mol/L]	0.69	0.56	0.50		0.00
x = [U]/[Ex]	0.35	0.28	0.25		0.00

Suppl. Table 10. Shear viscosities and distribution coefficients of DEHiBA diluted in dodecane in different concentrations and contacted with aqueous solutions containing 3 M nitric acid and uranyl in different concentrations

Extractant concentration	+ 240 g/L	+ 100 g/L	+ 0 g/L
1.5 M			
Shear Visc. At 50 1/s (25°C) [mPa*s]	32.1	12.1	5.3
Shear Visc. At 200 1/s (25°C) [mPa*s]	32.2	12.4	5.2
Shear Visc. At 795 1/s (25°C) [mPa*s]	32.4	12.8	5.7
dynamic viscosity before contact	3.5		
viscosity increase due to uranium (0 to x)	504%	128%	0%
viscosity increase due to uranium (0 _non contact to x)	818%	247%	52%
[U] in organic phase [g/L]	123.8	71.5	0.0
[U] in organic phase [mol/L]	0.52	0.30	0.00
x = [U]/[Ex]	0.35	0.20	0.00
[U] in aqueous phase [g/L]	113.2	30.5	0.0
[U] in aqueous phase [mol/L]	0.48	0.13	0.00
distribution coefficient	1.09	2.34	

Suppl. Table 11. Shear viscosities and distribution coefficients of DEHiBA diluted in Xylene in different concentrations and contacted with aqueous solutions containing 3 M nitric acid and uranyl in different concentrations

Extractant concentration	+ 240 g/L	+ 100 g/L	+ 0 g/L
1.5 M			
Shear Visc. At 50 1/s (25°C) [mPa*s]	14.0	6.3	2.9
Shear Visc. At 200 1/s (25°C) [mPa*s]	14.1	6.4	3.0
Shear Visc. At 795 1/s (25°C) [mPa*s]	14.6	6.8	3.3
dynamic viscosity before contact [mPa*s]	1.64		
viscosity increase due to uranium (0 to x)	382%	116%	0%
viscosity increase due to uranium (0 _non contact to x)	756%	284%	78%
[U] in organic phase [g/L]	120.5	75.5	0.0
[U] in organic phase [mol/L]	0.51	0.32	0.00
$x = [U]/[Ex]$	0.34	0.21	0.00
[U] in aqueous phase [g/L]	116.5	26.5	0.0
[U] in aqueous phase [mol/L]	0.49	0.11	0.00
distribution coefficient	1.04	2.85	

Suppl. Table 12. Shear viscosities and distribution coefficients of DEHiBA diluted in Isooctane in different concentrations and contacted with aqueous solutions containing 3 M nitric acid and uranyl in different concentrations

Extractant concentration	+ 240 g/L	+ 100 g/L	+ 0 g/L
1.5 M			
Shear Visc. At 50 1/s (25°C) [mPa*s]	17.5	4.9	3.1
Shear Visc. At 200 1/s (25°C) [mPa*s]	17.7	6.4	3.0
Shear Visc. At 795 1/s (25°C) [mPa*s]	18.3	7.0	3.4
dynamic viscosity before contact	2		
viscosity increase due to uranium (0 to x)	472%	60%	0%
viscosity increase due to uranium (0 _non contact to x)	775%	144%	53%
[U] in organic phase [g/L]	117.3	75.5	0.0
[U] in organic phase [mol/L]	0.49	0.32	0.00
$x = [U]/[Ex]$	0.33	0.21	0.00
[U] in aqueous phase [g/L]	121.7	25.5	0.0
[U] in aqueous phase [mol/L]	0.51	0.11	0.00
distribution coefficient	0.96	2.96	

Suppl. Table 13. Shear viscosities and distribution coefficients of DEHiBA diluted in 1-octanol in different concentrations and contacted with aqueous solutions containing 3 M nitric acid and uranyl in different concentrations

Extractant concentration	+ 240 g/L	+ 100 g/L	+ 0 g/L
1.5 M			
Shear Visc. At 50 1/s (25°C) [mPa*s]	46.5	25.9	15.1
Shear Visc. At 200 1/s (25°C) [mPa*s]	46.6	26.0	15.2
Shear Visc. At 795 1/s (25°C) [mPa*s]	46.8	26.3	15.5
dynamic viscosity before contact [mPa*s, estim.]	12		
viscosity increase due to uranium (0 to x)	209%	72%	0%
viscosity increase due to uranium (0 _non contact to x)	288%	116%	26%
[U] in organic phase [g/L]	114.9	51.7	0.0
[U] in organic phase [mol/L]	0.48	0.22	0.00
$x = [U]/[Ex]$	0.32	0.14	0.00
[U] in aqueous phase [g/L]	122.1	50.3	0.0
[U] in aqueous phase [mol/L]	0.51	0.21	0.00
distribution coefficient	0.94	1.03	

Suppl. Table 14. Shear viscosities and distribution coefficients of DEHiBA diluted in tert-butanol in different concentrations and contacted with aqueous solutions containing 3 M nitric acid and uranyl in different concentrations

Extractant concentration	+ 240 g/L	+ 100 g/L	+ 0 g/L
1.5 M			
Shear Visc. At 50 1/s (25°C) [mPa*s]	754.6	91.0	23.6
Shear Visc. At 200 1/s (25°C) [mPa*s]	746.0	91.2	23.7
Shear Visc. At 795 1/s (25°C) [mPa*s]	742.0	91.4	24.0
dynamic viscosity before contact [mPa*s, estim]	19		
viscosity increase due to uranium (0 to x)	3099%	286%	0%
viscosity increase due to uranium (0 _non contact to x)	3872%	379%	24%
[U] in organic phase [g/L]	151.7	78.6	0.0
[U] in organic phase [mol/L]	0.64	0.33	0.00
x = [U]/[Ex]	0.42	0.22	0.00
[U] in aqueous phase [g/L]	85.3	23.4	0.0
[U] in aqueous phase [mol/L]	0.36	0.10	0.00
distribution coefficient	1.78	3.36	

Suppl. Table 15. Shear viscosities and distribution coefficients of DEHDMBA diluted in xylene in different concentrations and contacted with aqueous solutions containing 3 M nitric acid and uranyl in different concentrations

Extractant concentration	+ 240 g/L	+ 100 g/L	+ 0 g/L
1.5 M			
Shear Visc. At 50 1/s (25°C) [mPa*s]	30.8	10.5	3.7
Shear Visc. At 200 1/s (25°C) [mPa*s]	30.9	10.6	3.8
Shear Visc. At 795 1/s (25°C) [mPa*s]	31.4	11.1	4.2
dynamic viscosity before contact [mPa*s, estim.]	2.00		
viscosity increase due to uranium (0 to x)	730%	183%	0%
viscosity increase due to uranium (0 _non contact to x)	1442%	425%	86%
[U] in organic phase [g/L]	140.2	88.7	0.0
[U] in organic phase [mol/L]	0.59	0.37	0.00
x = [U]/[Ex]	0.39	0.25	0.00
[U] in aqueous phase [g/L]	96.8	13.3	0.0
[U] in aqueous phase [mol/L]	0.41	0.06	0.00
distribution coefficient	1.45	6.67	

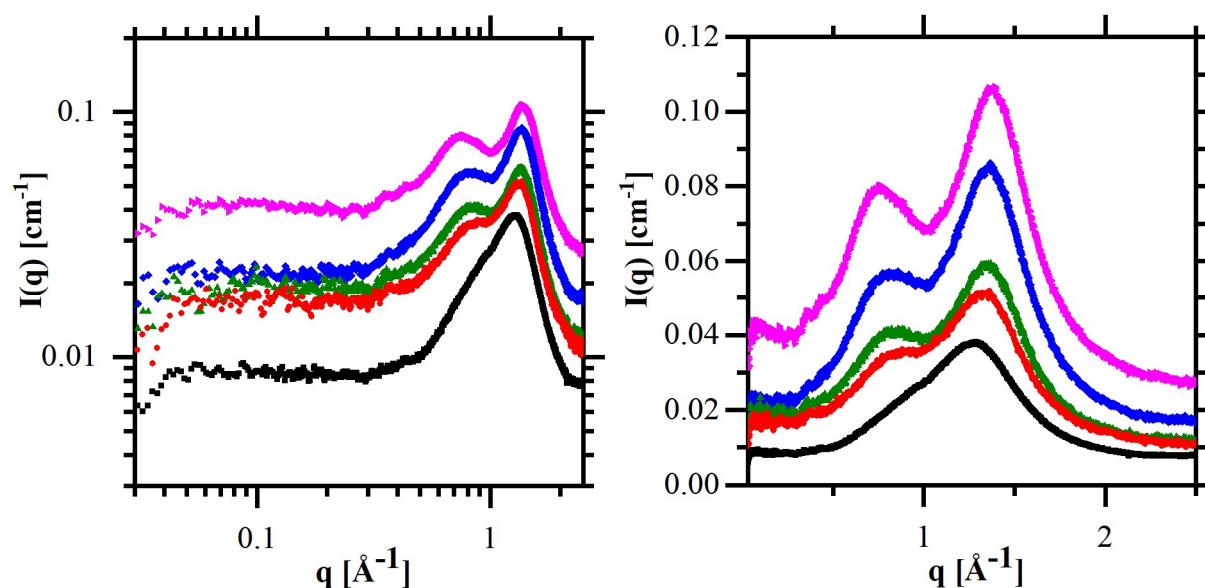
Suppl. Table 16. Shear viscosities and distribution coefficients of DEHDMBA diluted in octanol in different concentrations and contacted with aqueous solutions containing 3 M nitric acid and uranyl in different concentrations

Extractant concentration	+ 240 g/L	+ 100 g/L	+ 0 g/L
1.5 M			
Shear Visc. At 50 1/s (25°C) [mPa*s]	100.5	41.0	14.0
Shear Visc. At 200 1/s (25°C) [mPa*s]	100.5	41.1	14.1
Shear Visc. At 795 1/s (25°C) [mPa*s]	100.6	41.3	14.5
dynamic viscosity before contact [mPa*s, estim.]	13		
viscosity increase due to uranium (0 to x)	616%	192%	0%
viscosity increase due to uranium (0 _non contact to x)	673%	215%	8%
[U] in organic phase [g/L]	122.0	66.0	0.0
[U] in organic phase [mol/L]	0.51	0.28	0.00
x = [U]/[Ex]	0.34	0.18	0.00
[U] in aqueous phase [g/L]	115.0	36.0	0.0
[U] in aqueous phase [mol/L]	0.48	0.15	0.00
distribution coefficient	1.06	1.83	

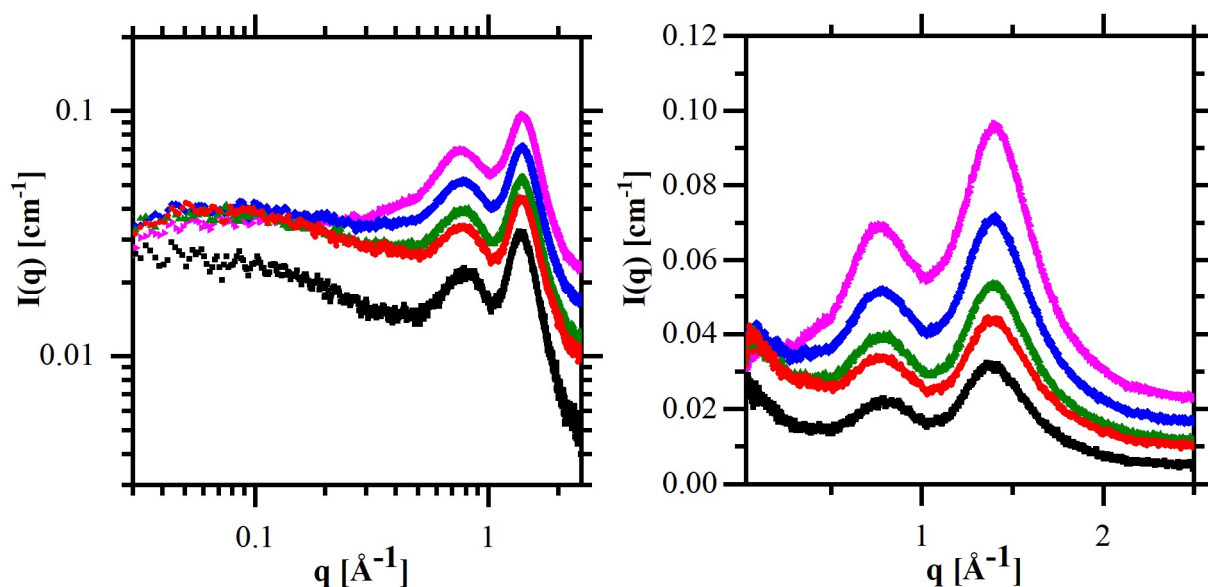
Suppl. Table 17. Shear viscosities and distribution coefficients of DEHDMBA diluted in tert-butanol in different concentrations and contacted with aqueous solutions containing 3 M nitric acid and uranyl in different concentrations

Extractant concentration	+ 240 g/L	+ 100 g/L	+ 0 g/L
1.5 M			
Shear Visc. At 50 1/s (25°C) [mPa*s]	4993.3	388.0	36.2
Shear Visc. At 200 1/s (25°C) [mPa*s]	4791.0	387.7	36.3
Shear Visc. At 795 1/s (25°C) [mPa*s]		385.5	36.6
dynamic viscosity before contact [mPa*s, estim.]	24.00		
viscosity increase due to uranium (0 to x)	13694%	972%	0%
viscosity increase due to uranium (0 _non contact to x)	20706%	1517%	51%
[U] in organic phase [g/L]	151.7	78.6	0.0
[U] in organic phase [mol/L]	0.64	0.33	0.00
$x = [U]/[Ex]$	0.42	0.22	0.00
[U] in aqueous phase [g/L]	85.3	23.4	0.0
[U] in aqueous phase [mol/L]	0.36	0.10	0.00
distribution coefficient	1.78	3.36	

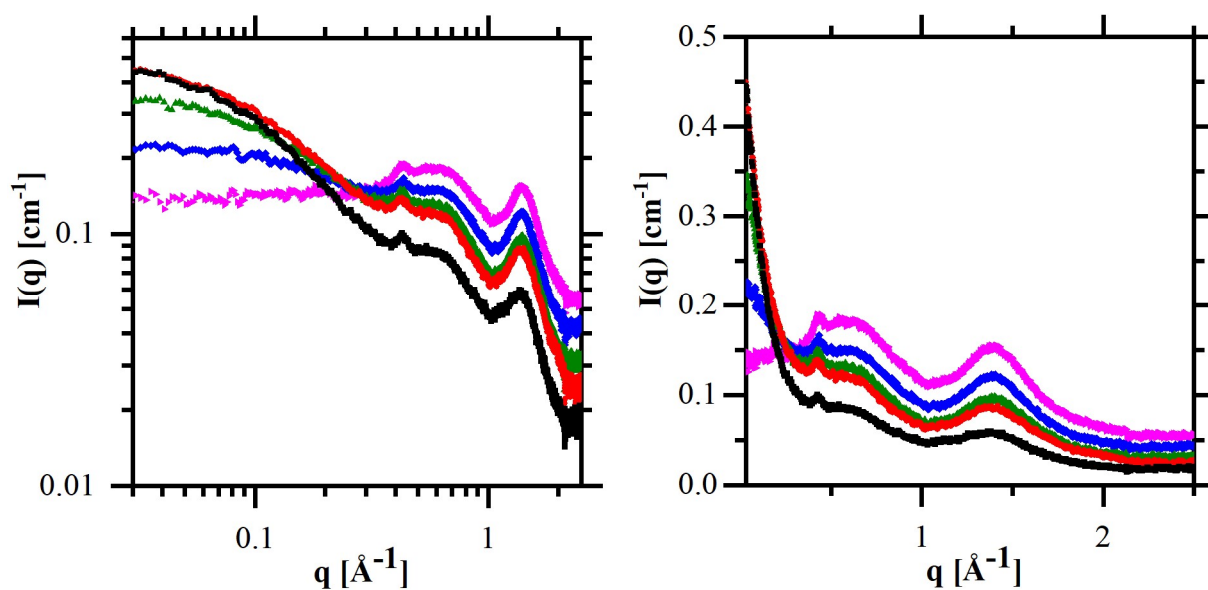
VII.6.4 Additional SWAXS spectra and presentation in log-log and lin-lin



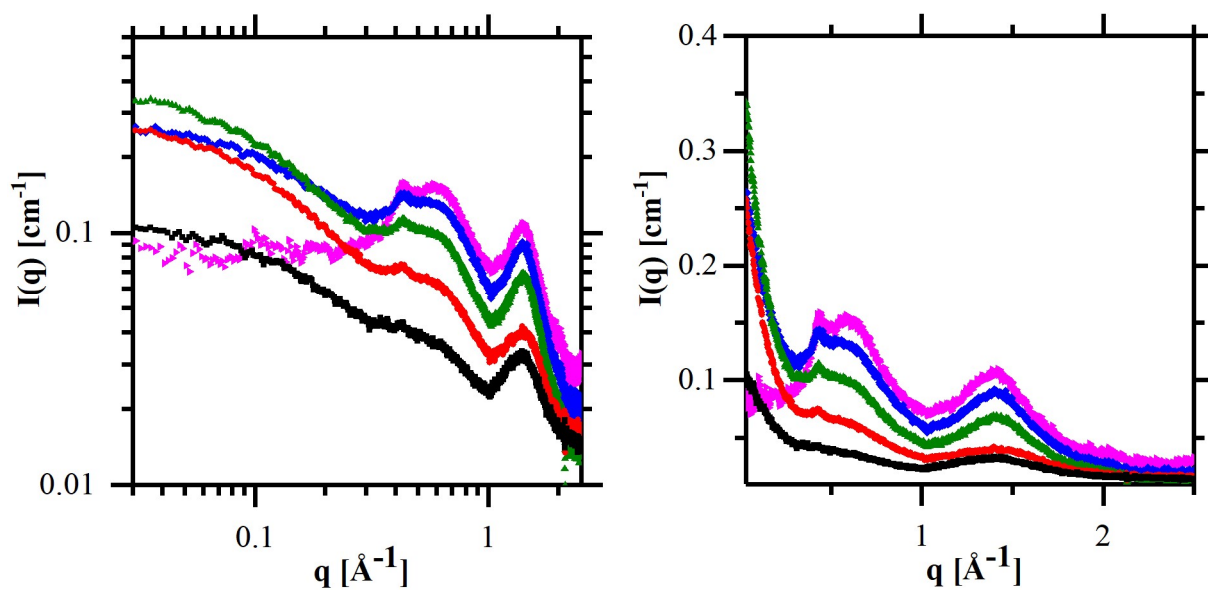
Suppl. Figure 11. SAXS spectra of organic phases containing \blacksquare 0.7 M \bullet 1.0 M \blacktriangle 1.2 M \blacklozenge 1.5 M \blacktriangleright 2.0 M DEHiBA dissolved in Isane IP 175 and contacted with pure water. **Left:** logarithmic scale (cf. Figure 46); **Right:** linear scale.



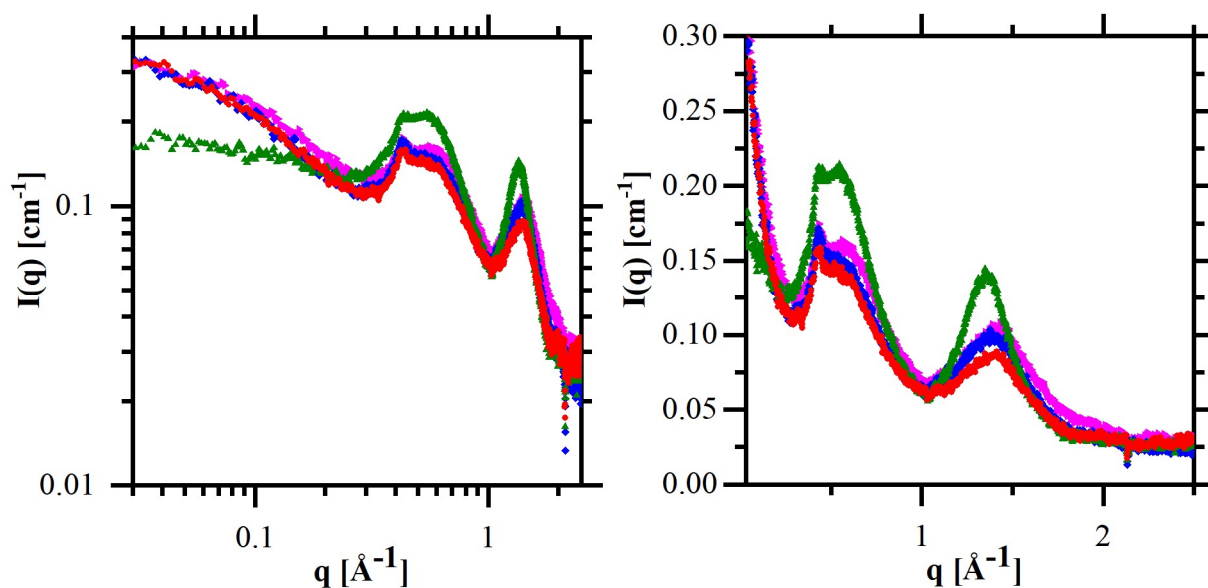
Suppl. Figure 12. SAXS spectra of organic phases containing \blacksquare 0.7 M \bullet 1.0 M \blacktriangle 1.2 M \blacklozenge 1.5 M \blacktriangleright 2.0 M DEHiBA dissolved in Isane IP 175 and contacted with 3 M HNO_3 . **Left:** logarithmic scale (cf. Figure 46); **Right:** linear scale.



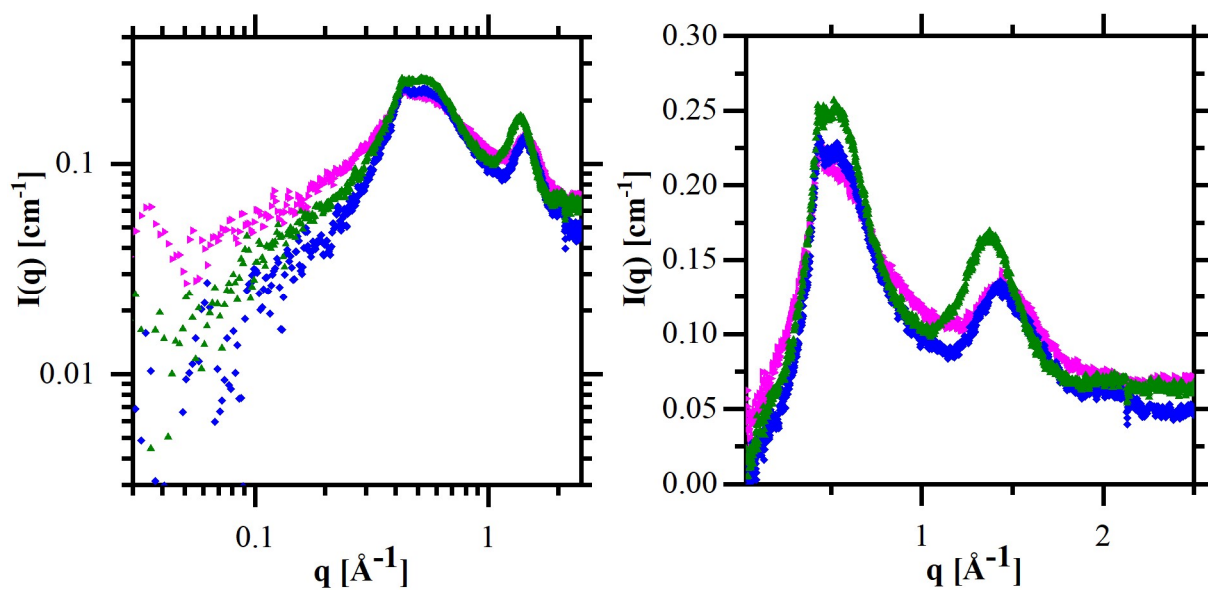
Suppl. Figure 13. SAXS spectra of organic phases containing DEHiBA in different concentrations dissolved in Isane IP 175 and charged a constant concentration of uranyl of 0.35 ± 0.05 M **Left:** \blacksquare 0.7 M (0.30 M U) \bullet 1.0 M (0.35 M U) \blacktriangle 1.2 M (0.35 M U) \blacklozenge 1.5 M (0.35 M U) \blacktriangleright 2.0 M (0.38 M U) DEHiBA dissolved in Isane IP 175. **Left:** logarithmic scale (cf. Figure 49), **Right:** linear scale.



Suppl. Figure 14. SAXS spectra of organic phases containing DEHiBA in different concentrations dissolved in Isane IP 175 and charged a constant uranyl/extractant ratio of 0.25. Extractant concentration ■ 0.4 M (0.1 M U) ● 0.8 M (0.2 M U) ▲ 1.2 M (0.3 M U) ◆ 1.5 M (0.375 M U) ▲ 2.0 M (0.5 M U) DEHiBA dissolved in Isane IP 175. **Left:** logarithmic scale (cf. Figure 49), **Right:** linear scale.

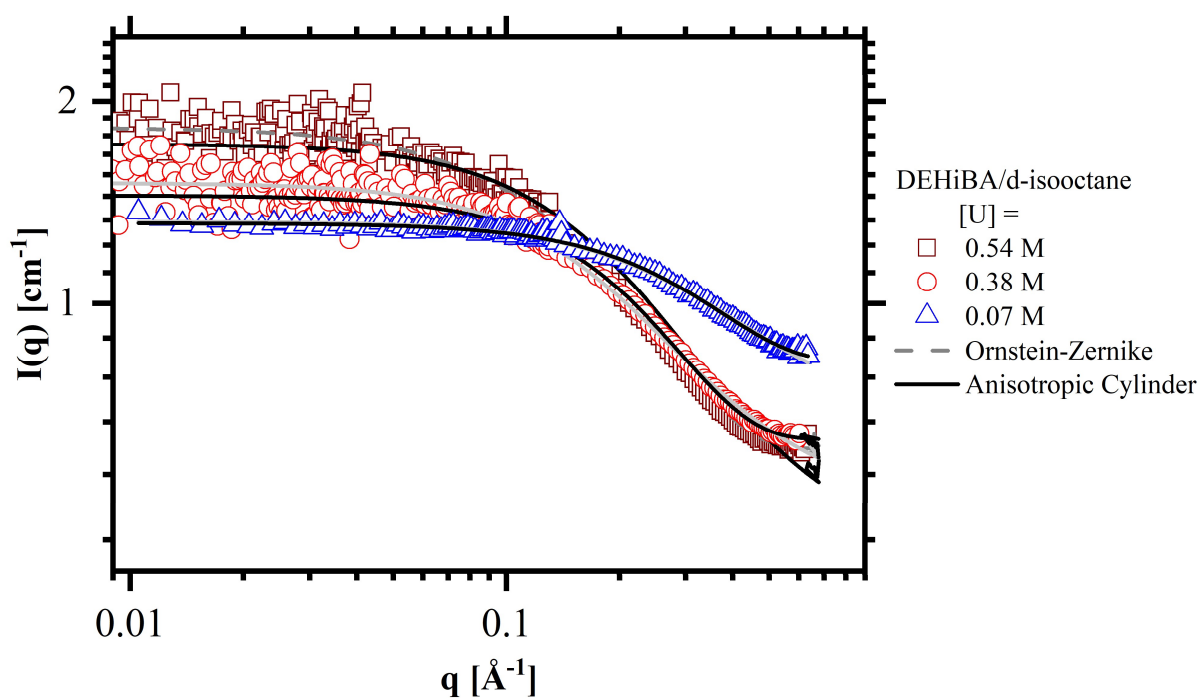


Suppl. Figure 15. SAXS spectra of organic phases containing 1.5 M monoamide extractant (● mixture of 0.9 M DEHiBA and 0.6 M DEHBA ▲ DEHDMBA ◆ DEHBA ▲ DEHiBA) dissolved in dodecane and charged with 0.5 M uranyl. **Left:** logarithmic scale (cf. Figure 51), **Right:** linear scale.

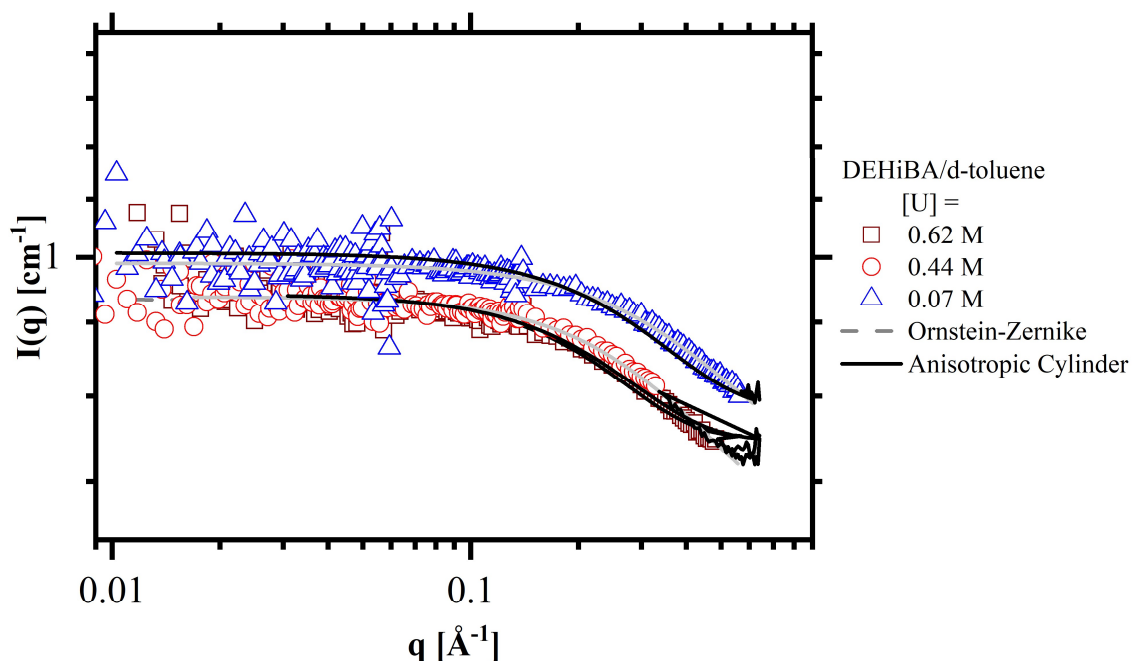


Suppl. Figure 16. SAXS spectra of organic phases containing 1.5 M monoamide extractant (\blacktriangle DEHDMBA \blacklozenge DEHBA \blacktriangleright DEHiBA) dissolved in toluene and charged with 0.5 M uranyl. **Left:** logarithmic scale (cf. **Figure 51**), **Right:** linear scale.

VII.6.5 Additional SANS spectra and fit results



Suppl. Figure 17. SANS spectra of organic phases containing 1.5 M DEHiBA in deuterated isooctane charged with \square 0.54 M \circ 0.38 M \triangle 0.07 M uranyl. Grey dashed lines represent fits obtained with a simple Ornstein-Zernike fit. Black lines represent fits using a local cylindrical form factor and random rod structure factor for anisotropic objects.



Suppl. Figure 18.. SANS spectra of organic phases containing 1.5 M DEHiBA in deuterated toluene charged with \square 0.62 M \circ 0.44 M \triangle 0.07 M uranyl. Grey dashed lines represent fits obtained with a simple Ornstein-Zernike fit. Black lines represent fits using a local cylindrical form factor and random rod structure factor for anisotropic objects.

Suppl. Table 18. Fit results for organic phases with increasing uranyl concentration. Investigations of the influence of penetrating diluents.

System: 1.5 M DEHiBA/d-isooctane	0.07 M Uranyl	0.38 M Uranyl	0.54 M Uranyl
Ornstein-Zernike			
Number density of scatterers N	0.42	0.405	0.42
Forward scattering I_0 [cm^{-1}]	0.9	2.5	3.1
Correlation length ζ [nm]	0.287	0.48	0.47
Background [cm^{-1}]	0.64	0.503	0.422
Anisotropic structure with local cylindrical form factor and random rod structure factor			
Number density of scatterers N [cm^{-3}]	3.6E+20	2.8E+20	6.0E+19
Most probable radius R [nm]	0.45	0.56	0.61
Radius width σ_R (logNorm)	0.09	0.15	0.03
Most probably length L of rod/segment [nm]	1.3	1.0	0.7
Width of length (logNorm)	0.4	0.4	0.6
$\eta(\text{object})$ [10^{10} cm^{-2}]	-0.08	-0.08	-0.08
$\eta(\text{diluent})$ [10^{10} cm^{-2}]	6.5	6.5	6.5
Background [cm^{-1}]	0.82	0.63	0.61

System: 1.5 M DEHiBA/d-toluene	0.07 M Uranyl	0.40 M Uranyl	0.62 M Uranyl
Ornstein-Zernike			
Number density of scatterers N	0.293	0.294	0.272
Forward scattering I_0 [cm^{-1}]	1.25	1.3	1.2
Correlation length ζ [nm]	0.201	0.233	0.285
Background [cm^{-1}]	0.622	0.56	0.611
Anisotropic structure with local cylindrical form factor and random rod structure factor			
Number density of scatterers N [cm^{-3}]	1.5E+20	4.1E+19	2.9E+19
Most probable radius R [nm]	0.44	0.53	0.61
Radius width σ_R (logNorm)	0.10	0.10	0.05
Most probably length L of rod/segment [nm]	1.1	1.4	1.2
Width of length (logNorm)	0.1	0.1	0.1
$\eta(\text{object})$ [10^{10} cm^{-2}]	-0.08	-0.08	-0.08
$\eta(\text{diluent})$ [10^{10} cm^{-2}]	5.7	5.7	5.7
Background [cm^{-1}]	0.72	0.72	0.76

VII.7 Supplementary information to Chapter III

VII.7.1 Hexagon definition and estimation of aggregation number per microphase

For the model, the aggregation number per microphase is needed since it has an influence on the free energy of bending per microphase and consequently on the microphase distribution. Since the size definition is also relevant for the hexagonal grid in the case of the Monte-Carlo-like simulation (*cf.* Chapter III.1.4), a hexagonal grid was also relevant for the estimation of the aggregation numbers per microphase. The microphase units were defined in a way that each unit fits approximately into one hexagon.

Endcaps:

Endcaps were defined as half a spherical aggregate with a core radius R_c and a total aggregate radius of R_{tot} . The resulting volume of the apolar part can be calculated as follows:

$$V_{apol}(\text{endcap}) = \frac{1}{2} \cdot \frac{4}{3} \pi \cdot (R_{tot}^3 - R_c^3) \quad (120)$$

It can be considered, if the volume of the endcaps is increased by a factor of around ~ 1.2 , in order to come closer to the real dumbbelled shape of endcaps.

Cylinder:

For cylinder units, a cylindrical aggregate with the same R_{tot} and the same R_c as in the case of endcaps was assumed. The length L of one cylinder unit was defined as the uranyl-uranyl distance of around 1 nm seen in SAXS measurements (*cf.* Chapter II.2.5). The volume of the apolar part of a cylinder unit can be estimated as:

$$V_{apol}(\text{cylinder}) = \pi \cdot (R_{tot}^2 - R_c^2) \cdot L \quad (121)$$

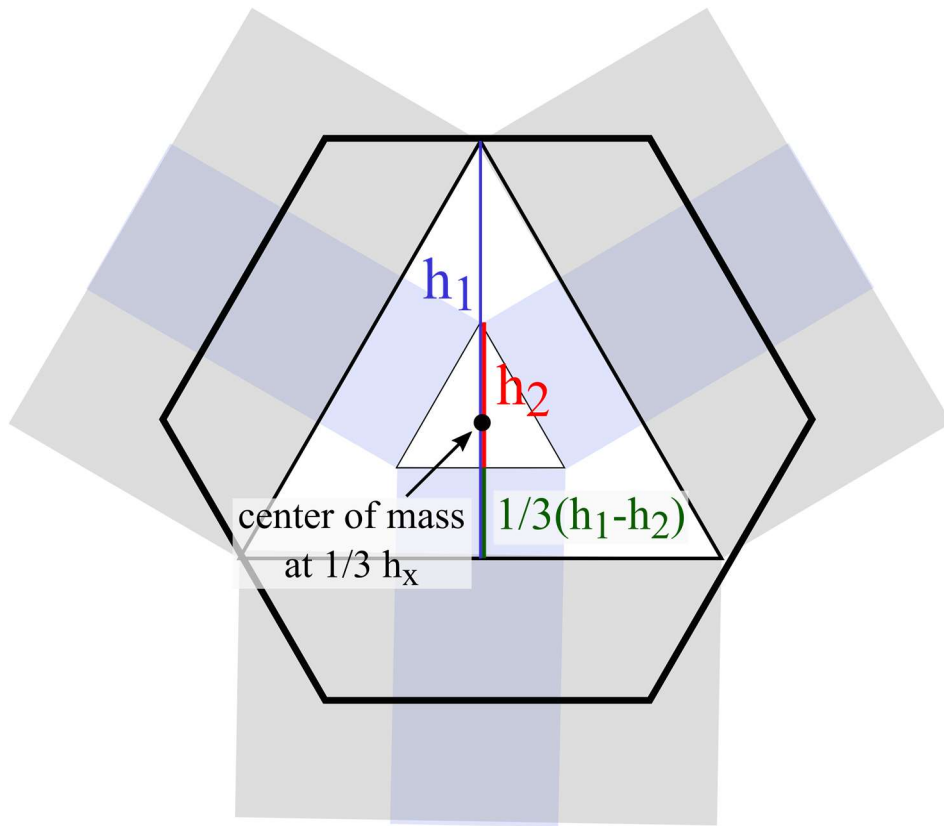
Junction:

The definition of junctions is more complex, since the shape of junctions can vary from system to system.^[344] Therefore, one junction units was put together of three cylinders of half the length of cylinder microphase units and a prism. The prism represents the bilayer part of a junction.^[344] As base area of a prism, a equilateral triangle was chosen. The side length of one triangle corresponds to the diameter of a cylinder unit, just as well as the height of this prism, allowing

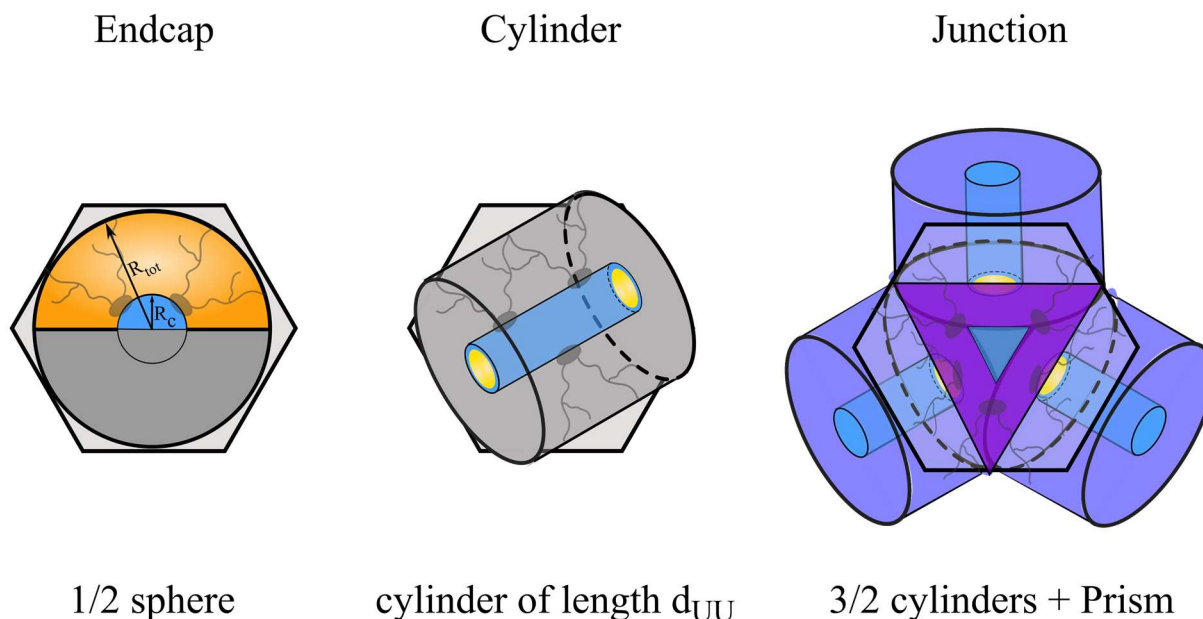
to connect this prism to all three small cylinder units to result in a junction. As polar part, three smaller cylinders and a smaller prism were chosen that are connected via three further cylinders. The length of these cylinders can be approximated as $1/3 \cdot (h_1 - h_2)$, since the center mass of an equilateral triangle lies on $1/3$ of the height. The characteristic lengths are shown in

$$V_{\text{apol}}(\text{junction}) = \frac{3}{2} V_{\text{apol}}(\text{cylinder}) + V_{\text{apol}}(\text{prism}) \quad (122)$$

$$V_{\text{apol}}(\text{prism}) = \frac{(2R_{\text{tot}})^2 \sqrt{3}}{4} - \frac{(2R_c)^2 \sqrt{3}}{4} - \frac{1}{3} \left(\frac{\sqrt{3}}{2} (2R_{\text{tot}} - 2R_c) \right) \quad (123)$$



Suppl. Figure 19. Scheme to calculate the volume of the apolar part of the junction



Suppl. Figure 20. Scheme of microphase definition with help of a hexagonal grid

In accordance with the thesis of Ferru^[191, p.168] the average core radius for a monoamide can be approximated as 4.5 Å, while the total radius of a spherical aggregate can be approximated as 8.5 Å. With these values, the aggregation number per microphase can be calculated as:

$$N_{agg}(\text{microphase}) = \frac{V_{apol}(\text{microphase})}{V_{apol}(\text{extractant})} \quad (124)$$

with $V_{apol}(\text{extractant})$ being the apolar volume of the extractant, in the case of two di-ethyl hexyl chains, $V_{apol}(\text{extractant})$ can be calculated from the table of Fedors^[206] as 486.5 Å³.

Applying these values, the following aggregation numbers can be estimated (*cf.* **Suppl. Table 19**).

Suppl. Table 19. Overview of estimated aggregation numbers per microphase as well as aggregation number N_{agg}/U per uranyl ion per microphase

microphase	$V_{apol}(\text{microphase}) [\text{Å}^3]$	$N_{agg}(\text{microphase})$	N_{agg}/U
Endcap	1095.4	2.3	4.6
Cylinder	1633.6	3.4	3.4
Junction	3073.3	6.3	2.1

As can be seen in the table above, about 2-3 extractants form an endcap unit, 3-4 extractant molecules a cylinder unit and 6-7 molecules form a junction unit. What is also notable, is that calculating the number of extractant molecules per uranyl ions seems to decrease from endcaps to junction. That means that at higher loading, the aggregation and structure is also driven towards cylinders and junctions due to stoichiometrical reasons.

VII.7.2 JavaScript Code

The HTML, CSS and JavaScript code can be accessed by pressing “F12” in Firefox Browser or by using the combination “Ctrl + Shift + I” in Chrome during running the Interface. Furthermore, the code can be downloaded to use it offline.

VII.7.3 Interfacial tension measurements of different extractants

For density measurements, a thermostatic Anton Paar DSA 5000 densimeter based on an oscillatory fork was used. Interfacial tensions were measured using the drop shape method using a Krüss DSA 100 tensiometer apparatus. The organic phases composed of extractant in diluent were precontacted with 3 M nitric acid. After that, the shape of a drop of organic phase in the surrounding aqueous phase was analyzed.

According to the Gibbs adsorption isotherm, the change in surface tension $d\gamma$ is related to changes in the chemical potential $d\mu_i$ through the surface excess Γ_i .^[58, pp.73–75]

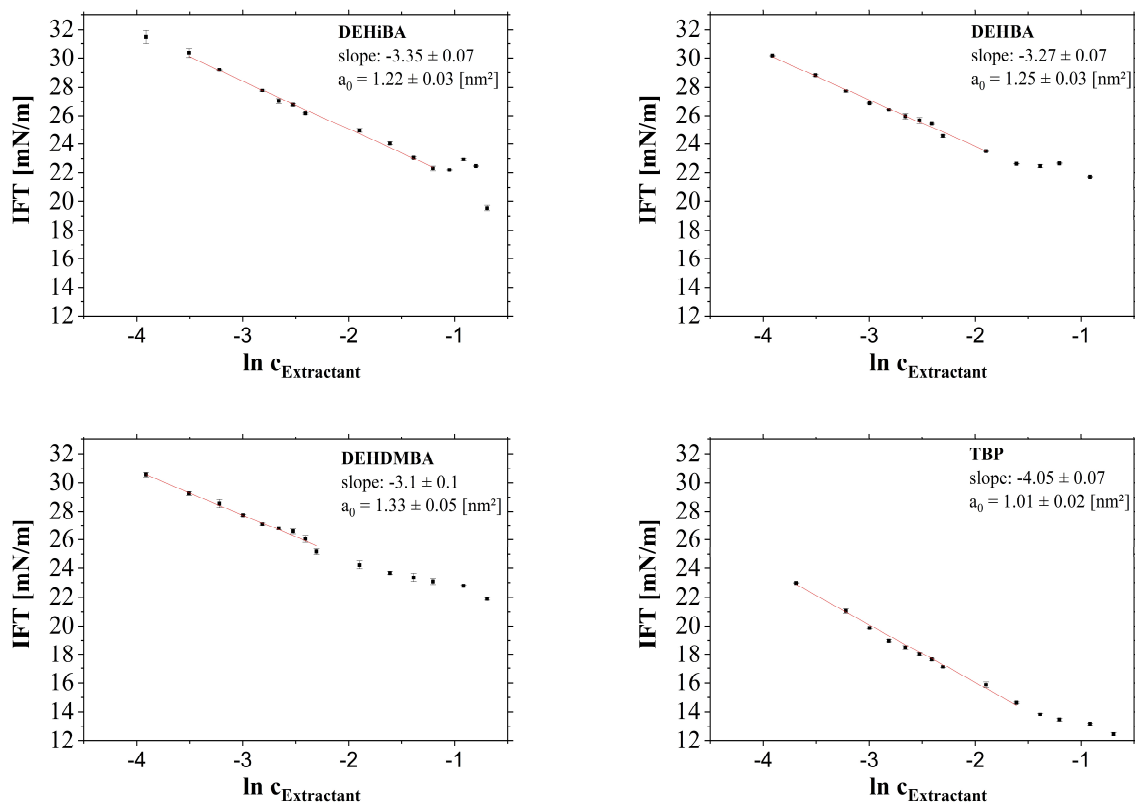
$$d\gamma = \frac{n_i^\sigma}{A} d\mu_i = \Gamma_i d\mu_i \quad (125)$$

with n_i being the number of particles at the Gibbs ideal surface and A being its area. The interface is defined as the plane where the surface excess of both phases is equal. With $d\mu_i = RT \ln c_i$, the change of the interfacial tension with solute concentration can be directly linked to the surface excess and consequently to the area per solute molecule.

$$\Gamma_i = -\frac{1}{RT} \frac{d\gamma}{d \ln c_i} \quad (126)$$

$$A_{\text{molecule}} = \frac{1}{N_A \Gamma_i} \quad (127)$$

with N_A being the Avogadro constant.



Suppl. Figure 21. Results of the IFT measurements at the aqueous-organic interface with increasing extractant concentration.

VII.8 Supplementary information to Chapter V

VII.8.1 Table with necessary input parameters

Suppl. Table 20. Input parameters to model the SLES curve as well as the impact of fragrance. Area per molecule was calculated as circular area with the radius of a sphere that corresponds to the molecular volume

	V_M [nm ³ /molecule]	$\log P$	λ	$a_0 (x = 0)$ [nm ²]	x [mol/mol]
SLES	0.577	-	-	1.005 ³	0.88-0.89
Vanillin	0.238	0.72	0	0.46	0.11
Limonene	0.269	5.40	0.07	0.50	0.12
Linalol	0.298	2.94	0.16	0.54	0.11
Citronellol	0.302	3.37	0.38	0.54	0.11

VII.8.2 Details on the estimation of packing parameter, aggregation number and volume per microphase on a hexagonal grid

The length of the nonpolar lauryl chain ($n_c = 12$) can be estimated from Tanford's formula to be 1.67 nm.^[72]

$$l_{chain} = 0.15 + 0.127 \cdot n_c \text{ [nm]} \quad (128)$$

The interfacial thickness was determined to be around 4-5 Å.^[271] Therefore, the molecular length l_{c+I} of SLES can be assumed to be around 2.1 nm.

The molar volume v_M of SLES can be calculated from the density of SLES ($\rho(25^\circ\text{C}) = 1.1 \text{ g/cm}^3$)^[126]. This volume is increased by hydration water, which was determined to be around 3 H₂O molecules by headgroup, resulting in a total effective volume of SLES of around 0.675 nm³/molecule.

The area per molecule a_{max} at low salt content was measured by Clancy *et al.* to be 1.05 nm². Assuming that the spontaneous packing parameter at $x = 8$ is close to 0.8 and that the change in effective molar volume as well as in length per molecule is negligible, the area per molecule of

³ S.F. Clancy, H.H. Paradies, Structure, Diffusivity and Linear Rheology of Sodium Ether Dodecylsulfate in Aqueous Solutions – (I), Zeitschrift für Physikalische Chemie 215 (2001) 189.

SLES a_{\min} has to be close to 0.4 nm².

Estimation of the aggregation number as well as volume per microphase

For the model, the aggregation number per microphase is needed, since it has an influence on the free energy of bending per microphase and consequently on the microphase distribution. In the following, the sizes of microphases are approximated by the help of hexagons, assuming that the single microphases can arrange themselves on a hexagonal grid.

Endcaps

Endcaps were defined as half a sphere with radius R_{c+I} . Their volume V can therefore be calculated by

$$V(endcap) = \frac{4\pi}{3} R_{c+I}^3 \cdot 0.5 \quad (129)$$

It can be considered, if the volume of the endcaps is increased by a factor of around ~ 1.2 , in order to come closer to the real dumbbelled shape of endcaps.

Cylinder

The radius of cylinders was assumed to be the same as of endcaps – R_{c+I} . The length of a cylinder segment was defined to be twice the cylinder radius. With this definition the cylinder can be fitted into a hexagon of edge length $\frac{2R_{c+I}}{\sqrt{3}}$. For this edge length, the projection of two endcaps form the in-circle of the hexagon and the corresponding volume is

$$V(cylinder) = R_{c+I}^2 \pi \cdot 2R_{c+I}^2 \quad (130)$$

Junctions

The definition of junctions is more complex, since the shape of junctions can vary from system to system. For a general estimation, junctions are approximated by a bilayer part represented by a prism and three short cylinders. As base area of the prism, an equilateral triangle of length b was chosen. The side length of one triangle corresponds to the diameter of a cylinder unit, just as well as the height of this prism, allowing the connection of this prism with all three small cylinder units to result in a junction. The three ‘half’ cylinders connected to the prism form three arms resulting in the junction. Therefore, the volume of a junction can be approximated on a hexagonal grid as

$$V(junction) = V(prism) + \frac{3}{2}V(cylinder) \quad (131)$$

$$V(prism) = \frac{b^2}{4}\sqrt{3} \cdot h_{prism} = \frac{(2R_{c+I})^2}{4}\sqrt{3} \cdot 2R_{c+I} \quad (132)$$

Aggregation number per microphase

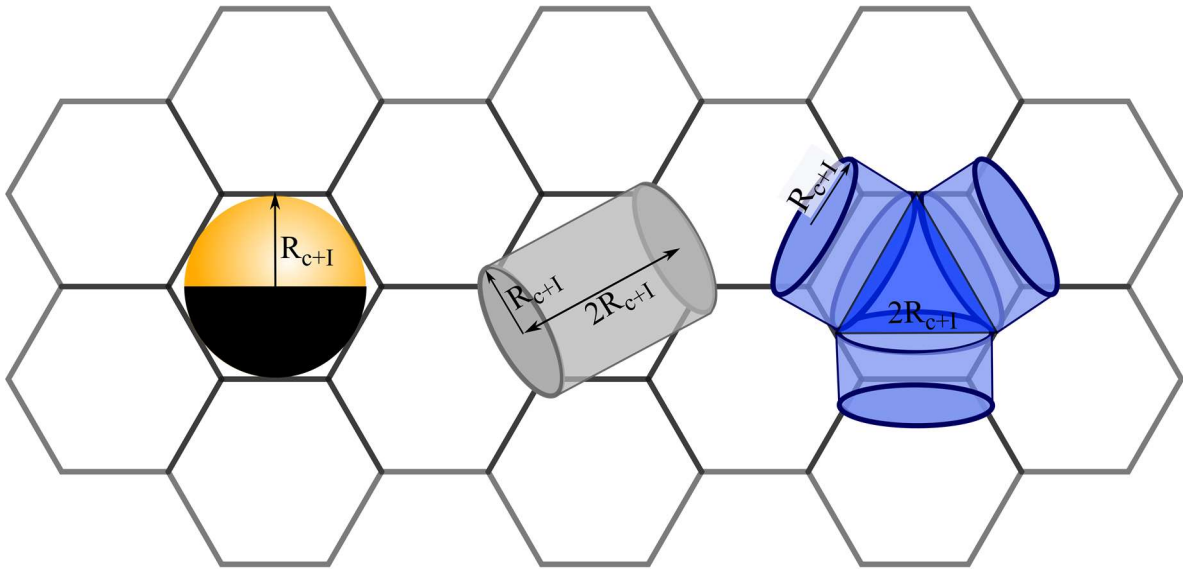
Aggregation numbers per defined microphase $N_{agg, microphase}$ can be approximated by the volume per microphase $V(microphase)$ divided by the effective molar volume of the surfactant-fragrance mixture v_{eff} . The latter was already defined in the main text and takes into account the molar volume of SLES v_{SLES} including hydration as well as the possible presence of fragrance.

$$N_{agg, microphase} = \frac{V(microphase)}{v_{eff}} \quad (133)$$

$$v_{eff} = v_{SLES} + x\beta v_{perfume} \quad (134)$$

$$\beta = \frac{10^{logP} \cdot \phi_{SLES}}{1 + 10^{logP} \cdot \phi_{SLES}} \quad (135)$$

with x being the mole fraction of fragrance and β a factor that reduces the mole fraction by the portion of fragrance molecules that is dissolved in the aqueous phase.



Suppl. Figure 22. Schematic representation of microphases on a hexagonal grid to estimate the aggregation number per microphase.

VII.9 References

- [1] G. E. P. BOX, J. S. HUNTER, W. G. HUNTER, Statistics for experimenters. *Design, innovation, and discovery*, Wiley-Interscience, Hoboken, NJ, **2005**.
- [2] M. L. FREE, Hydrometallurgy. *Fundamentals and Applications*, Wiley-TMS, Hoboken, **2013**.
- [3] European Commission, Critical Raw Materials for the EU. Report of the Ad-hoc group on defining Critical Raw Materials, **2010**.
- [4] S. MASSARI, M. RUBERTI, Rare earth elements as critical raw materials, *Resources Policy* **2013**, 38, 36.
- [5] M. FULP, What Makes a 'Critical' Metal or 'Strategic' Element?, Chicago Hard Assets Investment Conference 2012 Online Preview, **2012**.
- [6] A. MORALES, What makes a Material Critical?, CRM_InnoNet at Semicon Europe, **2014**.
- [7] Chemical Innovation Knowledge Transfer Network, "The Period Table of Endangered Elements. Green Chemistry", can be found under <https://www.acs.org/content/acs/en/greenchemistry/research-innovation/research-topics/endangered-elements.html>.
- [8] J. RYDBERG, Solvent extraction principles and practice, M. Dekker, New York, **2004**.
- [9] K. A. DILL, S. BROMBERG, Molecular driving forces. *Statistical thermodynamics in biology, chemistry, physics, and nanoscience*, Garland Science, London, **2011**.
- [10] T. LOPIAN, *Dissertation*, **2017**.
- [11] T. ZEMB, C. BAUER, P. BAUDUIN, L. BELLONI, C. DÉJUGNAT, O. DIAT, V. DUBOIS, J.-F. DUFRÊCHE, S. DOURDAIN, M. DUVAIL ET AL., Recycling metals by controlled transfer of ionic species between complex fluids, *Colloid Polym Sci* **2015**, 293, 1.
- [12] H.-J. BART, Reactive Extraction, Springer, Berlin, Heidelberg, **2001**.
- [13] M. SAGISAKA, T. NARUMI, M. NIWASE, S. NARITA, A. OHATA, C. JAMES, A. YOSHIZAWA, E. TAFFIN DE GIVENCHY, F. GUITTARD, S. ALEXANDER ET AL., Hyperbranched hydrocarbon surfactants give fluorocarbon-like low surface energies, *Langmuir : the ACS journal of surfaces and colloids* **2014**, 30, 6057.

- [14] J. DRADER, G. SAINT-LOUIS, J.M. MULLER, M.-C. CHARBONNEL, P. GUILBAUD, L. BERTHON, K. M. ROSCIOLI-JOHNSON, C. A. ZARZANA, C. RAE, G. S. GROENEWOLD ET AL., Radiation chemistry of the branched-chain monoamide di-2-ethylhexyl-isobutyramide, *Solvent Extraction & Ion Exchange* **2017**, 35, 480.
- [15] H. BAHRMANN, H. - D. HAHN, D. MAYER, G. D. FREY in *Ullmann's Encyclopedia of Industrial Chemistry*, American Cancer Society, **2013**.
- [16] F. DRAIN, R. VINOCHÉ, J. DUHAMET, 40 years of experience with Liquid-liquid Extraction Equipment in the Nuclear Industry, United States. Department of Energy. Office of Scientific and Technical Information, **2003**.
- [17] J. D. LAW, T. A. TODD, Liquid-Liquid Extraction Equipment, *Introduction to Nuclear Chemistry and Fuel Cycle Separations Course, Consortium for Risk Evaluation with Stakeholder Participation*, <http://www.cresp.org/education/courses/shortcourse> **2008**.
- [18] S. VEDANTAM, K. E. WARDLE, T. V. TAMHANE, V. V. RANADE, J. B. JOSHI, CFD Simulation of Annular Centrifugal Extractors, *International Journal of Chemical Engineering* **2012**, 2012, 1.
- [19] A. EINSTEIN, Über die von der molekularkinetischen Theorie der Wärme geforderte Bewegung von in ruhenden Flüssigkeiten suspendierten Teilchen, *Ann. Phys.* **1905**, 322, 549.
- [20] T. F. TADROS, Emulsion Formation and Stability, Wiley-VCH, s.l., **2013**.
- [21] I. WAGNER, J. STICHLMAIR, The Effect of Viscosity on Mass Transfer in Pulsed Sieve-Tray Extraction Columns, *Chemical engineering & technology* **2001**, 24, 616.
- [22] H. J. KARAM, J. C. BELLINGER, Deformation and breakup of liquid droplets in a simple shear field, *Industrial & Engineering Chemistry Fundamentals* **1968**, 7, 576.
- [23] C. Tropea (Ed.) *Springer handbook of experimental fluid mechanics*, Springer, Berlin, **2007**.
- [24] S. ABBOTT, "Surfactant Science", can be found under https://www.google.fr/url?sa=t&rct=j&q=&esrc=s&source=web&cd=1&cad=rja&uact=8&ved=0ahUKEwi7z9Llit_XAhWBF8AKHekID-cQFggrMAA&url=https%3A%2F%2Fwww.stevenabbott.co.uk%2F_downloads%2FSurfactant%2520Science%2520Principles%2520and%2520Practice.pdf&usg=AOvVaw04jxEo8E-j_5zF7Fpc4MUY, **2016**.
- [25] D. S. VISWANATH, Viscosity of liquids. *Theory, estimation, experiment, and data*, Springer, Dordrecht, **2007**.

- [26] B. K. PAUL, S. P. MOULIK, The viscosity behaviours of microemulsions: An overview, *PROCEEDINGS-INDIAN NATIONAL SCIENCE ACADEMY PART A* **2000**, 66, 499.
- [27] T. O. D. SUZUKI, INTERMOLECULAR MOMENTUM TRANSFER IN A SIMPLE LIQUID AND ITS CONTRIBUTION TO SHEAR VISCOSITY, *Microscale Thermophysical Engineering* **2001**, 5, 117.
- [28] W. D. MONNERY, W. Y. SVRCEK, A. K. MEHROTRA, Viscosity: a critical review of practical predictive and correlative methods, *The Canadian Journal of Chemical Engineering* **1995**, 73, 3.
- [29] S. G. BRUSH, Theories of Liquid Viscosity, *Chemical Reviews* **1962**, 62, 513.
- [30] Idea based on an online discussion about the temperature dependence of water viscosity, can be found under <https://chemistry.stackexchange.com/questions/14361/why-doesnt-the-viscosity-of-water-change-much-with-temperature-like-it-does-for>, **2014**.
- [31] E. B. BAGLEY, D. D. CHRISTIANSON, Swelling capacity of starch and its relationship to suspension viscosity - effect of cooking time, temperature and concentration, *J Texture Studies* **1982**, 13, 115.
- [32] D. SAHA, S. BHATTACHARYA, Hydrocolloids as thickening and gelling agents in food, *Journal of food science and technology* **2010**, 47, 587.
- [33] W. GRUBER, T. WIZANY, Die Genussformel. *Kulinarische Physik*, Ecowin, Salzburg, **2008**.
- [34] J. APPELL, G. PORTE, A. KHATORY, F. KERN, S. J. CANDAU, Static and dynamic properties of a network of wormlike surfactant micelles (cetylpyridinium chlorate in sodium chlorate brine), *J. Phys. II France* **1992**, 2, 1045.
- [35] K. OSSEO-ASARE, Aggregation, reversed micelles, and microemulsions in liquid-liquid extraction: the tri-n-butyl phosphatediluent-water-electrolyte system, *Advances in Colloid and Interface Science* **1991**, 37, 123.
- [36] P. GUILBAUD, T. ZEMB, Depletion of water-in-oil aggregates from poor solvents, *Current Opinion in Colloid & Interface Science* **2015**, 20, 71.
- [37] I. DANIELSSON, B. LINDMAN, The definition of microemulsion, *Colloids and Surfaces* **1981**, 3, 391.
- [38] J. H. SCHULMAN, W. STOECKENIUS, L. M. PRINCE, Mechanism of Formation and Structure of Micro Emulsions by Electron Microscopy, *J. Phys. Chem.* **1959**, 63, 1677.

- [39] S. NAVE, C. MANDIN, L. MARTINET, L. BERTHON, F. TESTARD, C. MADIC, T. ZEMB, Supramolecular organisation of tri-n-butyl phosphate in organic diluent on approaching third phase transition, *Phys. Chem. Chem. Phys.* **2004**, 6, 799.
- [40] F. TESTARD, T. ZEMB, P. BAUDUIN, L. BERTHON, Third-Phase Formation in Liquid-Liquid Extraction: A Colloidal Approach, *ChemInform* **2010**, 41, i.
- [41] H. F. EICKE, H. CHRISTEN, Nucleation process of micelle formation in apolar solvents, *Journal of Colloid and Interface Science* **1974**, 48, 281.
- [42] P. JOOS, D. VOLLHARDT, M. VERMEULEN, Interfacial tension of sodium dodecyl sulfate solutions at the hexane-water interface, *Langmuir : the ACS journal of surfaces and colloids* **1990**, 6, 524.
- [43] R. AVEYARD, B. P. BINKS, S. CLARK, J. MEAD, Interfacial tension minima in oil–water–surfactant systems. Behaviour of alkane–aqueous NaCl systems containing aerosol OT, *J. Chem. Soc., Faraday Trans. 1* **1986**, 82, 125.
- [44] C. TANFORD, The hydrophobic effect and the organization of living matter, *Science* **1978**, 200, 1012.
- [45] O. G. MOURITSEN, Life - As a Matter of Fat. *The Emerging Science of Lipidomics*, Springer-Verlag, Berlin-Heidelberg, **2005**.
- [46] J. N. ISRAELACHVILI, D. J. MITCHELL, B. W. NINHAM, Theory of self-assembly of hydrocarbon amphiphiles into micelles and bilayers, *J. Chem. Soc., Faraday Trans. 2* **1976**, 72, 1525.
- [47] A. J. HICKEY, H. D. C. SMYTH in *Pharmaco-Complexity: Non-Linear Phenomena and Drug Product Development* (Eds.: A. J. Hickey, H. D.C. Smyth), Springer US, Boston, MA, **2011**, pp. 5–18.
- [48] E. RUCKENSTEIN, R. NAGARAJAN, Aggregation of amphiphiles in nonaqueous media, *J. Phys. Chem.* **1980**, 84, 1349.
- [49] E. PAATERO, J. SJÖBLOM, Phase behaviour in metal extraction systems, *Hydrometallurgy* **1990**, 25, 231.
- [50] P. DANESI, R. CHIARIZIA, C. F. COLEMAN, The Kinetics of Metal Solvent Extraction, *C R C Critical Reviews in Analytical Chemistry* **2008**, 10, 1.
- [51] J.-F. DUFRÊCHE, T. ZEMB, Effect of long-range interactions on ion equilibria in liquid–liquid extraction, *Chemical Physics Letters* **2015**, 622, 45.

- [52] J. REY, S. DOURDAIN, L. BERTHON, J. JESTIN, S. PELLET-ROSTAING, T. ZEMB, Synergy in Extraction System Chemistry: Combining Configurational Entropy, Film Bending, and Perturbation of Complexation, *Langmuir : the ACS journal of surfaces and colloids* **2015**, 31, 7006.
- [53] J. N. ISRAELACHVILI, D.J. MITCHELL, A model for the packing of lipids in bilayer membranes, *Biochimica et Biophysica Acta (BBA) - Biomembranes* **1975**, 389, 13.
- [54] D. J. MITCHELL, B. W. NINHAM, Micelles, vesicles and microemulsions, *J. Chem. Soc., Faraday Trans. 2* **1981**, 77, 601.
- [55] K. SHINODA, E. HUTCHINSON, Pseudo-phase separation model for thermodynamic calculations on micellar solutions, *J. Phys. Chem.* **1962**, 66, 577.
- [56] C. TANFORD, The hydrophobic effect. *Formation of micelles and biological membranes*, Wiley, New York, **1973**.
- [57] J.-F. DUFRÊCHE, Chemical Potential, Online Cours INSTN: SPOC Recycling Chemistry: From Practice to Theory, **2017**.
- [58] D. F. EVANS, H. WENNERSTRÖM, The colloidal domain. *Where physics, chemistry, biology, and technology meet*, Wiley-VCH, New York, NY, **1999**.
- [59] J. N. ISRAELACHVILI, Intermolecular and surface forces, Academic Press, Burlington, MA, **2011**.
- [60] J. N. ISRAELACHVILI, S. MARČELJA, R. G. HORN, Physical principles of membrane organization, *Quart. Rev. Biophys.* **1980**, 13, 121.
- [61] W. HELFRICH, Elastic properties of lipid bilayers, *Zeitschrift für Naturforschung C* **1973**, 28, 693.
- [62] S. T. HYDE, The Language of shape. *The role of curvature in condensed matter-- physics, chemistry, and biology*, Elsevier, Amsterdam Netherlands, New York, **1997**.
- [63] S. A. SAFRAN, Statistical thermodynamics of surfaces, interfaces, and membranes, Addison-Wesley, Reading Mass., **1994**.
- [64] W. KUNZ, F. TESTARD, T. ZEMB, Correspondence between curvature, packing parameter, and hydrophilic-lipophilic deviation scales around the phase-inversion temperature, *Langmuir : the ACS journal of surfaces and colloids* **2009**, 25, 112.
- [65] A. FOGDEN, S. T. HYDE, G. LUNDBERG, Bending energy of surfactant films, *Faraday Trans.* **1991**, 87, 949.
- [66] E. GABA, "Wikimedia Commons - View of the planes establishing the main curvatures on a minimal surface", can be found under https://commons.wikimedia.org/wiki/File:Minimal_surface_curvature_planes-en.svg.

- [67] I. SZLEIFER, D. KRAMER, A. BEN - SHAUL, W. M. GELBART, S. A. SAFRAN, Molecular theory of curvature elasticity in surfactant films, *J. Chem. Phys.* **1990**, 92, 6800.
- [68] A. N. SEMENOV, A. R. KHOKHLOV, Statistical physics of liquid-crystalline polymers, *Soviet Physics Uspekhi* **1988**, 31, 988.
- [69] P. BAUDUIN, T. ZEMB, Perpendicular and lateral equations of state in layered systems of amphiphiles, *Current Opinion in Colloid & Interface Science* **2014**, 19, 9.
- [70] A. AROTI, E. LEONTIDIS, M. DUBOIS, T. ZEMB, Effects of monovalent anions of the Hofmeister series on DPPC lipid bilayers Part I, *Biophysical journal* **2007**, 93, 1580.
- [71] T. ZEMB, L. BELLONI, M. DUBOIS, A. AROTI, E. LEONTIDIS, Can we use area per surfactant as a quantitative test model of specific ion effects?, *Current Opinion in Colloid & Interface Science* **2004**, 9, 74.
- [72] C. TANFORD, Micelle shape and size, *J. Phys. Chem.* **1972**, 76, 3020.
- [73] S. T. HYDE, I. S. BARNES, B. W. NINHAM, Curvature energy of surfactant interfaces confined to the plaquettes of a cubic lattice, *Langmuir : the ACS journal of surfaces and colloids* **1990**, 6, 1055.
- [74] S. BULUT, I. ÅSLUND, D. TOPGAARD, H. WENNERSTRÖM, U. OLSSON, Lamellar phase separation in a centrifugal field. A method for measuring interbilayer forces, *Soft Matter* **2010**, 6, 4520.
- [75] G. GOMPPER, H. ENDO, M. MIHAILESCU, J. ALLGAIER, M. MONKENBUSCH, D. RICHTER, B. JAKOBS, T. SOTTMANN, R. STREY, Measuring bending rigidity and spatial renormalization in bicontinuous microemulsions, *EPL (Europhysics Letters)* **2001**, 56, 683.
- [76] U. OLSSON, H. WENNERSTRÖM, Globular and bicontinuous phases of nonionic surfactant films, *Advances in Colloid and Interface Science* **1994**, 49, 113.
- [77] M. GRADZIELSKI, Bending constants of surfactant layers, *Current Opinion in Colloid & Interface Science* **1998**, 3, 478.
- [78] J. OBERDISSE, T. HELLWEG, Structure, interfacial film properties, and thermal fluctuations of microemulsions as seen by scattering experiments, *Advances in Colloid and Interface Science* **2017**, 247, 354.
- [79] T. N. ZEMB, The DOC model of microemulsions, *Colloids and Surfaces A: Physicochemical and Engineering Aspects* **1997**, 129-130, 435.
- [80] J. REY, *Dissertation*, University of Montpellier, **2016**.

- [81] J. N. ISRAELACHVILI, D. J. MITCHELL, B. W. NINHAM, Theory of self-assembly of hydrocarbon amphiphiles into micelles and bilayers, *J. Chem. Soc., Faraday Trans. 2* **1976**, 72, 1525.
- [82] F. TESTARD, L. MARTINET, L. BERTHON, S. NAVE, B. ABECASSIS, C. MADIC, T. ZEMB, The four types of supramolecular organisation of extractant molecules used in separation processes, **2004**.
- [83] R. CHIARIZIA, M. P. JENSEN, M. BORKOWSKI, J. R. FERRARO, P. THIYAGARAJAN, K. C. LITTRELL, Sans Study Of Third Phase Formation In The U(vi)-HNO₃ /TBP- n -dodecane System, *Separation Science and Technology* **2003**, 38, 3313.
- [84] R. CHIARIZIA, M. P. JENSEN, M. BORKOWSKI, J. R. FERRARO, P. THIYAGARAJAN, K. C. LITTRELL, Third Phase Formation Revisited, *Solvent Extraction and Ion Exchange* **2003**, 21, 1.
- [85] L. LEFRANÇOIS, J.-J. DELPUECH, M. HÉBRANT, J. CHRISMENT, C. TONDRE, Aggregation and Protonation Phenomena in Third Phase Formation, *J. Phys. Chem. B* **2001**, 105, 2551.
- [86] V. RAO, P. R., Z. KOLARIK, A review of third phase formation in extraction of actinides by neutral organophosphorus extractants, *Solvent Extraction and Ion Exchange* **1996**, 14, 955.
- [87] L. BERTHON, L. MARTINET, F. TESTARD, C. MADIC, T. ZEMB, Solvent Penetration and Sterical Stabilization of Reverse Aggregates based on the DIAMEX Process Extracting Molecules, *Solvent Extraction and Ion Exchange* **2007**, 25, 545.
- [88] F. TESTARD, L. BERTHON, T. ZEMB, Liquid–liquid extraction, *Comptes Rendus Chimie* **2007**, 10, 1034.
- [89] I. LANGMUIR, The Role of Attractive and Repulsive Forces in the Formation of Tactoids, Thixotropic Gels, Protein Crystals and Coacervates, *J. Chem. Phys.* **1938**, 6, 873.
- [90] W. B. KLEIJN, A Model of Clay Swelling and Tactoid Formation, *Clays and Clay Minerals* **1982**, 30, 383.
- [91] M. MORVAN, D. ESPINAT, J. LAMBARD, T. ZEMB, Ultrasml- and small-angle X-ray scattering of smectite clay suspensions, *Colloids and Surfaces A: Physicochemical and Engineering Aspects* **1994**, 82, 193.

- [92] P. BAUDUIN, F. TESTARD, L. BERTHON, T. ZEMB, Relation between the hydrophile/hydrophobe ratio of malonamide extractants and the stability of the organic phase: investigation at high extractant concentrations, *Physical chemistry chemical physics : PCCP* **2007**, 9, 3776.
- [93] J.-F. PARISOT, Treatment and recycling of spent nuclear fuel. *Actinide partitioning : application to waste management*, CEA, Paris, **2008**.
- [94] L. BOSLAND, *Dissertation*, Paris, **2006**.
- [95] B. GANNAZ, *Dissertation*, Paris, **2006**.
- [96] H. DOZOL, C. BERTHON, Applications d'expériences DOSY à des systèmes agrégés en phase organique, *Comptes Rendus Chimie* **2006**, 9, 556.
- [97] B. A. MOYER (Ed.) *Ion Exchange and Solvent Extraction Series, Volume 21*, CRC Press, Boca Raton, **2014**.
- [98] C. BAUER, P. BAUDUIN, J. F. DUFRÊCHE, T. ZEMB, O. DIAT, Liquid/liquid metal extraction: Phase diagram topology resulting from molecular interactions between extractant, ion, oil and water, *Eur. Phys. J. Spec. Top.* **2012**, 213, 225.
- [99] L. LEFRANCOIS, F. BELNET, D. NOEL, C. TONDRE, An Attempt to Theoretically Predict Third-Phase Formation in the Dimethyldibutyltetradecylmalonamide (DMDBTDMA)/Dodecane/Water/Nitric Acid Extraction System, *Separation Science and Technology* **1999**, 34, 755.
- [100] P. N. PATHAK, A. S. KANEKAR, D. R. PRABHU, V. K. MANCHANDA, Comparison of Hydrometallurgical Parameters of N,N-Dialkylamides and of Tri-n-Butylphosphate, *Solvent Extraction and Ion Exchange* **2009**, 27, 683.
- [101] B. A. MOYER, Ion Exchange and Solvent Extraction, 19. *A Series of Advances*, CRC Press, Hoboken, **2009**.
- [102] B. ABÉCASSIS, F. TESTARD, T. ZEMB, L. BERTHON, C. MADIC, Effect of n - Octanol on the Structure at the Supramolecular Scale of Concentrated Dimethyldioctylhexylethoxymalonamide Extractant Solutions, *Langmuir* **2003**, 19, 6638.
- [103] Z.-J. YU, T. H. IBRAHIM, R. D. NEUMAN, Aggregation behavior of cobalt(II), nickel(II), and copper(II) bis(2-ethylhexyl) phosphate complexes in n -Heptane, *Solvent Extraction and Ion Exchange* **1998**, 16, 1437.
- [104] T. H. IBRAHIM, R. D. NEUMAN, Molecular modeling study of the aggregation behavior of nickel(II), cobalt(II), lead(II) and zinc(II) bis(2-ethylhexyl) phosphate complexes, *Journal of Colloid and Interface Science* **2006**, 294, 321.

- [105] E. V. YURTOV, N. M. MURASHOVA, Gelation in Extraction Systems with Basic Copper (II) and Neodymium (III) Alkyl Phosphates, *Russian Journal of Applied Chemistry* **2002**, 75, 1064.
- [106] D. C. STEYTLER, T. R. JENTA, B. H. ROBINSON, J. EASTOE, R. K. HEENAN, Structure of reversed micelles formed by metal salts of bis (ethylhexyl) phosphoric acid, *Langmuir* **1996**, 12, 1483.
- [107] T. SATO, The extraction of uranium (VI) from hydrochloric acid solutions by Di-(2-ethylhexyl)-phosphoric acid, *Journal of Inorganic and Nuclear Chemistry* **1965**, 27, 1853.
- [108] T. SATO, T. NAKAMURA, M. KAWAMURA, The extraction of vanadium(IV) from hydrochloric acid solutions by di-(2-ethylhexyl)-phosphoric acid, *Journal of Inorganic and Nuclear Chemistry* **1978**, 40, 853.
- [109] S. GAO, T. SUN, Q. CHEN, X. SHEN, Characterization of Reversed Micelles Formed in Solvent Extraction of Thorium(IV) by Bis(2-ethylhexyl) Phosphoric Acid. Transforming from Rodlike to Wormlike Morphology, *Radiochimica Acta* **2016**, 4, 457..
- [110] T. HARADA, M. SMUTZ, R. G. BAUTISTA, Characterization of iron and rare-earth polymers of di(2-ethylhexyl)phosphoric acid, *J. Chem. Eng. Data* **1972**, 17, 203.
- [111] E. ANTICÓ, A. MASANA, M. HIDALGO, V. SALVADÓ, M. IGLESIAS, M. VALIENTE, Solvent extraction of yttrium from chloride media by di(2-ethylhexyl)phosphoric acid in kerosene. Speciation studies and gel formation, *Analytica Chimica Acta* **1996**, 327, 267.
- [112] R. J. ELLIS, Y. MERIDIANO, J. MULLER, L. BERTHON, P. GUILBAUD, N. ZORZ, M. R. ANTONIO, T. DEMARS, T. ZEMB, Complexation-induced supramolecular assembly drives metal-ion extraction, *Chemistry* **2014**, 20, 12796.
- [113] R. J. ELLIS, T. L. ANDERSON, M. R. ANTONIO, A. BRAATZ, M. NILSSON, A SAXS study of aggregation in the synergistic TBP-HDBP solvent extraction system, *The journal of physical chemistry. B* **2013**, 117, 5916.
- [114] T. L. ANDERSON, A. BRAATZ, R. J. ELLIS, M. R. ANTONIO, M. NILSSON, Synergistic Extraction of Dysprosium and Aggregate Formation in Solvent Extraction Systems Combining TBP and HDBP, *Solvent Extraction & Ion Exchange* **2013**, 31, 617.
- [115] Z.-J. YU, R. D. NEUMAN, Giant rodlike reversed micelles, *Journal of the American Chemical Society* **1994**, 116, 4075.
- [116] M. E. CATES, S. M. FIELDING, Rheology of giant micelles, *Advances in Physics* **2006**, 55, 799.

- [117] M. E. CATES, Reptation of living polymers, *Macromolecules* **1987**, 20, 2289.
- [118] L. M. WALKER, Scattering from polymer-like micelles, *Current Opinion in Colloid & Interface Science* **2009**, 14, 451.
- [119] A. PURQON, A. SUGIYAMA, H. NAGAO, K. NISHIKAWA, Aperture, symmetry, isotropy, and compactness analysis and their correlation in spaghetti-like nanostructure dynamics, *Chemical Physics Letters* **2007**, 443, 356.
- [120] D. DANINO, Y. TALMON, H. LEVY, G. BEINERT, R. ZANA, Branched threadlike micelles in an aqueous solution of a trimeric surfactant, *Science* **1995**, 269, 1420.
- [121] J. YANG, Viscoelastic wormlike micelles and their applications, *Current Opinion in Colloid & Interface Science* **2002**, 7, 276.
- [122] R. ZANA (Ed.) *Surfactant science series, vol. 140*, Taylor & Francis, Boca Raton, **2007**.
- [123] G. PALAZZO, Wormlike reverse micelles, *Soft Matter* **2013**, 9, 10668.
- [124] M. E. CATES, S. J. CANDAU, Statics and dynamics of worm-like surfactant micelles, *Journal of Physics: Condensed Matter* **1990**, 2, 6869.
- [125] P. G. de GENNES, Reptation of a Polymer Chain in the Presence of Fixed Obstacles, *J. Chem. Phys.* **1971**, 55, 572.
- [126] A. PARKER, W. FIEBER, Viscoelasticity of anionic wormlike micelles, *Soft Matter* **2013**, 9, 1203.
- [127] M. E. CATES, Flow behaviour of entangled surfactant micelles, *Journal of Physics: Condensed Matter* **1996**, 8, 9167.
- [128] R. ANGELICO, B. BALINOV, A. CEGLIE, U. OLSSON, G. PALAZZO, O. SODERMAN, Water Diffusion in Polymer-like Reverse Micelles. 2. Composition Dependence, *Langmuir* **1999**, 15, 1679.
- [129] E. BARDEZ, N. C. VY, T. ZEMB, Counterion-driven sphere to cylinder transition in reverse micelles: a small angle X-ray scattering and conductometric study, *Langmuir* **1995**, 11, 3374.
- [130] C. A. DREISS, Wormlike micelles, *Soft Matter* **2007**, 3, 956.
- [131] P. MUKERJEE, Size distribution of small and large micelles. Multiple equilibrium analysis, *J. Phys. Chem.* **1972**, 76, 565.
- [132] P. SCHURTENBERGER, R. SCARTAZZINI, P. L. LUISI, Viscoelastic properties of polymerlike reverse micelles, *Rheologica Acta* **1989**, 28, 372.
- [133] P. SCHURTENBERGER, C. CAVACO, The static and dynamic structure factor of polymer-like lecithin reverse micelles, *J. Phys. II France* **1994**, 4, 305.

- [134] J. APPELL, G. PORTE, Polymerlike Behaviour of Giant Micelles, *EPL (Europhysics Letters)* **1990**, *12*, 185.
- [135] F. LEQUEUX, Reptation of Connected Wormlike Micelles, *EPL (Europhysics Letters)* **1992**, *19*, 675.
- [136] C. OELSCHLAEGER, M. SCHOPFERER, F. SCHEFFOLD, N. WILLENBACHER, Linear-to-Branched Micelles Transition, *Langmuir* **2009**, *25*, 716.
- [137] A. KHATORY, F. KERN, F. LEQUEUX, J. APPELL, G. PORTE, N. MORIE, A. OTT, W. URBACH, Entangled versus multiconnected network of wormlike micelles, *Langmuir* **1993**, *9*, 933.
- [138] E. CAPPELAERE, R. CRESSELY, Rheological behavior of an elongated micellar solution at low and high salt concentrations, *Colloid & Polymer Science* **1998**, *276*, 1050.
- [139] E. CAPPELAERE, R. CRESSELY, Influence of NaClO₃ on the rheological behaviour of a micellar solution of CPCI, *Rheol Acta* **2000**, *39*, 346.
- [140] T. IMAE, T. KOHSAKA, Size and electrophoretic mobility of tetradecyltrimethylammonium salicylate (C₁₄TASal) micelles in aqueous media, *J. Phys. Chem.* **1992**, *96*, 10030.
- [141] V. CROCE, T. COSGROVE, G. MAITLAND, T. HUGHES, G. KARLSSON, Rheology, Cryogenic Transmission Electron Spectroscopy, and Small-Angle Neutron Scattering of Highly Viscoelastic Wormlike Micellar Solutions, *Langmuir : the ACS journal of surfaces and colloids* **2003**, *19*, 8536.
- [142] A. KHATORY, F. LEQUEUX, F. KERN, S. J. CANDAU, Linear and nonlinear viscoelasticity of semidilute solutions of wormlike micelles at high salt content, *Langmuir* **1993**, *9*, 1456.
- [143] T. TLUSTY, *Dissertation*, **2000**.
- [144] T. TLUSTY, Defect-Induced Phase Separation in Dipolar Fluids, *Science* **2000**, *290*, 1328.
- [145] A. ZILMAN, T. TLUSTY, S. A. SAFRAN, Entropic networks in colloidal, polymeric and amphiphilic systems, *Journal of Physics: Condensed Matter* **2003**, *15*, S57.
- [146] N. DAN, S. A. SAFRAN, Junctions and end-caps in self-assembled non-ionic cylindrical micelles, *Advances in Colloid and Interface Science* **2006**, *123-126*, 323.

- [147] A. G. ZILMAN, S. A. SAFRAN, Thermodynamics and structure of self-assembled networks, *Physical review. E, Statistical, nonlinear, and soft matter physics* **2002**, 66, 51107.
- [148] B. BHARTI, A.-L. FAMEAU, M. RUBINSTEIN, O. D. VELEV, Nanocapillarity-mediated magnetic assembly of nanoparticles into ultraflexible filaments and reconfigurable networks, *Nature materials* **2015**, 14, 1104.
- [149] T. J. DRYE, M. E. CATES, Living networks, *J. Chem. Phys.* **1992**, 96, 1367.
- [150] G. CRISTOBAL, J. ROUCH, J. CURÉLY, P. PANIZZA, Phase separation in living micellar networks, *Physica A: Statistical Mechanics and its Applications* **1999**, 268, 50.
- [151] H.R. KRUYT, Colloid science, Elsevier Pub., **1949**.
- [152] P. Lindner, T. Zemb (Eds.) *Neutrons, X-rays and light*, Norh-Holland Elsevier, Amsterdam, **2002**.
- [153] V. A. PARSEGAN, Van der Waals forces. *A handbook for biologists, chemists, engineers, and physicists*, Cambridge University Press, Cambridge, **2006**.
- [154] L. ONSAGER, THE EFFECTS OF SHAPE ON THE INTERACTION OF COLLOIDAL PARTICLES, *Annals of the New York Academy of Sciences* **1949**, 51, 627.
- [155] L. ONSAGER, N. N. T. SAMARAS, The Surface Tension of Debye - Hückel Electrolytes, *J. Chem. Phys.* **1934**, 2, 528.
- [156] P. A. FORSYTH, S. MARČELJA, D. J. MITCHELL, B. W. NINHAM, Onsager transition in hard plate fluid, *J. Chem. Soc., Faraday Trans. 2* **1977**, 73, 84.
- [157] D. FENG, G. JIN, Introduction to condensed matter physics, World Scientific, Hackensack, NJ, **2005**.
- [158] S. TSUCHIYA, A. TANABE, T. NARUSHIMA, K. ITO, K. YAMAZAKI in *The 19th International Conference of the System Dynamics Society, System Dynamics Society, Atlanta, Georgia*, **2001**.
- [159] M. BORKOWSKI, R. CHIARIZIA, M. P. JENSEN, J. R. FERRARO, P. THIYAGARAJAN, K. C. LITRELL, Sans Study Of Third Phase Formation In The Th(iv)-hno 3 /tbp- n -octane System, *Separation Science and Technology* **2003**, 38, 3333.
- [160] C. ERLINGER, L. BELLONI, T. ZEMB, C. MADIC, Attractive Interactions between Reverse Aggregates and Phase Separation in Concentrated Malonamide Extractant Solutions, *Langmuir* **1999**, 15, 2290.

- [161] R. CHIARIZIA, M. P. JENSEN, M. BORKOWSKI, P. THIYAGARAJAN, K. C. LITTRELL, Interpretation of Third Phase Formation in the Th(IV)-HNO₃, TBP- n - Octane System with Baxter's "Sticky Spheres" Model, *Solvent Extraction and Ion Exchange* **2004**, 22, 325.
- [162] R. CHIARIZIA, K. L. NASH, M. P. JENSEN, P. THIYAGARAJAN, K. C. LITTRELL, Application of the Baxter Model for Hard Spheres with Surface Adhesion to SANS Data for the U(VI)-HNO₃, TBP- n -Dodecane System, *Langmuir* **2003**, 19, 9592.
- [163] P. BAUDUIN, F. TESTARD, T. ZEMB, Solubilization in alkanes by alcohols as reverse hydrotropes or "lipotropes", *The journal of physical chemistry. B* **2008**, 112, 12354.
- [164] A. EINSTEIN, Eine neue Bestimmung der Moleküldimensionen, *Annalen der Physik* **1906**, 324, 289.
- [165] M. MOONEY, The viscosity of a concentrated suspension of spherical particles, *Journal of colloid science* **1951**, 6, 162.
- [166] V. VAND, Viscosity of solutions and suspensions. I. Theory, *J. Phys. Chem.* **1948**, 52, 277.
- [167] M. MIGUIRDITCHIAN, L. CHAREYRE, C. SOREL, I. BISEL, P. BARON, M. MASSON, Development of the GANEX process for the reprocessing of Gen IV spent nuclear fuels, *Proc. of ATALANTE 2008* **2008**.
- [168] Director General, "Nuclear Technology Review 2016", can be found under https://www.iaea.org/About/Policy/GC/GC60/GC60InfDocuments/English/gc60inf-2_en.pdf, **2016**.
- [169] World Nuclear Association, "Radioactive Waste Management", can be found under <http://www.world-nuclear.org/information-library/nuclear-fuel-cycle/nuclear-wastes/radioactive-waste-management.aspx>, **2016**.
- [170] J. BRUNO, R. C. EWING, Spent Nuclear Fuel, *Elements* **2007**, 2, 343.
- [171] IAEA, "Spent Fuel Reprocessing Options".
- [172] N. DESCOULS, J. C. MORISSEAU, C. MUSIKAS, Process for the extraction of uranium (VI) and/or plutonium (IV) present in an aqueous solution by means of N,N-dialkylamides, **1988**, Google Patents, can be found under <http://www.google.ch/patents/US4772429>.
- [173] H. H. ANDERSON, M. NEWTON, L. B. ASPREY, C. RICHMOND, Solvent extraction process for plutonium, United States Patent Office, Patent no 2,924,506, **1960**.

- [174] M. NILSSON, K. L. NASH, Review article: A review of the development and operational characteristics of the TALSPEAK process, *Solvent Extraction and Ion Exchange* **2007**, 25, 665.
- [175] M. NILSSON, K. L. NASH in *Proceedings Atalante*, **2008**, pp. 19–23.
- [176] K. L. NASH, The chemistry of TALSPEAK: a review of the science, *Solvent Extraction and Ion Exchange* **2015**, 33, 1.
- [177] B. WEAVER, F. A. KAPPELMANN, TALSPEAK: A new method of separating americium and curium from the lanthanides by extraction from an aqueous solution of an aminopolyacetic acid complex with a monoacidic organophosphate or phosphonate, **1964**.
- [178] X. HÉRÈS, P. BARON, C. HILL, E. AMEIL, I. MARTINEZ, P. RIVALIER, The separation of extractants implemented in the DIAMEX-SANEX process, *ATALANTE (Nuclear Fuel Cycles for a Sustainable Future)* **2008**.
- [179] C. MADIC, F. TESTARD, M. J. HUDSON, J.-O. LILJENZIN, B. CHRISTIANSEN, M. FERRANDO, A. FACCHINI, A. GEIST, G. MODULO, A. GONZALEZ-ESPARTERO ET AL., Partnew-New solvent extraction processes for minor actinides-final report, **2004**.
- [180] E. ANEHEIM, *Dissertation*, **2012**.
- [181] E. ANEHEIM, C. EKBERG, Foreman, Mark R. S., E. LÖFSTRÖM-ENGDAHL, N. MABILE, Studies of a Solvent for GANEX Applications Containing CyMe 4 -BTBP and DEHBA in Cyclohexanone, *Separation Science and Technology* **2012**, 47, 663.
- [182] T. H. SIDDALL, EFFECTS OF STRUCTURE OF N,N-DISUBSTITUTED AMIDES ON THEIR EXTRACTION OF ACTINIDE AND ZIRCONIUM NITRATES AND OF NITRIC ACID 1, *J. Phys. Chem.* **1960**, 64, 1863.
- [183] T. H. SIDDALL III, Application of amides as extractants, **1961**.
- [184] P. N. PATHAK, N,N-Dialkyl amides as extractants for spent fuel reprocessing, *J Radioanal Nucl Chem* **2014**, 300, 7.
- [185] P. K. VERMA, P. N. PATHAK, N. KUMARI, B. SADHU, M. SUNDARARAJAN, V. K. ASWAL, P. K. MOHAPATRA, Effect of successive alkylation of N,N-dialkyl amides on the complexation behavior of uranium and thorium: solvent extraction, small angle neutron scattering, and computational studies, *The journal of physical chemistry. B* **2014**, 118, 14388.

- [186] P. N. PATHAK, L. B. KUMBHARE, V. K. MANCHANDA, Structural effects in N,N-dialkyl amides on their extraction behavior towards uranium and thorium, *Solvent Extraction and Ion Exchange* **2001**, 19, 105.
- [187] N. CONDAMINES, C. MUSIKAS, The extraction by N,N-Dialkylamides. II. Extraction of actinide cations, *Solvent Extraction and Ion Exchange* **1992**, 10, 69.
- [188] M. J. SANSFIELD, M. HELLIWELL, Extending the chemistry of the uranyl ion: Lewis acid coordination to a U=O oxygen, *Journal of the American Chemical Society* **2004**, 126, 1036.
- [189] R. G. PEARSON, Hard and soft acids and bases—the evolution of a chemical concept, *Coordination Chemistry Reviews* **1990**, 100, 403.
- [190] C. RABBE, *Thesis*, University of Rouen, **1996**.
- [191] G. FERRU, *Thesis*, University of Montpellier, **2013**.
- [192] C. BERTHON, C. CHACHATY, NMR and IR Spectrometry studies of monoamide complexes with plutonium(IV) and lanthanide(III) nitrates, *Solvent Extraction and Ion Exchange* **1995**, 13, 781.
- [193] C. BERTHON, C. CHACHATY, Conformational analysis of monoamides complexed with plutonium nitrate in organic phase, **1993**.
- [194] G. FERRU, L. BERTHON, C. SOREL, O. DIAT, P. BAUDUIN, J.-P. SIMONIN, Influence of Extracted Solute on the Organization of a Monoamide Organic Solution, *Procedia Chemistry* **2012**, 7, 27.
- [195] G. FERRU, D. GOMES RODRIGUES, L. BERTHON, O. DIAT, P. BAUDUIN, P. GUILBAUD, Elucidation of the structure of organic solutions in solvent extraction by combining molecular dynamics and X-ray scattering, *Angewandte Chemie (International ed. in English)* **2014**, 53, 5346.
- [196] F. RODRIGUES, G. FERRU, L. BERTHON, N. BOUBALS, P. GUILBAUD, C. SOREL, O. DIAT, P. BAUDUIN, J. P. SIMONIN, J. P. MOREL ET AL., New insights into the extraction of uranium(VI) by an N,N-dialkylamide, *Molecular Physics* **2014**, 112, 1362.
- [197] W. DAVIES, U. GRAY, A rapid and specific titrimetric method for the precise determination of uranium using iron (II) sulphate as reductant, *Talanta* **1964**, 11, 1203.
- [198] A. R. EBERLE, M. W. LERNER, C. G. GOLDBECK, C. J. RODDEN in *Safeguards techniques*, **1970**.

- [199] J. KOHLBRECHER, "SASfit: A program for fitting simple structural models to small angle scattering data", can be found under <https://kur.web.psi.ch/sans1/SANSSoft/sasfit.html>, **2014**.
- [200] S. SCHÖTTL, J. MARCUS, O. DIAT, D. TOURAUD, W. KUNZ, T. ZEMB, D. HORINEK, Emergence of surfactant-free micelles from ternary solutions, *Chemical Science* **2014**, 5, 2949.
- [201] S. SCHÖTTL, D. TOURAUD, W. KUNZ, T. ZEMB, D. HORINEK, Consistent definitions of "the interface" in surfactant-free micellar aggregates, *Colloids and Surfaces A: Physicochemical and Engineering Aspects* **2015**, 480, 222.
- [202] S. SCHÖTTL, D. HORINEK, Aggregation in detergent-free ternary mixtures with microemulsion-like properties, *Current Opinion in Colloid & Interface Science* **2016**, 22, 8.
- [203] H. E. STANLEY, Phase transitions and critical phenomena, Clarendon Press, Oxford, **1971**.
- [204] T. ZEMB, O. DIAT, What can we learn from combined SAXS and SANS measurements of the same sample containing surfactants?, *J. Phys.: Conf. Ser.* **2010**, 247, 12002.
- [205] C. BAUER, Thesis, University of Montpellier, **2011**.
- [206] R. F. FEDORS, A method for estimating both the solubility parameters and molar volumes of liquids, *Polym. Eng. Sci.* **1974**, 14, 147.
- [207] P. GUILBAUD, L. BERTHON, W. LOUISFREMA, O. DIAT, N. ZORZ, Determination of the Structures of Uranyl-Tri-n-butyl-Phosphate Aggregates by Coupling Experimental Results with Molecular Dynamic Simulations, *Chemistry (Weinheim an der Bergstrasse, Germany)* **2017**, 23, 16660.
- [208] H. GÄRTNER, H. GASCHA, Formelsammlung. *Mathematik, Physik, anorganische Chemie*, Compact, München, **2013**.
- [209] K. WYNNE, The Mayonnaise Effect, *The journal of physical chemistry letters* **2017**, 8, 6189.
- [210] E. D. C.N. ANDRADE, LVIII. A theory of the viscosity of liquids .—Part II, *The London, Edinburgh, and Dublin Philosophical Magazine and Journal of Science* **2009**, 17, 698.
- [211] S. ARRHENIUS, Über die Reaktionsgeschwindigkeit bei der Inversion von Rohrzucker durch Säuren, *Zeitschrift für physikalische Chemie* **1889**, 4, 226.

- [212] N. OUERFELLI, Z. BARHOUMI, O. IULIAN, Viscosity Arrhenius Activation Energy and Derived Partial Molar Properties in 1,4-Dioxane + Water Binary Mixtures from 293.15 to 323.15 K, *J Solution Chem* **2012**, *41*, 458.
- [213] S. G. E. GIAP, The hidden property of Arrhenius-type relationship, *J. Phys. Sci* **2010**, *21*, 29.
- [214] O. O. OKOTURO, T. J. VANDERNOOT, Temperature dependence of viscosity for room temperature ionic liquids, *Journal of Electroanalytical Chemistry* **2004**, *568*, 167.
- [215] W. LEGRUM, Riechstoffe, zwischen Gestank und Duft. *Vorkommen, Eigenschaften und Anwendung von Riechstoffen und deren Gemischen*, Vieweg+Teubner Verlag / Springer Fachmedien Wiesbaden GmbH Wiesbaden, Wiesbaden, **2011**.
- [216] COSMOlogic - Predicting Solutions, COSMOtherm Reference Manual C 3.0, **2017**.
- [217] T. ARAKI, H. TANAKA, Wetting-induced depletion interaction between particles in a phase-separating liquid mixture, *Physical review. E, Statistical, nonlinear, and soft matter physics* **2006**, *73*, 61506.
- [218] J. W. CAHN, Critical point wetting, *J. Chem. Phys.* **1977**, *66*, 3667.
- [219] M. TOMSIC, A. JAMNIK, G. FRITZ-POPOVSKI, O. GLATTER, L. VLCEK, Structural properties of pure simple alcohols from ethanol, propanol, butanol, pentanol, to hexanol, *J. Phys. Chem. B* **2007**, *111*, 1738.
- [220] J. F. RHODES, R. J. ABBUNDI, D. W. COOKE, V. K. MATHUR, M. D. BROWN, Temperature dependence of fluorescence spectra from x-ray-excited single-crystal CaF₂, *Phys. Rev. B* **1985**, *31*, 5393.
- [221] D. J. MITCHELL, G. J. T. TIDY, L. WARING, T. BOSTOCK, M. P. MCDONALD, Phase behaviour of polyoxyethylene surfactants with water. Mesophase structures and partial miscibility (cloud points), *J. Chem. Soc., Faraday Trans. 1* **1983**, *79*, 975.
- [222] P. R. DANESI, G. F. VANDEGRIFT, Activity coefficients of bis(2-ethylhexyl) phosphoric acid in n-dodecane, *Inorganic and Nuclear Chemistry Letters* **1981**, *17*, 109.
- [223] K. VOGTT, G. BEAUCAGE, M. WEAVER, H. JIANG, Scattering Function for Branched Wormlike Chains, *Langmuir : the ACS journal of surfaces and colloids* **2015**, *31*, 8228.
- [224] R. J. ELLIS, T. DEMARS, G. LIU, J. NIKLAS, O. G. POLUEKTOV, I. A. SHKROB, In the Bottlebrush Garden: The Structural Aspects of Coordination Polymer Phases formed in Lanthanide Extraction with Alkyl Phosphoric Acids, *The journal of physical chemistry. B* **2015**, *119*, 11910.

- [225] K. SHINODA, E. HUTCHINSON, Pseudo-phase separation model for thermodynamic calculations on micellar solutions, *J. Phys. Chem.* **1962**, 66, 577.
- [226] C. R. SAFINYA, E. B. SIROTA, D. ROUX, G. S. SMITH, Universality in interacting membranes, *Physical review letters* **1989**, 62, 1134.
- [227] P. PIERUSCHKA, S. MARČELJA, Statistical mechanics of random bicontinuous phases, *J. Phys. II France* **1992**, 2, 235.
- [228] A. G. ZILMAN, S. A. SAFRAN, Role of cross-links in bundle formation, phase separation and gelation of long filaments, *EPL (Europhysics Letters)* **2003**, 63, 139.
- [229] D. D. L. MINH, D. LE MINH, Understanding the Hastings Algorithm, *Communications in Statistics - Simulation and Computation* **2014**, 44, 332.
- [230] B. P. BINKS, H. KELLAY, J. MEUNIER, Effects of alkane chain length on the bending elasticity constant k of aot monolayers at the planar oil-water interface, *EPL (Europhysics Letters)* **1991**, 16, 53.
- [231] B. FARAGO, D. RICHTER, JS. HUANG, SA. SAFRAN, ST.MILNER, Shape and size fluctuations of microemulsion droplets, *Physical review letters* **1990**, 65, 3348.
- [232] J. DUHAMET, H. MÖHWALD, M. PLEINES, T. ZEMB, Self-Regulated Ion Permeation through Extraction Membranes, *Langmuir* **2017**, 33, 9873.
- [233] K. S. GANDHI, M. C. WILLIAMS, Solvent effects on the viscosity of moderately concentrated polymer solutions, *J. polym. sci., C Polym. symp.* **1971**, 35, 211.
- [234] F. ECKERT, "COSMOtherm Reference manual, Version C3.0, Release 17.01. COSMOlogic GmbH & Co. KG", can be found under <http://www.cosmologic.de>, **2017**.
- [235] R. ODA, S. J. CANDAU, I. HUC, Gemini surfactants, the effect of hydrophobic chain length and dissymmetry, *Chem. Commun.* **1997**, 2105.
- [236] CR. SAFINYA, RB. SIROTA, D. ROUX, GS. SMITH, Universality in interacting membranes, *Physical review letters* **1989**, 62, 1134.
- [237] M. MIGUIRDITCHIAN, P. BARON, M. S. LOPES, G. MILANOLE, C. MARIE, WO2017017193 A1, **2017**.
- [238] ExxonMobil, "Solvesso - Heavy aromatic solvents", can be found under <https://www.exxonmobilchemical.com/en/products-and-services/solvents/heavy-aromatic-solvents>, **2018**.
- [239] Isofol C12- C23 - Guerbet alcohols - technical data sheet, "Sasol Performance Chemicals", can be found under <http://www.sasoltechdata.com/tds/ISOFOL.pdf>, **2017**.
- [240] M. C. BOURNE, Limitations of rheology in food texture measurements, *J Texture Studies* **1977**, 8, 219.

- [241] R. LAMBOURNE, T. A. STRIVENS, Paint and surface coatings. *Theory and practice*, Woodhead Pub, Cambridge, Eng, **1999**.
- [242] J. YANG, Viscoelastic wormlike micelles and their applications, *Current Opinion in Colloid & Interface Science* **2002**, 7, 276.
- [243] S. EZRAHI, E. TUVAL, A. ASERIN, Properties, main applications and perspectives of worm micelles, *Advances in Colloid and Interface Science* **2006**, 128-130, 77.
- [244] H. REHAGE, Rheological properties of viscoelastic surfactant solutions, *Dynamics of surfactant self-assemblies* **2005**, 125, 419.
- [245] H. HOFFMANN, W. ULBRICHT in *Handbook of applied surface and colloid chemistry* (Ed.: K. Holmberg), Wiley, Chichester, **2002**, pp. 189–214.
- [246] M. IN, Linear rheology of aqueous solutions of wormlike micelles, *SURFACTANT SCIENCE SERIES* **2007**, 140, 249.
- [247] H. REHAGE, H. HOFFMANN, Rheological properties of viscoelastic surfactant systems, *J. Phys. Chem.* **1988**, 92, 4712.
- [248] H. REHAGE, H. HOFFMANN, Viscoelastic surfactant solutions, *Molecular Physics* **1991**, 74, 933.
- [249] S. J. CANDAU, A. KHATORY, F. LEQUEUX, F. KERN, Rheological behaviour of wormlike micelles, *J. Phys. IV France* **1993**, 03, C1-197-C1-209.
- [250] D. BALZER, S. VARWIG, M. WEIHRAUCH, Viscoelasticity of personal care products, *Colloids and Surfaces A: Physicochemical and Engineering Aspects* **1995**, 99, 233.
- [251] A. SCHMALSTIEG in *Handbook of applied surface and colloid chemistry* (Ed.: K. Holmberg), Wiley, Chichester, **2002**.
- [252] DR. MUNDEN, Effect of perfumes on the viscosity of surfactant systems, *Cosmetics and toiletries* **1988**, 103, 65.
- [253] M. KAMADA, S. SHIMIZU, K. ARAMAKI, Manipulation of the viscosity behavior of wormlike micellar gels by changing the molecular structure of added perfumes, *Colloids and Surfaces A: Physicochemical and Engineering Aspects* **2014**, 458, 110.
- [254] E. FISCHER, W. FIEBER, C. NAVARRO, H. SOMMER, D. BENCZÉDI, M. I. VELAZCO, M. SCHÖNHOF, Partitioning and Localization of Fragrances in Surfactant Mixed Micelles, *J Surfact Deterg* **2009**, 12, 73.
- [255] Y. TOKUOKA, H. UCHIYAMA, M. ABE, K. OGINO, Solubilization of synthetic perfumes by nonionic surfactants, *Journal of Colloid and Interface Science* **1992**, 152, 402.

- [256] Y. TOKUOKA, H. UCHIYAMA, M. ABE, S. D. CHRISTIAN, Solubilization of some synthetic perfumes by anionic-nonionic mixed surfactant systems. 1, *Langmuir* **1995**, *11*, 725.
- [257] Z. MITRINOVA, S. TCHOLAKOVA, N. DENKOV, Control of surfactant solution rheology using medium-chain cosurfactants, *Colloids and Surfaces A: Physicochemical and Engineering Aspects* **2018**, *537*, 173.
- [258] X. TANG, W. ZOU, P. H. KOENIG, S. D. MCCONAUGHY, M. R. WEAVER, D. M. EIKE, M. J. SCHMIDT, R. G. LARSON, Multiscale Modeling of the Effects of Salt and Perfume Raw Materials on the Rheological Properties of Commercial Threadlike Micellar Solutions, *The journal of physical chemistry. B* **2017**, *121*, 2468.
- [259] H. WANG, X. TANG, D. M. EIKE, R. G. LARSON, P. H. KOENIG, Scission Free Energies for Wormlike Surfactant Micelles, *Langmuir : the ACS journal of surfaces and colloids* **2018**, *34*, 1564.
- [260] F. HOFMEISTER, 24. Zur Lehre von der Wirkung der Salze, *Archiv f. experiment. Pathol. u. Pharmacol* **1890**, *27*, 395.
- [261] F. HOFMEISTER, Zur Lehre von der Wirkung der Salze, *Archiv f. experiment. Pathol. u. Pharmacol* **1891**, *28*, 210.
- [262] N. VLACHY, B. JAGODA-CWIKLIK, R. VACHA, D. TOURAUD, P. JUNGWIRTH, W. KUNZ, Hofmeister series and specific interactions of charged headgroups with aqueous ions, *Advances in Colloid and Interface Science* **2009**, *146*, 42.
- [263] W. KUNZ, J. HENLE, B. W. NINHAM, 'Zur Lehre von der Wirkung der Salze' (about the science of the effect of salts), *Current Opinion in Colloid & Interface Science* **2004**, *9*, 19.
- [264] K. D. COLLINS, Ions from the Hofmeister series and osmolytes, *Methods (San Diego, Calif.)* **2004**, *34*, 300.
- [265] W. KUNZ, R. NEUEDER, Specific ion effects, World Scientific Pub. Co, Singapore, Hackensack, N.J, **2010**.
- [266] N. VLACHY, B. JAGODA-CWIKLIK, R. VÁCHA, D. TOURAUD, P. JUNGWIRTH, W. KUNZ, Hofmeister series and specific interactions of charged headgroups with aqueous ions, *Advances in Colloid and Interface Science* **2009**, *146*, 42.
- [267] S. MAY in *Giant micelles. Properties and applications* (Ed.: R. Zana), Taylor & Francis, Boca Raton, **2007**, pp. 41–80.

- [268] M. GRADZIELSKI, D. LANGEVIN, T. SOTTMANN, R. STREY, Droplet microemulsions at the emulsification boundary, *The Journal of chemical physics* **1997**, *106*, 8232.
- [269] Y. CHEVALIER, L. BELLONI, J. B. HAYTER, T. ZEMB, Effect of interfacial charge on micellar structure, *J. Phys. France* **1985**, *46*, 749.
- [270] Y. CHEVALIER, T. ZEMB, The structure of micelles and microemulsions, *Rep. Prog. Phys.* **1990**, *53*, 279.
- [271] S. F. CLANCY, H. H. PARADIES, Structure, Diffusivity and Linear Rheology of Sodium Ether Dodecylsulfate in Aqueous Solutions – (I), *Zeitschrift für physikalische Chemie* **2001**, *215*, 403.
- [272] B. CABANE, R. T. DUPLESSIX, T. ZEMB, High resolution neutron scattering on ionic surfactant micelles, *Journal de Physique* **1985**, *46*, 2161.
- [273] B. L. BALES, A Definition of the Degree of Ionization of a Micelle Based on Its Aggregation Number, *The journal of physical chemistry. B* **2001**, *105*, 6798.
- [274] M. BENRRAOU, B. L. BALES, R. ZANA, Effect of the Nature of the Counterion on the Properties of Anionic Surfactants. 1. Cmc, Ionization Degree at the Cmc and Aggregation Number of Micelles of Sodium, Cesium, Tetramethylammonium, Tetraethylammonium, Tetrapropylammonium, and Tetrabutylammonium Dodecyl Sulfates, *The journal of physical chemistry. B* **2003**, *107*, 13432.
- [275] N. V. LEBEDEVA, A. SHAHINE, B. L. BALES, Aggregation number-based degrees of counterion dissociation in sodium n-alkyl sulfate micelles, *The journal of physical chemistry. B* **2005**, *109*, 19806.
- [276] V. TCHAKALOVA, F. TESTARD, K. WONG, A. PARKER, D. BENCZÉDI, T. ZEMB, Solubilization and interfacial curvature in microemulsions. I. Interfacial expansion and co-extraction of oil, *Colloids and Surfaces A: Physicochemical and Engineering Aspects* **2008**, *331*, 31.
- [277] V. LUTZ-BUENO, S. ISABETTINI, F. WALKER, S. KUSTER, M. LIEBI, P. FISCHER, Ionic micelles and aromatic additives, *Physical chemistry chemical physics : PCCP* **2017**, *19*, 21869.
- [278] Y. FAN, H. TANG, R. STRAND, Y. WANG, Modulation of partition and localization of perfume molecules in sodium dodecyl sulfate micelles, *Soft Matter* **2016**, *12*, 219.
- [279] PubChem DATABASE, "PubChem CIDs 1183; 8842; 6549; 440917", can be found under <https://pubchem.ncbi.nlm.nih.gov>.

- [280] V. TCHAKALOVA, F. TESTARD, K. WONG, A. PARKER, D. BENCZÉDI, T. ZEMB, Solubilization and interfacial curvature in microemulsions. II. Surfactant efficiency and PIT, *Colloids and Surfaces A: Physicochemical and Engineering Aspects* **2008**, 331, 40.
- [281] V. TCHAKALOVA, W. FIEBER, Classification of Fragrances and Fragrance Mixtures Based on Interfacial Solubilization, *J Surfact Deterg* **2012**, 15, 167.
- [282] W. FIEBER, S. FRANK, C. HERRERO, Competition between surfactants and apolar fragrances in micelle cores, *Colloids and Surfaces A: Physicochemical and Engineering Aspects* **2018**, 539, 310.
- [283] D. ROUX, C. COULON, M. E. CATES, Sponge phases in surfactant solutions, *J. Phys. Chem.* **1992**, 96, 4174.
- [284] T. TLUSTY, S. A. SAFRAN, Microemulsion networks, *Journal of Physics: Condensed Matter* **2000**, 12, A253.
- [285] A. AROTI, E. LEONTIDIS, M. DUBOIS, T. ZEMB, G. BREZESINSKI, Monolayers, bilayers and micelles of zwitterionic lipids as model systems for the study of specific anion effects, *Colloids and Surfaces A: Physicochemical and Engineering Aspects* **2007**, 303, 144.
- [286] E. LEONTIDIS, Chaotropic salts interacting with soft matter, *Current Opinion in Colloid & Interface Science* **2016**, 23, 100.
- [287] L. ABEZGAUZ, K. KUPERKAR, P. A. HASSAN, O. RAMON, P. BAHADUR, D. DANINO, Effect of Hofmeister anions on micellization and micellar growth of the surfactant cetylpyridinium chloride, *Journal of Colloid and Interface Science* **2010**, 342, 83.
- [288] S. DENGLER, A. KLAUS, G. J. T. TIDDY, W. KUNZ, How specific are ion specificities?, *Faraday Discuss* **2013**, 160, 121.
- [289] C. OELSCHLAEGER, P. SUWITA, N. WILLENBACHER, Effect of counterion binding efficiency on structure and dynamics of wormlike micelles, *Langmuir : the ACS journal of surfaces and colloids* **2010**, 26, 7045.
- [290] Y. MARCUS, Thermodynamics of solvation of ions. Part 5.—Gibbs free energy of hydration at 298.15 K, *Faraday Trans.* **1991**, 87, 2995.
- [291] H. I. PETRACHE, T. ZEMB, L. BELLONI, V. A. PARSEGIAN, Salt screening and specific ion adsorption determine neutral-lipid membrane interactions, *Proceedings of the National Academy of Sciences of the United States of America* **2006**, 103, 7982.

- [292] B.-Y. HA, D. THIRUMALAI, Bending Rigidity of Stiff Polyelectrolyte Chains, *Macromolecules* **2003**, 36, 9658.
- [293] R. A. ABDEL-RAHEM, M. REGER, M. HLOUCHA, H. HOFFMANN, Rheology of Aqueous Solutions Containing SLES, CAPB, and Microemulsion, *Journal of dispersion science and technology* **2013**, 35, 64.
- [294] J. EASTOE, D. SHARPE, Properties of Phosphocholine Microemulsions and the Film Rigidity Model, *Langmuir : the ACS journal of surfaces and colloids* **1997**, 13, 3289.
- [295] P. BAUDUIN, D. TOURAUD, W. KUNZ, M.-P. SAVELLI, S. PULVIN, B. W. NINHAM, The influence of structure and composition of a reverse SDS microemulsion on enzymatic activities and electrical conductivities, *Journal of Colloid and Interface Science* **2005**, 292, 244.
- [296] L. FORET, A. WÜRGER, Discontinuous bending rigidity and cosurfactant adsorption of amphiphile layers, *Physical review letters* **2001**, 86, 5930.
- [297] D. DANINO, Y. TALMON in *Molecular Gels. Materials with Self-Assembled Fibrillar Networks*, pp. 251–272.
- [298] L. ZISERMAN, L. ABEZGAUZ, O. RAMON, S. R. RAGHAVAN, D. DANINO, Origins of the viscosity peak in wormlike micellar solutions. 1. Mixed catanionic surfactants. A cryo-transmission electron microscopy study, *Langmuir : the ACS journal of surfaces and colloids* **2009**, 25, 10483.
- [299] F. KERN, P. LEMARECHAL, S. J. CANDAU, M. E. CATES, Rheological properties of semidilute and concentrated aqueous solutions of cetyltrimethylammonium bromide in the presence of potassium bromide, *Langmuir* **1992**, 8, 437.
- [300] V. SCHMITT, F. LEQUEUX, Surfactant Self-Diffusion in Wormlike Micelles, *Langmuir : the ACS journal of surfaces and colloids* **1998**, 14, 283.
- [301] E. LEONTIDIS, A. AROTI, L. BELLONI, Liquid expanded monolayers of lipids as model systems to understand the anionic hofmeister series, *The journal of physical chemistry. B* **2009**, 113, 1447.
- [302] M. MONKENBUSCH, O. HOLDERER, H. FRIELINGHAUS, D. BYELOV, J. ALLGAIER, D. RICHTER, Bending moduli of microemulsions; comparison of results from small angle neutron scattering and neutron spin-echo spectroscopy, *J. Phys.: Condens. Matter* **2005**, 17, S2903.
- [303] V. TCHAKALOVA, F. TESTARD, K. WONG, A. PARKER, D. BENCZÉDI, T. ZEMB, Solubilization and interfacial curvature in microemulsions, *Colloids and Surfaces A: Physicochemical and Engineering Aspects* **2008**, 331, 40.

- [304] Z. J. YU, G. XU, Physicochemical properties of aqueous mixtures of tetrabutylammonium bromide and anionic surfactants. 1. Temperature-induced micellar growth and cloud point phenomenon, *J. Phys. Chem.* **1989**, 93, 7441.
- [305] A. Z. NAQVI, Kabir-ud-Din, Clouding phenomenon in amphiphilic systems, *Colloids and surfaces. B, Biointerfaces* **2018**, 165, 325.
- [306] W. BROWN, R. JOHNSEN, P. STILBS, B. LINDMAN, Size and shape of nonionic amphiphile (C12E6) micelles in dilute aqueous solutions as derived from quasielastic and intensity light scattering, sedimentation, and pulsed-field-gradient nuclear magnetic resonance self-diffusion data, *J. Phys. Chem.* **1983**, 87, 4548.
- [307] J. A. L. WAN, G. G. WARR, L. R. WHITE, F. GRIESER, Reappraisal of neutron scattering results on micellar solutions of dodecylhexaoxyethylene glycol monoether (C12E6), *Colloid and polymer science* **1987**, 265, 528.
- [308] M. CORTI, V. DEGIORGIO, Quasi-elastic light scattering study of intermicellar interactions in aqueous sodium dodecyl sulfate solutions, *J. Phys. Chem.* **1981**, 85, 711.
- [309] M. CORTI, C. MINERO, V. DEGIORGIO, Cloud point transition in nonionic micellar solutions, *J. Phys. Chem.* **1984**, 88, 309.
- [310] V. DEGIORGIO, R. PIAZZA, M. CORTI, C. MINERO, Critical properties of nonionic micellar solutions, *J. Chem. Phys.* **1985**, 82, 1025.
- [311] J. B. HAYTER, M. ZULAUF, Attractive interactions in critical scattering from non-ionic micelles, *Colloid and polymer science* **1982**, 260, 1023.
- [312] M. ZULAUF, J. P. ROSENBUSCH, Micelle clusters of octylhydroxyoligo (oxyethylenes), *J. Phys. Chem.* **1983**, 87, 856.
- [313] D. J. CEBULA, R. H. OTTEWILL, Neutron scattering studies on micelles of dodecylhexaoxyethylene glycol monoether, *Colloid and polymer science* **1982**, 260, 1118.
- [314] O. GLATTER, G. FRITZ, H. LINDNER, J. BRUNNER-POPELA, R. MITTELBAACH, R. STREY, S. U. EGELHAAF, Nonionic micelles near the critical point, *Langmuir* **2000**, 16, 8692.
- [315] L. A.M. RUPERT, A thermodynamic model of clouding in ethoxylate mixtures, *Journal of Colloid and Interface Science* **1992**, 153, 92.
- [316] A. BERNHEIM-GROSWASSER, E. WACHTEL, Y. TALMON, Micellar Growth, Network Formation, and Criticality in Aqueous Solutions of the Nonionic Surfactant C 12 E 5, *Langmuir : the ACS journal of surfaces and colloids* **2000**, 16, 4131.

- [317] A. BERNHEIM-GROSWASSER, T. TLUSTY, S. A. SAFRAN, Y. TALMON, Direct Observation of Phase Separation in Microemulsion Networks, *Langmuir : the ACS journal of surfaces and colloids* **1999**, 15, 5448.
- [318] A. ZILMAN, S. A. SAFRAN, T. SOTTMANN, R. STREY, Temperature Dependence of the Thermodynamics and Kinetics of Micellar Solutions, *Langmuir : the ACS journal of surfaces and colloids* **2004**, 20, 2199.
- [319] K. D. DANOV, P. A. KRALCHEVSKY, S. D. STOYANOV, J. L. COOK, I. P. STOTT, E. G. PELAN, Growth of wormlike micelles in nonionic surfactant solutions, *Advances in Colloid and Interface Science* **2018**, 256, 1.
- [320] P. G. NILSSON, B. LINDMAN, Water self-diffusion in nonionic surfactant solutions. Hydration and obstruction effects, *J. Phys. Chem.* **1983**, 87, 4756.
- [321] T. SHIKATA, M. OKUZONO, N. SUGIMOTO, Temperature-Dependent Hydration/Dehydration Behavior of Poly(ethylene oxide)s in Aqueous Solution, *Macromolecules* **2013**, 46, 1956.
- [322] G. SMITH, Physical Chemistry and Performance Properties of Guerbet Ethoxylates, Norman (Oklahoma), **2018**.
- [323] SASOL, "Surfactants - Product range", can be found under <http://www.sasoltechdata.com/MarketingBrochures/Surfactants.pdf>, **2010**.
- [324] W. C. GRIFFIN, Classification of surface-active agents by "HLB", *J. Soc. Cosmet. Chem.* **1949**, 1, 311.
- [325] P. A. WINSOR, Solvent properties of amphiphilic compounds, Butterworths Scientific Publications, **1954**.
- [326] K. SHINODA, H. ARAI, The correlation between phase inversion temperature in emulsion and cloud point in solution of nonionic emulsifier, *J. Phys. Chem.* **1964**, 68, 3485.
- [327] J. L. SALAGER, J. C. MORGAN, R. S. SCHECHTER, W. H. WADE, E. VASQUEZ, Optimum formulation of surfactant/water/oil systems for minimum interfacial tension or phase behavior, *Society of Petroleum Engineers Journal* **1979**, 19, 107.
- [328] S. QUESTE, J. L. SALAGER, R. STREY, J. M. AUBRY, The EACN scale for oil classification revisited thanks to fish diagrams, *Journal of Colloid and Interface Science* **2007**, 312, 98.

- [329] E. J. ACOSTA, The HLD–NAC equation of state for microemulsions formulated with nonionic alcohol ethoxylate and alkylphenol ethoxylate surfactants, *Colloids and Surfaces A: Physicochemical and Engineering Aspects* **2008**, 320, 193.
- [330] E. ACOSTA, E. SZEKERES, D. A. SABATINI, J. H. HARWELL, Net-Average Curvature Model for Solubilization and Supersolubilization in Surfactant Microemulsions, *Langmuir : the ACS journal of surfaces and colloids* **2003**, 19, 186.
- [331] P. G. de GENNES, C. TAUPIN, Microemulsions and the flexibility of oil/water interfaces, *J. Phys. Chem.* **1982**, 86, 2294.
- [332] S. ZARATE-MUÑOZ, A. BOZA TRONCOSO, E. ACOSTA, The Cloud Point of Alkyl Ethoxylates and Its Prediction with the Hydrophilic-Lipophilic Difference (HLD) Framework, *Langmuir : the ACS journal of surfaces and colloids* **2015**, 31, 12000.
- [333] S. K. KIRAN, E. J. ACOSTA, Predicting the Morphology and Viscosity of Microemulsions Using the HLD-NAC Model, *Ind. Eng. Chem. Res.* **2010**, 49, 3424.
- [334] M. DUVAIL, J.-F. DUFRÊCHE, L. ARLETH, T. ZEMB, Mesoscopic modelling of frustration in microemulsions, *Physical chemistry chemical physics : PCCP* **2013**, 15, 7133.
- [335] T. HELLWEG, D. LANGEVIN, Bending elasticity of the surfactant monolayer in droplet microemulsions, *Physical Review E* **1998**, 57, 6825.
- [336] TOTAL SPECIAL FLUIDS, "Isane - Isoparaffin products - Product Information", can be found under <http://www4.total.fr/pdf/fluides-speciaux/brand/isane-101027-2.pdf>, **2017**.
- [337] T. G. MEZGER, The Rheology Handbook. *4th Edition*, Vincentz Network, Hannover, **2014**.
- [338] V. J. ANDERSON, J. R.A. PEARSON, E. S. BOEK, The rheology of worm-like micellar fluids, *Rheology reviews* **2006**, 2006, 217.
- [339] A. KLAMT, Conductor-like screening model for real solvents, *J. Phys. Chem.* **1995**, 99, 2224.
- [340] A. KLAMT, V. JONAS, T. BÜRGER, J. C. W. LOHRENZ, Refinement and parametrization of COSMO-RS, *The Journal of Physical Chemistry A* **1998**, 102, 5074.
- [341] A. KLAMT, F. ECKERT, W. ARLT, COSMO-RS, *Annual review of chemical and biomolecular engineering* **2010**, 1, 101.
- [342] M. DUVAIL, S. VAN DAMME, P. GUILBAUD, Y. CHEN, T. ZEMB, J.-F. DUFRÊCHE, The role of curvature effects in liquid-liquid extraction, *Soft Matter* **2017**, 13, 5518.

- [343] A. F. KAPUSTINSKY, LIPILINA, II, The densities of aqueous uranyl nitrate solutions, and the apparent molar volumes of uranyl nitrate, *Russian Chemical Bulletin* **1956**, 5, 661.
- [344] S. MAY, Y. BOHBOT, A. BEN-SHAUL, Molecular Theory of Bending Elasticity and Branching of Cylindrical Micelles, *The Journal of Physical Chemistry B* **1997**, 101, 8648.